Optimization of Photovoltaic Performance for Luminescent Solar Concentrator Systems

Thesis by

Megan Elisabeth Phelan

In Partial Fulfillment of the Requirements for the
degree of
Doctor of Philosophy

CALIFORNIA INSTITUTE OF TECHNOLOGY
Pasadena, California

2023
(Defended November 17, 2022)

Megan Elisabeth Phelan
ORCID: 0000-0002-4968-7128

ACKNOWLEDGMENTS

Athletics have been an integral part of my life since I was a child; they instilled in me the importance of team. When it comes to this PhD and the achievements that came along the way, this race has truly been a team sport. No goal was achieved without immense support from my deep community of colleagues, friends, and family; thank you to everyone with whom I have worked, by whom I was supported, or simply those who distracted me from the woes of research.

First and foremost, I would like to thank my advisor and 'coach,' Harry Atwater. Harry, I feel so incredibly fortunate to have spent the last five years working in your lab. The enthusiasm and passion you bring to every new project is infectious and has expanded my intellectual curiosity throughout this PhD. However, most important to me has been Harry's unending support. Regardless of the challenges that confronted me throughout this PhD—from broken gloveboxes to a torn ACL—Harry has *always* been there to remind me that no challenge is insurmountable and often bares little effect on the end result. Harry, thank you for believing in me and pushing me to reach my full potential in everything that I take on.

Next, I thank my committee members: Keith Schwab, Ralph Nuzzo, and Joseph Falson. Keith, my committee chair, taught me the fundamentals of solid-state physics and encouraged my appreciation of nature when outside the lab. I have moreover been incredibly fortunate to collaborate with and be advised by Ralph on several of the projects that line this thesis. These projects have all been among my favorites, largely because of Ralph's scientific guidance, support, and genuine joy. Finally, I thank Joe for the sage advice he offered me when he first joined as faculty at Caltech: the productivity of your work/time in lab is far more important than working unproductively simply for face-time.

I further thank my colleagues, those teammates who collaborated with me throughout the numerous projects that built this thesis. Two colleagues, in particular, deserve special recognition: David Needell and Haley Bauser. David gave me the crash course on LSCs in my first year, but that was just the beginning. From travelling the world together to ba-nano pancakes, our friendship extends far beyond Caltech. I was lucky to share both research projects and an office with Haley, who has always been a sounding board and true friend regardless of how crazy our projects or life became. Additionally, I have had the pleasure to collaborate extensively while working on LSCs, so I would also like to thank everyone with whom I have worked on LSC-related projects, including Colton Bukowsky, Catherine Ryczek, Yuying Lin, Maggie Potter, Phil Jahelka, Pilar Espinet, and Mike Kelzenberg.

I have had the privilege to be part of several exciting collaborations throughout my PhD. I would like to thank each person with whom I have worked as part of the EFRC-PTL, ARPA-e, QESST, and SSPP collaborations, as well as the advisors who led the efforts. Each of these groups has advanced my scientific development and piqued my intellectual curiosity. And retreats/all-hands meetings have been lots of fun along the way!

The Atwater Group as a whole has been an incredible team of which to be a part. Specifically, I would like to thank Alex, Cora, Eowyn, Kyle, Prachi, Rebecca, Lucy, Annette, Hamid, Melissa, Komron, Joeson, and many others for their support and friendship. I have been fortunate during my time at Caltech to also have outstanding friends outside of the lab—Amy, Elyse, Sophie, Rebecca G.—thank you for your friendship and constant scientific curiosity, even when our respective research sounded like a foreign language.

While my scientific team has been integral to my academic success, support from friends and family have driven the rest. Alex and the entire Welch family have welcomed me and made sure I never felt alone while on the other side of the country, even if my name sometimes was forgotten in the shuffle. Alex, I cannot imagine what my life would have looked like the past 5 years had it not been for our Napa road trip. Thank you to my taco crew—Alex W., Sophie, Kendall, Alex C., Jamie, Kristine, John, Alexander, Eowyn, Spencer, Jason, Claire, Lauren, Taylor, Alex S., Sydney—for always giving me a place to go on Tuesdays, and for truly being my LA family. You have been there for me on countless occasions and I am so grateful to call each and every one of you friends. My Lake Avenue Church Evening Break table has been an incredible community, and I would like to thank Rebecca in particular for her exceptional friendship.

Most important, I thank my family, who has acted as my support system from the very beginning and laid the foundation for my success; namely, my Mom and Dad, my brothers, Greg and Matt, and my sisters-in-law, Joann and Lisa. My entire family has been my biggest advocate—encouraging me, never letting me believe I was anything less than capable, and always reminding me that a swim or visit to the ocean is the best panacea. My parents instilled in me a desire to work hard, a love of learning, and the importance of a positive attitude. My brothers have and will always be my role models; unfortunately they are both incredibly successful in everything they take on—from academics to athletics to parenting—making it difficult for my competitive self to keep up. My biggest appreciation goes to my mom, who on two (!!) occasions uprooted her life and came to live with me during my PhD to act as my personal nurse and the best grandmother in the world. I would not be the woman I am today without each of you—thank you.

And finally, all of my love goes to Gabriel, who tagged along as my writing buddy on several occasions. This thesis (countless sleepless typohs and all) is for you, my precious angel.

ABSTRACT

The luminescent solar concentrator (LSC), an emerging photovoltaic (PV) technology with myriad potential application areas, could help further spur global solar adoption. At its core, an LSC absorbs and down-shifts incident irradiation via luminophores, and then redirects the emitted photoluminescence through a dielectric waveguide towards small-area PV cells. Given this design, an LSC describes a planar concentrating technology that *i)* maintains low system costs by using small amounts of high-efficiency PV material and *ii)* enables concentration of both direct and diffuse irradiation. The underlying structure of an LSC—including flexibility, material versatility, and variable transparency—facilitates application areas that span utility, building integrated, and space-based solar power.

This thesis explores the optimization of LSC systems, measured based on photovoltaic performance, across each application area. We begin by examining photovoltaic device considerations for LSC integration, including device form factor, luminophore pairing, and microcell fabrication. We outline ideal component parameters for optimal LSC performance and fabricate a silicon heterojunction microcell with a record V_{OC} of 588mV. Next, we design and fabricate single-junction LSCs for two application areas: building-integrated PV and space-based solar power. Through simulations and technoeconomic analyses, we find that such designs are able to achieve 7% efficiency with a forecasted cost as low as 2.22 $/W for the building-integrated application, and a specific power up to 11.55 kW/kg with an associated cost as low as 0.24 $/W for the space-based application. Finally, we investigate the potential to combine luminescent concentration with conventional solar technologies, including each a silicon subcell and geometric concentrators. We demonstrate that hybridization of luminescent concentrators with certain conventional designs has the potential to boost PV performance in both direct and diffuse lighting.

We conclude by investigating future directions for LSCs, including improved overall system performance, as well as next-generation designs for each building-integrated and space-based applications.

PUBLISHED CONTENT AND CONTRIBUTIONS

Portions of this thesis have been drawn from the following publications:

[1] **Phelan, M.**; Needell, D. R.; Bauser, H.; Su, H.; Deceglie, M.; Theingi, S.; Koscher, B.; Nett, Z.; Bukowsky, C. R.; Ilic, O.; Stradins, P.; Geisz, J.; Nuzzo, R.; Alivisatos, A. P.; Atwater, H. A. Outdoor Performance of a Tandem InGaP/Si Photovoltaic Luminescent Solar Concentrator. *Sol. Energy Mater. Sol. Cells* 2021, 223 (October 2020), 110945. https://doi.org/10.1016/j.solmat.2020.110945.
***M.E.P.** fabricated the LSC devices, performed the outdoor testing measurements, performed the data analysis, and wrote the manuscript.*

[2] Potter, M. M. $^{\top}$; **Phelan, M. E.** $^{\top}$; Balaji, P.; Jahelka, P.; Bauser, H. C.; Glaudell, R. D.; Went, C. M.; Enright, M. J.; Needell, D. R.; Augusto, A.; Atwater, H. A.; Nuzzo, R. G. Silicon Heterojunction Microcells. *ACS Appl. Mater. Interfaces 2021*, 13 (38), 45600–45608. https://doi.org/10.1021/acsami.1c11122.
***M.E.P.** fabricated the laser cut microcell devices, performed all measurements, contributed to the data analysis, and wrote the manuscript.*

[3] **Phelan, M. E.** $^{\top}$; Potter, M. M. $^{\top}$; Balaji, P.; Jahelka, P. R.; Bauser, H. C.; Glaudell, R.; Needell, D. R.; Enright, M.; Augusto, A.; Nuzzo, R.; Atwater, H. A. Fabrication Techniques for High-Performance Si Heterojunction (SHJ) Microcells. In *2021 IEEE 48th Photovoltaic Specialists Conference (PVSC)*; IEEE, 2021; pp 0330–0334.
https://doi.org/10.1109/PVSC43889.2021.9518579.
***M.E.P.** fabricated the laser cut microcell devices, performed all experimental measurements, performed the data analysis, and wrote the conference proceeding.*

[4] Needell, D.R.; Potter, M.M.; **Phelan, M.E.**; Jahelka, P.R.; Bauser, H.C.; Korus, D.; Velarde, A.; Balaji, P.; Augusto, A.; McDaniel, H.; Geisz, J.F.; Nuzzo, R.G., Atwater, H.A. Performance Limits and Applications of Area-scalable Luminescent Solar Concentrator Photovoltaic Devices. Submitted to *Advanced Energy Materials*, 2022.
***M.E.P.** contributed to the project conceptualization and LIV measurements, and wrote sections of the manuscript.*

[5] **Phelan**, **M. E.**; Needell, D. R.; Potter, M. M.; Bauser, H. C.; Nuzzo, R. G.; Atwater, H. A. Photovoltaic Thermal Management in Luminescent Solar Concentrators. Accepted to *2022 IEEE 49th Photovoltaic Specialists Conference (PVSC)*; IEEE, 2022.
https://doi.org/10.1109/PVSC48317.2022.9938634
***M.E.P.** performed the simulation and data analysis, and wrote the conference proceeding.*

Additional published content related to this thesis includes the following publications:

[6] Needell, D. R.; Bauser, H.; **Phelan, M.**; Bukowsky, C. R.; Ilic, O.; Kelzenberg, M. D.; Atwater, H. A. Ultralight Luminescent Solar Concentrators for Space Solar Power Systems. In *2019 IEEE 46th Photovoltaic Specialists Conference (PVSC)*; IEEE, 2019; pp 2798–2801. https://doi.org/10.1109/ PVSC40753.2019.8981161.
***M.P.** contributed to the project conceptualization and edited the conference proceeding.*

[7] Theingi, S.; Needell, D. R.; Bauser, H. C.; **Phelan, M. E.**; Nemeth, W.; Findley, D.; Su, H.; Koscher, B. A.; Nett, Z.; Ilic, O.; Bukowsky, C. R.; Nuzzo, R. G.; Alivisatos, A. P.; Geisz, J. F.; Stradins, P.; Atwater, H. A. Luminescent Solar Concentrator Tandem-on-Silicon with above 700mV Passivated Contact Silicon Bottom Cell. In *2019 IEEE 46th Photovoltaic Specialists Conference (PVSC)*; IEEE, 2019; pp 0747–0749. https://doi.org/10.1109/ PVSC40753.2019.8980809.
M.E.P. *contributed to the project conceptualization, performed measurements, and edited the conference proceeding.*

[8] Lunardi, M. M.; Needell, D. R.; Bauser, H.; **Phelan, M.**; Atwater, H. A.; Corkish, R. Life Cycle Assessment of Tandem LSC-Si Devices. *Energy 2019*, 181, 1–10. https://doi.org/10.1016/j.energy.2019.05.085.
M.P. *contributed to the project conceptualization and provided input on the manuscript.*

[9] Bauser, H. C.; Bukowsky, C. R.; **Phelan, M.**; Weigand, W.; Needell, D. R.; Holman, Z. C.; Atwater, H. A. Photonic Crystal Waveguides for >90% Light Trapping Efficiency in Luminescent Solar Concentrators. *ACS Photonics 2020*, 7 (8), 2122–2131. https://doi.org/10.1021/acsphotonics.0c00593.
M.P. *performed the concentration factor calculations and edited the manuscript.*

[10] Potter, M. M.; Yoder, M. A.; Petronico, A.; Lehman, S. E.; Nicolau, B. G.; Enright, M. J.; **Phelan, M.**; He, J.; Atwater, H. A.; Nuzzo, R. G., Autonomous Light Management in Flexible Photoelectrochromic Films Integrating High Performance Silicon Solar Microcells. *ACS Applied Energy Materials* **2020,** *3* (2), 1540-1551.
https://doi.org/10.1021/acsaem.9b01987
M.P. *contributed to spectral measurements and provided input on the manuscript.*

[11] Needell, D. R.$^{\top}$; **Phelan, M. E.** $^{\top}$; Hartlove, J. T.; Atwater, H. A. Solar Power Windows: Connecting Scientific Advances to Market Signals. *Energy 2021*, 219, 119567. https://doi.org/10.1016/j.energy.2020.119567.
M.E.P. *conducted all interviews, processed data, and wrote the manuscript.*

[12] Bauser, H.; Bukowsky, C. R.; **Phelan, M.**; Weigand, W.; Needell, D. R.; Holman, Z. C.; Atwater, H. A. Luminescent Solar Concentrators with High Concentration Using Photonic Crystal Waveguides. *High Contrast Metastructures X*; SPIE, 2021; Vol. 11695, p 13. https://doi.org/10.1117/12.2576720.
M.P. *performed the concentration factor calculations and provided input on the conference proceeding.*

[13] Enright, M.J.; Jasrasaria, D.; Hanchard, M.M.; Needell, D.R.; **Phelan, M.E.**; Weinberg, D.; McDowell, B.M.; Hsiao, H.W.; Akbari, H.; Kottwitz, M.; Potter, M.M.; Wong, J.; Zuo, J.M.; Atwater, H.A.; Rabani, E.; Nuzzo, R.G. Role of Atomic Structure and Exciton Delocalization on Photoluminescence in NIR Emissive InAs/InP/ZnSe Quantum Dots. *Journal of Physical Chemistry C,* 2022.
https://doi.org/10.1021/acs.jpcc.2c01499
M.E.P. *contributed to the idea for the project, sample preparation and lifetime measurements, plotted data for the manuscript, and provided input on the manuscript.*

[14] Bauser, H.C.; Foley, M.; **Phelan, M.E.**; Weigand, W.; Needell, D.R.; Holman, Z.C.; Atwater, H.A. Amorphous Silicon Carbide High Contrast Gratings as Highly Efficient Spectrally Selective Visible Reflectors. *Optics Express*, 2022.
https://doi.org/10.1364/OE.456898
***M.E.P.** contributed to the spectral measurements and data analysis and provided input on the manuscript.*

[15] Meyer A. R.; Theingi, S.; **Phelan**, **M. E.;** Hinkle, K.; Allridge, E.; Chen, K.; Hartenstein, M.; Lima Salles, C.; Nemeth, W.; Lenahan, P. M.; Agarawal, S.; Atwater, H. A.; Stradins, P. Miniature Passivated Contact Si Solar Cells: From Electrically Detected Magnetic Resonance to Space. Accepted to *AIP Proceedings SiliconPV 2022.*
***M.E.P.** provided IV measurements and wrote sections of the proceeding.*

[16] Needell, D.R.; **Phelan, M.E.**; Korus, D.; Bauser, H.C.; Kelzenberg, M.D.; Loke, S.; Theingi, S.; McDaniel, H.; Stradins, P.; Geisz, J.F.; Nuzzo, R.G.; Atwater, H.A. Luminescent Solar Concentrators Flown in Lower Earth Orbit. *In Progress*, 2023.
***M.E.P.** contributed to project conceptualization, fabricated samples, and provided input on the manuscript.*

TABLE OF CONTENTS

LIST OF FIGURES

LIST OF TABLES

Number *Page*

CHAPTER 1: INTRODUCTION

Since the industrial revolution, the average temperature on earth has risen by approximately 1 degree Celsius, and is projected to hit 1.5°C by 2040 if the current warming rate continues [1]. Rising temperatures lead to myriad consequences—including increased natural disasters, unsteady climates, heightened pollution, and changes in agricultural growth—all of which threaten life on Earth. Since 1960, the incidence of natural disasters, specifically, has increased by tenfold [2]. As shown in Figure 1, consequences from rising temperatures occur at various discrete checkpoints—e.g., coral bleaching begins when average temperature rises above 0.8°C, whereas a substantial burden on health services occurs at 3.3°C [3]. Given our current 1°C rise above pre-industrial levels, our planet is already experiencing irreversible global impacts, including water shortages/droughts, coral bleaching, negative impacts on food production, increased storms and flooding, malnutrition, and heightened mortality from natural disasters (see Figure 1) [1], [4]. As temperatures continue to rise, the global burden in each of these areas will intensify and result in additional consequences.

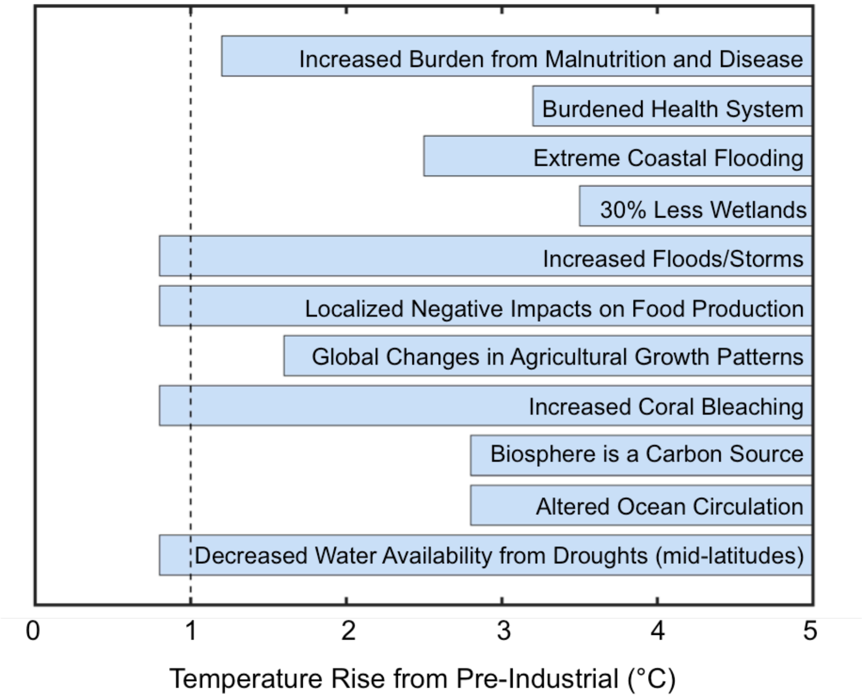

Figure 1: Consequences of increased temperatures on earth.
Temperature rise, from the pre-industrial era, associated with the initiation of each global consequence. The dotted vertical line indicates the current status of heightened temperatures, and the consequences that have already begun as a result. Adapted from [3].

Global warming is attributed to an increase in greenhouse gas emissions [1], [3], [5]. Greenhouse gases refer specifically to those molecules that cannot be broken down by the atmosphere and therefore accumulate in the troposphere, the lowest layer of the atmosphere. These gases absorb infrared radiation, which would otherwise escape the troposphere after being reflected from Earth's surface, thereby contributing to heightened average global temperatures [6], [7]. Emissions can be specifically broken down by each individual greenhouse gas—CO_2, CH_4, N_2O, and F-gases—as shown in Figure 2a [8], [9]. As shown, CO_2 makes up the vast majority of all greenhouse gas emissions. In Figure 2b, we further see how greenhouse gases are emitted by sector, demonstrating that the energy sector is the largest contributor of greenhouse gases [10]. In order to prevent heightened warming, we need to alter our current human behavior. One main way to do so is to reduce CO_2 emissions in the energy sector by reducing our dependence on fossil fuels and increasing the usage of renewable energy [1], [11].

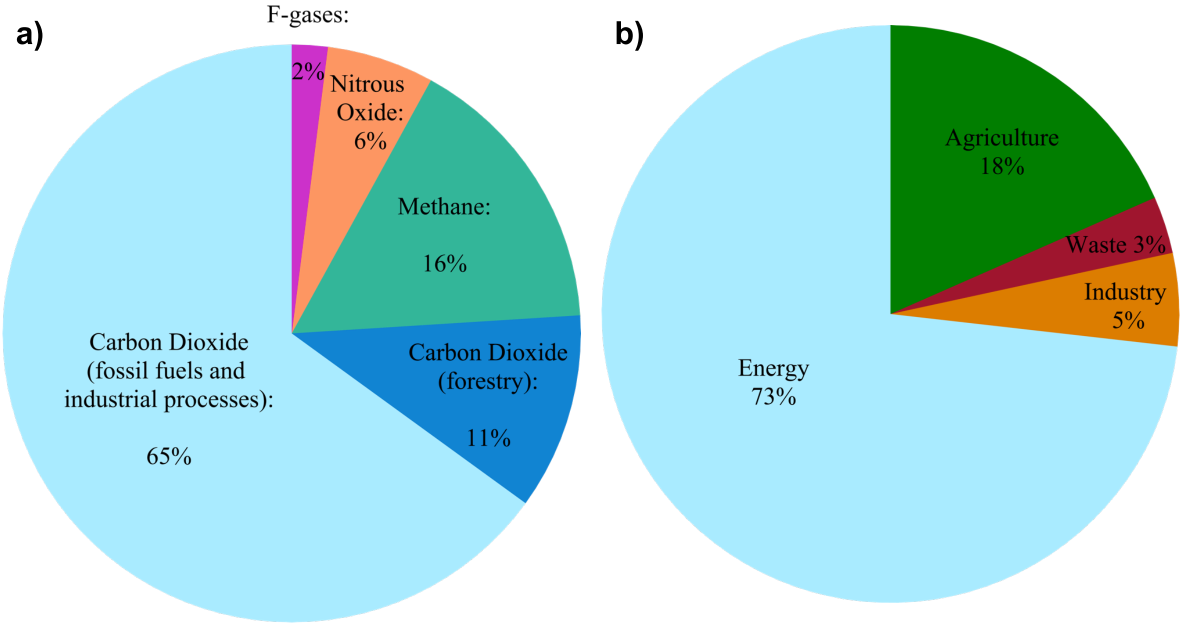

Figure 2: Greenhouse gas emissions by a) gas and b) sector.
Data as of 2020, adapted from [8] and [9].

1.1. Fundamentals of Solar Energy

Renewable energy refers to any energy source that is not depleted upon use, with solar being the most abundant renewable resource. 173,000 TWh of solar energy are incident on Earth at any given moment, approximately 10,000 times more energy than is used globally each year [12], [13].

However, in order to convert incident solar radiation to usable electricity, photovoltaic devices, or solar cells, must be implemented. As described by its name, photovoltaics convert photons (quanta of light, photo-) to electricity (-voltaics). In other words, photovoltaics convert electromagnetic power to electrical power. Photovoltaic devices are made specifically from semiconductor materials, a class of materials where electrons are able to jump from the valence to conduction band given excitement by sufficient photon energy. A semiconductor material can either be a material from group IV of the periodic table (e.g., silicon), a combination of group III and group V materials (e.g., GaAs), or a combination of group II and group VI materials (e.g., CdTe) [14], [15].

Traditional photovoltaic (PV) devices work by driving an electron through a pn-junction, as shown in Figure 3. To generate electrical power—power (P) = current (I) * voltage (V)—high voltage and current must be generated. When a photon is absorbed by a semiconductor, an electron is excited from the valence band to the conduction band—the difference between the valence and conduction band energy is known as the band gap—as shown in Figure 3, leaving behind a hole [16], [17]. The excited electron moves through the conduction band to the n-type layer, and the positive hole moves towards the p-type layer through the valence band, as shown by the purple and gray arrows, respectively, in Figure 3. When this happens, electric current is generated, given the flow of electrons through the conduction band. Voltage is also generated during this process, given the additional energy gained by the electron when the photon is absorbed, as shown by the quasi-Fermi level splitting (ΔE_F) in Figure 3.

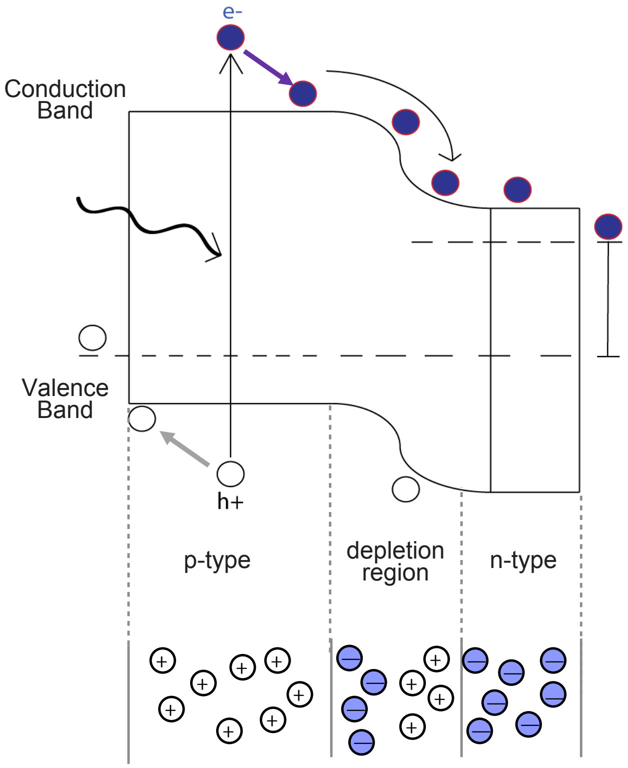

Figure 3: Photon excitation in a pn-junction.
Working mechanisms of a photovoltaic device, showing electron excitation occurs from the valence to conduction bands, in which a hole is left at the valence band. The figure depicts band bending for a pn-junction, where one side is p-type doped (left) and the other is n-type doped (right), as shown by the charge carriers on the bottom of the figure.

Electric current is thus generated in response to the flow and transport of carriers upon excitation. Carriers movement, or lack thereof, can be categorized by three scenarios: 1) free carriers that move randomly within the semiconductor lattice, 2) carriers that continue in a set direction until they collide with a lattice atom, and 3) no net carrier movement. Electrons in the conduction band (i.e., non-excited electrons) and holes in the valence band are considered free carriers [18]. Carrier transport in a semiconductor device can be described by the drift-diffusion model, as shown by the equation below. Here, $J_{n(p)}$ is the current density for electrons and holes, respectively, q is the electron charge, $\mu_{n(p)}$ is the electron and hole mobility, respectively, n(p) is the electron and hole concentrations, E(x) is the electric field in the x-direction, and $D_{n(p)}$ is the diffusion coefficient for electrons and holes [14], [15].

$$J_{n(p)} = q\mu_{n(p)} n(p) * E(x) + qD_{n(p)} \frac{dn(p)}{dx}$$

In this model, drift refers to carrier transport resulting from an imposed electric field and diffusion refers to carrier transport due to a concentration gradient. When light is absorbed by a semiconductor device, both phenomena contribute to carrier transport. In the equation above, total carrier transport is shown, in which the electric current term is E(x), and the second term in the equation is the diffusion gradient, $\frac{dn(p)}{dx}$ [15].

While solar energy may be the most abundant renewable source, and the working mechanisms of photovoltaic devices are well-established, without the proper economics PV will not be adopted. Finding PV that are scalable and low cost has spurred continued research in the field.

1.2. Cost Drivers for Photovoltaic Adoption

In the past two decades, global solar PV capacity has grown more than 600-fold[19]. One driver for this market growth stems from the more than 99.9% cost decrease in crystalline Si (c-Si) PV cells since 1980 [20]—where c-Si cells currently comprise approximately 93% of total installed PV [21]. During this same time frame, record c-Si cell power conversion efficiency (PCE) has gone from 13% to 26.1% [22]. Given these drastic reductions in cost at the module level, the vast majority of capital expenditure for c-Si PV occurs at the material growth and wafer level. As shown by the technoeconomic analysis below, 45.4% of total capital expenditure is due to three steps—trichlorosilane (TCS) production, Siemens chemical vapor deposition (CVD), and Czochralski growth—all of which occur in material growth or wafer stages [23]. Thus, in order to further reduce ultimate module costs, less material must be used in next generation technologies.

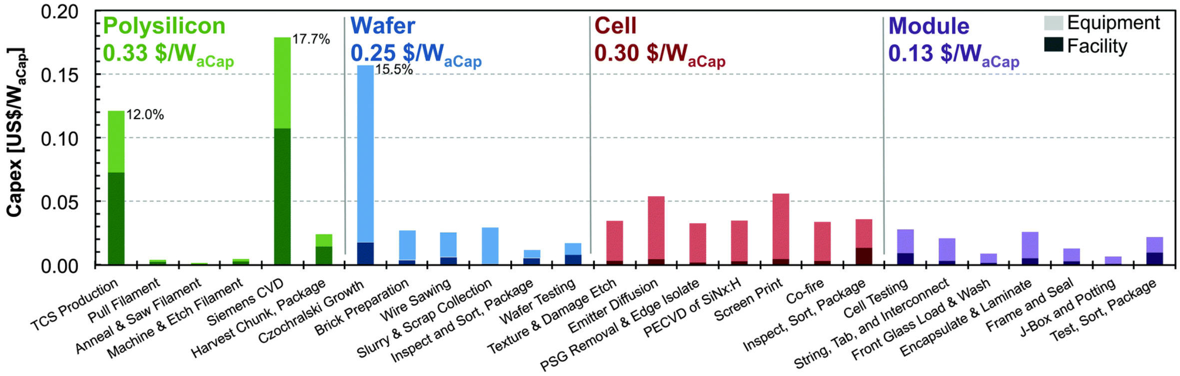

Figure 4: Capital Expenditures for c-Si PV production.
Taken from: Powell et al., 2015 [23].

Researchers are searching for new PV technologies that can far exceed the performance of current Si PV devices, while maintaining comparable systems-level cost. As such, new PV technologies must achieve low manufacturing costs via less material use. Concentrating solar technologies aim to address the reduction in hardware costs, while still achieving high performance via efficiency. High-efficiency photovoltaic materials (e.g., III−V cells) boast lab-recorded efficiencies of up to 29.1% for single junction devices [22] and 68.9% under laser light [24], yet cost nearly 1000x more to grow relative to c-Si solar cells [25]. Thus, to make high-efficiency materials cost competitive, next generation technologies must either reduce the cost of these materials, or be able to use smaller amounts of the high-cost material to achieve similar efficiency performance (i.e., concentration). However, even if using c-Si materials, less material must be used in order to reduce the ultimate module cost, as shown in Figure 4.

In addition to materials cost, the overall cost of installation must be considered. As a result of these rapid reductions in cell and module cost per Watt since 1980, approximately 57% of the costs in 2019 for utility-scale PV systems come from soft costs (e.g. installation labor, sales tax, overhead) and balance of systems (BoS) costs [26]. To address the BoS costs, next generation solar energy technologies must be integrated into existing infrastructure, as is further discussed in Chapter 4 of this thesis via building integrated photovoltaics.

1.3. Fundamentals of Solar Concentration

One such technological area aiming to tackle these challenges of high system-level costs for PV adoption is through solar concentration of high-efficiency devices [27]. Typically, high-quality, high-efficiency PV materials (e.g., GaAs) have high materials and growth costs when compared to conventional c-Si devices. In order to reduce the system-level cost for such materials, solar concentration aims to use smaller quantities of high-cost PV material while maintaining high illumination areas. Traditionally, solar concentration refers to passive concentrators, in which the photon energy remains unchanged, but the photon path is redirected by external lenses that are implemented on the system, as shown in Figure 5 [28], [29]. Passive concentration can be achieved through a variety of technologies—including Fresnel lenses, concentrating towers, compound parabolic concentrators (CPC, as shown in Figure 5), among others [30]—which leverage geometric designs in order to redirect the photon path.

Passive concentrators may enable the use of less PV material, however this technology comes at a performance cost. First off, passive concentration of solar radiation results in high operating temperatures, since the incident photon energies are conserved and essentially added together. These high temperatures can result in lower operating efficiency for the PV device; the physics behind the PV efficiency and operating temperature is discussed further in Chapter 2 of this thesis. Additionally, passive concentrators maintain small acceptance angles (θ_1), typically only a few degrees, as shown by the concentration relationship below for a CPC, where θ_2 is the outgoing angle and *n* is the refractive index of the geometric concentrator [29].

$$C \leq \frac{\sin^2 \theta_2}{\sin^2 \theta'_1} = \frac{n^2 \sin^2 \theta_2}{\sin^2 \theta_1}$$

As such, concentration is inversely proportional to acceptance angle. To account for these small acceptance angles, passive concentrators typically require trackers—mechanical mounts that move the system to track the sun's daily path –, which are bulky and costly [28], [31].

As a result of these performance issues, passive (or geometric) concentrators are commonly used today as thermal concentrators as opposed to light concentrators, thereby removing the PV component entirely [30], [32].

Luminescent solar concentrators, or active concentrators, present an alternative to passive concentration for PV. Luminescent concentrators downshift incident photon energies, and trap the downshifted photoluminesce within a waveguide with an embedded PV device, as shown in Figure 5b, thus resulting in active concentration. By employing isotropic absorption of incident photons via luminophores, flat-plate luminescent waveguides are able to absorb photons at all angles of incident, thereby reducing the need for tracking while still achieving concentration for high-efficiency, high-cost PV devices [28], [33], [34].

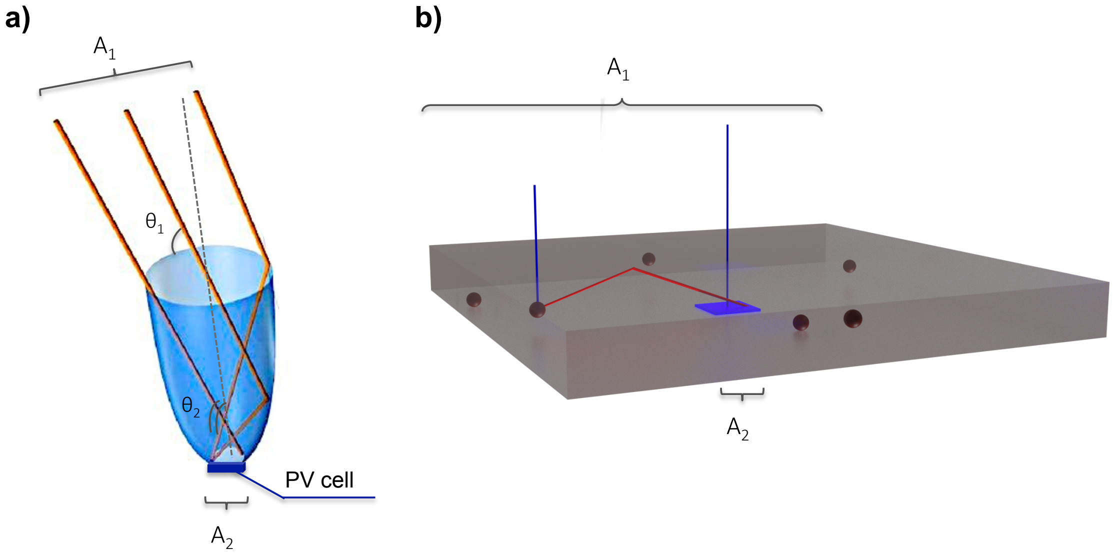

Figure 5: Schematics of passive and active (luminescent) concentrators.
a) Passive concentration via a concentric parabolic concentrator (CPC), displaying the path of an accepted photon as it is funneled to the photovoltaic (PV) cell at the bottom. The incident photon arrives at an acceptance angle (θ_1) and is redirected through the CPC via Snell's law until it hits the PV cell at an angle of θ_2. The PV cell has an area (A_2) that is much smaller than the acceptance area (A_1), thus resulting in solar concentration. b) Active concentration is shown for a luminescent waveguide, displaying the path of an accepted photon through luminophore absorption, photoluminescence and waveguide trapping. High-energy photons (blue lines) are absorbed by the quantum dot luminophore (red spheres) which photoluminesces a downshifted photon (red lines). The photoluminescence is trapped within the polymer waveguide until it hits and is absorbed by the PV cell (blue square).

1.4. The Case for Luminescent Solar Concentrators

Traditional flat plate PV devices often exhibit inconstant power conversion under varied illumination conditions. For instance, operation under diffuse lighting conditions can lead to a 20% reduction in power conversion efficiency (PCE) for monocrystalline silicon cells relative to direct solar irradiance [35], [36]. Moreover, standard solar radiation data compiled across the United States suggests that diffuse irradiance can compose between 20 and 40% of the global radiation, depending upon geographical region and time of year [31], [37]. Solar technologies equipped with diffuse-light capture mechanisms stand to further increase adoption of PV systems.

Considerable research is currently being directed toward developing scalable, thin-film tandem or tandem-on-silicon PV cells and modules, which have potential for efficiencies beyond the practical and theoretical limits [38] of single-junction devices by utilizing a larger portion of the solar spectrum [39]. Currently, the highest efficiency stabilized thin-film tandem PV performance has been achieved using III−V compound semiconductor tandems, with the highest efficiency devices composed of III−V materials grown on silicon [40]. However, at present, the costs for III−V materials in thin-film or silicon tandem device configurations is too high to be economical for large-scale applications [41]. Other pathways for tandem PV devices are being actively explored. Among these, notable high efficiency lead halide perovskite on silicon tandem prototypes have been reported, although the long-term stability of these tandem devices is, as of today, unproven [42].

An alternative approach to high efficiency tandem modules with potential to reduce the overall module cost of III−V/Si tandems is to concentrate incident sunlight onto an array of small III−V micro-cells, thereby minimizing the amount of III−V material required per watt of generated electricity [33], [43]. Uniquely among PV concentrators, luminescent solar concentrators (LSCs) enable concentration of both diffuse and direct light [33], [44]. LSCs can also be developed in flat-plate, fixed-axis modules that do not require sun tracking, enabling such technology to be particularly suitable to applications of conventional, single-junction PV modules. Functionally, LSCs trap incident sunlight within a dielectric waveguide through total internal reflection (TIR). The trapped light is then redirected to small area PV cells for energy conversion. LSCs employ luminophores uniformly dispersed within the waveguide that isotropically absorb high energy photons and re-radiate down-converted photons as photoluminescence (PL) with a high radiative efficiency, or photoluminescence quantum yield (PLQY). Initial studies demonstrate the ability of stand-alone LSCs to capture both direct and diffuse irradiance, allowing sustained performance in varied lighting conditions [45]–[47]. The concentration of luminophores dispersed within the waveguide determines the amount of irradiance absorbed, quantified as a spectrally dependent optical density. Ideal luminophores require a large Stokes shift—the downshift between absorbed and emitted photon energies—in order to reduce reabsorption losses [48]. PL radiation is trapped within the waveguide as a result of coupling into guided optical modes, arising from TIR. Since TIR traps only a portion of the PL, LSCs often employ additional external reflectors enclosing the top and bottom surfaces of the waveguide [49]–[51].

Given the working mechanisms of an LSC, we can break the system down into three key components—the luminophore, waveguide trapping, and the PV collector—each of which are described in detail in sections 1.4.2 – 1.4.4 of this thesis. In order for the LSC to reach maximal performance, each of these three components must be optimized individually, as well as matched spectrally at the system level (e.g., the luminophore emission should match the photovoltaic collector bandgap). Each of these components contributes to one or more paths of potential loss in the LSC system. Figure 6 below details seven potential loss paths in a luminescent waveguide and motivates the need for optimized components.

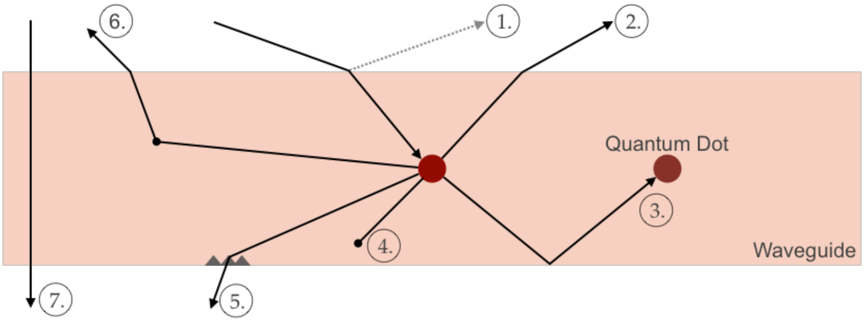

Figure 6: Potential loss mechanisms in an LSC.
Here we detail a quantum dot as the luminophore within a polymer waveguide. Potential loss paths of incident photons include: 1) reflection off the waveguide surface; 2) photoluminescence emitted within the escape cone; 3) non-radiative absorption by luminophore; 4) absorption by the waveguide matrix; 5) solar cell losses; 6) internal waveguide scattering into the escape cone; and 7) transmission through waveguide matrix without interacting with luminophore species or solar cell. Figure adapted from Debije et al. (2012) [33].

1.4.1. Consideration of Luminescent Thermodynamic Limits

Unlike geometric concentrators, which rely on acceptance angle for concentration, the concentration limit for luminescent concentrators depends instead on the incoming and outgoing photon energy, e_1 and e_2, respectively. Given the second law of thermodynamics ($\Delta S_{system} \geq 0$), we know that light concentration in a luminescent waveguide must result in an entropy increase[48]. For a luminescent waveguide, we must account for the entropy changes associated with each the incident light field (I_1) and the concentrated light field (I_2). For our incident field, the entropy change (ΔS_1) refers to changes associated with the loss of a photon to the field, and can be modeled as shown below, where K is the Boltzmann constant, n is the refractive index, v_1 is the frequency of the incident photon, and B_1 is the brightness of the incident field.

$$\Delta S_1 = -K \log\left(1 + \frac{8\pi n^2 v_1^2}{c^2 B_1}\right)$$

For the concentrated field, the entropy change (ΔS_2) refers to changes associated with the luminesced photon, and thus we have the opposite sign. We further must account for thermalization, due to Stokes shift, at an ambient temperature, T, as shown by the additional term below.

$$\Delta S_2 = K \log\left(1 + \frac{8\pi n^2 v_2^2}{c^2 B_2}\right) + \frac{h(v_1 - v_2)}{T}$$

As such, the total entropy of the system is a combination of these two terms ($\Delta S_1 + \Delta S_2$):

$$\Delta S_{system} = \Delta S_1 + \Delta S_2 \geq 0$$

$$-K \log\left(1 + \frac{8\pi n^2 v_1^2}{c^2 B_1}\right) + K \log\left(1 + \frac{8\pi n^2 v_2^2}{c^2 B_2}\right) + \frac{h(v_1 - v_2)}{T} \geq 0$$

Using this relationship, we can simplify the above terms as follows, to determine a relationship between the brightness of each field (B_1 and B_2) and the photon frequencies (v_1 and v_2).

$$K \log\left(1 + \frac{8\pi n^2 v_1^2}{c^2 B_1}\right) / \left(1 + \frac{8\pi n^2 v_2^2}{c^2 B_2}\right) \leq \frac{h(v_1 - v_2)}{T}$$

$$\left(1 + \frac{8\pi n^2 v_1^2}{c^2 B_1}\right) / \left(1 + \frac{8\pi n^2 v_2^2}{c^2 B_2}\right) \leq \exp\left(\frac{h(v_1 - v_2)}{KT}\right)$$

$$\left(\frac{v_1^2}{B_1}\right) / \left(\frac{v_2^2}{B_2}\right) \leq \exp\left(\frac{h(v_1 - v_2)}{KT}\right)$$

Using the brightness relationship of the outgoing vs. incident fields (B_2 vs. B_1), as discussed in Yablonovitch [48], we can assess the concentration of the system as a function of the ratio of these two values.

$$C = \frac{B_2}{B_1} \leq \frac{v_2^2}{v_1^2} \exp\left(\frac{h(v_1 - v_2)}{KT}\right)$$

Given the derivation above, we see that the potential concentration for a luminescent concentrator is exponentially dependent on the Stokes shift ($v_1 - v_2$)—hence, a larger luminophore Stokes shift results in a higher potential concentration factor. As such, one of the main factors to consider when choosing an LSC luminophore is the Stokes shift, as will be discussed in the next section.

1.4.2. Luminophore Requirements in an LSC

Luminophores refer to the materials that are dispersed within the waveguide that provide the luminescent properties for luminescent concentrators. Luminophores absorb incident light, depending on their absorption profile, and reemit absorbed photons as photoluminescence. Ideal luminophores have an emission wavelength that matches the bandedge of the PV collector. In doing so, thermalization occurs at the luminophore instead of at the solar cell, thereby reducing negative effects of thermalization on solar cell performance. In addition to bandedge matching, luminophore species should be optimized for the following properties, among others: *i)* photoluminescence quantum yield (PLQY), *ii)* Stokes shift, *iii)* full-width at half maximum (FWHM), and *iv)* the Stokes ratio between the absorption and photoluminescence profiles [33], [34], [51]–[53].

PLQY refers to the luminescence efficiency, or the percent of absorbed photons that are luminesced in the luminophore. In other words, for a PLQY of 100%, all absorbed photons are re-emitted, however for a PLQY of 50%, one in two absorbed photons are lost as heat due to non-radiative recombination within the luminophore. Stokes shift refers to the down-shift in energy of the emitted vs. absorbed photon. A large Stokes shift separates the absorption and PL spectra, thereby reducing the risk of a luminesced photon from getting reabsorbed by another luminophore and potentially lost due to non-unity PLQY. As discussed in the previous section, a higher Stokes shift enables a larger potential concentration for a luminescent concentrator. The FWHM of a luminophore describes the width of the photoluminescence peak; ideal luminophores have narrow FWHM. A wide FWHM may indicate an overlap of absorption and PL peaks, resulting in re-absorption events and increased probability of non-radiative recombination. Moreover, for a large FWHM, there is a larger mismatch of luminescence and PV band edge alignment. Finally, the Stokes ratio describes the ratio of the coefficient of absorption at the absorption edge (α_1) to the coefficient of absorption at the photoluminescence peak (α_2). A larger Stokes ratio indicates decreased probability of absorption events at for photoluminesced photons [54].

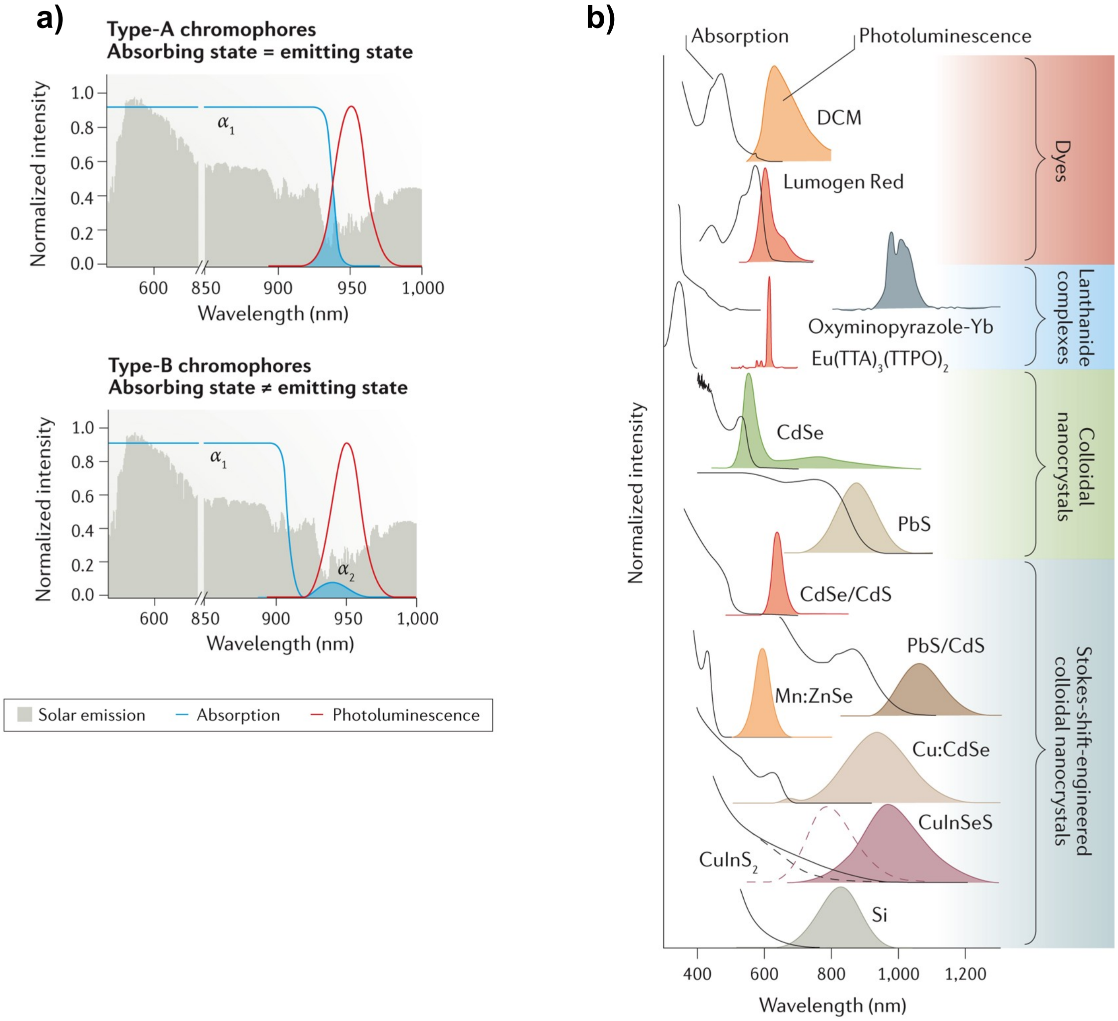

Figure 7: A survey of common luminophore materials for LSC integration.
(a) Spectral schematics of Type-A and Type-B luminophore species given their absorption and photoluminescence profiles. (b) A survey of various potential luminophore materials, both of Type-A and Type-B profiles, which include dyes, lanthanide complexes, colloidal nanocrystals, and Stokes-shift-engineered colloidal nanocrystals. Adapted from Meinardi et al. (2017) [55].

Luminophores may further be split into Type-A and Type-B species, based on their absorption and photoluminescence profiles, as shown in Figure 7a [55]. Type-A luminophores have a step-like absorption spectrum, with a large absorption coefficient, α, where the light absorbing processes and radiation occur in the same physical structure. These luminophores require large Stokes shifts and narrow FWHM in order to minimize reabsorption events due to overlap between absorption and PL spectra. In contrast, Type-B luminophores feature materials in which absorption and photoluminescence are decoupled. These luminophores consist of multiple materials (e.g., core/shell quantum dots), in which one layer is responsible for photon absorption, which then tunnels the exciton to the emitter layer at a lower energy-level. Here, the light-harvesting state has a broad-band absorption coefficient (α_1) that is independent from the absorption-coefficient in the emitting state (α_2); typically α_2 is negligible such that $\alpha_1 >> \alpha_2$, resulting in a large Stokes ratio. Given the decoupled energy levels, Type-B luminophores result in a tunable Stokes shift, dependent on material selection and particle size [55].

Given the successful engineering of high Stokes-shift colloidal nanocrystals, as shown in Figure 7b, this thesis will focus primarily on Stokes-shifted quantum dots as the luminophore species of interest.

1.4.2. Light Trapping in an LSC

Once a photon is luminesced, it must be trapped within the LSC waveguide to increase the probability of interacting with and being collected by the PV cell [51], [54]. For an LSC waveguide that is in direct contact with air (i.e., there are no external trapping filters or mechanisms), total internal reflection (TIR) dominated the trapping potential. TIR is determined based on the refractive index of the waveguide material; for typical polymer waveguides—e.g., poly-methyl methacrylate (PMMA), poly-lauryl methacrylate (PLMA)—refractive indices are 1.4 – 1.5. Given Snells' Law, a polymer of this refractive index in contact with air results in a trapping potential of ~70—75% due to TIR and solid angles. As such, over 25% of photoluminescence is lost due to escape cone losses for an LSC that relies solely on total internal reflection.

In order to improve the trapping potential in the luminescent waveguide, additional external trapping mechanisms must be employed. Possible trapping mechanisms include Bragg stack filters [34], reflecting mirrors [51], [56], and photonic crystals [57]. However, each of these technologies comes with advantages and disadvantages. Bragg stack filters are typically able to achieve high reflectivities at target photon wavelengths, but experience blue shifting at increased angles of incidence. This means that for an accepted photon that is off normal incidence, the Bragg stack filter may not transmit/reflect in the desired wavelength spectra. Reflecting mirrors are strong candidates for back reflectors on the bottom of an LSC given their ability to recycle any incident photon that hits the backside. However, back reflecting mirrors have limited application and cannot be used for technologies in which the LSC needs to transmit photons to a subcell, such as in a tandem LSC/Si module as discussed in Chapter 6. Photonic crystals provide many potential advantages for trapping within an LSC, given their light weight, high reflectivity, and spectral selectivity based on material. While there is still myriad ongoing research on photonic crystals, recent advances suggest they would be good candidates for LSC trapping, as briefly discussed in chapter 2 [57].

1.4.4. Light Collection in an LSC

Once photoluminescence has been successfully trapped, the luminesced photon travels within the waveguide until it interacts with and is collected by the photovoltaic device. Typically, solar cells are aligned vertically, along the waveguide edge, as shown in Figure 5; however solar cells may be oriented either vertically or planar within the waveguide, as is discussed in Chapter 2 of this thesis. In addition to orientation within the luminescent waveguide, the solar cell may be selected based on material and device architecture.

As discussed in Section 1.1, PV performance is driven, in part, by material selection. The selected PV material must, first and foremost, be spectrally matched with the other components of the LSC. Of note, the solar cell band edge, based on the external quantum efficiency, should match the luminophore photoluminesce peak and the target reflected wavelength, if there are external trapping filters. Often times, the choice of solar cell material in an LSC is based on the application of interest. For example, power-generating windows require solar cells with bandgaps in the near infrared, for aesthetic purposes, whereas space-based solar requires high efficiency and lightweight modules. PV device selection based on LSC application will be further discussed in Chapters 4 – 5.

1.5. The Scope of This Thesis

In Chapter 1, we provide the necessary background for understanding the motivation and fundamental science behind this thesis. This includes the motivation and physics of solar cells, as well as the case for luminescent solar concentrators. We discuss the physics and optimization problem for each aspect of luminescent solar concentrator systems, thereby preparing the reader for the subsequent research and measurements in the rest of the thesis.

In Section I, we discuss photovoltaic (PV) device considerations for integration in luminescent solar concentrator systems. This section is broken into two chapters, Chapters 2 and 3. In Chapter 2, we investigate the fundamentals behind the metrics used to assess performance of single-junction luminescent concentrators. We discuss the benefits of luminescent waveguides to reduce PV operating temperatures, and model the effects of each PV orientation and trapping efficiency on system concentration factor. In Chapter 3, we design and fabricate a new type of PV cell form factor: a silicon heterojunction microcell. These devices leverage high efficiency bulk wafers (silicon heterojunctions) in a microscale form factor, and thus have applications in various electronics, including as solar collectors in luminescent solar concentrators. We measure and report the highest silicon microcell V_{OC} to date (588 mV) and outline a path to achieve silicon microcell efficiencies upward of 15%.

In Section II, we explore two potential applications for single-junction luminescent solar concentrators: building integrated PV and space-based solar power. In Chapter 4, we examine the motivation for collocating solar energy at the location of use (e.g., commercial buildings). We further demonstrate how luminescent solar concentrators, specifically, can be used as power-generating windows and discuss the trade-off between power performance and aesthetics. To demonstrate this optimization question, we model the effects of varying certain parameters (e.g., geometric gain and optical density) on each efficiency and visual acuity. In Chapter 5, we introduce the concept of luminescent solar concentrators for space-based solar power generation and discuss why it is a promising technology for space-based solar energy applications. Here, we design a luminescent concentrator and fabricate such a device for a mission that will launch into low-earth orbit in December 2022. We then design the next generation of space-based luminescent waveguides—ultra-thin LSCs—and provide an in-depth techno-economic analysis for such devices.

In Section III, we explore beyond the use case of single-junction luminescent solar concentrators. Instead, we look into the potential for luminescent concentrators to be used in combination with conventional solar technologies (e.g., silicon PV) for utility-scale applications. In Chapter 6, we design and fabricate a tandem InGaP/Si PV luminescent solar concentrator, in which the top junction is a luminescent solar concentrator that utilizes InGaP microcells in a coplanar array, and the bottom junction is a conventional silicon solar cell. We perform the first ever outdoor testing of such a device, and demonstrate how the luminescent waveguide enables sustained performance in diffuse lighting conditions. In Chapter 7, we continue to explore beyond stand-alone luminescent waveguides and introduce a new concept for a hybrid luminescent-geometric concentrator. Here, we design and fabricate two different hybrid concentrators, each leveraging different geometric concentrating systems—reflective hemisphere and concentric parabolic concentrators. We present the performance of both hybrid systems and outline next steps for next-generation hybrid concentrator designs.

Chapter 8 highlights the work done in this thesis, gives an outlook for luminescent solar concentrators, and offers potential directions for future research on luminescent solar concentrators.

Finally, Appendix A provides detailed methods and additional measurements for the silicon heterojunction microcell fabrication. Appendix B presents a business-model analysis that examines the value chain and value propositions for power-generating window, which was motivated following participation in the National Science Foundation I-Corps program.

SECTION I: PHOTOVOLTAIC DEVICE CONSIDERATIONS FOR LSC INTEGRATION

CHAPTER 2: EFFECTS OF DESIGN OPTIMIZATION AND COMPONENT PARAMETERIZATION ON SINGLE-JUNCTION LSC PERFORMANCE

Performance of luminescent solar concentrator (LSC) systems may be assessed via various parameters—*i)* power conversion efficiency, *ii)* photovoltaic (PV) operating temperature, and *iii)* concentration factor. By challenging the traditional design for an LSC and varying component parameters, we investigate the effects of these modifications on each performance metric. To do so, we explore the effects of varied microcell form factors, luminophore properties, and alternate trapping mechanisms. We demonstrate that absorbed radiation and thermalization losses are redistributed away from the photovoltaic cell to the waveguide in an LSC, thereby lowering PV operating temperatures within the waveguide. We examine the effects of PV cell orientation on PV operating temperature and concentration factor, suggesting that the traditional edge-lined PV orientation may not be the optimal form factor for performance. By modeling PV operating temperatures and LSC module efficiencies for varied luminophore species, we show that ideal luminophores have a high Stokes shift and a photoluminescence peak that is closely matched to the embedded PV bandedge. Finally, we investigate the effects of photonic crystal waveguides for improved photoluminescence trapping in an LSC and demonstrate how implementation of such structures could enable LSC systems with concentration factors >100.

2.1. Introduction

With rising global temperatures there is a subsequent demand for clean, renewable energy sources; solar energy provides a potential solution. Luminescent solar concentrators (LSCs) represent an attractive photovoltaic technology given their ability to concentrate both direct and diffuse light [33], reduced use of photovoltaic (PV) material [34], [58], flexible components [59], and variable opacity [33], [55], [60]. A traditional LSC consists of three components: *i)* a polymeric waveguide that absorbs high-energy light via *ii)* embedded luminophores that re-radiate the light as photoluminescence (PL) at lower energies, directed by the waveguide to impinge upon, *iii)* edge-lining PV material for photon collection and energy conversion [48], [61]–[63]. To maximize performance, each of these components must be *i)* optimized to minimize photonic losses and *ii)* spectrally matched to one another.

Current state of the art LSCs rely upon an edge-lined geometric form factor of the solar cells, however this results in limited power performances when scaled to full module sizes [33], [64]–[66]. Moreover, luminophores with low quantum yield or overlapping absorption and photoluminescence bands can cause heightened reabsorption and nonradiative absorption events [55]. Finally, without ideal trapping by the polymeric waveguide, photoluminesced photons are lost through the escape cone [33]. To this day, the highest efficiency reported for an LSC is 7.1% [67]. By optimizing luminophore properties, re-designing the form factor, and exploring alternate trapping mechanisms, we investigate the impact of each of these components on LSC performance. Given that an LSC is a concentrating system, not a traditional PV cell, we assess LSC performance through multiple criteria, including but not limited to efficiency. In this chapter, we discuss three distinct metrics for measuring solar cell performance in a luminescent solar concentrator—*i)* power conversion efficiency, *ii)* PV operating temperature, and *iii)* concentration factor—and investigate how altering the design and properties of an LSC system may optimize each performance metric.

One of the most common ways to assess PV device performance, irrespective of the technology type, is via the power-conversion efficiency (η) of the cell; in other words, the ratio of maximum output power (P_{MP}, or P_{OUT}) versus input power (P_{IN}). As discussed in Chapter 1, PV devices work by driving electrons across a pn-junction, thereby generating electric current [68]. Maximum power output occurs when the voltage times the generated current-density is maximized, typically at the knee of the current-voltage (IV) curve, also known as the maximum power point (P_{MP}) [18], [69].

$$\eta = \frac{P_{OUT}}{P_{IN}} = \frac{P_{MP}}{P_{IN}} = \frac{I_{MP} * J_{MP}}{P_{IN}}$$

$$where\ FF = \frac{I_{MP} * V_{MP}}{I_{SC} * V_{OC}},$$

$$I_{MP} * V_{MP} = FF * I_{SC} * V_{OC}$$

$$Hence,\ \ \eta = \frac{FF * I_{SC} * V_{OC}}{P_{IN}}$$

As such, PV efficiency is calculated as a function of the three intrinsic performance parameters for a PV cell—the open-circuit voltage (V_{OC}), the short-circuit current-density (J_{SC}), and the fill factor (FF). In order to improve the PV efficiency, each of these parameters must also be maximized. For most terrestrial solar cell measurements, we assume a constant input power (e.g., AM1.5G); hence, improvements in FF, J_{SC}, and V_{OC} directly impact device efficiency. Typically, J_{SC} is associated with the optical properties (absorption and reflection) of the semiconductor material, whereas V_{OC} measures the amount of recombination in the cell, and is thus a measure of material quality for the device. As such, improvements to J_{SC} are tend to be incremental, whereas V_{OC} improvements can be significant; V_{OC} improvements are most commonly used as a proxy for material quality and subsequent efficiency improvements [69].

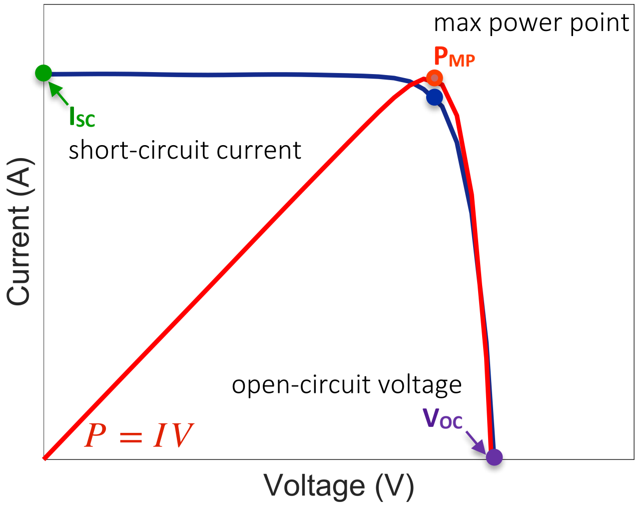

Figure 8: Light-induced current-voltage (IV) curve for PV sample cell.
Representative light-current (IV) curve for an illuminated photovoltaic device shown by the blue line, with the calculated power output (power = current*voltage, P=IV) plotted in red. I_{SC} indicates the short-circuit current (when V = 0) and V_{OC} is the open-circuit voltage (when I = 0), shown by green and red circles, respectively. The max power point (P_{MP}, red circle) occurs at the knee of the IV curve, as shown by the blue circle below the max power point.

The second measure of PV performance that we look at is device operating temperature. PV operating temperature can adversely affect solar cell performance, particularly for silicon devices, and thus act as a proxy for PV efficiency. Crystalline silicon solar cells conventionally exhibit temperature coefficients up to -0.54%/°C. As solar cells are exposed to higher radiation and warm ambient air, their operating temperatures can increase significantly due to balance between heating resulting from carrier thermalization from photon absorption, and convective and radiative emission cooling [70].

As a semiconductor device, increased temperature induces a decrease in solar cell bandgap [71]. This occurs because as semiconductor devices are heated up, electron energy within the material increases, and thus a lower energy is needed to break the bond. As a result, J_{SC} increases slightly with temperature, since more photons are able to form electron-hole pairs when the bandgap is lowered [71]. However, V_{OC} decreases significantly with temperature due to changes in the intrinsic carrier concentration, as shown in Figure 9. Intrinsic carrier concentration, n_i, is driven up with lower bandgaps, given the negative exponential dependence on bandgap, as shown below.

$$n_i^2 = 4\left(\frac{2\pi kT}{h^2}\right)^3 (m_e^* m_h^*)^{\frac{3}{2}} \exp\left(-\frac{E_g}{kT}\right)$$

$$= BT^3 \exp\left(-\frac{E_g}{kT}\right)$$

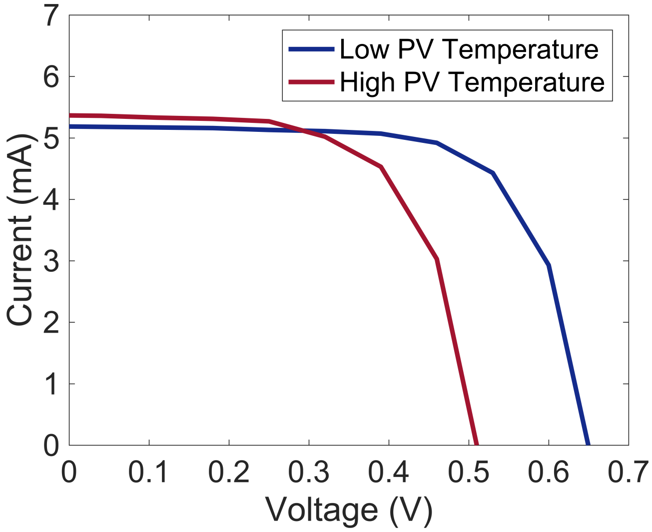

Figure 9: Light IV curve for a silicon cell under each low and high operating temperatures.

As such, the dark saturation current, I_0, can be approximated by the following association: $I_0 = An_i^2$, where A is a constant that includes recombination parameters and is independent of temperature. Given this relationship, we can re-write the equation for V_{OC} in terms of n_i. As shown below, V_{OC} is linearly dependent on temperature, however is logarithmically dependent on n_i^{-2}, which exponentially grows with operating temperature.

$$V_{OC} = \frac{nkT}{q}\ln\left(\frac{I_L}{I_0} + 1\right)$$

$$\approx \frac{nkT}{q}\ln\left(\frac{I_L}{An_i^2}\right)$$

$$= \frac{nkT}{q}\ln\left(\frac{I_L}{ABT^3 \exp\left(-\frac{E_g}{kT}\right)}\right)$$

$$= \frac{nkT}{q}\left(\frac{E_g}{kT} - \ln\left(\frac{I_L}{ABT^3}\right)\right)$$

$$\approx \frac{nE_g}{q}$$

Given the above approximation, we see that V_{OC} is directly affected by changes in bandgap, and thus we will see significant decrease in V_{OC} with temperature given the impact on bandgap and intrinsic carrier concentration [71]. Given these trends in performance parameters vs. temperature shown in Figure 9—lowered V_{OC} and slightly higher J_{SC}—the overall efficiency of the demonstrated silicon cell decreases with temperature, driven by the changes in V_{OC}. While these trends are still seen in other semiconductor devices (e.g., III−Vs), the decrease in V_{OC} and efficiency is less extreme for other materials, given direct bandgaps and higher bandgap energies, in comparison to silicon [72].

The final metric we investigate to assess PV performance in an LSC, specific to concentrating systems, is the concentration factor (C). For solar concentrators, the illuminated area is larger than the active PV area, and as such the concentration factor represents the enlargement factor of active PV area. As shown in the equation below, C is a function of the optical efficiency (η_{opt}) of the system and the geometric gain (GG). Here we define optical efficiency as the ratio of total photon flux collected per exposed PV area (Φ_{out}) to the total photon flux incident per illuminated area (Φ_{in}). Geometric gain is defined as the ratio of the total light illuminated area (A_{ill}) to the total exposed PV area (A_{PV}).

$$C = \frac{\Phi_{out}}{\Phi_{In}} * \frac{A_{ill}}{A_{PV}} = \eta_{opt} * GG$$

$$where \;\; \eta_{opt} = \eta_{abs} * \eta_{wg} * \eta_{PL} * \eta_{trap}$$

Concentration factor is thus affected by several parameters in a luminescent concentrator system—absorption potential (η_{abs}), waveguide performance (η_{wg}), luminophore photoluminescence efficiency (η_{PL}), trapping efficiency (η_{trap})—since each of these parameters affects the optical efficiency of an LSC. As shown in Figure 10 below, concentration factor may under- or out-perform geometric gain based on the system's optical efficiency. For an ideal optical efficiency of η_{opt}= 1, where the total photon flux collected by the PV cell equals the total incident flux on the illuminated PV area, we expect concentration factor to equal geometric gain, as shown by the black dashed line in Figure 10. However, if the embedded solar cell were able to recycle photons and operate above unity efficiency (i.e., η_{opt}> 1), such as through electro-luminescent cooling [73], this would result in C > G, as shown by the solid green line in Figure 10. Under-performing systems may occur if any component of the optical efficiency—η_{abs}, η_{WG}, η_{PL}, η_{trap} —is not optimized. Figure 10 (red lines) displays systems with low trapping potential (e.g., relying solely on total internal reflection), as well as systems that strongly underperform in all aspects of optical efficiency. In either case, concentration factor underperforms geometric gain for these $\eta_{opt} < 1$ systems.

In this chapter, we challenge the traditional LSC design and investigate the effects of design and component parameterization on each of these three performance metrics. Specifically, we vary the microcell form factor, luminophore properties, and waveguide trapping. First, we examine why LSCs are strong candidates for maintaining low PV operating temperature within the waveguide. Given these properties, we study the effects of cell orientation on PV operating temperature within an LSC waveguide, as well as its effects on overall module power conversion efficiency and concentration factor. We next investigate how luminophore properties influence each PV operating temperature and efficiency. Finally, we depart from the traditional polymeric waveguide and model the effects of a photonic crystal waveguide, with high trapping potential, on LSC concentration factor. By tracking multiple performance metrics, we ultimately aim to understand whether all benchmarks are equivalent for assessing LSC performance—e.g., can PV operating temperature act as a proxy for LSC efficiency, as it does for conventional PV devices?

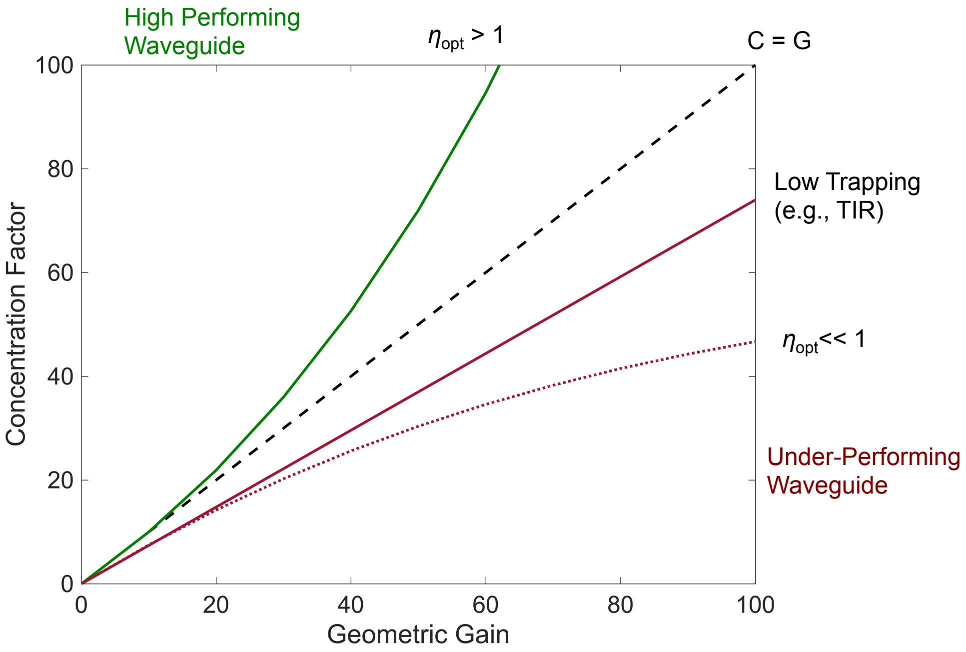

Figure 10: Concentration Factor vs. Geometric Gain for varied waveguide performances.
We plot C = G (black dashed line) to demonstrate C vs. G for $\eta_{opt} = 1$. High- and low-performing waveguides are shown in green and red regions, respectively. Under-performing waveguides are broken down to those without external trapping mechanisms (i.e., TIR only), which are otherwise decent waveguides, in solid red, as well as those with optical efficiencies much less than 1 (dotted red line).

2.2. Photovoltaic Thermalization in LSCs

In addition to the traditional appeal associated with luminescent solar concentrators (LSCs)—ability to concentrate diffuse light, variable degree of module transparency, etc. [33], [34]—LSC modules are able to maintain low PV operating temperatures, a property which is particularly advantageous for materials such as silicon, which have high temperature coefficients [72], [74]. Previous studies have reported reduced operating temperatures for a PV cell embedded within an LSC compared to a conventional wafer PV cell [74], yet little research has been conducted to understand the thermalization pathways in an LSC and how various properties affect the PV operating temperature and overall module performance.

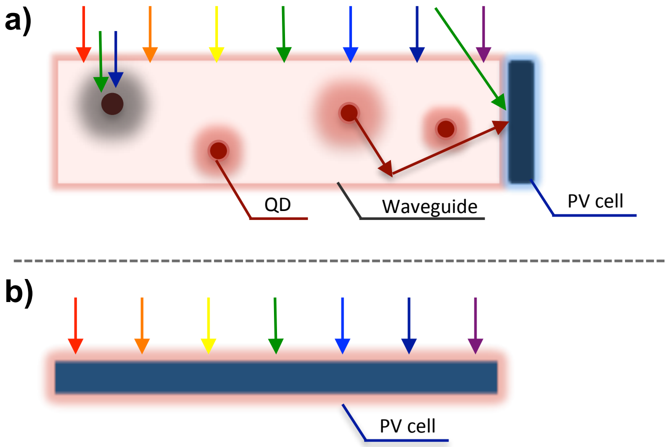

Figure 11: Thermal radiation in LSC and conventional Si wafer systems.
Heating from incident thermal radiation is split between each the polymer waveguide, QD luminophore, and photovoltaic cell in the edge-lined LSC design (top). For a conventional wafer planar PV cell, the PV cell is subject to all incident radiation.

In an LSC module, the thermal properties of the module are influenced by the *i)* polymer waveguide, *ii)* embedded luminophore species, *iii)* photovoltaic material, and *iv)* surrounding ambient thermal environment [48], as shown in Figure 11a. A small amount of the incident radiation is absorbed as heat by the polymer itself, depending on the polymer material, as depicted by the glowing purple waveguide in Figure 11a. The majority of optical absorption occurs in the luminophores; total absorption depends on the luminophore material and their optical density in the waveguide [75]. Photons that are not absorbed by the luminophores or polymer pass through the LSC and do not incur additional absorption. In the case of luminophore optical absorption, heating may occur via multiple pathways. For example, in the case of core/shell quantum dots (QDs), thermalization may occur due to *i)* relaxation of absorbed photons to the QD core: $Q = h\nu - E_{PL}$, and *ii)* absorbed heat due to non-unity quantum yield: $Q = E_g * (1 - \eta_{PL})$[76]. These two phenomena are depicted schematically by the glowing red and black QDs, respectively, in Figure 11a. This produced heat is then trapped within the polymer waveguide. Since luminophore photoluminescence (PL) emission wavelengths are typically matched to the bandgap of the edge-lined PV cell [77], carrier thermalization largely occurs at the luminophore, as opposed to at the PV cell. Finally, the ambient air surrounding the polymer waveguide acts as a cooling medium, enabling heat dissipation via convection. For each thermalization (and cooling) pathway, the majority of thermalization occurs within the LSC waveguide, thereby redistributing heat away from the PV cell [75]. By contrast, a conventional flat planar PV module incurs heat absorption from carrier thermalization uniformly across its area, with total magnitude related to the cell bandgap and reflection properties [78], [79], as shown by Figure 11b.

The ability for LSCs to maintain low photovoltaic temperatures could be particularly advantageous for space-based solar power applications, as will be further discussed in chapter 5. Given the lack of atmosphere (convection coefficient = 5x10-3) in space, space-based photovoltaic devices are not able to rely on convective cooling for temperature control [80]. As such, photovoltaic devices employed in space could benefit from additional cooling properties. LSCs have previously been presented as potential candidates for space-based PV, given the light weight, flexibility and low-cost of the modules [59], and thus their intrinsic cooling properties could make them even stronger space-solar candidates.

Given the ability for LSCs to maintain cool PV operating temperatures, we investigate whether these lower operating temperatures can be used as a standalone proxy to assess LSC performance. To do so, we first examine performance trends—for both PV operating temperature and efficiency—across varied solar cell form factors.

2.3. Effects of Cell Orientation on PV Operating Temperature

To optimize PV operating temperature in an LSC, we first study how form factor and solar cell orientation affects performance. LSCs consist of a luminescent waveguide coupled to a photovoltaic device; however, the orientation and geometry of the device is not specified. As a base case to assess thermal management, we compare thermal performance of a Si PV edge-lined LSC, the conventional LSC form factor, to a flat plane Si solar cell. Given their widespread use, we focus our study on Si PV cells [72]. Thermal performance is modeled using the heat transfer module in the COMSOL Multiphysics simulation environment. Our model accounts for incident thermal irradiation in Los Angeles, CA and simulates module heating based on conduction in the polymer waveguide, thermalization at the QD luminophore, thermalization at the PV cell, and convective cooling assuming an ambient air temperature of 20°C.

The simulated edge-lined LSC consists of *i)* a 1cm x 1cm x 200µm waveguide with embedded CdSe/CdS QD luminophores (quantum yield = 99%) and *ii)* an edge-line silicon PV cell (thickness = 80µm), as shown in Figure 12a. The modeled conventional wafer Si PV cell has the same dimensions as the LSC waveguide (1cm x 1cm x 200µm), as shown in Figure 12b. In Figure 12c, we model a waveguide optical density of 0.3 and record data for both modules after 5 min of constant AM1.5g irradiation (P = 1000 W/m^2) exposure. As shown in Figure 12, the Si PV cell attains an operating temperature of 28.2°C when in the LSC waveguide, whereas the conventional wafer Si cell reaches a 44.6°C operating temperature. Further, the LSC keeps the Si cell nearly 3°C cooler than the waveguide center, where the majority of heat is confined, whereas the conventional Si cell is at 44.6°C across its surface, with ~0.01°C variation at the device edges.

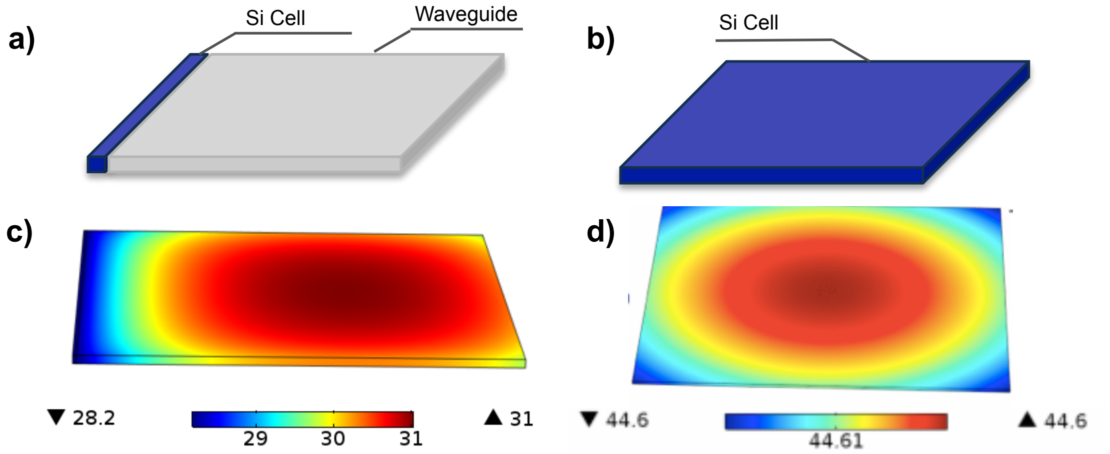

Figure 12: Heat transfer simulations for LSC systems and conventional Si.
Design for simulated (a) edge-lined LSC and (b) conventional wafer Si PV cell. Temperature distribution across the device after 5 min of constant 1000W/m^2 AM1.5g exposure is shown for (c) the LSC device and (d) the conventional wafer Si cell.

We next use this model to challenge the conventional edge-lined form factor and simulate myriad PV cell configurations within the LSC waveguide. As shown in table 1, we model four different PV orientations—edge lined, edge lined along all 4 edges, coplanar along the bottom of the waveguide, and inverted coplanar along the waveguide top. Each orientation assumes identical PV material and cell dimensions (1cm x 200µm x 80µm). As shown, PV temperature is affected by orientation within the waveguide, with edge-lined orientations outperforming coplanar. However, all LSC cell configurations still outperform the conventional wafer PV operating temperature in similar conditions (44.6ºC) by over 10ºC.

PV Orientation	PV Temp (ºC)	Waveguide Temp (ºC)
Edge-Lined (one edge)	28.1	31
Edge-Lined (all edges)	28.2	30.6
Bottom Coplanar	30.3	30.8
Top Coplanar	32.5	32.4

Table 1: Operating temperature for varied placement orientations of a 1cm x 200µm x 80µm Si cell in a 1cm x 1cm x 200µm waveguide.

From this analysis, we see that a vertical cell orientation, or an edge-lined form factor, outperforms a coplanar orientation in terms of PV operating temperature. Given the association between PV operating temperature and PV efficiency, due to the bandgap shift discussed in the Introduction, one may assume that a lower PV operating temperature would equate to lower LSC module efficiencies, as would be true for a conventional silicon cell. This idea assumes constant direct illumination, as would be experienced by a Si wafer; however, in an LSC, solar cells absorb light via photoluminescence, which may not be collected equally throughout the waveguide. As we will see in Section 2.4, PV operating temperature alone may not be a suitable proxy for LSC performance. In order to understand how PV orientation affects overall LSC performance, we must investigate the effects of cell orientation on module efficiency and concentration factor.

2.4. Effects of Cell Orientation on PV Efficiency and Concentration Factor

As discussed, traditional luminescent solar concentrators arrange the solar cell(s) to optically couple flat against the perimeter edge of a rectangular waveguide, as shown by the blue cell along the edge wall in Figure 13a. While advantageous in its operating temperature, as shown in Section 2.3, and ease of fabrication on the lab-scale, the ratio of illuminated waveguide surface area (A_{LSC}) to photovoltaic collection area (A_{PV}) grows proportionally to the overall module size. More specifically, if we assume a square luminescent waveguide of edge length, ℓ, and height, $\hbar$, we observe that this area ratio (i.e., the geometric gain, GG) simplifies to:

$$GG_{traditional} = \frac{A_{LSC}}{A_{PV}} = \frac{\ell^2}{4\ell\hbar} = \frac{\ell}{4\hbar}$$

where the above equation orients a single solar cell to border the perimeter edge of the waveguide. As shown by previous studies, power conversion and optical efficiencies monotonically decrease with increasing geometric gain [81], [82]. If instead we employ a luminescent solar concentrator whose solar cells lie coplanar with the waveguide, as illustrated in Figure 13b, the solar cells can be arranged in a two-dimensional grid-like pattern and thereby achieve a geometric gain independent of the waveguide top surface area. As a proof of concept, we forego any discussion of the assembly and interconnection for such an array of cells—although various studies have discussed similar, large-area designs for alternative applications [83]–[89]. As seen by the below equation, the total photovoltaic area for this modified luminescent solar concentrator depends exclusively on the fractional area density of the cell grid, ρ_{grid}. This design enables a constant average photon collection length by the photovoltaic component(s) for ever-increasing module areas.

$$GG_{de-coupled} = \frac{A_{LSC}}{A_{PV}} = \frac{\ell^2}{\rho_{\text{grid}} \cdot \ell^2} = \frac{1}{\rho_{\text{grid}}}$$

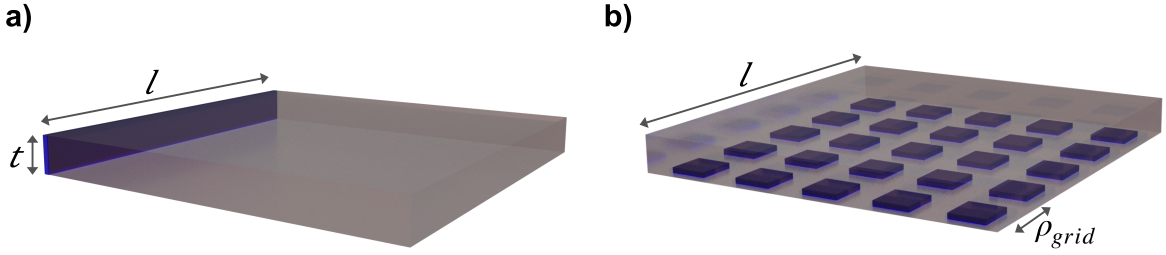

Figure 13: Edge vs. coplanar PV orientations in an LSC.
LSC modules comparing PV orientation in the waveguide: a) traditional edge-lined, of dimensions *l x t*, and b) coplanar, arranged in a grid separated by distance ρ_{grid}.

While the advantage of the coplanar array is evident by the enabled grid-like pattern and maintained geometric gain, we aim to understand the effects on performance via efficiency and concentration factor for these varied PV orientations within the luminescent waveguide. In Figure 14 we display solar cells of identical dimensions arranged in both vertical (maroon, cyan) and coplanar (magenta, orange, navy and green) orientations. We further alter the placement (middle of waveguide, along edge, top of waveguide, etc.) of each of these cells to examine the effects of both orientation and cell placement. Given the role of the luminescent waveguide to trap and tunnel photons towards the photovoltaic device, in this study we aim to understand how concentration factor is affected at the system level for varied PV orientations and placements.

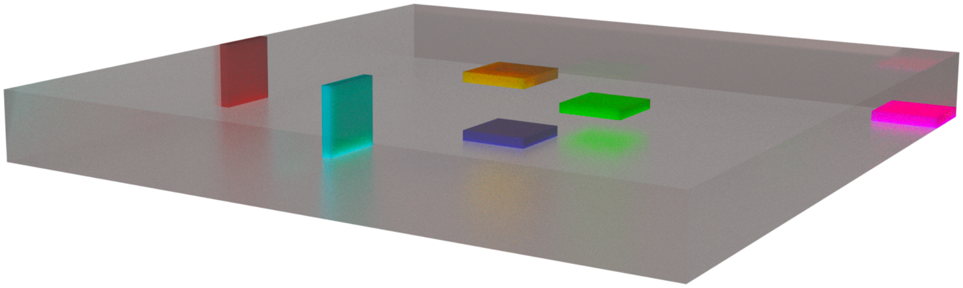

Figure 14: Varied cell orientation in an LSC Waveguide.
LSC square microcells are shown for six different orientation configurations—1) coplanar with the cell along the bottom, center of the waveguide (dark blue), 2) coplanar in the middle of the waveguide (green), 3) coplanar (inverted, such that the active PV material is face down) at the top of the waveguide (orange), 4) coplanar at the bottom along edge of the waveguide (magenta), vertical along the edge of the waveguide (crimson), and vertical in the center of the waveguide (cyan).

We assess the performance of each of the solar cell orientations shown in Figure 14 by modeling the module efficiency, and thus calculating the concentration factor, via Monte Carlo Ray Tracing simulations for an LSC with each PV configuration. In Figure 15 we show simulated concentration factor results across each varied geometric gain and optical density. For this analysis, we model a silicon photodiode (Luna Optoelectronics PDB-C152SM) of fixed area that is arranged in varied orientations and placements within an LSC, matching those rendered in Figure 14. We additionally assume CdSe/CdS quantum dots (PLQY = 95%) as the luminophore species, near-perfect (98%) reflectors along the waveguide edges, and a specular back reflector. Given these parameters, as shown in Figure 15, device orientation (coplanar vs. vertical) drives performance rather than device placement within the waveguide. We see that regardless of placement within the waveguide (at the edge vs. in the center of the waveguide), the vertical cells perform comparably as do the coplanar configurations, with the exception of the inverted coplanar cell placed on the top of the waveguide. However, at high geometric gains, the top inverted cell performance converges with the other coplanar configurations (Figure 15b). This occurs due to the negative effects of shadowing loss for the inverted configuration at low geometric gains, which prevents significant photon absorption and photoluminescence.

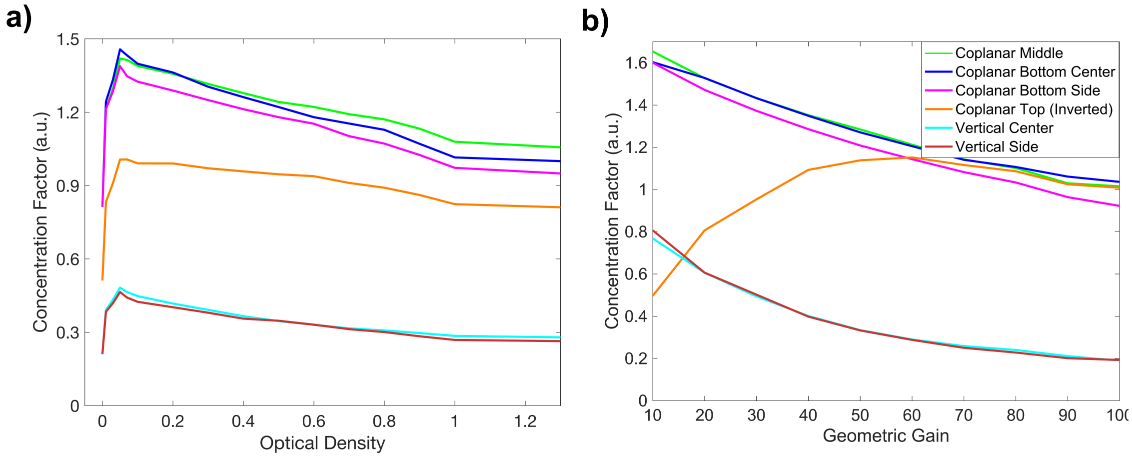

Figure 15: PV Performance for Varied Cell Orientation in an LSC.
Simulated concentration factor for a silicon photodiode arranged in varied orientations within an LSC module across varied a) optical densities (GG held constant at 30) and b) geometric gains (OD constant at 0.1).

Given the results of Figure 15, we see that coplanar cells outperform vertical configurations for concentration factor measurements. This study implies that photoluminescence is not collected equally across a luminescent waveguide, as we expect given escape cone losses at the waveguide surface. This suggests that the coplanar orientation is advantageous to both maintain constant geometric gains, regardless of module area, as well as for heightened LSC concentration factor performance. This analysis further implies that, given the different trends for operating temperature vs. solar cell orientation in Section 2.3 compared to those shown for concentration factor in Section 2.4, PV operating temperature alone cannot be used as a proxy for overall LSC performance.

2.5. Luminophore Optimization for Minimized PV Operating Temperatures

We next investigate the role of luminophore material and properties on both PV operating temperature and LSC module efficiency. Figure 16 displays the spectral properties for three different quantum dot materials—CdSe/CdS, InAs/InP/ZnS, and $CuInS_2$/ZnS. We use these quantum dots to simulate three different LSC systems. In each system, we assume the same base case LSC—a single edge-lined PV cell in a polymer waveguide—as this configuration was shown to have the lowest operating temperature in details the operating temperatures for each the Si PV device and the luminophore waveguide for each of the three quantum dot systems.

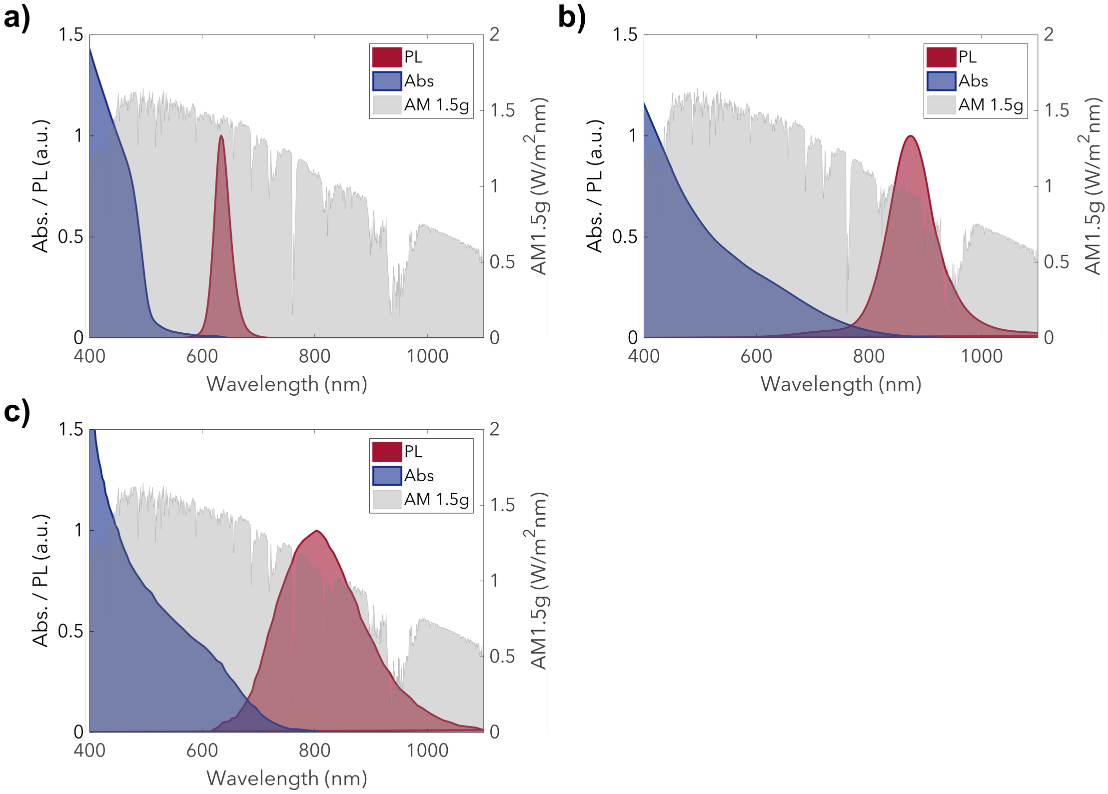

Figure 16: Absorption and PL spectra for three investigated quantum dot systems.
(a) CdSe/CdS, (b) InAs/InP/ZnSe, and (c) CuInS$_2$/ZnS.

QD System	PV Temp (ºC)	Waveguide Temp (ºC)
CdSe/CdS	28.1	31
InAs/InP/ZnS	32	34.7
CuInS$_2$/ZnS	32.4	35.1

Table 2: Operating temperature for a 1cm x 200µm x 80µm edge-lined Si cell in a 1cm x 1cm x 200µm waveguide with varied quantum dot luminophores.

To determine the effects of each luminophore property, we vary the location of each the *i)* QD PL peak, *ii)* absorption edge, and *iii)* optical density within the LSC waveguide. As shown in Figure 17, optical density logarithmically affects PV operating temperature in an LSC. This logarithmic relationship is expected, given the additional photons absorbed as optical density increases in accordance with the Beer-Lambert law [90]. We further see in Figure 17a that as the PL peak is red shifted, PV temperature decreases. By red-shifting towards 1000nm, the PL peak is approaching the Si solar cell bandedge. This improved performance via red-shifting towards the bandedge supports previous studies which suggest that LSC module efficiency should improve for a red-shifted luminophore system [52]. In contrast, PV temperature increases when the QD absorption edge is red-shifted (Figure 17b), given the additional irradiation that is absorbed by the LSC waveguide.

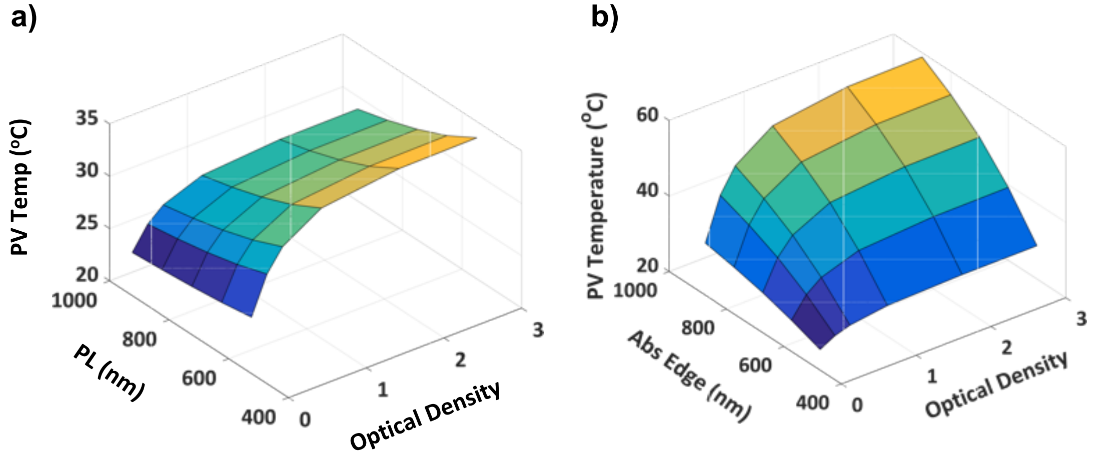

Figure 17: Effects of QD parameters on PV Operating Temperatures in LSC systems.
PV operating temperature for (a) varied QD luminophore PL peak location and optical density (absorption edge held constant at 500nm), and (b) varied QD absorption edge and optical density (PL peak held constant at 950nm).

As discussed in Sections 2.3 and 2.4, a lower PV operating temperature in an LSC does not necessarily imply improved efficiency performance, as would be the case for a conventional wafer, due to unequal photoluminescence collection across the waveguide. Thus, to understand how these luminophore results affect overall module performance, we use Monte Carlo ray-tracing simulations to model power conversion efficiency for the specified conditions and modeled operating PV temperature. Given the calculated power conversion efficiencies, we calculate the temperature coefficient for the solar cell:

$$C_{eff} = \frac{\eta_1 - \eta_2}{T_1 - T_2}; \ C_{Voc} = \frac{V_{OC,1} - V_{OC,2}}{T_1 - T_2}$$

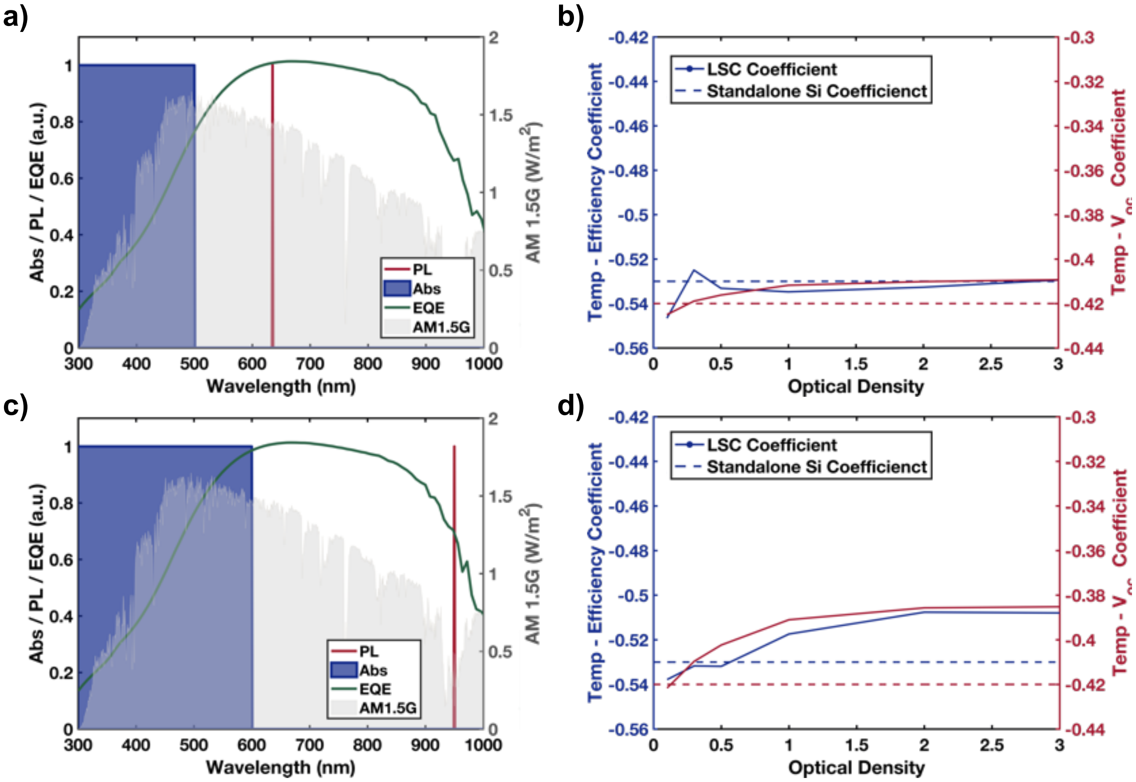

Figure 18: Simulated temperature coefficients for ideal quantum dot systems
Both systems assume a Stokes shift of 0.42meV. Absorption and PL spectra are shown in a) and c), with the PV temperature coefficients for the respective LSC system in b) and d).

In Figure 18, we model the temperature coefficient—for each efficiency (blue) and V_{OC} (red)—for a Si cell in an LSC waveguide (solid lines) and conventional wafer device (dotted lines). We model two different (ideal) QD systems, keeping the Stokes shift constant (0.42meV) for both systems, with the absorption/PL spectra shown in Figure 18a,c. For a 15.7% efficient Si cell (assuming ambient conditions of 20°C), the temperature coefficient for a conventional homojunction Si wafer device is -0.53% /°C, as was modeled in Sentaurus. As shown in Figure 18b, the Si temperature coefficient when embedded in the LSC, across varied optical densities, is comparable to that of a conventional wafer device. However, for a red-shifted QD system (Figure 18c,d), where the Stokes shift is held constant but the PL peak (950nm) is closer to the Si bandedge, we see significant improvement in the temperature coefficient. For optical densities greater than 0.3, the temperature coefficient for the LSC module is consistently higher (less negative), with efficiency coefficients of (-0.49% /°C), in comparison to that of the conventional wafer Si device (-0.53% /°C). As such, we demonstrate that an LSC device with a PL peak matched to the PV bandedge is optimal for improved module performance, with efficiency coefficient improvements up to 0.04% for every degree Celsius.

2.6. Photonic Crystal Waveguide Impact on Concentration Factor

Lastly, we analyze the concentration factor of an LSC upon varying the trapping efficiency via use of a photonic crystal slab waveguide. We can further define optical efficiency as a function of absorption efficiency (η_{abs}), photoluminescence quantum yield (PLQY, or η_{PL}), trapping efficiency (η_{trap}), and waveguide efficiency (η_{wg}). Given this definition, concentration factor is now dependent on each of these parameters.

$$\eta_{opt} = \eta_{abs} * \eta_{wg} * \eta_{PL} * \eta_{trap}$$

$$C = GG * \eta_{opt}$$

$$= GG * \eta_{abs} * \eta_{wg} * \eta_{PL} * \eta_{trap}$$

Thus far, we have examined the impact of both varied PV orientations and luminophore properties on total LSC optical efficiency, whether as a function of concentration factor or power conversion efficiency. We now isolate the trapping efficiency portion of the optical efficiency parameter to understand its effects on LSC concentration factor. To do so, we vary the trapping mechanisms for the system, including total internal reflection (TIR) and high performance photonic crystal trapping waveguides. By using amorphous-silicon carbide (a-SiC) photonic crystal waveguides, as discussed in Bauser et al., we can improve the trapping efficiency in the LSC system, and thus improve the concentration factor. In this study, we examined various photonic crystal waveguide structures—of both hole arrays and rod arrays within the a-SiC material—each with varied trapping efficiencies.

Given that concentration factor represents the enlargement factor of active PV area for an LSC, we aim to achieve high concentration factors in order to maximize the PV active area within the LSC. We define concentration factor as a function of the LSC geometric gain (GG), device absorptance (η_{abs}), waveguide efficiency (η_{wg}), luminophore PLQY (η_{PL}), and trapping efficiency (η_{trap}), in accordance with the analytical analysis of concentration factor by Klimov et al. [35]. Here we define geometric gain as the ratio of LSC area (length * width) to the area of the photovoltaic material. Device absorptance refers to the fraction of incident light that is absorbed by the luminophores, waveguide efficiency is the fraction of PL that reaches the PV material, and trapping efficiency is the fraction of PL trapped within waveguide modes and TIR. Hence, higher trapping efficiencies, as described in this paper, directly enable heightened concentration factors.

Trapping System	Average Trapping Efficiency (%)
TIR Only	74.13
Rod Array: QD at substrate interface	92.56
Hole Array: QDs 100% infilled for hole volume	93.32
Hole Array: QDs 93% infilled for hole volume	92.30
Hole Array: QDs in center disk	95.36

Table 3: Trapping efficiency as a function of waveguide type and QD placement.

For this analysis, we assume an LSC that uses InGaP cells with a band edge matched to the emission of the QDs [6,9]. We analyze the concentration factor of the LSC system as a function of geometric gain. Here, we show how increasing the trapping efficiency affects potential achievable concentration factors as a function of the geometric gain. Figure 19a shows how the concentration factor improves when employing the rod array, compared to designs in which luminophores that are dispersed in a polymer waveguide are only trapped by TIR. Figure 19b performs this analysis for the hole array configurations; in this figure we compare the performance of i) TIR alone, ii) employment of a narrow disk of QDs in the center of the hole array, iii) filling 93% of the hole with QDs, and iv) filling the entire hole with QDs. The average trapping efficiencies for each of these designs can be found in Table 3. We see that higher concentration factors are achieved with the highest trapping efficiency configurations. Since the trapping efficiencies of all of these designs are > 92%, each of these configurations has the potential to improve on a traditional QD waveguide by nearly 30%, which rely on TIR; these results agree with the conclusions of Rousseau and Wood [26].

Figure 19c,d repeats the analyses by assuming an optimized absorption coefficient for the CdSe core (α_2) of the QD for each the rod and hole configurations, respectively. By assuming an α_2 of 10, we are able to achieve concentration factors beyond 100 for both the rod and hole arrays. Furthermore, the concentration factor enhancement remains robust for the hole array infilling options allowing for flexibility in fabrication and optical density of the QDs.

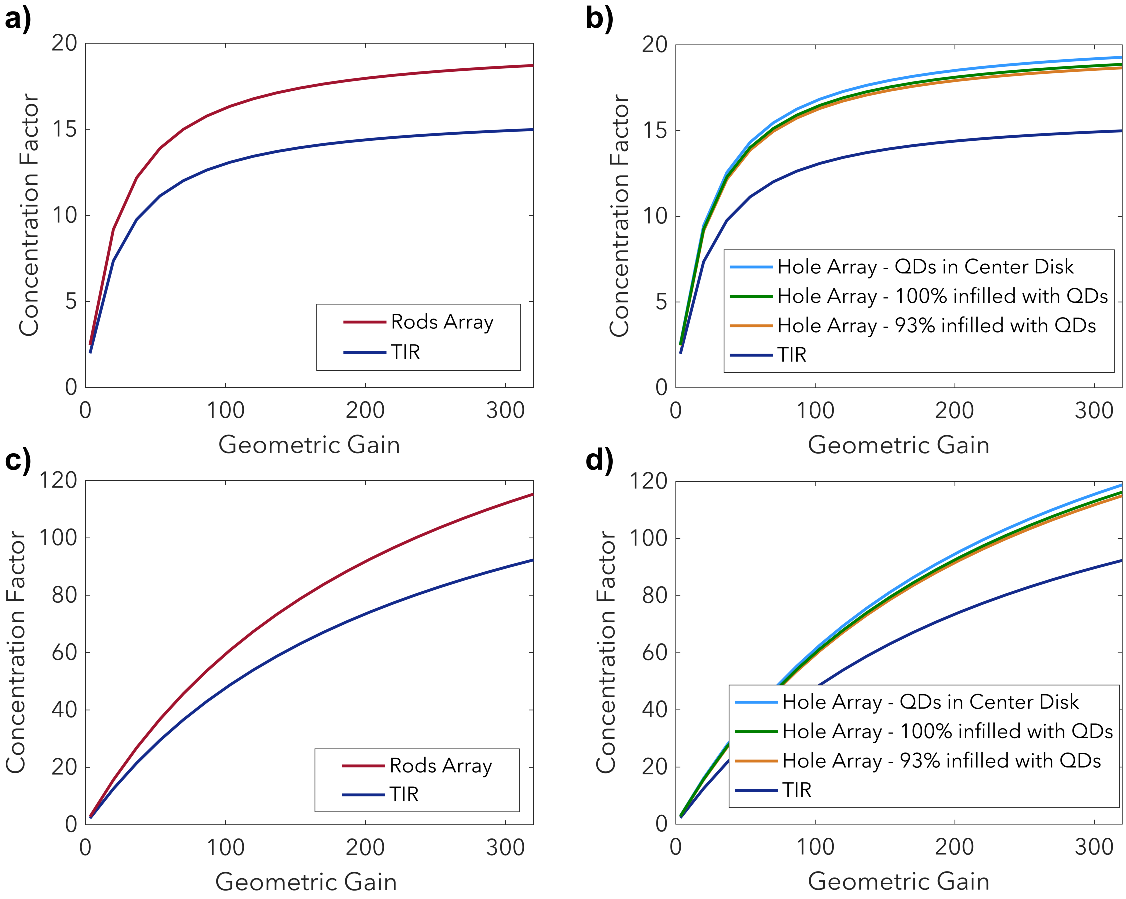

Figure 19: Concentration factor vs. geometric gain for photonic crystal waveguide LSC systems.
Here we examine an edge-lined LSC, using CdSe/CdS QDs and InGaP PV cells. We show the concentration factor performance in comparison to TIR for the proposed a) rod array, and b) hole configurations with varied ways of filling the QDs in the holes. Figures c) and d) display the concentration factor performance for each the rods and holes, respectively, for an idealized CdSe/CdS quantum dot.

2.6. Conclusions

Luminescent solar concentrators may be assessed via various performance metrics—including efficiency, PV operating temperature, and concentration factor. By varying the solar cell form factor, luminophore materials, and waveguide trapping, we simulate how each of these components affects the performance metrics. In terms of operating temperature, LSCs are a promising technology to lower photovoltaic operating temperatures in comparison with their conventional wafer Si PV counterpart. Our models, however, suggest that lowered PV operating temperature, based on cell orientation, does not necessarily correlate with improved LSC module efficiency and concentration factor, and thus operating temperature alone cannot be used as a proxy for LSC performance. Our results indicate that photoluminescence is not collected homogenously in a luminescent waveguide, and that coplanar configurations present an advantageous option for both maintaining constant geometric gains regardless of module size, as well as heightened efficiency. We further demonstrate that optimal PV performance, via temperature efficiency coefficient, occurs when the LSC luminophore PL peak is closely matched to the PV bandedge. Finally, we demonstrate how a-SiC:H rod and hole photonic waveguides, coupled with CdSe/CdS QDs, can be used to improve the concentration factor within an LSC and achieve concentration factors over 100. By expanding our study in each of these component areas—PV device, luminophore, and trapping—we expect that these results can be further improved upon and applied to a variety of LSC systems.

CHAPTER 3: SILICON HETEROJUNCTION MICROCELLS

We report the design, fabrication, and characterization of silicon heterojunction microcells, a new type of photovoltaic cell that leverages high efficiency bulk wafers in a microscale form factor, while also addressing the challenge of passivating microcell sidewalls to mitigate carrier recombination. We present synthesis methods exploiting either dry etching or laser cutting to realize microcells with native oxide-based edge passivation. Measured microcell performance for both fabrication processes is compared to simulations. We characterize the dependence of microcell open-circuit voltage (V_{OC}) on cell area-perimeter ratio, and examine synthesis processes that affect edge passivation quality, such as sidewall damage removal, passivation material, and deposition technique. We report the highest Si microcell V_{OC} to date (588 mV, for a 400 μm × 400 μm × 80 μm device), demonstrate V_{OC} improvements with deposited edge passivation of up to 55 mV, and outline a pathway to achieve microcell efficiencies surpassing 15% for such device sizes.

3.1. Introduction

Over the past several decades, silicon photovoltaics have transformed the renewable electricity generation landscape, with worldwide solar installations of >100 GW/year [91], [92]. Microscale solar cells, defined as photovoltaic (PV) devices with a top area less than 1 mm^2 [93], are expanding the reach of solar electricity generation beyond applications typified by solar farm and rooftop installations [85], [93]–[95]. Applications of PV microcells, as demonstrated in previous works, include autonomous electrochromic windows[93], luminescent solar concentrators [34], [43], [51], [52], [96], and self-powered sensors[97]. Microscale form factors, when obtained from large wafers and placed in a coplanar fashion, as shown in **Figure 20**, can enable: *i*) increased module mechanical flexibility; *ii*) partial optical transparency via assembly in sparse arrays on transparent substrates[51], [84], [86], [87], [89], [93], [98]; and *iii)* self-powered systems. As such, microcells may present alternatives to organic PV and thin film perovskites for flexible and transparent self-powering systems [97], [99] for applications in internet of things [100], advanced sensors [101], building integrated PV [60], [93], [99], integrated power subsystems for portable consumer electronics [102], and wearable electronics [103].

Silicon (Si) presents advantages as a PV material given its low toxicity, natural abundance, and compatibility with robust micro-processing techniques [104]–[108]. Low open-circuit voltages (V_{OC}) for Si microcells, however, have limited applications to technologies with low power requirements (e.g., electrochromic windows). To date, the highest reported efficiency of a Si-based microcell device is 13.7%, with an associated V_{oc} of 560 mV, at dimensions 1.5 mm × 200 µm × 30 µm [95]. Given the large contribution of recombination currents attributable to the device edge at small sizes, opportunities to achieve efficiencies approaching that of their macro-scale counterparts are realized by improving V_{OC} via optimization of device structure, geometry, and surface passivation [95].

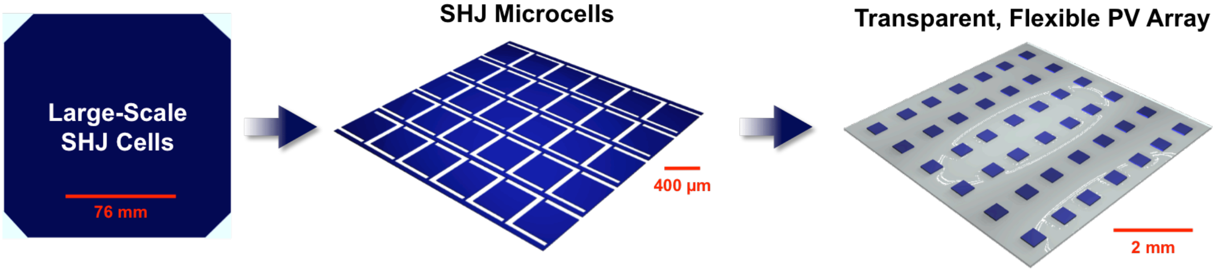

Figure 20: Process flow for dicing large-scale SHJ wafers into suspended microcell wafers.
These suspended microcells can then be removed and printed into a coplanar array on a transparent, flexible substrate, at a target spacing.

In this work, we demonstrate the first generation of a new type of Si microcell based on a silicon heterojunction (SHJ) architecture that enables improved V_{OC} [108]–[116]. We compare two methods of microfabrication for SHJ microcells from wafer-scale SHJ cells—deep reactive ion etching (DRIE) and laser cutting. To demonstrate the scientific challenge of achieving high-performance microcells by mitigating edge effects when carrier diffusion lengths are on the order of the device size, we choose to work with a 400 µm × 400 µm × 80 µm exemplary system. We employ device physics simulations to model V_{OC} for square-shaped SHJ microcells across varying lateral dimensions, thicknesses, and edge recombination velocities (ERVs). For each fabrication method, we characterize the damage to the device edges after dicing by examining microcell V_{OC}, comparing both measured and simulated results. We assess the impact of both microfabrication techniques on the resulting V_{OC} for varying microcells widths (200 µm up to 1000 µm). We further demonstrate improved performance via sidewall damage removal and passivation, and measure the highest recorded V_{OC} (588 mV) for a Si microcell. Finally, we outline routes to further increase V_{OC} and suggest pathways to optimize SHJ microcell performance.

3.2. Silicon Heterojunction Microcell Fabrication Techniques

Microscale devices have been fabricated using a variety of methods—DRIE, laser micromachining, UV LIGA, and X-ray LIGA—with varying results to achieve high-aspect-ratio etching of Si materials [97]. To fabricate SHJ microcells, we employ each DRIE and laser cutting processes to understand how different micromachining methods influence performance. As mentioned, square-shaped devices, 400 μm × 400 μm in size, are used as an exemplary microcell system with dimensions commensurate with carrier diffusion lengths. An overview of SHJ microcell fabrication via DRIE and laser cutting is outlined in Figure 21, and details are provided in Appendix A (Figure S1). Large-scale, non-metallized SHJ wafers (6 in × 6 in × 80 μm) [108], [111], [115] are used as the starting material. Voltage measurements for the SHJ bulk wafers, taken using a Suns- V_{OC} instrument [116], are provided in Table S1 in Appendix A. Bulk wafers are coated with 360 nm of silicon nitride (SiNx) to serve as a protective layer for the underlying indium tin oxide (ITO). The wafers are then diced via DRIE (Figure 21a-c) or laser cutting (Figure 21d-e), according to a pattern that includes 15 μm bars to anchor the microcells to the source substrate, as indicated by the red arrow in the confocal image in Figure 21a. In the case of laser cutting, material removed during dicing is re-deposited along the sidewalls and top device perimeter, as shown in Figure S2. Both DRIE and laser cutting dicing processes result in damaged Si along the device edges that is removed by etching the suspended microcell array in a 3 M KOH/2 M IPA solution [117]. A subset of the suspended microcell array, featuring a device with removed sidewall damage, is shown in the scanning electron microscope (SEM) images in Figure 21f-i for both DRIE- and laser cutting-based methods.

Both presented micro-fabrication techniques yield (from a geometric perspective) high quality diced microcell arrays, at the target lateral dimensions, that are suspended on the sample wafer via their 15 μm anchor bars, as shown in Figure 22a. This design enables a microcell array patterned sample that yields ca. 700 microcells (for the 400 μm × 400 μm device size). To qualitatively compare how each fabrication technique affects the microcell performance along the dicing line, we examine the microcell edges using SEM. A rendered image of the region of interest—the microcell edge—is shown in Figure 22b. Representative SEM images of the microcell edges are shown directly following dicing (i.e., as-cut) in Figure 22c,d for DRIE and laser cut microcells, respectively. The horizontal scallops along the microcell sidewall are a byproduct of the DRIE Bosch process (Figure 22c), which cycles between etching and deposition of a fluorocarbon to achieve a highly vertical etch profile. The effects of trench width on sidewall morphology during DRIE etching are shown in Figure 62a in Appendix A. We observe characteristic horizontal Bosch scallops along the sidewalls within the wider trenches of the pattern and vertical striations within the narrower trenches [110]. In contrast, laser cut processing results in a nonuniform sidewall morphology (Figure 22d) due to recast material and physical/thermal damages (i.e., heat affected zone) resulting from the laser cutting process [110].

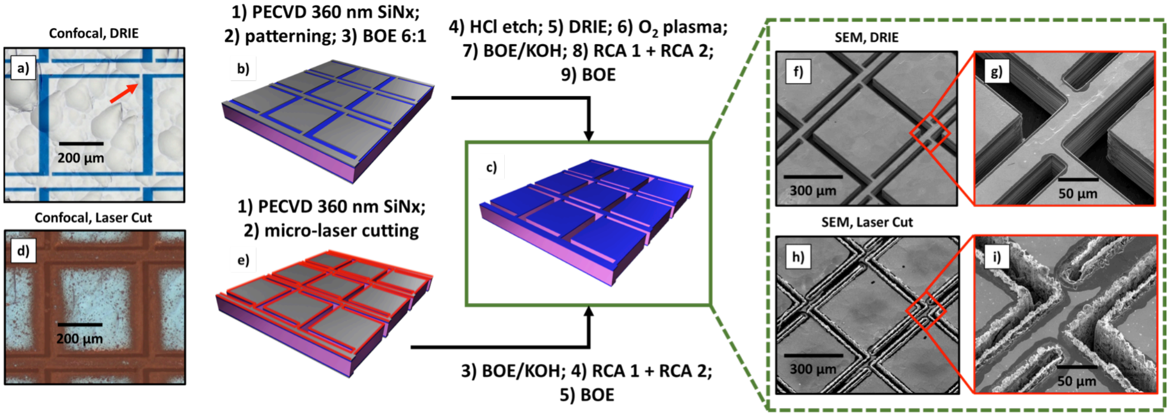

Figure 21: SHJ microcell processing steps for each DRIE and laser cutting
For the DRIE process (top portion of figure), 360 nm of SiNx is first deposited via PECVD on the SHJ wafer, and then the target pattern is etched into the SiNx layer using a BOE 6:1 etch, as shown in the confocal image in (a) (the red arrow indicates 15-µm anchor bars) and the rendered image in (b). The final etched substrate is shown in (c) following the final etching and cleaning steps for each process. For the laser cutting process (bottom portion of figure), 360nm of SiNx is again deposited on the SHJ wafer as a protective layer, and the target pattern is laser cut into the wafer, as shown in the confocal image in (d) (copper color shows the deposited damaged Si powder along the microcell perimeter) and rendered image in (e). Note, the red outline in (e) represents damaged Si powder that is redeposited along the microcell perimeter following laser cutting. Profile imaging and sidewall morphology is shown via scanning electron microscope (SEM) images for DRIE microcells at each (f) 5× and (g) 20× magnifications, and for laser cut microcells at each (h) 5× and (i) 20× magnifications.

Sidewall images following damage removal (3 M KOH/2 M IPA and RCA processes, as described in Methods) are shown in Figure 22e,f for the DRIE and laser cut microcells, respectively. As shown, the damage removal processes result in considerably smoother sidewall morphologies for both dicing techniques, in comparison to the morphologies/textures seen in the as-cut SEM images. Damage removal on DRIE-processed microcells enables smoother sidewalls, on average, than damage removal on laser cut microcells (Figure 62b), due to the alignment of the vertical profiles of each with the <110> planes of the device substrate, which etch at a local minimum rate compared to other processing-developed features in the 3 M KOH/2 M IPA wet etchant solution [109]. After laser cutting, the microcell sidewalls are tapered outward slightly, and the initial recast Si material does not uniformly correspond to any particular crystal plane, and is likely to be amorphous. Even so, the damage removal process successfully reveals the <110> plane in most areas along the device sidewalls, as shown in the SEM image.

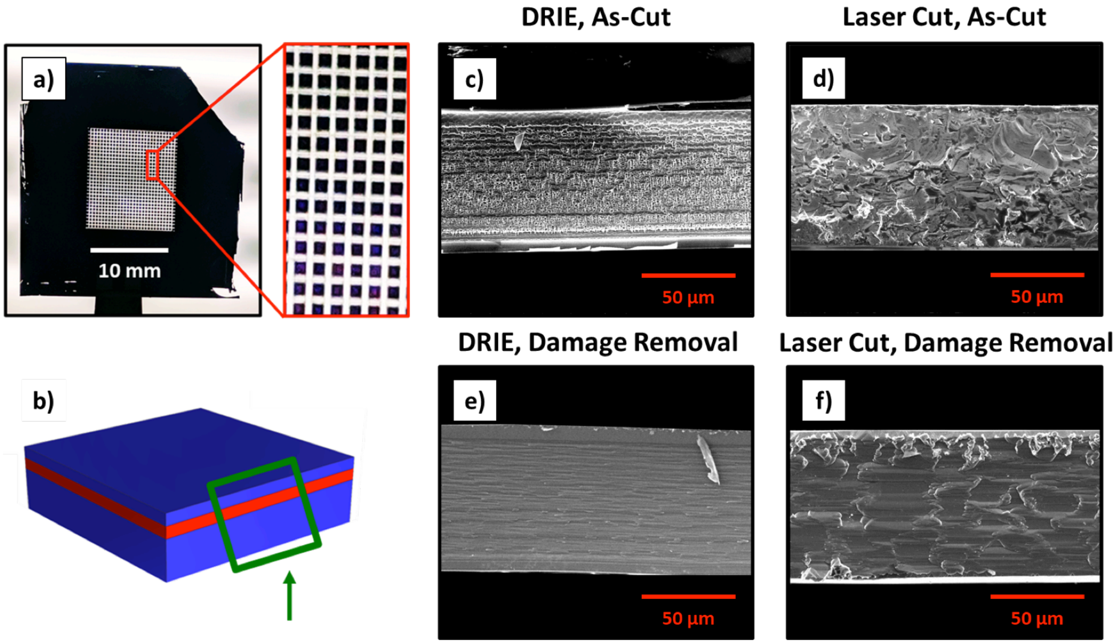

Figure 22: Sidewall morphology of diced SHJ microcells, for each DRIE and laser cut samples. A camera image of an etched 400 µm × 400 µm microcell wafer is shown in (a), with a zoom-in to display the grid-like pattern in which the microcells are suspended. The rendered image in (b) shows the microcell sidewall region that is imaged in c-e, including a red line indicating the p-n junction. SEM images of as-cut microcell sidewalls, prior to any damage removal processing, are shown for (c) DRIE cells and (d) laser cut cells. The effects of chemical etching and cleaning procedures on SHJ microcell sidewall morphology are shown through SEM images for each (e) DRIE cells and (f) laser cut cells.

Sidewall morphologies tend to vary after the 3 M KOH/2 M IPA damage removal process for both the DRIE and laser cutting process, as shown in Figure 63 in Appendix A. In the case of DRIE, we have noted pinned etchant features that arise as a consequence of reaction product (H_2) bubbles forming and either attaching to or passing by the device sidewalls [111], [112]. Similar effects have also been noted related to etchant inhomogeneities and product removal in ways most deeply impacting the laser cut devices [112]. The current etchants and methods do not temper this impact from mass and heat transfer, which will require a more robust mitigation strategy in a more fully optimized process design to reduce variations in sidewall morphology (e.g., implementation of a flow reactor for damage removal).

3.3. Silicon Heterojunction Microcell Performance Modeling

To predict how device geometry and quality of edge passivation influences SHJ microcell performance metrics, we develop a device physics model of the SHJ microcells [118]. In particular, we model square-shaped microcell devices with varying lateral dimensions, employing high-quality passivation (SRV = 2 cm/s) [109], [119], [120] at the top and bottom surfaces and lower quality passivation at the device edges. A schematic of the SHJ microcell device architecture is shown in Figure 23a (shape-based model details are shown in Figure 64). The effects of varying SHJ microcell geometry (thickness, width) on performance parameters are shown in Figure 65 in Appendix A. At small thicknesses, the short-circuit current (J_{SC}) decreases quickly due to the low absorption coefficient inherent to silicon [121]–[124], thereby dominating microcell efficiency in this regime. For microcell thicknesses greater than 40 μm, efficiency is driven by device width. V_{OC} increases with decreasing device thickness (Figure 23c), due to reduced recombination in both the bulk and at the device edges [108], [114], however, this effect is not large enough to overcome the negative influence of the decreasing J_{SC} on device efficiency. As microcell width is altered, the parameter primarily affected is V_{OC}; V_{OC} increases with width [115], [125]–[127] for small-area Si PV cells [128]–[130]. Edge surface area and perimeter length is minimized at small thickness and large width, and thus V_{OC} is maximized under these circumstances. Fill factor (FF, Figure 65 in Appendix A) shows minimal variation with device width and thickness. Therefore, as a result of the competing effects of V_{OC} and J_{SC}, simulated SHJ microcell efficiencies vary from 11.6% for microcells of the smallest width (200 μm) and thickness (10 μm) to 16.1% at the largest width (1000 μm) and thickness (150 μm).

Given the dependence of V_{OC} on edge recombination, V_{OC} is used to evaluate device performance as a function of sidewall passivation. To assess how sidewall passivation affects the impact of recombination at device edges, we vary the ERV from 2 cm/s, as would be characteristic of a surface with high-quality passivation (e.g., a-Si:H or TiO_2) [120], [131], [132], up to $2x10^6$ cm/s, characteristic of a surface with poor-quality passivation, surface damage, or contamination [133]. Figure 23b,c plots efficiency and V_{OC}, respectively, as a function of ERV and device width at a fixed thickness (80 μm), further illustrating the importance of edge passivation quality, in addition to device size, for achievement of high performance microcells.

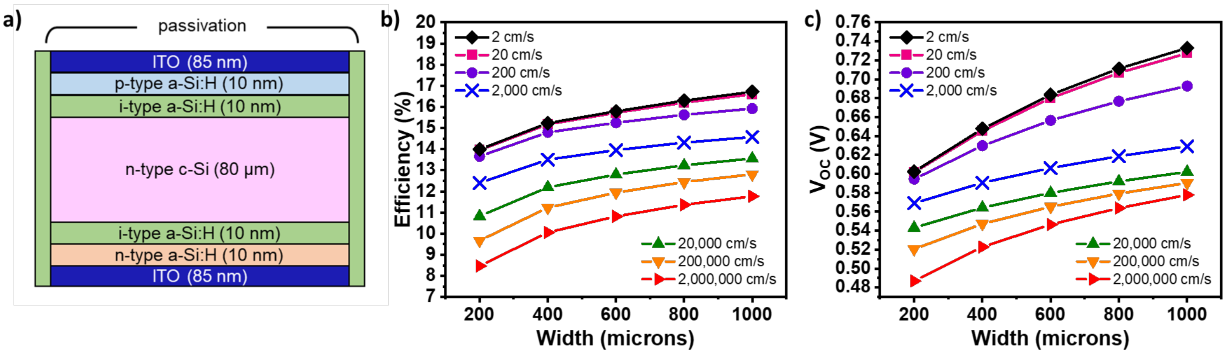

Figure 23: Simulated results for SHJ microcell performance.
Simulations are shown for the indicated (a) SHJ device architecture. Simulated device (b) efficiency and (c) V_{OC} with varying width and varying ERV at a fixed device thickness of 80 μm.

3.5. Measured Silicon Heterojunction Microcell Performance

For each dicing method, we compare measured performance of the fabricated 400 μm × 400 μm × 80 μm SHJ microcell devices relative to both the bulk SHJ devices ($pV_{oc} \approx 740$ mV) and the simulated results. Figure 24 compares DRIE and laser cut microcells with native oxide passivation before and after damage removal both qualitatively and quantitatively. Light beam induced current (LBIC) mapping for each microcell dicing technique after damage removal, while limited in capability of providing insight to recombination at the device edges, qualitatively suggests that photocurrent is collected evenly with regard to absorption, with occasional defects, across the microcell surface (Figure 24a,b). Laser cutting processing results in some additional minor defects, particularly around microcell edges.

Quantitative microcell performance metrics, for both as-cut devices and devices after sidewall damage removal, are shown via JV curves in Figure 24c,d, and are detailed in Table 12 in Appendix A. As shown in Table 12 in Appendix A, we observe both device-to-device (i.e., device variation across the same wafer) and wafer-to-wafer variation (i.e., inherent process variation across many wafers) in performance, with value ranges that are consistent with Si-PV cell processing carried out in both laboratory and non-optimized industrial settings [108]. The V_{OC} values are compared for each dicing and damage removal process in Figure 24e, including sample standard deviation among devices and wafers. As shown (Figure 24c-e, purple squares), as-cut DRIE processing results in a higher V_{OC} (531 mV) and FF (65.5%) relative to laser cut processing (V_{OC} = 387 mV, FF = 48.3%) due to significantly less damage induced by the former. These V_{OC} measurements match simulated results for an ERV of nearly $1x10^6$ cm/s and $2x10^9$ cm/s, respectively, thereby suggesting the existence of extensive contamination and/or damage along the as-cut microcell sidewalls.

Following damage-removal processing, the device edges are passivated with naturally growing native oxide. As shown in Figure 24c-e, devices with average results (blue circle JV curves) display improved device V_{OC} from the average as-cut state (purple square JV curves) for both the DRIE- and laser cut-based processes. This improvement is due to a reduction in recombination sites along the device edges. After initial damage removal, the laser cut devices (V_{OC} = 532 mV, FF = 68.2%) quite remarkably perform similarly to DRIE devices (V_{OC} = 540 mV, FF = 64.4%), doing so in spite of the devices marked differences in thermal histories and the noted levels of irregularities and damage present along the sidewalls for as-cut devices. Limiting performance found in either case, as shown in Figure 24c,e for the highest-performing DRIE device (green cross) sourced from the highest-performing wafer (red triangle), boasts a V_{OC} of 588 mV, corresponding to a modeled ERV of $3x10^3$ cm/s. Notably, as shown in Figure 24c-e in dotted black, this device performs similarly to the model in terms of J_{SC} (model J_{SC} = 29.1 mA/cm^2) and V_{OC} (model V_{oc} = 609 mV, ERV = $7x10^2$ cm/s) for SHJ microcells of these dimensions. Underperformance relative to the model likely results from residual sidewall damage, increased surface roughness along the device sidewalls, or possible contamination associated with products of unintentional etching of ITO in HF-based solutions. Additionally, we note that while we are unsure of the sources of the high degree of variance in our results, possible explanations based on both starting material or processing-based origins include: i) sample degradation; ii) variation in DRIE processing from etch-to-etch in terms of the extent of initial sidewall damage and scallop depth; and iii) non-optimal processing conditions associated with the environment, equipment, and lack of fully automated process control for all processing steps.

Finally, we note that the measured microcell FF (58%—68%) is lower than that predicted by our model (79%). This difference is potentially due to: *i)* series resistance unaccounted for in the model related to thickness/properties of the i-type a-Si:H layer, or lateral resistive losses in the ITO due to partial oxidation over time [134]; and *ii)* shunting associated with variations in the damage removal processing.

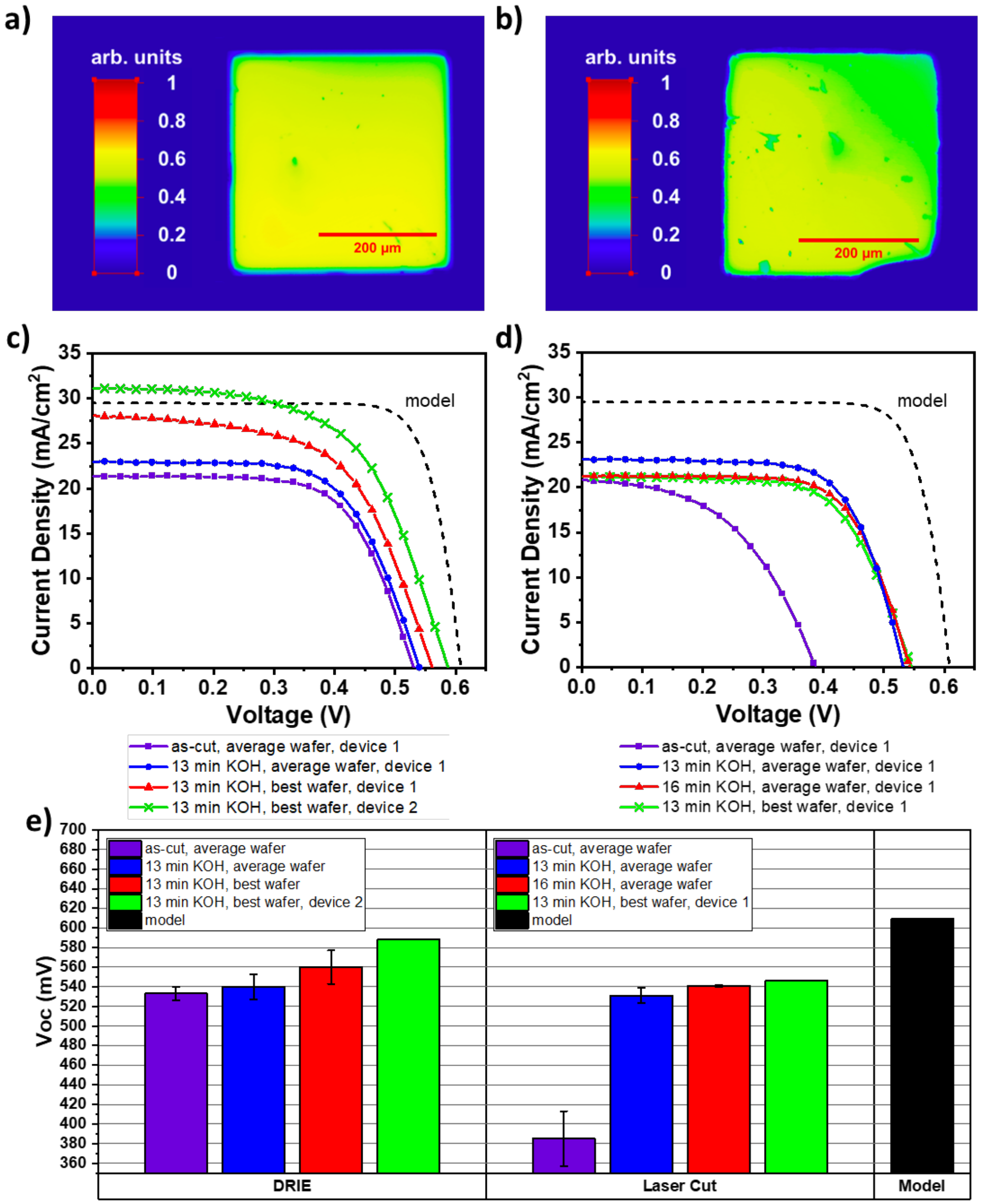

Figure 24: SHJ microcell performance comparison for each dicing technique.
Light beam induced current (LBIC) measurements show predominantly homogenous photocurrent mapping for both (a) DRIE cells and (b) laser cut cells, with slight defects around the perimeter of the laser cut cell. Note, the slight photocurrent drop in the top-right corner of both cells is a result from probe shadowing. JV testing, under AM1.5g solar simulation, shows the performance comparison of varied samples and devices against the modeled JV curve, for 400 µm × 400 µm microcells with native oxide passivation, for each (c) DRIE cells and (d) laser cut cells. A comparison of each measured V_{OC} for the devices plotted in (c) and (d) is shown in (e), with error bars representing the sample standard deviation.

While the highest-performing 400 μm DRIE devices after damage removal (efficiency = 10.7%) outperform the highest-performing laser cut samples (efficiency = 8.4%) in the characteristic measurements in Figure 24, we note that these SHJ microcells were fabricated with a single DRIE machine and a single type of commercial laser cutter. From these performance comparisons, we note that both processes are suitable micro-fabrication techniques for SHJ microcells and have unique advantages and challenges. The results suggest further work is needed to best optimize processing for a given application and set of materials.

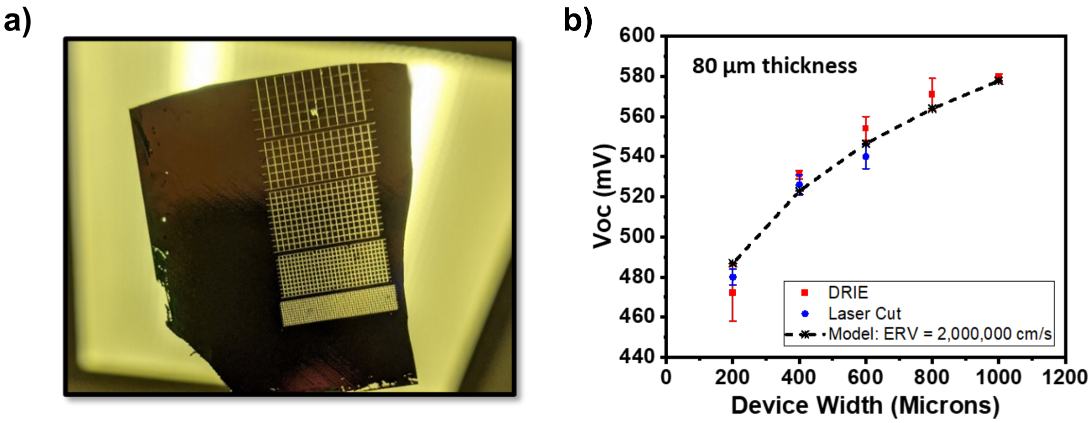

Figure 25: Device performance as a function of SHJ microcell width.
A camera image of suspended SHJ microcells of five different sizes is shown in (a), displaying microcells of constant thickness (80 μm) and varied microcell widths—1000 μm, 800 μm, 600 μm, 400 μm, and 200 μm—from top to bottom of the wafer. (b) V_{OC} dependence on SHJ microcell size, for both simulated results and experimental (DRIE and laser cut) microcell measurements, including error bars calculated across all device measurements (ca. 20). Simulated results are plotted assuming an ERV of 2,000,000 cm/s.

We further investigate the effects of SHJ microcell dimensions, at a constant thickness of 80 μm, as shown in Figure 25. To understand performance versus size, SHJ microcells are diced using either fabrication technique (DRIE or laser cutting) with a pattern that targets five different widths—200 μm, 400 μm, 600 μm, 800 μm, 1000 μm—on the same SHJ bulk wafer sample (Figure 25a). Sidewall damage removal processing using 3 M KOH/2 M IPA is subsequently employed. JV measurements were taken for DRIE devices from 200 μm to 1000 μm in width, and for a smaller processing constrained but overlapping range of laser cut devices (up to 600 μm in width). As the microcell width increases, V_{OC} increases according to a logarithmic trend (Figure 25b) for both the simulated and measured (DRIE and laser cut) data, from an average of 480 mV at the smallest device size (200 μm) to 579 mV at the largest device size (1000 μm). The results from both sets of measurements (DRIE and laser cut) correspond to a modeled ERV of $2x10^6$ cm/s, suggesting the need for improved damage removal in terms of both efficacy and variance to reach full performance potential.

3.6. Microcell Performance Improvements with Edge Passivation

To further improve the SHJ microcell performance vis-à-vis V_{OC}, we explore the impacts of depositing passivation coatings at the edges of these first generation SHJ microcells. For either dicing technique, the microcell edges are passivated with native oxide grown under ambient conditions after the damage removal process. As discussed in the SI, lifetime measurements are taken on (110) Si test wafers, the same orientation as the microcell sidewalls. Measurements of naturally grown native oxide on clean and damage-free test wafers, reveal an SRV of 708 cm/s, thereby suggesting that implementation of different passivation materials may improve microcell sidewall passivation. We compare device performance for various passivating materials and deposition techniques at low temperature ($T < 200°C$) conditions: *i)* native oxide grown under ambient; *ii)* a-Si:H/SiNx via plasma-enhanced chemical vapor deposition (PECVD); and *iii)* TiO_2 via atomic layer deposition (ALD). As shown in Table 14 in Appendix A, the a-Si/SiNx (10 nm/80 nm) and TiO_2 (1.5 nm) passivation coatings exhibit SRVs of 135 cm/s and 62 cm/s, respectively, on clean and damage-free (110) Si test wafers based on lifetime measurements. These measured SRVs serve as the input ERVs to the model. As shown (Table 14 in Appendix A, passivated model), an ideal device passivated with a-Si/SiNx along the edges results in a V_{OC} of 635 mV (a 26 mV improvement from native oxide edge passivation) and an efficiency of 14.9%. Similarly, passivation along the device edges with TiO_2 (1.5 nm) results in a V_{OC} of 641 mV (a 32 mV improvement from native oxide edge passivation) and an efficiency of 15.1%.

As shown in the SEM image in Figure 26a, the PECVD process allows for coating of the microcell edges with a total a-Si/SiNx thickness of 80 nm, with reflection high-energy electron diffraction measurements (RHEED) confirming the amorphous nature of the a-Si material. TiO_2 coatings are deposited via ALD at a deposition thickness of 1.5 nm. In the case of PECVD, the samples are re-patterned via photolithography and a-Si/SiNx is removed exclusively from the top surface using reactive ion etching (RIE), while protecting coatings on the edges, for the purpose of making an exposed electrical contact. In the case of ALD, the passivation coatings are thin enough on the top surface that puncture with a probe is sufficient for contact to the device, and additional photolithographic/etching steps are not needed. Dicing was performed using a modified low-throughput DRIE process to allow for smooth sidewalls prior to applying passivation coatings.

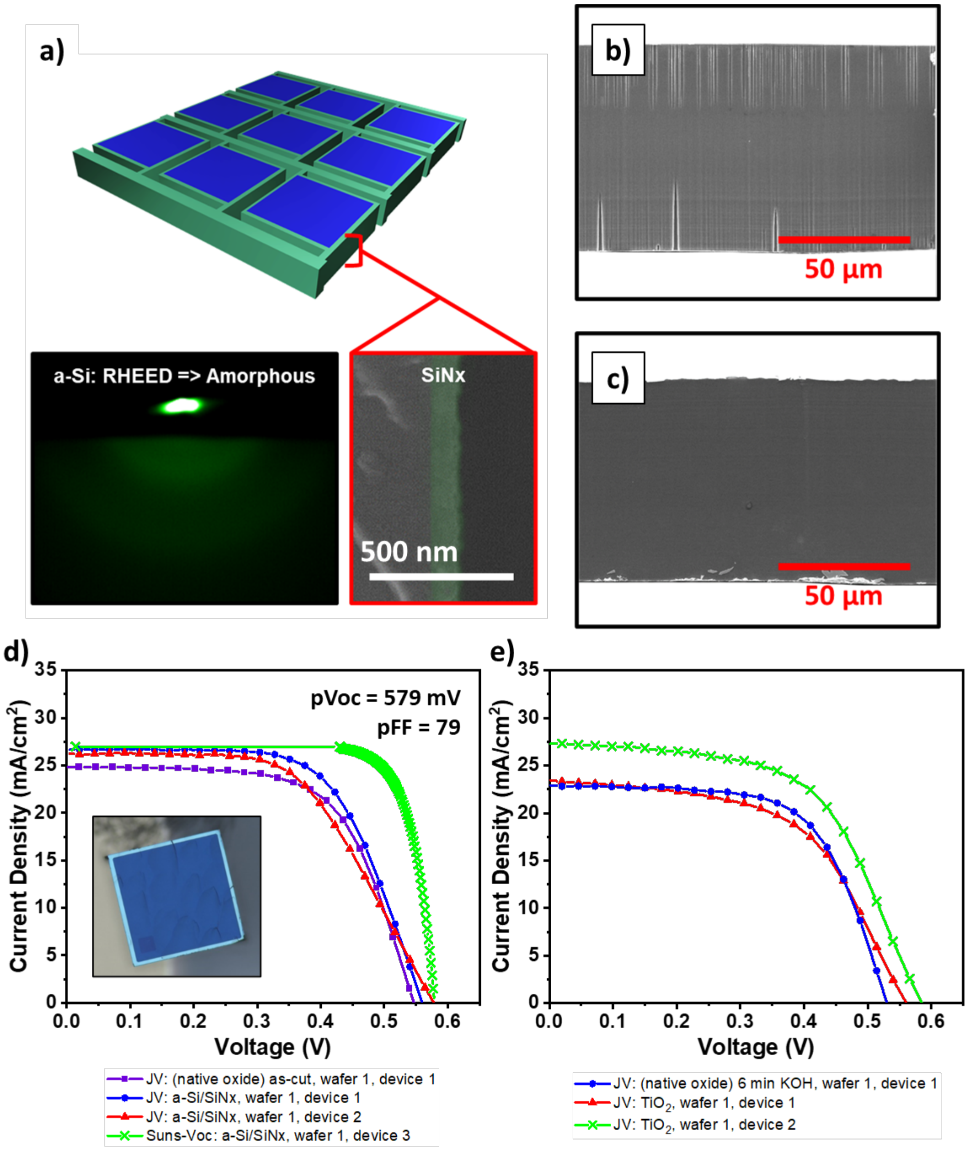

Figure 26: Sidewall passivation of SHJ microcells.
(a) Rendered image of an SHJ microcell with applied sidewall passivation, as shown in green outline, with an inset SEM sidewall image and RHEED measurements displaying the deposited a-Si:H + SiNx along the microcell edge (scale bar = 500 nm). SEM images of microcell edges are shown for each (b) a slow rate DRIE sample with no damage removal, and (c) a slow rate DRIE sample with a 6 min 3 M KOH/2 M IPA etch. JV curves are shown to display microcell performance for sidewall passivation of each (d) a-Si:H + SiNx and (e) 1.5nm TiO_2. The inset in (d) shows a confocal image of a device passivated with a-Si:H + SiNx after removal of the a-Si:H and SiNx from the device top using RIE.

As shown in Table 15 in Appendix A, it is possible to obtain higher V_{OC} and efficiency (passivated, model) with the application of a-Si/SiNx and TiO2 passivation coatings than those measured here (passivated, measured). As mentioned, the primary reason for underperformance relative to the model is likely related to residual surface damage, increased surface roughness, or contamination prior to deposition of the passivation coatings specifically along device sidewalls; the DRIE-based processing methods do not compromise performance of the top/bottom surfaces. Our measurements indicate that on a non-ideal edge surface (i.e., on a surface with some degree of residual damage, as indicated by low V_{OC} values with native oxide passivation), passivation coatings result in higher ERV values (and thus lower microcell V_{OC}) than those applied to smooth, damage- and contamination-free surfaces. Given the high variance associated with the damage removal processing, it is difficult to consistently achieve high-quality damage/contamination removal (as evidenced by high-quality native oxide passivation) on processed microcell sidewalls prior to the application of additional passivation coatings, as previously shown in Figure 26. Nonetheless, improved sidewall passivation enables an ERV decrease of roughly three orders of magnitude, even on microcells with incomplete sidewall damage removal and lower-quality native oxide as a starting passivation material, as shown in Table 14 for TiO_2 passivation.

According to our model, a higher microcell V_{OC} (up to 641 mV) is possible on microcell surfaces with extensive damage removal and low surface roughness prior to edge passivation. Achievement of such surfaces is indicated by a low initial native oxide passivated device ERV of $7\text{x}10^2$ cm/s. The application of passivation coatings on smooth, damage-free surfaces could enable high efficiencies (up to 15.1% for a 400 μm × 400 μm × 80 μm microcell). Notably, as discussed for Figure 25, V_{OC} increases with device width; for a 1000 μm x 1000 μm x 80 μm device, the current methods employed for damage removal and passivation would result in an ERV decrease of three orders of magnitude (ERV = $2\text{x}10^6$ cm/s to ERV = $2\text{x}10^3$ cm/s), and consequently an increase in V_{OC} from 579 mV up to 629 mV. With starting materials and passivation coatings optimized for maximum FF, this correlates to an increase in efficiency from 11.7% to 14.6% for such a device (1000 μm x 1000 μm x 80 μm; ERV of $2\text{x}10^3$ cm/s).

To realize the highest efficiencies and the benefits of high-quality passivation at the device edges, future work should aim to achieve smooth sidewalls and complete sidewall damage/contamination removal. Minimization of initial damage during the dicing process may be enabled by using improved DRIE and laser cutting equipment and dicing parameters, or by investigating different dicing techniques (e.g., UV-LIGA [104]). Optimization of sidewall damage removal may be realized by exploring different processing conditions (e.g., flow reactor) and etchants (different etchant types, temperatures, and times). Potential contamination could be avoided by implementing dry etching processes for steps that result in exposure of ITO to wet etchants. Finally, improved starting materials (i.e., bulk SHJ wafers) could enable minimal series resistance and maximum V_{OC} by improving the quality of the a-Si layers on the top/bottom of the device. Given optimizations that explore suggestions outlined above, high-performing SHJ microcells can be achieved by applying high-quality a-Si:H passivation with an SRV of 2 cm/s on damage- and contamination-free, smooth edge surfaces. Our model suggests that such high-performance SHJ microcells, of dimensions 400 µm × 400 µm × 80 µm, have the potential of reaching a V_{OC} of 646 mV and an efficiency of 15.1%, a record for Si microcells. Even higher V_{OC} and efficiency is possible with larger device geometries (1000 µm x 1000 µm x 80 µm) as shown previously in Figure 23.

3.7. Simulated Microcell Performance Under Varied Illumination Conditions

We model current density—voltage (JV) performance for optimized SHJ microcells, independent of dicing technique, using Synopsis' Sentaurus. Given the low absorption coefficient across the visible spectrum, silicon wafers are typically much thicker than other PV materials (e.g., perovskites, III−Vs) [121], [123]. These thick wafers result in a microcell thickness that is of the same order of magnitude as the microcell width/length, and thus low face-to-edge area ratio. As such, we aim to understand microcell performance at each microcell surface. We evaluate performance for varied lighting conditions (top illumination vs. edge illumination) and microcell dimensions.

As shown in Figure 27, SHJ microcell performance (e.g., VOC, JSC) is affected by the microcell dimensions (width, thickness). For the case of V_{OC}, as microcell width increases, incident photons are subject to less fractional edge recombination. As a result, V_{OC} increases with microcell width, as shown in figure 3, for both top and edge illumination. However, as the device gets thicker, photons across more wavelengths are absorbed, dictated by the absorption depth for silicon, when the cell is illuminated from the top surface [124]. These absorbed low-energy photons are now additionally subject to recombination at the edges, resulting in a V_{OC} that decreases with thickness for top illumination. When the microcell is illuminated instead at the edge surface, the V_{OC} is unaffected by changes in cell thickness, as shown by the overlapping dotted lines in Figure 27. This trend occurs due to the fact that absorption depth is dictated by cell width, and thus the flux per unit area is constant for a cell that is illuminated on its edge. Given a constant flux per unit area, there is no change in recombination per unit area for varied cell thickness under edge illumination conditions.

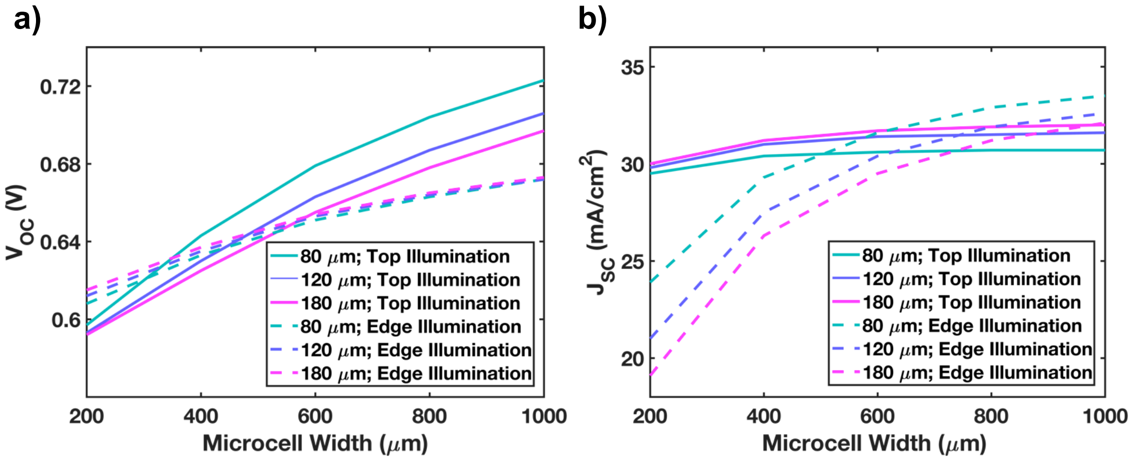

Figure 27: SHJ microcell performance under top- and edge-illumination conditions.
Simulated a) V_{OC} and b) J_{SC} values for SHJ microcells of varied widths and thicknesses under top surface illumination (solid lines) and edge surface illumination (dotted lines).

J_{SC} is further affected with varied microcell dimensions. Under edge illumination, absorption depth is dictated by the microcell width. Hence, as microcell width increases, more photons are absorbed and more carriers are generated under edge illumination, resulting in a heightened J_{SC}, as shown in Figure 27. Absorption depth for top illumination, in contrast, is controlled by cell thickness. As width is varied under top illumination, flux per unit area remains constant; J_{SC} is largely unchanged with increased microcell width under top illumination. Unlike microcell width, changes in microcell thickness result in J_{SC} variations for both illumination conditions: as microcell thickness increases, J_{SC} increases under top illumination and decreases under edge illumination, as shown in Figure 27. For increased microcell thicknesses, carriers experience a longer distance for which to diffuse to the junction. Hence, for edge illumination, where absorption depth is dictated by cell width and is thus unchanged by cell thickness, J_{SC} decreases with increased cell width. However, as microcell thickness increases under top illumination, lower energy wavelength photons are absorbed, resulting in a higher flux of absorbed photons. This increase in photon flux outweighs the heightened carrier diffusion distance leading to an increased J_{SC} with microcell thickness under top illumination.

As shown in Figure 28, for an 80μm SHJ microcell, J_{SC} and V_{OC} performance under top and edge illumination intersect around a microcell width of 400μm. As such, the JV curve in Figure 28 indicates that optimized 400μm x 400μm x 80μm SHJ microcells should perform similarly when illuminated on either the top or edge surfaces. This suggests that SHJ microcells of these dimensions are promising PV candidates for micro-electronic applications with traditional as well as unique form factors as they are able to absorb photons along the edges at equally high performance as absorption at the top surface.

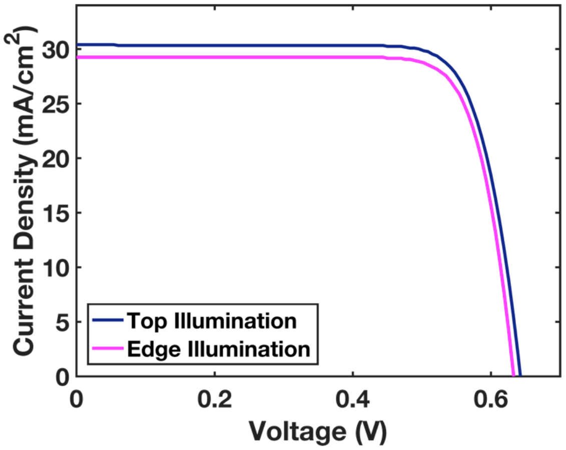

Figure 28: Simulated JV curves for 400μm x 400μm x 80μm SHJ microcells.
We compare top surface illumination (blue line) vs. edge surface illumination (magenta line) for an SHJ microcell.

In addition to JV characteristic curves, varied microcell illumination conditions (top vs. edge) additionally affect SHJ microcell quantum efficiency. We simulate the external quantum efficiency (EQE) for an SHJ microcell of the target dimensions from Figure 28—400μm x 400μm x 80μm. As shown in Figure 29, the EQE for an SHJ microcell that is illuminated along its edge is higher in the blue portion of the AM1.5G spectrum (λ<600nm) than for an SHJ microcell illuminated along its top surface. When a Si cell is illuminated on the top, it experiences parasitic absorption from both the deposited from indium tin oxide (ITO) and doped a-Si:H layers [121]; however, upon illuminating on the device edge, negligible incidence occurs with ITO and doped a-Si:H layers, resulting in minimal parasitic absorption and thus heightened EQE. This reduction in parasitic absorption for edge illumination results in a higher internal quantum efficiency (IQE) in the blue compared to top illumination. Here, we define IQE as the ratio of microcell EQE to the absorption spectra. For a microcell of 80μm thickness and 400μm width, fewer photons are absorbed from top illumination than from edge illumination, due to limited absorptivity depth for low-energy photons.

As a result, IQE in the red portion of the AM1.5G spectrum (λ>600nm) is higher for top-illuminated microcells, as shown in Figure 29.

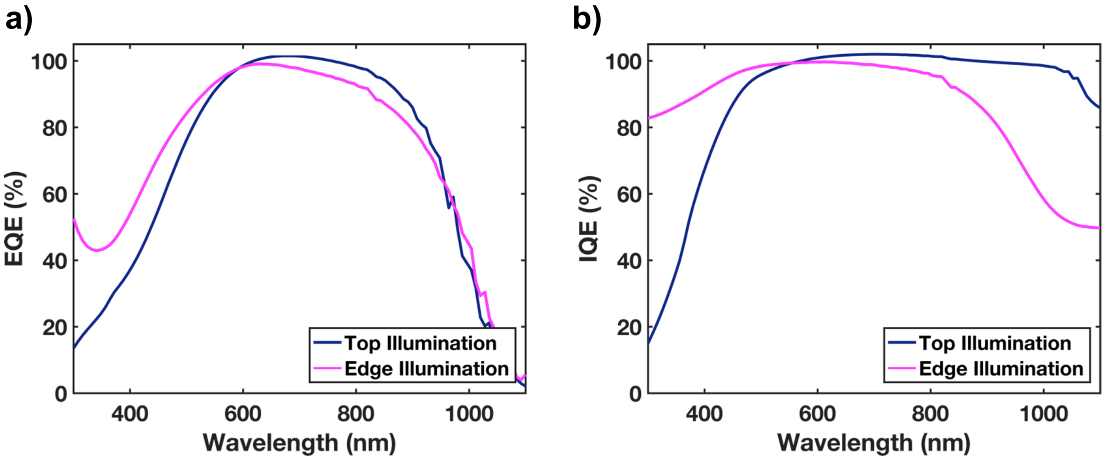

Figure 29: Microcell quantum efficiency curves for top- and edge-illuminated conditions.
Simulated a) EQE and b) IQE curves for 400µm x 400µm x 80µm SHJ microcells. We compare top surface illumination (blue line) vs. edge surface illumination (magenta line) for an SHJ microcell.

We validate simulated results with experimental measurements for fabricated 400µm microcells from each of our dicing and etching techniques—DRIE and laser cutting. Given the simulated JV curves in Figure 28, we present experimental data for top illumination, as we expect performance for edge and top illumination to be similar at this device size.

As shown in Table 4, we significantly improve laser-cut microcell performance, from 4.8% to 8.6%, through an optimized chemical etch, in comparison to cleaning via sonication. Further, we see that the optimized DRIE and laser cut microcells perform similarly, with the DRIE slightly outperforming (10.7% vs. 8.6%) due to minimized device damage. We note that these measurements were derived from a single DRIE machine and a single commercial laser cutter; optimized fabrication results may be achieved from varied equipment. As such, both processing techniques (DRIE and laser cutting) appear to be viable options for fabrication of SHJ microcells.

As shown, experimental, chemically-etched SHJ microcell efficiencies approach the simulated non-optimized results (12.3%), with room for experimental improvements. The simulated ideal microcell efficiency (15.4%) displays the high-performance potential for SHJ microcells.

Dicing Technique	Result Type	Efficiency (%)
Laser-Cut; Sonicated	Experimental	4.8
Laser-Cut; Chemical Etch	Experimental	8.6
DRIE; Chemical Etch	Experimental	10.7
Non-optimized Microcell	Simulated	12.3
Ideal Microcell	**Simulated**	**15.4**

Table 4: Experimental and simulated efficiencies for 400µm x 400µm x 80µm SHJ microcells. We show measurements for both laser-cut and DRIE processing techniques, including improvements on the laser-cut samples by using a chemical etch instead of sonication. Simulated results are also presented for both non-optimized and ideal 400µm SHJ microcell devices.

3.8. Conclusions

SHJ microcells, when assembled in sparse arrays, expand the reach of SHJ materials to include applications that benefit from transparent, flexible energy harvesting. We report modeling and fabrication of first-generation PV microcells derived from silicon heterojunction (SHJ) wafers, and report the highest Si microcell V_{OC} to date—588 mV—for a 400 µm × 400 µm × 80 µm device, with native oxide passivation. We compare two processing routes for fabricating SHJ microcells—DRIE and laser cutting—and discuss differences in dicing quality in terms of V_{OC}. We further demonstrate efficiency improvements after dicing via sidewall damage removal. We examine the effects of device geometry and illustrate the impact of passivation on SHJ microcell performance, with V_{OC} improvements up to 55 mV when applying passivation along the device edges. Additionally, we highlight how sidewall damage removal and surface preparation prior to passivation is crucial to achieve a high V_{OC}, and provide suggestions to further improve performance via processing modifications and improved starting materials. Given these optimizations and our device physics simulations, we propose design strategies and factors to consider for the next generation SHJ microcells, with optimized damage removal processing and passivation coatings allowing for Si microcell efficiencies beyond 15%.

SECTION II: SINGLE JUNCTION LSCS AND THEIR APPLICATIONS

CHAPTER 4: LSCS FOR BUILDING INTEGRATED SOLAR APPLICATIONS

This chapter investigates the requirements for building integrated photovoltaics and proposes a luminescent solar concentrator design for a power-generating window technology. Urban populations continue to grow; yet solar rooftop power generation is limited for these areas. Despite improvement in solar photovoltaic (PV) energy efficiencies, current systems underperform in cloudy environments and urban light settings. Additionally, PV arrays located outside city centers waste between 6 and 13% of the generated power due to transmission losses. Building integrated PV technology tackles both of these problems and increases the clean energy generating capacity of urban buildings. A luminescent solar concentrator (LSC) building integrated PV window technology can be scaled to any window size without sacrificing power efficiency. This design consists of an optical waveguide with dispersed luminophores that isotropically absorb incident sunlight and re-emit as photoluminescence for PV conversion. Here we introduce a visibly-transparent LSC that maintains the power conversion efficiency for any window area by employing a grid-like array of microcells. We model the electrical, optical, and technoeconomic performance of an LSC power-generating window that employs an array of microcell PV collectors, coupled to quantum dot luminophores with PL bands in the infrared regime. We find such an LSC design to reach approximately 7% efficiency at 30% visual transparency, with a forecasted cost per watt between 2.22 and 2.77 $\$/W_p$ for such devices.

4.1 Introduction to Building Integrated Photovoltaics

As discussed in Section 1.2 of this thesis, approximately 57% of the costs in 2019 for utility-scale photovoltaic (PV) systems came from soft costs (e.g. installation labor, sales tax, overhead) and balance of systems (BoS) costs [135]. As such, new application areas and market opportunities are being explored to reduce these BoS costs. Building integrated PV (BIPV) technology enables traditional building materials (e.g., walls, windows, roof shingles) to be equipped with PV power generation capability—where PV BoS and soft costs can be minimized or even absorbed into the construction costs of a building. Shown in Figure 30a, the number of U.S. high-rise buildings (>125 ft in height) continues to increase every year, as indicated in blue, with over 3,000 new projects developed since 1980 [136]. While U.S. PV capacity in this same time frame has grown at a near exponential rate, reaching over 70 GW of installed systems by the end of 2019 (Figure 30a, red), BIPV installations have significantly lagged their utility c-Si counterparts, with less than 0.50 MW capacity in 2019 (Figure 30a, green) [137].

Buildings alone are responsible for approximately 28% of global CO¬2 emissions in the US, and when building-related construction is also considered, that number jumps to over 40% [138]. Given limited rooftop areas of most urban high-rise buildings, typical commercial rooftop PV installations cannot economically offset electricity demands of the building [55]. And while utility-scale solar PV offers off-site generation to urban centers, around 10% of generated PV electricity can be lost due to electric power transmission losses [139]. It is thus interesting to consider how direct integration of PV components into the building façade (i.e., curtain wall and windows) can enable a reduction in installation and systems costs [140], while also providing on-site electricity and mitigating building-related CO_2 emissions, shown in Figure 30b.

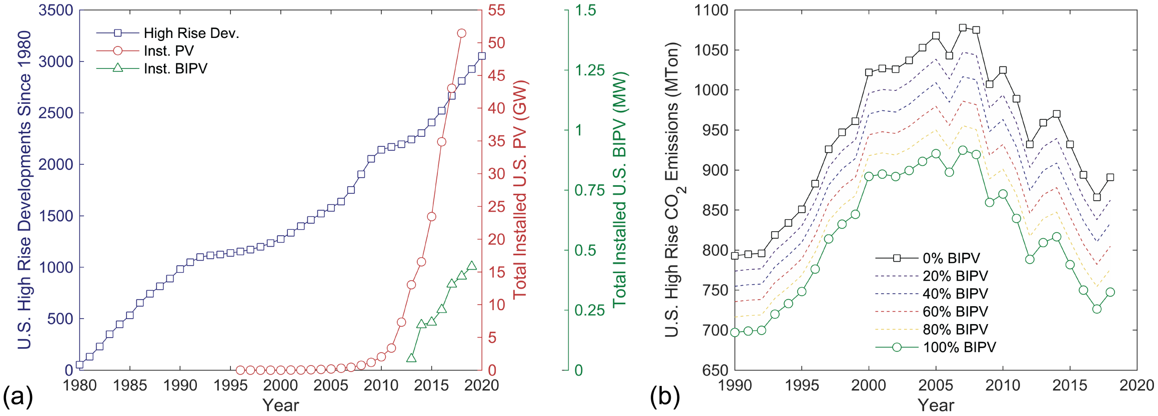

Figure 30: Projected BIPV potential versus historic US high-rise development since 1980.
(a) A comparison of the number of U.S. high-rise developments since 1980 (left y-axis, blue) against the total installed U.S. PV capacity (right y-axis, red) in gigawatts (GW) and the total installed U.S. BIPV capacity (far right y-axis, green) in megawatts (MW). (b) An estimate for the amount of CO_2 emissions in megatons (MTon) resulting from U.S. high-rise buildings with respect to varying total amount of BIPV integration. Here we assume energy production of a BIPV module operating at 5% power conversion efficiency at a temperate, sunny climate comparable to Los Angeles, CA[26], [136], [141]–[144].

While BIPV installations currently occupy less than 0.001% of the overall solar market share, as shown in Figure 30a, active research and commercialization efforts are underway to develop integrable BIPV technology [99], [145]–[149]. Given the historical trends for utility-scale PV, BIPV researchers commonly assume that the most influential figures of merit for increased market adoption are those related to on-site electricity generation and, consequently, avoided use of grid electricity. Thus, figures of merit have often considered technical performance factors, such as power conversion efficiency (PCE) and cost per unit area. However, as has been suggested in previous reports, BIPV must also incorporate non-technical factors (e.g., aesthetics, business models) when evaluating the marketability of a new technology [150]–[153].

In this chapter, we first survey potential technologies for power-generating window criteria and capabilities. We then describe and characterize a BIPV module that uses luminescent solar concentrator technology. We evaluate the visual aesthetics for such a BIPV window design given these cell and luminophore designs, followed by a description of the impact of the micro-PV grid density (i.e. the GG) on the overall module PCE. Finally, we provide a rigorous technoeconomic analysis for this LSC window system, assessing the price per power (US$/W) competitiveness of such a module and forecasting decreased module costs given possible reductions in materials prices and manufacturing steps.

4.2 A Survey of Electricity-Generating Window Technology

Unlike conventional utility PV modules, BIPV window applications must respond to aesthetic requirements (e.g., color, average visible light transparency (AVT), image clarity) in addition to power production. Consequently, a variety of power-generating window technologies have been developed over the past several decades to address these features. Despite a myriad of BIPV window concepts, each share at least one operating characteristic: one or more surface(s) of the insulated glass unit (IGU) window absorbs a portion of incident sunlight for electrical power conversion. Given that a portion of visible light must pass through the window to reach the building occupant, a reduced spectrum of light is usable for power conversion in BIPV windows. As a result of this reduced amount of usable light, the power production of the device is limited, creating a trade-off between window AVT and PCE. Figure 31a depicts PV power generation by light absorption and electron-hole pair generation at the inside surface of the exterior glass pane (known in the window industry as surface 2, or S2).

While BIPV windows share a common feature of incident sunlight to electrical power conversion in semi-transparent modules, the underlying PV technology varies widely, as shown in Figure 31b-e. Among others, organic PV (OPV) [147], [154], luminescent solar concentrator PV (LSC-PV) [55], thin-film PV [147], [155], and perovskite PV [147] all enable partial light absorption and have been researched for power-generating window applications. Figure 31b-e illustrate typical components found for thin film structures for each of these PV technologies. As shown, each design includes at least one glass surface serving as either the front or back pane. OPV and perovskite PV include electron and hold transport layers encasing the organic/perovskite material, respectively. Recent advances in these devices exhibit PCEs beyond 8% and 10% under direct 1-sun illumination at over 25% AVT for OPVs and perovskite devices, respectively [147].

For the case of thin-film PV technology (e.g., thin films of a-Si), PCEs can surpass 5% at more than 30% AVT [149]. Finally, LSC-PV prototypes demonstrate recent milestones such as beyond 2% PCE at more than 44% AVT for large-area ($100 cm^2$) module sizes [156].

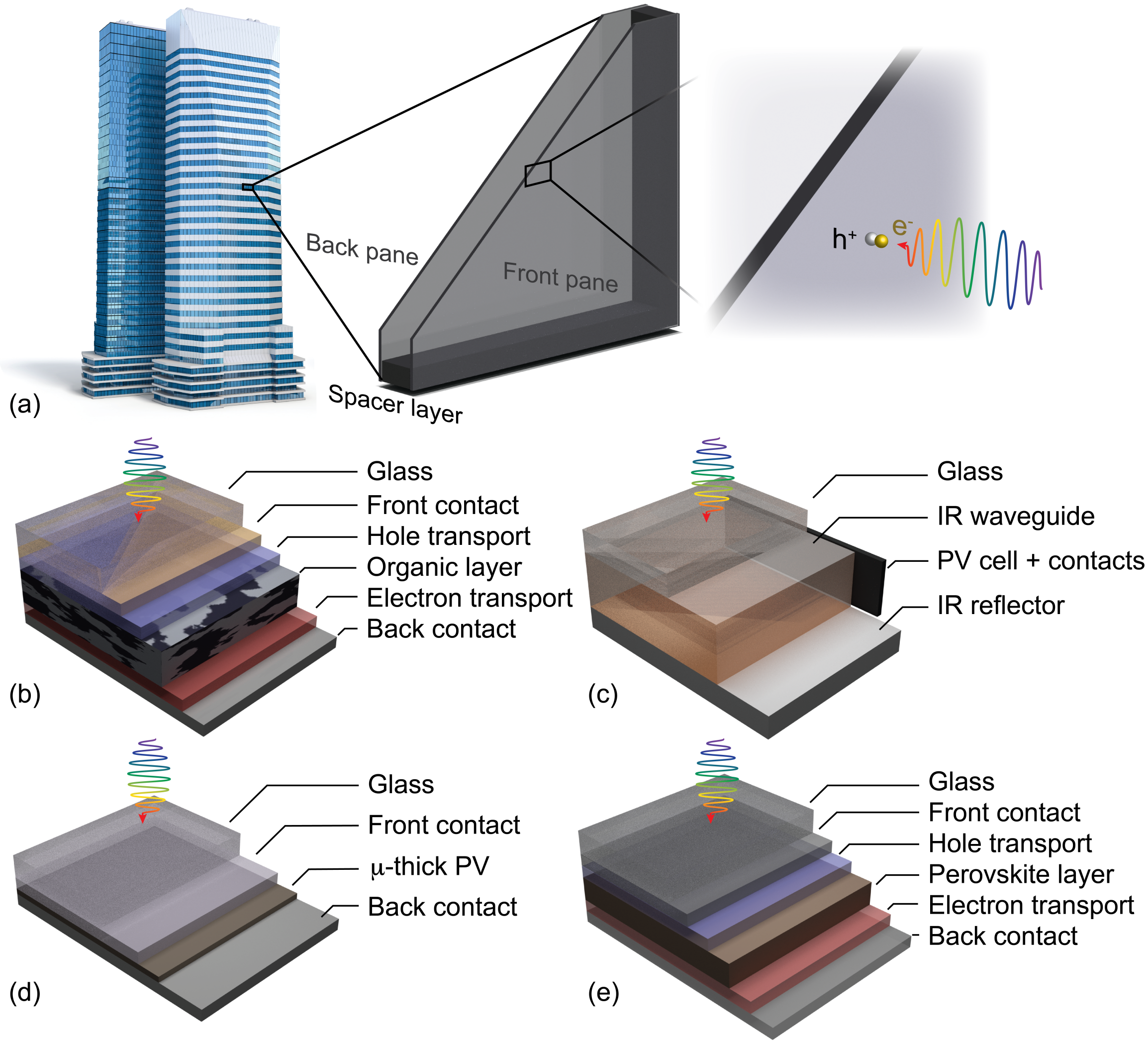

Figure 31: An overview of various technologies and their respective structures for a BIPV window IGU. (a) An illustration of the structure for a double paned IGU with the front pane layer containing the PV technology resulting in a photogenerated exciton (h^+,e^-). (b), (c), (d), and (e) Renderings of four commonly-employed BIPV window devices including organic PV, LSC-PV, thin-film PV, and perovskite PV structures, respectively.

Despite decades of device research and product development, the amount of installed BIPV (e.g., BIPV windows) technology has not experienced the same growth, or even the same trend, as its utility PV counterpart (Figure 30a). Moreover, research into how to further integrate BIPV windows into the commercial buildings market remains an active area of study in both academia and industry [150]–[153]. One possible reason is that BIPV window modules have not yet achieved sufficiently high PCE and annualized energy production in order to meaningfully offset building electrical loads. Yet, despite advances in PV efficiency and durability, BIPV window adoption remains limited in this commercial, high-rise market. Another possible reason for lagging adoption is due to aesthetics. In addition to the production of on-site electricity, BIPV systems require aesthetic indistinguishability from its non-PV building component counterpart. Specifically for BIPV windows, visible light transparency, image clarity, and power efficiency are primary metrics in determining the success of market adoption and building implementation [148]. Additionally, as BIPV modules are intended to reduce BoS costs, the cost of each the installed module and the generated energy must also be minimized. For the remainder of this chapter, we will focus on LSCs as the selected candidate for BIPV window systems and assess how the designed LSC performs against each of these target metrics—efficiency, transparency, image clarity, and module cost.

4.3 Design Criteria for an LSC Power Window

Originally developed in 1973 as a cost-effective PV system [157], [158], LSCs present a promising pathway toward the realization of transparent BIPV window technology given their unique optical and geometric structure. The idea of employing LSCs as power-generating window modules regained traction in 2007 due to a push from architects and building developers to incorporate PV in urban areas [33]. LSCs became a strong candidate given their semi-transparent waveguide and potential low-cost production. Yet, to this day, LSCs still exhibit limited PCEs primarily due to limited waveguide trapping as the area of the device approaches conventional window sizes. For most LSC devices, including those intended for BIPV purposes, photoluminescence (PL) is guided to the perimeter edge of the LSC waveguide, where bandgap-matched PV cells line the borders of the optical waveguide and convert the PL into usable electricity [29], [33], [48], [55], [56], [65], [67], [159], [160]. Due to the tunability of the luminophores and optical structure of the waveguide, many studies focus solely on how to increase the optical waveguiding efficiency [161]–[164].

We design an LSC, capable of operating with a PCE up to 7%, under both direct and diffuse lighting conditions, with variable opacity for use as a window in building and engineering applications. To do so, we first select each a photovoltaic collector, luminophore species, and photoluminescence trapping filters that spectrally match one another. Specifically, this power-generating window architecture employs silicon heterojunction microcells as the PV collector, highly efficient InAs/InP/ZnSe quantum dots (QDs) as the luminophore species for uniform isotropic light absorption across the visible spectrum with infrared photoluminescence (PL), and two short-pass polymeric filters for thermal insulation and PL-trapping mechanisms. The spectral characteristics for each component are shown in Figure 32.

Unlike previous iterations of LSC windows, we design an LSC module that leverages a grid-like pattern of PV microcells, as discussed in Chapter 2 of this thesis. As previously discussed, the geometric gain (GG) for such edge-lined LSCs increases linearly with the edge length. However, as has been demonstrated in numerous LSC studies, PCE decreases monotonically with increasing GG due to increased PL travel lengths to reach the perimeter PV [81], [82], [159], [161]. To achieve LSC devices scalable to meter-scale window applications, it is crucial to decouple the GG from the edge length of an LSC. The grid-like microcell pattern enables this decoupling. For the microcell collector, we use silicon heterojunction (SHJ) microcells, of dimensions 800μm x 800μm x 80μm, as discussed in Chapter 3 of this thesis.

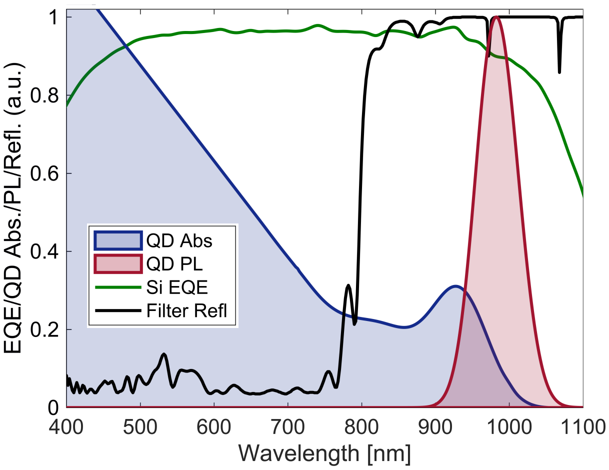

Figure 32: Spectral features of the LSC power window device.
We show the absorption and PL spectra of the luminophore, EQE of the modeled Si microcell at the 800μm x 800μm x 80μm cell size, and the reflectance profile of the optimized IR reflector at normal incidence.

To achieve a neutral color density LSC, we assume the use of InAs/InP/ZnSe core/shell/shell quantum dot (QD) luminophores [165]–[167] within a poly(lauryl) methacrylate (PLMA) waveguide layer. Figure 32 displays the broadband absorption and infrared PL spectra (blue and red regions, respectively) of the InAs-based QDs, as colloidally synthesized in previous studies [53], [165]–[167]. As seen in the PL spectrum, the peak emission centers at approximately

1000nm. As shown in Figure 32 (green line), the external quantum efficiency (EQE) of the SHJ microcells matches this PL regime.

To trap the emitted PL, we employ PL-trapping filters to both the front and back of the device. We design aperiodic dielectric stack filters with a short-pass, long-stop profile as shown in Figure 32 (black line). Previous studies detail how similar PL-trapping filters increase waveguiding efficiencies [43], [50], [51], [168], [169]; as shown here, we achieve greater than 99.9% reflectance in the PL wavelength regime. While this PL-reflector directly benefits the PCE performance of the LSC module, such infrared filters also play a pivotal role in achieving high thermal insulation properties for the window [170].

4.4 InAs/InP/ZnSe Quantum Dot Luminophore Optimization

Here we investigate how additional optimizations of InAs-based luminophores could further improve power efficiencies for an LSC power-generating window application. The luminophore species dispersed within the optical waveguide determines the thermodynamic light concentration limit for any LSC system [29], [48]. As such, the absorption and PL profiles set the limit of PCE. The amount of incident light absorption sets the total amount of light the luminophore can convert into PL. The amount of absorption that lies within the PL regime (i.e., the Stokes ratio [51], [96] or quality factor [161]) determines the probability for downconverted light to occupy waveguide modes without subsequent re-absorption events. Similarly, the luminophore Stokes shift and PL full-width at half-maximum (FWHM) contribute to the LSC concentration limit. Beyond the spectral shape of absorption/PL and the interplay between the two, the PL quantum yield (QY) indicates the efficiency by which the absorbed photon downconverts into PL.

Among candidate semiconductor materials, indium arsenide (InAs) offers potential advantages as a central core for QDs with NIR optical gaps for such an LSC system. Most notable is the body of prior work that demonstrates good prospects for developing InAs-based QDs offering higher PLQYs than other comparable NIR materials, including rare earth nanocrystals, silver chalcogenide nanocrystals, carbon nanotubes, Si nanoparticles, and organic dyes [171]–[176]. Unshelled, InAs cores have very low PLQYs—typically less than 2% due to rapid surface trapping of charges from poor surface passivation and states resulting from surface oxidation. These impacts can be remediated in part by encapsulation of the InAs core within a wide-bandgap, epitaxial shell material. Effective shell phases narrow emission linewidths and increase radiative recombination efficiencies through charge carrier confinement and passivation of the InAs core [177]–[179]. With few exceptions, the highest PLQY InAs QDs described in the current literature are ones passivated by cadmium chalcogenide (CdSe or CdS) protective shells, with luminescent quantum yields in excess of 80% being reported [180]. The increased brightness is often accompanied by large bathochromic shifts, which are changes of the spectral band position toward longer wavelengths, of several hundred meV that can push the emission band beyond the bandgap of a solar cell [178], [180]–[182]. These shifts are a confluence of both the extension of the excitonic wavefunction into the shell and cation exchange between cadmium and indium to give cadmium pnictide products, thereby posing a challenge to the heterostructure development needed for technologies that require operation within a narrow emission range [183], [184].

We examine InAs/InP/ZnSe QDs—heavy-metal free, core-multishell heterostructure luminophores with exceptional promise for utilization as the active absorber/emitter materials for our target LSCs power-generating windows. The necessary improvements in materials properties are well illustrated in Monte Carlo ray-tracing simulations of InAs/InP/ZnSe QDs in LSCs, which are shown in Figure 33. Here we calculate expected LSC performance parameters based on explicit tunable luminophore characteristics, including QD brightness, Stokes ratio, and emission full width at half maximum (FWHM). As the simulations demonstrate, high PLQY QDs with increased Stokes ratios and narrow FWHM have the potential to greatly improve luminophore performance and LSC solar conversion efficiency. Both optical efficiency (the fraction of photons retained within a waveguide) and solar conversion efficiency (overall LSC light harvesting performance including a solar cell) improve exponentially with increases in the PLQY.

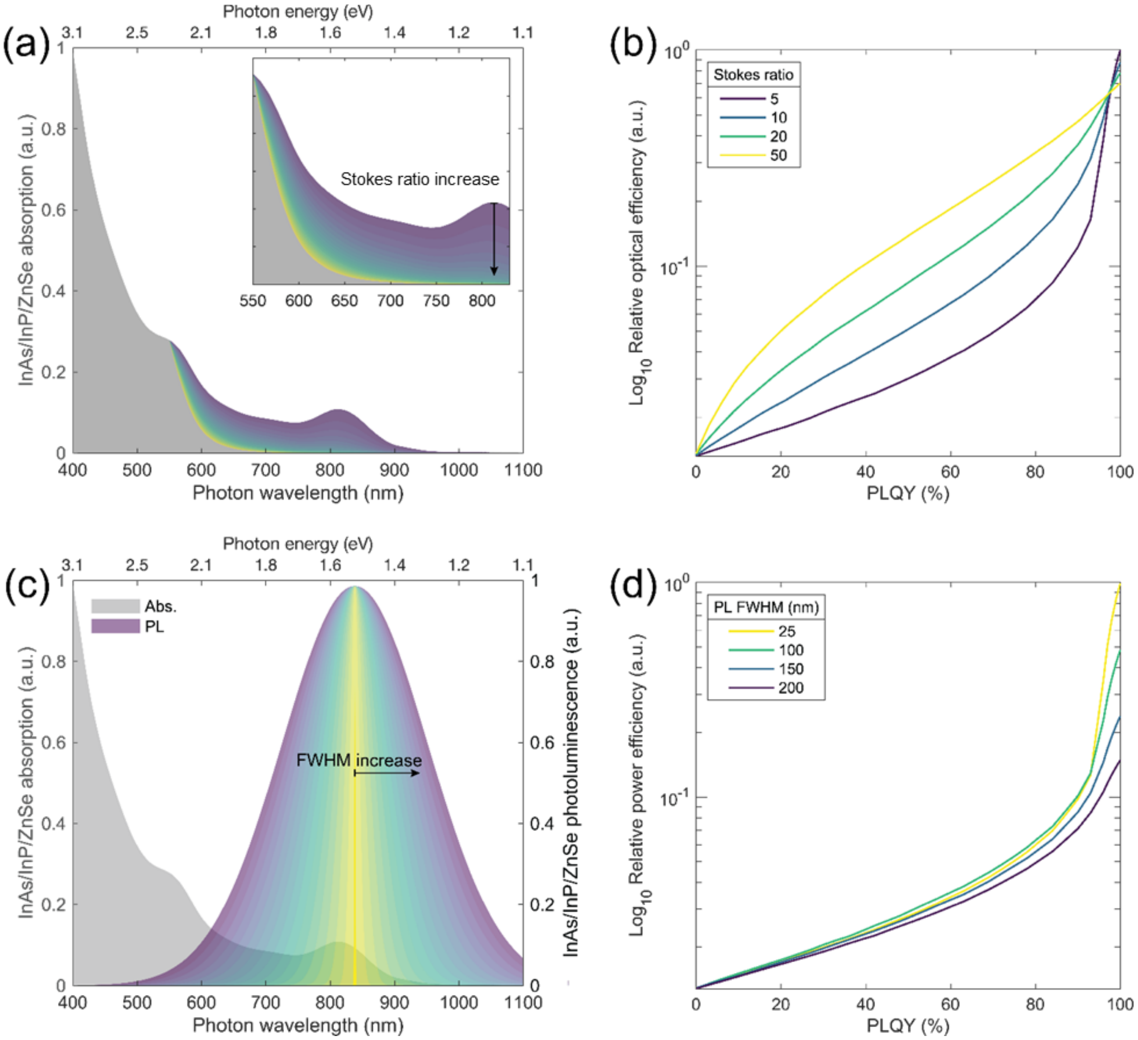

Figure 33: Modeled impacts of synthetically tunable properties of InAs/InP/ZnS QDs on LSCs performance. Absorption and emission profiles of QDs are based on experimentally derived InAs/InP/ZnSe QDs. The Stokes ratio modified absorbance profile (a) uses a fixed absorption in the visible region at 550 nm across variable NIR absorption from InAs cores where the Stokes ratio increases from violet to yellow. The insert highlights increased Stokes ratio with decreasing NIR absorption. A fixed optical density in the visible region enables a comparison of relative waveguide optical efficiency across Stokes ratio (b). The variable emission FWHM increases from yellow to violet about a fixed emission maximum (c). Monodisperse QDs give narrower FWHM and decrease losses below the solar cell band edge and improve module efficiency (d). Optical and power efficiency improve exponentially with PLQY, with more than 5-fold increases to optical and power efficiencies between 90-100% PLQY. A logarithmic scale is applied to highlight the impacts of Stokes ratio and FWHM on LSC efficiencies at <90% PLQY. Relative optical and power efficiencies are reported compared to an overall highest theoretical efficiency for any Stokes ratio or photoluminescence FWHM. Across all simulations, module performance increases from violet to yellow traces. Taken from Enright et al. [53]

Even without near-unity PLQY, increasing the Stokes ratio and narrowing emission FWHM significantly improve module optical efficiency and power efficiency, respectively. Regarding the former, Figure 33a simulates the absorbance spectra of QDs with constant optical density in the visible region up to 550nm with progressively decreasing NIR light absorption. These spectra simulate an increased Stokes ratio representative of the optical properties achieved through increasing InP shell thickness synthetically. The optical efficiencies of LSC waveguides so tuned are seen to improve markedly with increases in the Stokes ratio (Figure 33b). The FWHM, valuable for limiting the number of photons reemitted with energies below the bandgap of the solar harvester, is strongly impacted by the mass distribution (i.e. monodispersity) of the QDs. Figure 1c shows illustrative simulations using the emission spectra of QDs with variable FWHM at a fixed emission maximum wavelength to demonstrate this point. Narrow FWHM, especially at high PLQY, are essential to maximize LSC module power efficiency, which includes the absorption profile of GaAs and Si solar cells (Figure 33d). For example, at <80% PLQY, the benefits from reduced parasitic reabsorption at longer wavelength below the absorbance profile for wide FWHM offsets the losses from photons emitted below the solar cell bandgap. As the PLQY increases and parasitic reabsorption is no longer the primary loss mechanism, narrow emission leads to significant increases in LSC performance. High Stokes ratios greatly enhance optical efficiency through reducing parasitic reabsorption and bolster LSC efficiencies most significantly at low PLQY, while narrow FWHM reduces sub bandgap losses at the solar cell and yield the highest gains at high PLQY. Narrow FWHM, high Stokes ratios, and >90% PLQY NIR QD luminophores are essential requirements for a high efficiency LSC-PV technology.

To date, only visibly emissive QDs have been successfully developed to these standards. Notably CdSe/CdS QDs with >95% PLQY, Stokes ratios >30 (defined in Bronstein *et al.* as the ratio of absorption at 450nm to the extinction at the peak luminescence wavelength), and emission linewidths around 100 meV are the gold standard for brightest QD emitters [76], [185]. The encapsulation of III−V QDs within wide-bandgap II-VI shells has yielded a second, structurally distinct class with >80% PLQYs reported for InP/ZnSe and InP/ZnSeS [186]–[188]. Taken together with Figure 33, such metrics would enable exceptional LSC performance if matched by NIR QDs, though these same levels of broadly tunable photophysical performance needed from NIR emitters to support a high PCE LSC-PV technologies are not yet developed. For the InAs shelled QDs of interest, this is primarily due to the large lattice mismatches between InAs and prospective wide bandgap protective ZnSe (6.4%) and ZnS (10.7%) shells that limit defect free growth of those layers to only a few monolayers at most [178], [189]. Studies investigating the incorporation of multiple intermediate layers and alloys to relieve strain and facilitate thicker ZnSe or ZnS shell growth (e.g., the continuous-injection synthesis of InAs/In(Zn)P/ZnSe/ZnS and InAs/InZnP/GaP/ZnSe with a gradient composition GaP shell), yielded emitters with only modest PL quantum efficiencies (25 and 23%, respectively) [167], [178]. Further efforts using an alloyed core and a large interior shell obtained 75% PLQY for In(Zn)As/In(Zn)P/GaP/ZnS QDs [190]. Bright, NIR emissive InAs/InP/ZnSe QDs with 76% PLQY have also been reported, though the specific structural and electronic attributes that enable bright quantum yields are not yet understood, especially when contrasted with the <30% PLQYs typically observed InAs/InP/ZnSe QDs [165].

4.5 Window Aesthetics and Transparency Analysis

In addition to light trapping and efficiency, a key metric to evaluate the viability of a BIPV power window system, as previously described, is the visual transparency and color tint of the module [55]. Here we first analyze how the visible transparency at 450nm (indigo shade) and PLQY affect the overall PCE. As shown in Figure 34a, only PLQYs beyond 90% and visible transparencies below 50% yield PEs above 3%. In terms of coloration, window color tinting is agnostic to PLQY, as the absorption band primarily determines this characteristic. We additionally observe that with the proposed filter and luminophore material, the color remains a neutral gray across all visible transparencies. Due to finite front/back filter reflectance, 100% visible transparency of the waveguide (i.e. a bare PLMA waveguide with no QD doping) still exhibits a finite amount of tinting. Further, given the minimal light scattering of PLMA and efficient trapping of PL, we expect no discernable image clarity difference between the two.

We next assess the effects of geometric gain on PCE and visual clarity. In the limit where GG becomes unity, i.e., when the entire LSC waveguide illumination area and PV cell area are equal, we recover our single-junction SHJ cell efficiency—covered with a QD waveguide film. Yet, when the entire LSC is covered in PV material, visual clarity approaches zero. For a large GG (i.e., a sparse array of micro-cells), the amount of active PV cell area decreases. In this limit, the requirement for near-perfect light trapping increases, as photons must travel farther distances to reach the embedded PV cells. However, larger GGs imply less active cell material as well as increased visual clarity of the window. As such, we observe an optimization problem of efficiency vs. visual clarity for varied GG. Figure 34b illustrates how the GG of the LSC directly impacts the PCE of the module. As shown, a strict dependence exists between PLQY and PCE for GGs that extend beyond 10 due to increased probability for re-absorption and non-radiative termination events as well as waveguide scattering. For a GG of 1, the SHJ micro-PV cell achieves a PCE of approximately 17%, nearly recovering the 1-sun illumination efficiency of 19.7%; the slightly lowered PCE is due to slight reflection and absorption losses from the waveguide. For a GG of 10 and PLQY above 95%, we observe a PCE greater than 5%**.**

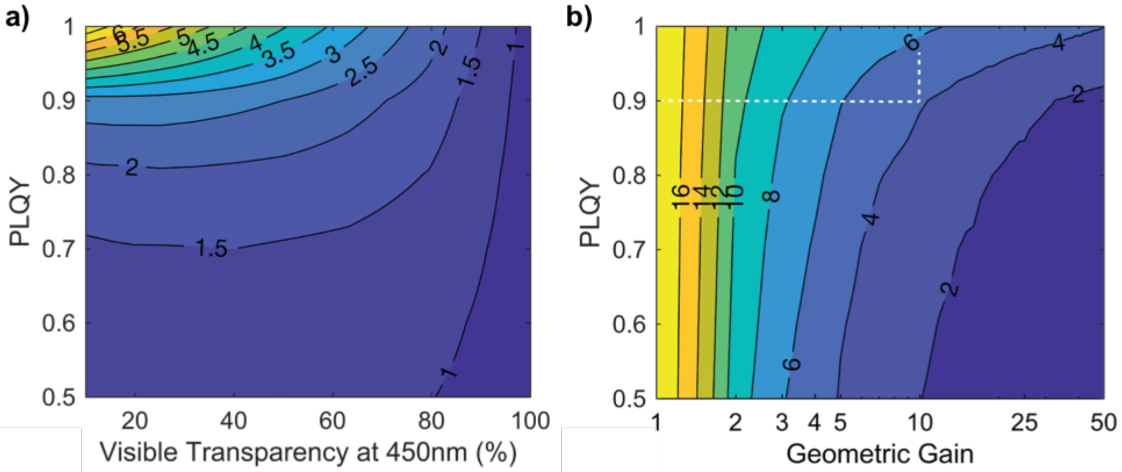

Figure 34: Simulated efficiencies for an LSC power window device.
a) Overall LSC module efficiency as a function of the luminophore PLQY and the concentration of luminophores dispersed within the waveguide (measured as visible transparency at 450nm given by the optical density of luminophores). Simulations assume a GG of 20. b) The impact of the geometric gain (GG—given as the ratio of overall waveguide illumination surface area to total SHJ microcell area) and luminophore PLQY on module power efficiency for the ranges of GG 1 to 50 and PLQY 0.5 to 1.0, with dotted lines indicating the optimal performance region for PLQY > 0.9 and GG < 10. Simulations assume a visible transparency of 30% at 450nm.

To demonstrate the effects of transparency, color tint, and the microcell array on window aesthetics, we build full-size mechanical mock-up window prototypes that evaluate each of these parameters. To do so, we design screen-printed transparent sheets of microcell grid mockups for 800µm x 800µm microcells, spaced at a geometric gain of 20, and connected by interconnects that are 15µm wide. These microcell sheets are placed directly atop the double-pane window, as would be the case for a functioning LSC. To mimic the quantum dot waveguide, acrylic sheets, of varied tint and transparency, are finally placed atop the microcell grid. The aesthetic effects of such variables are shown in Figure 35.

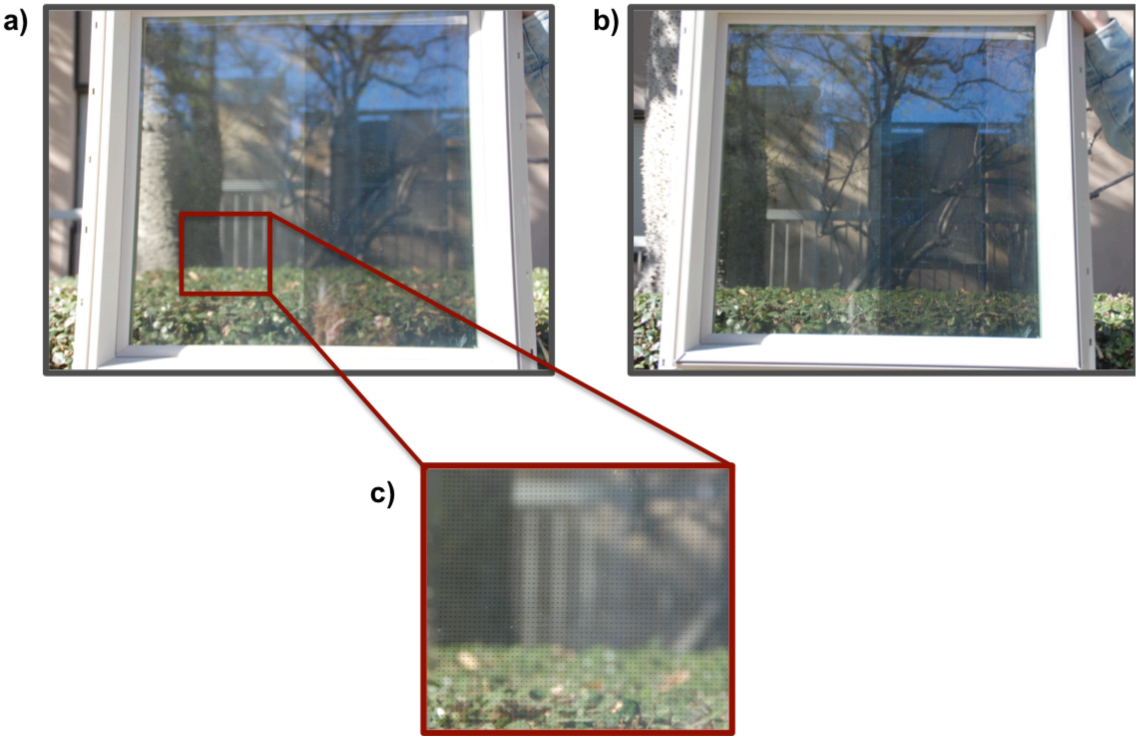

Figure 35: Realistic window mockups that show the aesthetic effects of window transparency (i.e., AVT) and color tint.
Each window consists of i) a standalone double pane window, ii) a grid of printed 1mm x 1mm microcells (GG = 20), and iii) two acrylic sheets (on each the left and right side of the window) to emulate waveguides of varied OD and absorption spectra. In a) brown toned windows with AVT = 56% (left panel) and AVT = 26% (right panel). In b) gray toned windows with AVT = 28% (left panel) and AVT = 26% (right panel). The zoomed in image in c) focuses on the microcell sheet, to show the visual perception of the microcells.

4.6 Technoeconomic Analysis for an LSC Power Window

As discussed in the introduction, and in Appendix B, BIPV technologies must take into account cost and the product value chain, in addition to PCE and aesthetics. Put simply, the cost of manufacturing and installing the LSC module dictates the extent to which such a window technology can be incorporated in future architecture. To estimate the cost for such an LSC BIPV, we build a technoeconomic analysis (TEA) that models to-scale manufacturing and materials costs in order to generate a range of cost per area ($\$/m^2$) and cost per Watt ($\$/W_p$) values for this technology [41], [191]–[195]. For the purposes of reducing uncertainty and variability, we do not take into account framing of the window module.

Here we develop a manufacturing process flow, assuming a fixed yearly production volume of 500,000 unframed window modules. We take into account the transparency of the window (i.e., the concentration of QD luminophores) and the GG of the cell array, the two primary price-driving device parameters of the system. The former sets the total amount of luminophores required to achieve the set annual production, while the latter determines the amount of cell material and processing steps and labor. We assume both the QD luminophores and commercially-available SHJ cells as raw material inputs. All information relating to the model parameters, inputs, raw materials and processing costs, capital expenditure, operating expenditures, and references that detail raw materials' cost values can be found in the supporting information.

As shown in figure Figure 36, the GG and OD of the LSC module significantly alter the cost of the device as well as the power performance. Here we analyze the technoeconomics of this technology as a unit of cost per power generated—assuming peak performance at an irradiance of 1000 W/m^2. From our cost estimates, we find that the QD luminophores occupy the majority (44%–63%) of the operating expenditure. We therefore split our analysis into an upper and lower cost of QDs (Figure 36a,c and Figure 36b,d, respectively). Given these two ranges, we find that for a visual transparency of 30% at 450nm, and a GG of 10 yield a maximum and minimum cost per peak watt of \$2.77/W$_p$ and \$2.22/W$_p$, or a cost per 1.5m^2 window of \$290 and \$230, respectively. As shown in Figure 36a,b, this price point can range from under \$2/W$_p$ in the low transparency, low GG case to over \$10/W$_p$ in the high transparency, high GG case. Such a power per watt range results from the convolution of the two distinct drivers given the inputs of transparency and GG: the performance of the window and the cost of the window. The former performs optimally with low GG and low transparency (i.e. increased amount of incident light absorbed by the luminophores). The latter reaches low costs when GG and transparency are kept high (owing to less material in the LSC).

In addition to the cost analysis shown in Figure 36a,b, historical trends of the Si-PV market demonstrate the enormous material and processing cost reductions possible given increased manufacturing output [196]–[198]. As such, figure Figure 36c,d illustrate the cost per window unit (assumed to be an area of 1x1.5m^2) and cost per watt of the module given possible material and manufacturing cost reductions. Assuming a reduction by 50% of each the cost of QD material, maintenance of the production line processing, and capital expenditure of the tools, we find a cost of approximately \$165 per window module at \$1.57/W$_p$ in the upper QD cost range and \$135 per module at \$1.29/W$_p$ in the lower QD cost range.

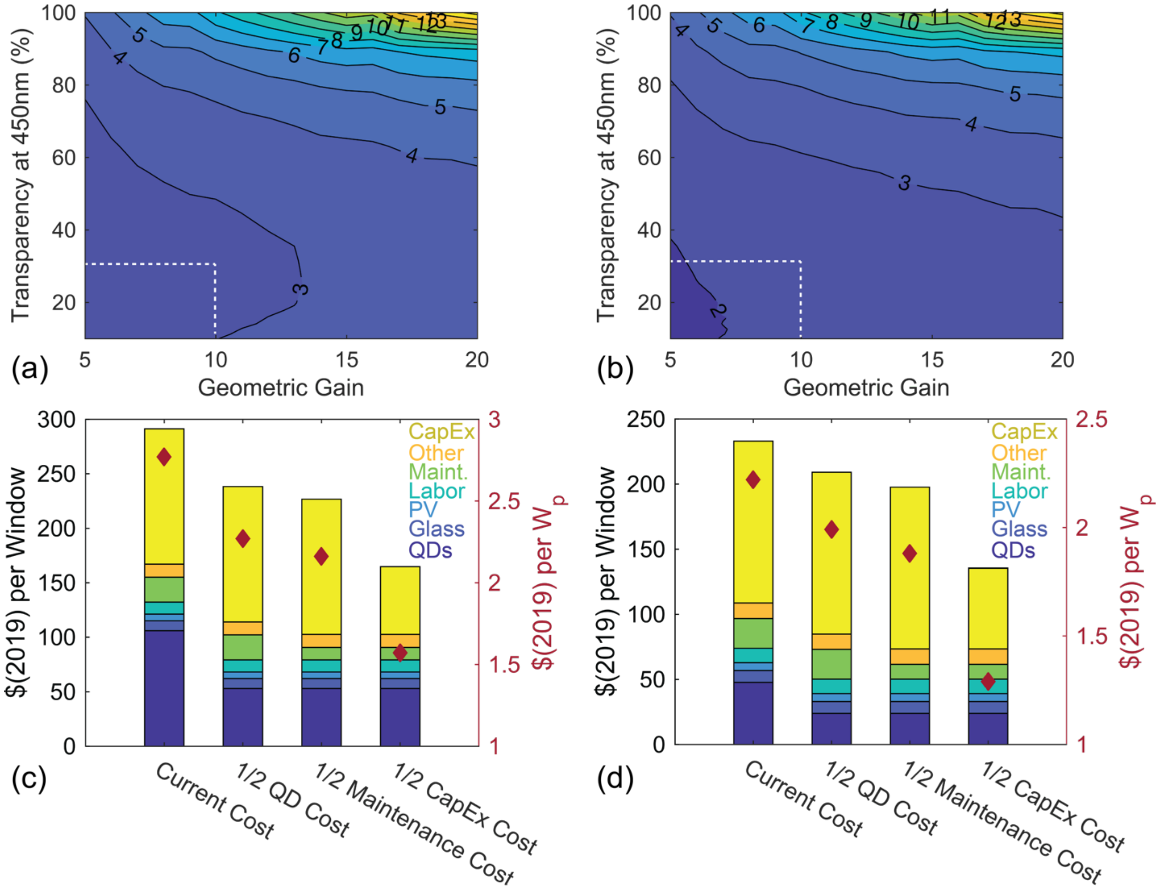

Figure 36: A technoeconomic analysis of a 1x1.5 m^2 LSC power window module.
(a) and (c) assume an upper limit of QD materials costs ($70 per m^2) from original equipment manufacturers (OEMs), while (b) and (d) assume a lower limit ($31 per m^2). Here (a) and (b) evaluate the overall price per watt, US$(2019) per watt, of such a window module by varying the LSC GG and transparency (i.e. QD loading). (c) and (d) illustrate the breakdown of primary window costs by category (QDs, glass pane, PV micro-cells, production line labor, tool maintenance and repair, other materials costs, and capital expenditure) on both the cost per module and cost per watt metrics, assuming a GG of 10 and transparency at 450nm of 30%, shown as dashed white lines in (a) and (b). We forecast possible cost outcomes given the decrease of specified components.

Details of our TEA model are described in the bullets below, and specified parameters/ assumption are presented in Tables 1 – 3.

1.1. Annual production volume is set at 500,000 windows per year.

1.2. The LSC PV manufacturer locates at Los Angeles, CA.

1.3. The window dimension is 1.5 m^2, which is a standard window size in the market.

1.4. LSC module geometric gain (the ratio of the area of window face to the active GaAs PV area) is 150.

1.5. The quantum dot luminophores in the waveguide have an set optical density, measured at 450nm, of 1.0.

1.6. The total plant operation time is defined as 2,000 h/yr, corresponding to 8 hours per day, and 250 operating days per year.

1.7. Maximum allowed line utilization for LSC manufacturing is assumed to be 85%.

1.8. To quantify depreciation of physical properties owned by the manufacturer, we assume a 10% discount rate over a 10 year line lifetime.

1.9. The total manufacturing time throughout is 6.25 hours/batch for each window production line, corresponding to a cycle time of 0.5 hr/batch for IR-filter deposition, 0.5 hr/batch for GaAs microcell processing, 5.0 hr/batch for microcell array printing, 0.1 hr/batch for QD-LMA dispersion, 0.1 hr/batch for LSC deposition, and 0.05 hr/batch for front glass encapsulation. Each batch assumes a total of 10 LSC windows.

1.10. The footprint of 1 production line is estimated to be 1,650 ft^2, with a one-time floor space cost of $300/$ft^2$.

1.11. Labor cost for manufacturing work, engineering, and management is set at $15 per hour. We assign the number of workers per line at each step as follows: IR-filter deposition requires (1) worker/line for sputtering labor; microcell processing requires (1) worker/line for laser cutting labor and (1) worker/line for sputtering labor; microcell array printing requires (0.5) worker/line for screen printing labor and (0.5) worker/line for pick-and-place labor; QD-LMA dispersion requires (0.5) worker/line for mixing and sonication labor; LSC deposition requires (1) worker/line for doctor blading labor; and front glass encapsulation requires (0.5) worker/line for vacuum lamination labor. Additionally, (3) managers and (3) engineers are required per line.

1.12. Electricity costs in LA are assumed to be 0.06 $/kWh, consistent with the average price of electricity to industrial customers.

1.13. For the GaAs microcell processing, we assume the material usage yield efficiency is 99%.

1.14. The maintenance costs for the facilities are set to be 3% of the total equipment capital costs.

1.15. This analysis assumes a mature manufacturing process, thus expenses from R&D cost are not included as it is expected to be negligible.

Operating Parameters	Value	Units
Production Volume (PV)	500,000	windows / year
Daily PV	2,000	windows / day
Geometric Gain	150	unitless
Optical Density (at 450nm)	1.0	unitless
Operating Days per Year	250	days / year
Operating Hours per Operating Day	8	hours / day
Maximum Allowed Line Utilization	85%	unitless

Table 5: Operating parameters assumed for large-scale LSC window production.

Stage	Raw Material	Cost Rates		Materials Cost ($/window)
IR-filter deposition	Si (sputter target)	44.14	$/kg	0.36
IR-filter deposition	Ti (sputter target)	22.20	$/kg	1.04
IR-filter deposition	Glass pane (OEM)	3.00	$/kg	9.09
Microcell processing	HIT Cell (OEM)	6,400.00	$/m^2	43.53
Microcell processing	Ag (sputter target)	58.77	$/kg	0.002
Microcell array printing	Al (paste)	52.00	$/kg	0.02
Microcell array printing	Cu soldering tabs	0.0007	$/m	0.00001
QD-LMA Dispersion	InAs/InP/ZnSe QDs (OEM)	140.00	$/m^2	212.12
QD-LMA Dispersion	LMA	15.44	$/kg	4.06
QD-LMA Dispersion	EGDMA	22.84	$/kg	0.73
QD-LMA Dispersion	Trioctylphosphene	82.31	$/kg	0.83
QD-LMA Dispersion	Photoinitiator	65.37	$/kg	0.01
Front glass encapsulation	EVA	1.54	$/m^2	4.61

Table 6: Materials cost for reference window module, used when calculating operating expenditures.

No.	Equipment	Footprint (ft^2)	Unit Price ($k)
1	Roll-to-roll vacuum coating system	200	6,060
2	Precision laser cutter	160	60
3	SiNx PECVD Reactor	20	1,496
4	a-Si:H PECVD Reactor	20	7,325
5	Pick-and-Place Machine	100	212
6	Screen Printer	60	353
7	Laminator	100	446

Table 7: Equipment costs and the associated footprint used to calculate capital expenditures.

4.7 Conclusion

Building integrated solar power windows could enable on-site clean energy production in dense, urban environments. Unlike conventional solar, power generating windows must be assessed for aesthetics (e.g., transparency and color tint), in addition to power efficiency and cost metrics. While several technologies are potential candidates for this application, none have yet to reach widespread implementation. We propose and design a luminescent solar concentrator for use as a power-generating window. This architecture employs a grid-like array of silicon heterojunction microcells as the photovoltaic device, highly efficient InAs/InP/ZnSe quantum dots (QDs) for uniform isotropic light absorption across the visible spectrum with infrared photoluminescence (PL), and two short-pass polymeric filters for thermal insulation and PL-trapping mechanisms. Given this design, we optimize the embedded quantum dot luminophore spectra, PV cell design, micro-cell interspacing, and visible window transparency to yield a champion window module performance reaching approximately 7% power conversion efficiency. Aesthetically, this design enables controllable transparency and no projected color tint. We additionally develop a technoeconomic model for the materials and manufacturing of an individual LSC power window unit, prior to framing. We find a cost range from 2.22–2.77 $\$/W_p$ for a GG of 10 and visual transparency of 30%.

CHAPTER 5: LSCS FOR SPACE-BASED SOLAR ENERGY APPLICATIONS

Solar energy is limited on Earth due to location, inconsistent weather patterns, and diurnal cycles. If solar power were instead to be harvested in outer space and beamed back to Earth, clean renewable energy could be consistently available from any location on Earth. Significant research is still needed to realize such a concept, including development of radiation-hard, flexible, lightweight photovoltic systems. Luminescent solar concentrators meet each of these criteria and thus present a strong candidate for a space-based solar power technology. We design and fabricate the first ever luminescent solar concentrators to be launched into low-earth orbit, using both Si- and GaAs-based devices. The modules will be launched in November 2022 with ongoing results recorded until Spring 2023. We further design the next-generation of luminescent solar concentrators for space, which boast a lightweight, ultrathin design capable of achieving a specific power up to 11.55 kW/kg. Technoeconmic analysis shows that these ultralight modules could be fabricated at a competitive cost as low as 0.24 $/W.

5.1. Introduction

Despite abundant solar irradiance on Earth, solar energy transmission is limited by location, weather, and time of day; clouds, atmosphere, and nighttime all create environments that are not conducive to solar energy. Moreover, approximately 30% of incident solar energy is reflected back into space by Earth's atmosphere [199], [200]. Instead of tracking ideal solar conditions for solar energy conversion, which leads to inaccessibility to solar energy for much of the planet, space-based solar power suggests collecting solar power in space and transmitting the energy down to Earth via microwaves. In doing so, solar power could be available from any location on Earth, at any time of day. Moreover, this technology could enable solar energy to reach remote communities without requiring a traditional grid to transport the energy [199], [201].

To achieve such a technology, photovoltaic (PV) cells must be launched into space via RF or microwave transmitting satellites. Figure 37 displays a schematic representation of how space-based PV tiles can be modularly arranged to make up a full spacecraft array [201]. Such satellites would need to orbit around 35,000 km above earth's surface, known as geosynchronous equatorial orbit (GEO), however initial tests of SBSP will use low earth orbit (LEO) as it is easier and cheaper to access[199]. Generated power would then be converted into radio frequency (RF) or microwaves and beamed back to a power-receiving station on Earth to be added to the electric grid.

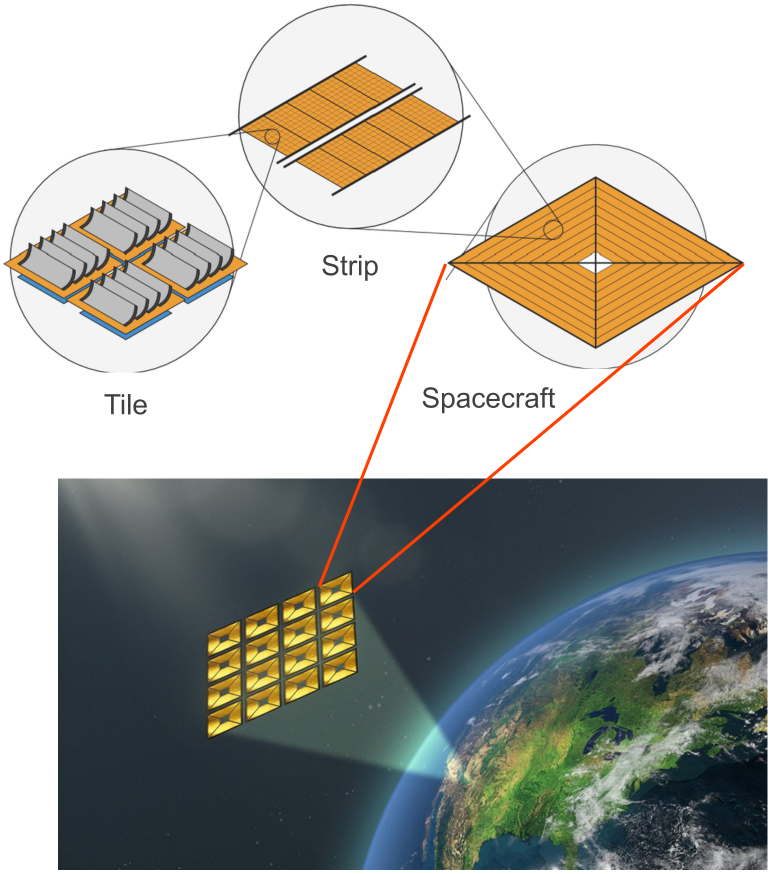

Figure 37: Schematic of Space-Based Solar Power spacecraft array.
Ultralight, flexible PV cells make up the PV tiles, shown on the left. These tiles are then arranged in a grid to make up a PV strip, which then make up a single spacecraft. By placing multiple PV-enabled spacecraft together, a full spacecraft array is realized, which then beams power back to Earth. Adapted from [80], [201].

The idea of space-based solar power (SBSP) dates back to 1941, in Isaac Asimov's science-fiction story "Reason;" however the first technical paper proposing the idea was in 1968 by Peter Glaser [201][202]. By the 1970s, SBSP gained popularity among NASA, as demonstrated by several technical reports, but traction was never achieved due to economic infeasibility [203]–[205]. As the price of photovoltaic cells has drastically decreased since 1970, SBSP has become a possibility once again. It is now estimated that SBSP may be economically viable within the next 20 years [206], [207]. As of 2020, several countries—including the US, India, the UK, Russia, Japan, and China—are all actively pursuing SBSP, at a mix of government, university, and private institutions [206], [208], [209]. China, for example, is planning a SBSP test in low earth orbit (LEO) in 2028, and then in GEO, which is further and more difficult to reach, in 2030 [210].

However, the idea of SBSP has multiple challenges that must be addressed before the technology is competitive and implementable. To begin with, launching materials into space is highly costly, resulting in production costs in the tens of billions of dollars; power satellites in GEO must cost less than \$200/kg for SBSP to be competitive. As background, the rocket Ariane V cost \$17,000/kg to launch to LEO [211], while SpaceX's Falcon Heavy, which boasts cheaper launch costs, still clocks in at nearly \$2,000/kg to LEO, an order of magnitude higher than what is necessary [212]. SpaceX claims that the next rocket, which is fully reusable and thus lower cost, could result in launches as low as \$10/kg [213], an achievement that would strongly benefit SBSP.

In addition to exorbitant launch costs, the projected location of SBSP satellites poses added concerns. The environment in GEO is highly hazardous—due to electron irradiation, space debris, and additional degradation—yet the inaccessibility of a satellite in GEO makes maintenance of a damaged panel near impossible. In fact, PV panels in GEO are projected to suffer eight times the degradation as those on Earth [214]. Moreover, the broadcast frequency of the SBSP microwaves would require isolation from other satellites in GEO [215].

Finally, transmission of such energy raises further challenges. In order to receive the incoming transmission, the terrestrial receiver would need to be several kilometers in diameter [199], resulting in an estimated cost of at least \$1 billion for 5 GW by SBSP[216]. Moreover, transmission over such a distance would result in significant energy losses and heat waste, as photons are converted to electrons to photons and back to electrons in several conversion phases [217]. Given all of these enumerated challenges—from launch costs, to PV location, to transmission—there is a strong need for additional scientific research and development in order to make SBSP a reality.

Specifically, we look at the requirements needed for PV to succeed in GEO. Given the challenging environment that space poses, space-based photovoltaics require additional performance metrics to their terrestrial counterparts. Specifically, modules require components that are each mechanically stable, radiation hard, and mechanically flexible. Additionally, high launch costs motivate ultra-light, high-efficiency—i.e., high specific power—designs in order to merit the cost of launch. Research is actively underway to identify emerging technologies with such properties, including multijunction III−V solar cells, nanowire cells, perovskites, 2D materials, and luminescent solar concentrators (LSCs) [59], [218]–[220]. For the remainder of this chapter, we will investigate the opportunity of LSCs as a SBSP candidate technology and advances in this research.

5.2. LSCs as Space-Based Systems

Luminescent solar concentrators (LSCs) represent a strong candidate for space-based solar technology. LSCs meet the criteria, as described in the introduction, needed for viability in space—mechanically flexible, low cost, radiation hard materials—and boast a potential for high power conversion efficiency. Moreover, LSCs have the potential to achieve high specific costs (generated power per kilogram, kW/kg) by designing an ultralight module, as detailed in Section 5.4.

By virtue of the LSC design, each component allows for a fully flexible module, particularly if removed from a substrate. The waveguide can be a polymer or an ultra-thin photonic crystal waveguide, as introduced in Section 2.6 and discussed further in Section 5.4 of this thesis. Given the material and thickness of both waveguide choises (~30μm thickness for polymer; <1μm thickness for photonic crystal), either design allows for a flexible waveguide. For an LSC with a co-planar PV grid, utilizing thin (<10μm) micro-PV cells at a high geometric gain, the thin cells and large spacing between microcells further results in a flexible design. Finally, if an external PL trapping filter is applied, the dielectric materials can be deposited directly atop the waveguide, thereby contributing negligible impact on module flexibility. Further discussion into designing a next generation ultra-thin, flexible LSC for space is present in Section 5.4.

In order for emerging PV technologies to be competitive, they must also be low cost [201], [206]. LSCs enable use of high-efficiency solar material (e.g., GaAs) at a low cost integrated module due to the concentratin factor. As the gemometric gain increases, i.e., the spacing between PV cells increases, expensive PV costs decrease dramatically [33], [34]. A full analysis on the technoeconmic costs of LSCs for space is detailed in section 5.4.

Finally, photovoltaic devices intended for use in space must be robust against the harsh environment in outer space, including electron radiation. We design LSC modules that consist of commercially available PV materials (e.g., GaAs cells), space-quality polymers (e.g., CP1), quantum dot luminophores, and photoluminescence (PL) trapping filters. Both the PV material and proposed polymer are previously shown to be capable of being radiation hard [221], [222], yet little is known as of now about radiation testing on colloidal quantum dots. To test these properties, we expose colloidal quantum dots to electron irradiation conditions that are similar to those in space. Specifically, we test CdSe/CdS quantum dots, as these have been commonly used in LSC modules and are exemplarly colloidal quantum dot structures. We test CdSe/CdS waveguides of two optical densities—0.39 and 0.68—to see if there is a difference in robustness based on QD loading. The QDs are exposed to 1MeV electron irradiation at a fluency of 1 x 1015. For each waveguide, half of the waveguide is covered by tin-foil in order to block the electron irradiation. PL measurements are taken before and after irradiation testing. As shown in Figure 38, the relative PL of each QD sheet maintains a strong PL response, even after electron irradiation. QDs exposed to electron irradiation displayed a PL response that was 88% and 95% of the initial PL response for ecah the OD = 0.38 and OD = 0.69 samples, respectively. For sheets that are covered by tin, we see minimal PL degradation, thus showing the effectiveness of tin as an elecrton shield. These results indicate that CdSe/CdS quantum dots show minimal degradation under space-like irradiation conditions and are thus are sufficiently radiation hard for space-based applications.

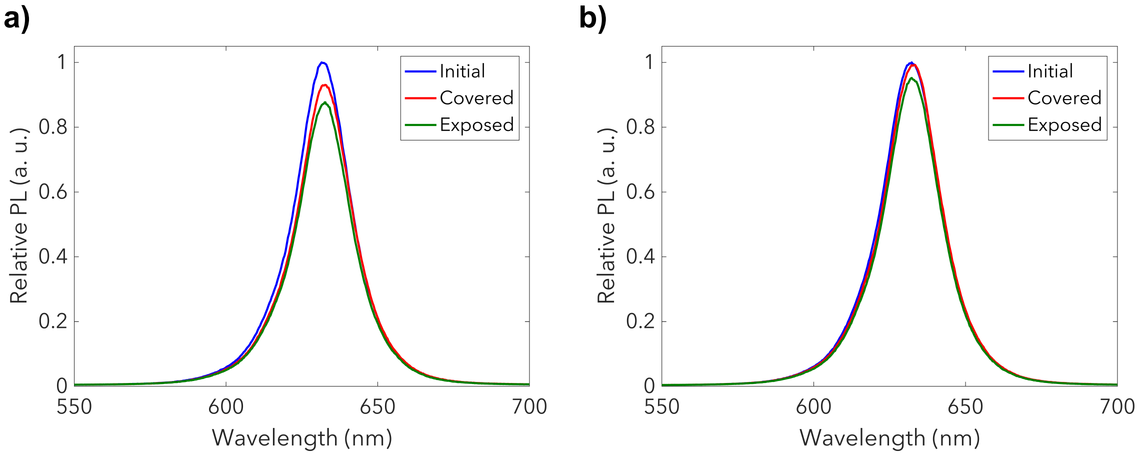

Figure 38: Effects of electron irradiation on quantum dot photoluminescence. CdSe quantum dots are used with an a) OD = 0.39 and b) OD = 0.68.

In addition to the mechanical and economic requirements discussed above, PV for space-based applications must perform with high efficiencies to merit the cost of the launch. Moreover, since launch costs are based on weight, space-based PV should be as lightweight as possible. Specific power (kW/kg) is thus used as the figure of merit for SBSP [59], [80], [223]. Previous work has shown that LSC systems with a CdSe/CdS quantum dot polymer waveguide and InGaP PV microcells, arraged in a coplanar grid, could reach efficiencies of 11.72%, or 15.91 mW/cm^2

generated power in AM0 [59]. Given the calculated weight of this polymer waveguide design, this equates to a specifc power of 1.155 kW/kg, a factor of 10 higher than currently employed commercial technologies, which have specific powers of 80—100 W/kg [224]. Further analysis for ultra-lightweight, high specific power LSC designs are discussed in Section 5.4.

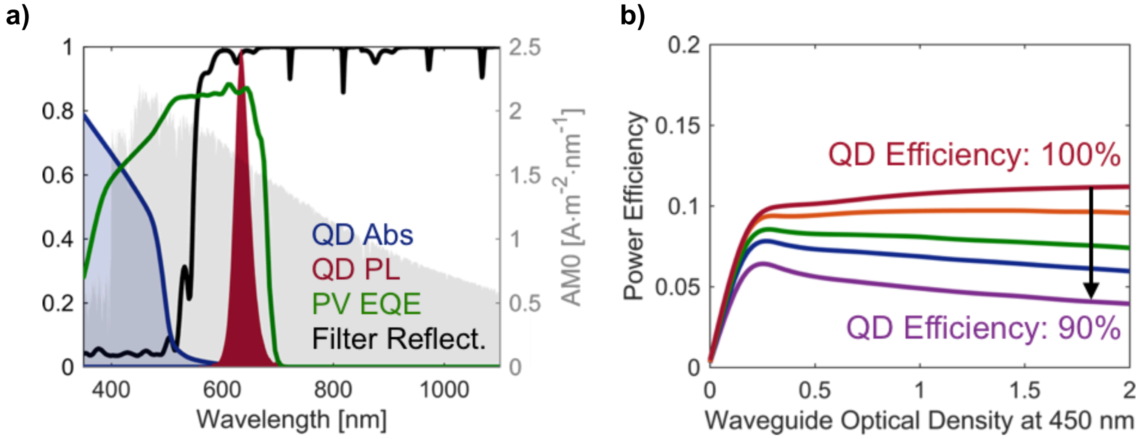

Figure 39: Simulated Efficiency for LSC System in AM0
Modeled CdSe/CdS quantum dot LSC system with an InGaP PV microcell and dielectric short-pass filter, with corresponding a) spectral characteristics and b) simulated efficiencies for varied quantum dot PLQY.
Adapted from Needell et al. [59].

5.3. LSC Launch via Alba Mission

The first launch of LSC modules into space will take place via the Alba mission, as part of Caltech's Space Solar Power Project (SSPP). The launch will test the performance of numerous emerging solar PV technologies—including ultralight and rigid perovskites, InP and GaAs nanowires, thin-film Si, CIGS, and LSCs—many of which having yet to be flown into outer space. The mission consists of a modular circuit board design, thereby enabling a diverse combination of cells to test at once. The launch is set to happen in December 2022 via a SpaceX Falcon 9 rocket. The samples will be launched on a satellite in low-earth orbit (LEO) and actively collect data for 2 weeks, followed by 3 months of non-operational time in LEO. During this time, autonomous measurements will be performed throughout flight to track the efficiency and degradation of each technology. Measurements including current-voltage (I-V), temperature, insolation, and sun incidence angle data will be recorded for analysis. The objective of this mission is to monitor and assess the performance and stability of each of these experimental PV technologies—as well as the designed structure and RF transmission—during operation in LEO.

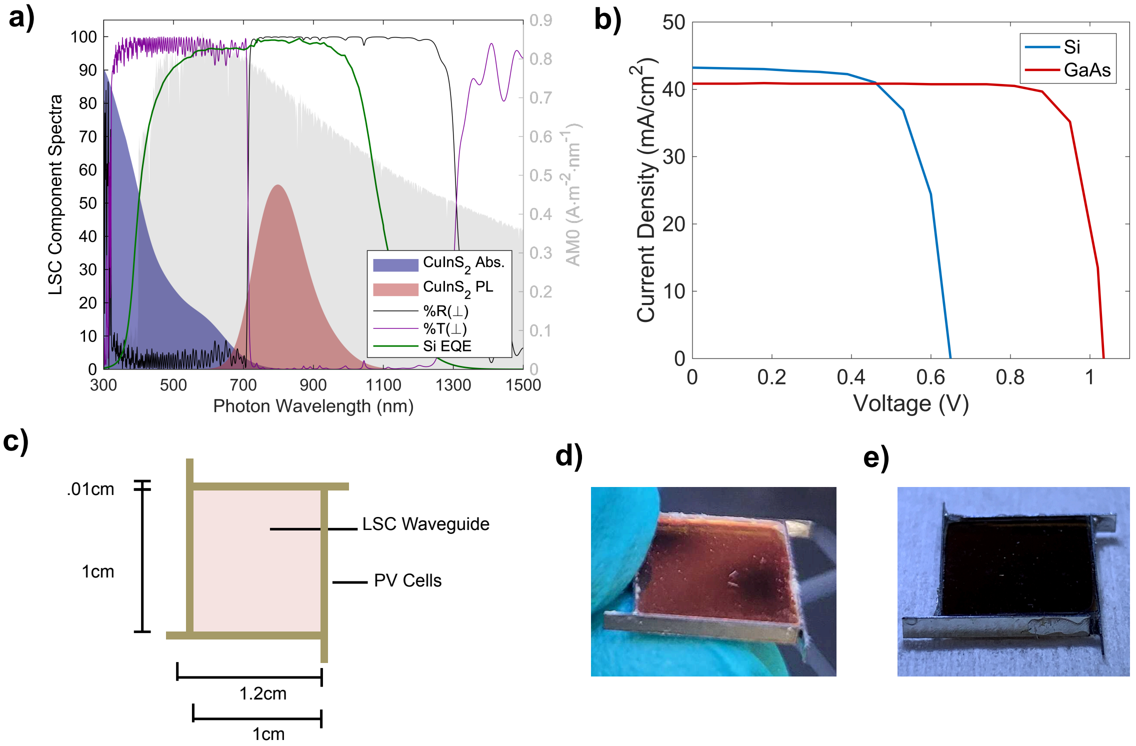

Figure 40: Performance metrics and design for Alba LSC modules.
Pictures of fabricated modules with and without the top dielectric filter are shown in d) and e), respectively.

For the Alba mission, we have fabricated four unique LSC modules to launch. Each LSC module consists of a 1cm x 1cm quantum dot waveguide surrounded by four 1.2cm x 1mm x 100µm PV cells placed along the edges in a staggered (e.g., pinwheel) orientation, as shown in Figure 40c. Two of the modules use GaAs cells as the edge-lined PV cells, while the other two use passivated Si cells. Current-density voltage (JV) measurements are shown for each cell type—Si and GaAs—in Figure 40b to demonstrate their respective performance characteristics. As shown, both PV cells have similar J_{SC}, with Si boasting a slightly higher J_{SC} (43.2 mA/cm2 for Si; 40.8 mA/cm2 for GaAs), whereas GaAs has a much higher V_{OC} (0.65V for Si; 1.03V for GaAs), thus resulting in a much more efficient GaAs cell (25.4% vs. 14.5%), as expected for a III−V structure. For each the GaAs- and Si-based modules, a dielectric stack short-pass top filter is applied to one of the modules, while the other module has no top filter, as shown in the photographs in figures Figure 40d and e, respectively. For all modules, $CuInS_2/ZnS$ quantum dots are used as the luminophore species and an Ag bottom reflector is applied. The spectral response for the Si-based module, including the top filter, is shown as an example in Figure 40a.

These modules are designed so as to maximize PL trapping. The staggered (i.e., pinwheel) PV orientation is used so as to enable the most PL trapping from the waveguide. By placing the cells along the edges, PL that would otherwise leak from the waveguide edges is instead incident on the PV cells; moreover, the pinwheel configuration prevents PL leakage at edge corners. Ag bottom reflectors are used to act as the LSC substrate for high reflectance (>99%) at the target PL wavelengths, thereby trapping PL that hits the back surface. Finally, the top filter used is designed as an aperiodic, dielectric multilayer stacks with high transmittance (>95%, unpolarized at normal incidence) between 350 and 740nm and high reflectance (>95%, unpolarized at normal incidence) between 740 and 1200nm, thus enabling transmission of high-energy photons, which are absorbed by the quantum dot luminophores as shown in Figure 40a, while reflecting back the subsequent PL at the top surface. As shown in Figure 40d, modules with a top filter reflect back dark red, corresponding with the expected spectral response, whereas modules without a top filter (Figure 40e) do not display a noticeable reflective response.

Initial testing indicates thermal stability for the Si-based modules. During this testing, the modules are exposed to thermal cycles from –100°C to 60°C for nearly 70 hours of constant illumination under AM0. As shown in Figure 41a, decreased power output is experienced for higher ambient temperatures, as expected; however, minimal overall performance degradation is recorded throughout thermal cycles. Since III−V PV cells have smaller temperature coefficients (i.e., are less sensitive to temperature change), as discussed in Chapter 2, we expect increased thermal stability for the GaAs-based modules. Figure 41b displays the JV curves for each the Si-based and GaAs-based LSC modules with a top filter present. As expected from the initial JV curves in Figure 40b, both systems have similar current densities, however the GaAs-based system boasts a higher V_{OC}, thus resulting in higher efficiencies as well. Finally, we see the advantageous effects of using a top filter given the EQE improvements for the Si-based modules shown in Figure 41c.

The results of this mission are ongoing and expected to be received in Spring of 2023 for further analysis.

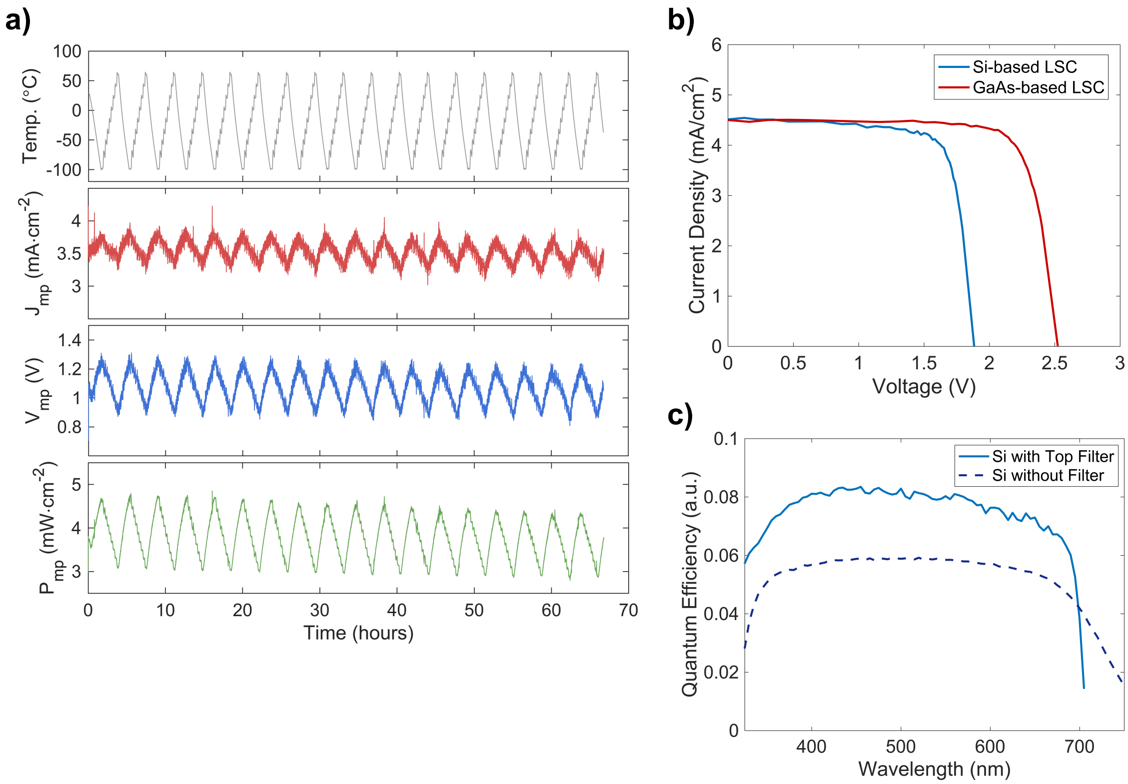

Figure 41: Initial testing of fabricated LSCs for Alba Mission.
Results for a) temperature testing for the Si-based module, cycling from -100°C to 60°C for 67 hours, b) current-voltage testing under AM0 solar simulation for each the Si- and GaAs-based modules with a top filter and c) EQE measurements for the Si-based modules.

5.4. Design Criteria for Next-Generation Ultralight LSCs for Space-Based Solar

To further improve the specific power of space-based LSCs, next-generation modules must be lighter, while still maintaining high efficiencies. To do so, each component of the LSC module must be as thin, and therefore flexible, as possible. To achieve such a goal, we redesign the LSC and leverage an ultrathin photonic crystal waveguide (PCWG) in place of the polymer waveguide. By using a PCWG, the waveguide thinkness is reduced from ~30μm to <1μm. Moreover, the PCWG enables PL trapping, thereby eliminating the need for the PL trapping dielectic filter. The glass substrate (~500μm) is replaced with an ultrathin polymer substrate (<2μm), furthering the ultrathin, flexible module. Finally, ultrathin III−V PV microcells are placed in a grid, coplanar to the PCWG. As such, the design is essentially only two layers: *i)* an ultrathin substrate and *ii)* a microcell-PCWG layer that is in-filled with quantum dots. This design enables a flexible module with a total thickness of ~4μm.

Given the design described above, three main components are needed to realize ultrathin LSCs for space-based applications: *i)* thin (~1μm) III−V PV cells, *ii)* ultrathin (< 2μm) CP1 polymer substrate, and *iii)* an a-SiC PCWG with high reflectivity at the PL peak. A rendered image of this layered design is shown in Figure 42c, with zoom in images of a rendered photonic crystal waveguide (Figure 42a) and a microscope image of a microcell (Figure 42b). Given the low absorption depth for III−V cells[225]–[227], ultrathin III−V cells are commercially available; however, a-SiC PCWG and ultrathin CP1 substrates are novel materials.

Figure 42d,e displays how we have been able to successfully achieve both of these remaining components. Figure 42d demonstrates how PL is trapped within the photonic crystal waveguide, where the glowing red PL remains in the plane of the photonic rods (small rectangles in the center of the figure). An a-SiC hole array PCWG, as discussed in Bauser et al. [185], is fabricated with a nanopillar array with an optimal pitch of 242nm, a pillar radius of 61nm, and a pillar thickness of 1.21μm. This design has demonstrated a possible trapping efficiency of 92.56% for a CdSe/CdS quantum dot system, with no detectable blue-shifting at high angles of incidence, as is present in dielectic stack filters. In Figure 42e, a fabricated CP1 substrate is shown to have a sustained thickness of < 2μm. Ultrathin CP1 substrates are achieved using a 0.65:0.35 ratio of CP1 polyimide to diglyme solution that was spin coated at 6000rpm for 60 seconds. The solution is deposited on a polypropylene sheet and then peeled off after it has cured to realize a standalone ultrathin sheet, which displays mechanical stability when placed under windy conditions up to 73 km/hr.

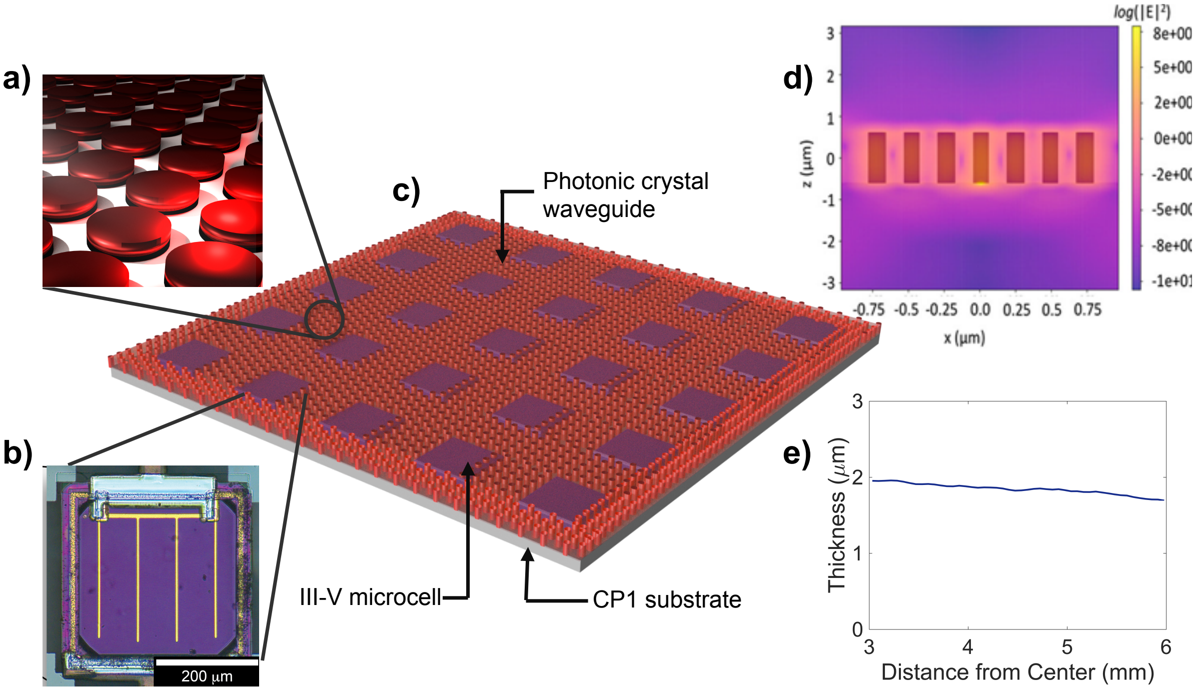

Figure 42: Ultrathin design for space-based LSCs.
The module consists of a) a photonic crystal waveguide fabricated by a-SiC rods, with an embedded grid of III-V microcells, as shown by the b) microscope image of a III-V microcell. The microcell-PCWG layer is fabricated atop on ultrathin CP1 substrate, resulting in c) a total integrated rendered representation of an ultra-light LSC design. Demonstrated performance for each component is shown for a fabricated d) a-SiC photonic crystal waveguide with sustained in-plane PL trapping, and e) CP1 standalone substrate with a sustained thickness of < 2µm.

Using Monte Carlo ray-tracing simulations, as discussed in Chapter 2, we model the potential efficiency of such a design. We model an LSC system that utilizes CdSe/CdS quantum dot luminophores with InGaAs microcells (400µm x 400µm x 2µm). The applied PCWG is modeled to have a PL trapping efficiency of 92.3%. Assuming near-perfect materials—QD PLQY = 1, OD = 3.0, GG = 20—this system could achieve a power conversion efficiency up to 9.8%, or a power output of 13.30 mW/cm^2 under AM0 illumination. To determine the specific power of such a module, we calculate the total module weight, as shown for each component in Table 8. This ultralight system weighs a combined total of 11.503 g/m^3, resulting in a specific power of 11.55 kW/kg. This potential specific power corresponds to a factor of 10 greater than the previously discussed LSC technology (Section **5.2**) and a factor of 100 greater than currently employed commercial space PV[224].

	Thickness	Weight (g/m^2)
InGaAs Cells	2 μm	5.1 (for GG = 20)
Interconnects (Cr/Al)	200 nm	0.0013
Bus Bars (Cr/Al)	200 nm	0.00176
a-SiC PCWG	1.2 μm	3.3
CP1 substrate	2 μm	3.1
Total	4 um	**11.503**

Table 8: Calculated total weight for ultralight LSC design.

5.5. Technoeconomic Analysis for Ultralight LSCs

To determine the viability of ultralight LSCs for space-based solar, we must understand the cost drivers and technoeconomics for each step of fabrication. We develop a technoeconomic analysis that investigates the total cost for fabricating ultralight LSCs at industry-scale (1 GW). Total costs are calculated for both capital expenditures (CapEx) and operating expenditures (OpEx), where OpEx consists of each materials, labor and electricity costs.

To build this model, we first must determine the process flow for fabricating an ultrathin LSC at industry-scale. Figure 43 details the projected process flow for such a working line. Fabrication is broken down into five main process steps—*i)* CP1 deposition, *ii)* microcell processing, *iii)* microcell array printing, *iv)* PCWG fabrication, and *v)* LSC-QD integration. Steps in the same column (e.g., CP1 deposition and microcell processing) indicate that both processes are completed in parallel. CP1 deposition involves spin coating an ultrathin (< 2 μm) CP1 sheet, as described in Section 5.4. Microcell processing refers to laser cutting of large-scale III—V (e.g., InGaAs) wafers and applying printing Ag contact pads upon each cell. During microcell array printing, subsequent laser cut microcells are printed onto the fabricated CP1 sheet and interconnected via Ag lines and Cu busbars. PCWG fabrication then occurs directly atop the printed microcell array and quantum dots are deposited into PCWG holes via spin-coating during the LSC integration step.

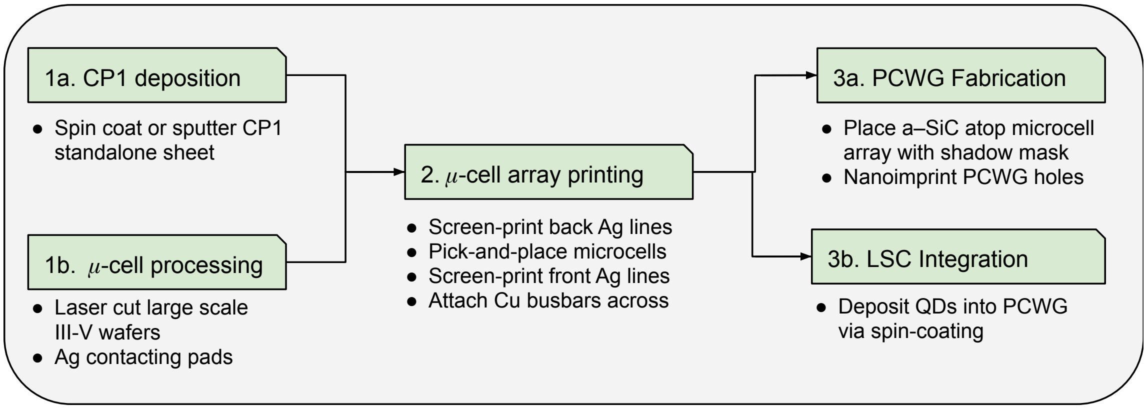

Figure 43: Process flow for an ultralight LSC intended for space-based solar.

By separating OpEx and CapEx by process step, we determine that the driving cost comes from the III−V cell material, as shown in Figure 44b. Conventional GaAs wafers, for example, cost roughly \$100 per 6-inch wafer, nearly \$5,000/m2. As such, the LSC module cost is almost entirely influenced by the geometric gain and thereby the amount of PV material used, as shown in Figure 44a. The next most expensive material in the entire analysis is the quantum dot solution—\$3.8/mg, or \$12.4/m2 at the target OD—which is over two orders of magnitude cheaper than the III−V cells. For ultralight LSCs to be economically viable, cheaper PV materials are needed. Recent advances in III−V growth via HVPE have demonstrated the ability to achieve low-cost cells at \$1 per 6-inch wafer, without sacrificing cell performance [195]. By replacing conventionally-grown III−V wafers with HVPE-grown wafers in our analysis, as shown in Figure 44c,d, the microcell processing step is no longer the main driver for LSC module cost, and the geometric gain only influence module cost at small GG (< 20). Ultrathin LSC modules thus become far more affordable and viable option economically.

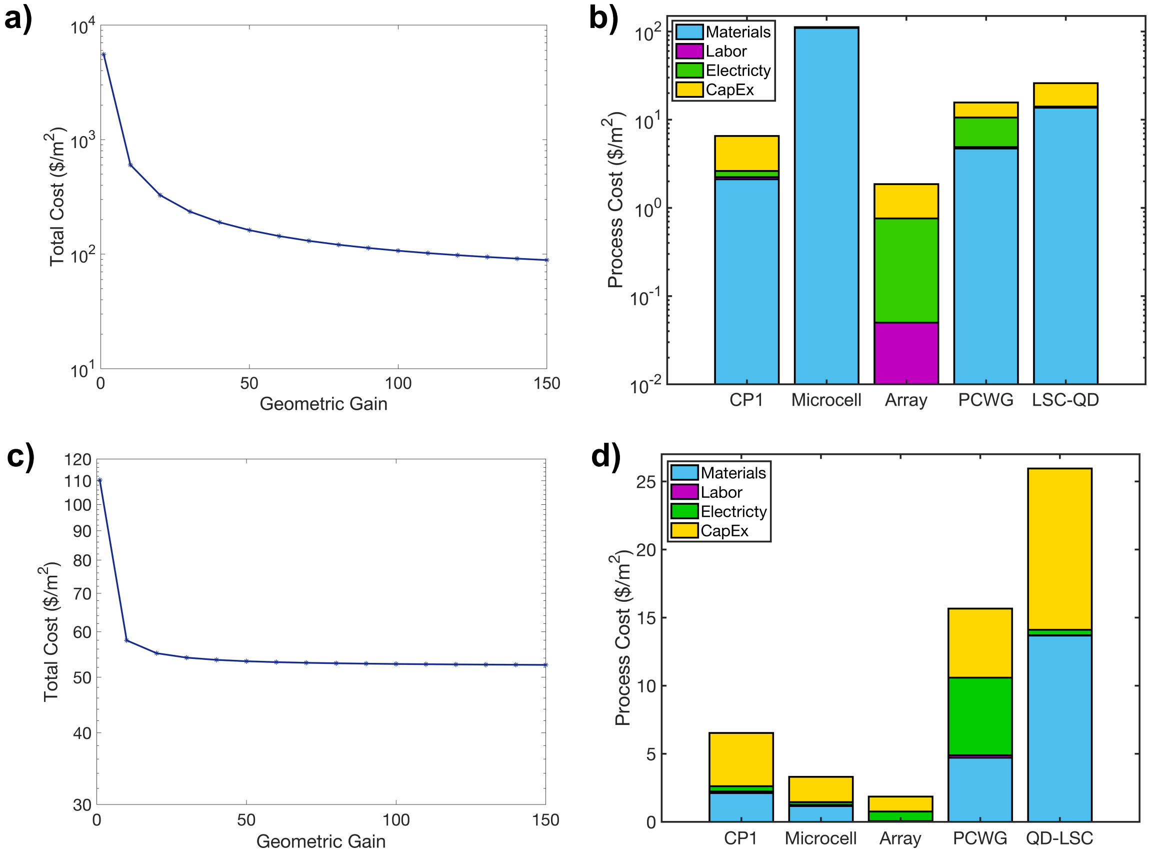

Figure 44: TEA results for ultra-light LSC design.
Module cost versus geometric gain for a) conventionally-grown III−V wafers and c) HVPE-grown low-cost wafers. Broken down OpEx and CapEx by process step for b) conventionally-grown III−V wafers and d) HVPE-grown low-cost wafers. Note, for the analysis using conventionally-grown III−V wafers, a) and b), results are shown on a log-scale given the drastic cost difference for III−V material.

Assuming a module efficiency of 9.0% and a GG of 20, consistent with our simulations, our analysis when using conventional GaAs wafers as microcells results in a levelized cost of 1.98 $/W, which is still far cheaper than current III−V costs of over $50/W [195]. However, by using low-cost HVPE-grown III—V cells, as shown in c and d, that cost drops to 0.24 $/W, making ultrathin LSC modules competitive with c-Si costs.

Details of our TEA model are described in the bullets below, and specified parameters/ assumption are presented in Tables 1—3.

1.1. Annual design capacity is set at 1 GW per year.
1.2. Production plant size is 1,000 sq ft.
1.3. Module power conversion efficiency is assumed to be 9.0%.

1.4. LSC module geometric gain (the ratio of the area of window face to the active PV area) is assumed as an input variable.
1.5. The quantum dot luminophores in the waveguide have a set optical density, measured at 600nm, of 2.0.
1.6. AM0 irradiation is assumed, with built in functionality to change irradiation conditions.
1.7. Maximum allowed line utilization for LSC manufacturing is assumed to be 90%.
1.8. We assume a year of analysis of 2018 and a plant life of 5 years.
1.9. Straight line depreciations used with a breakdown of 40% debt financing and 60% equity financing, and a 3.7% interest rate on debt.
1.10. Inflation rate is set at 1.9%, with state taxes at 6.0% and federal taxes at 21.0%.
1.11. Working capital (% of yearly change in operating cost) is set at 15%, after-tax IRR is 12%, and the inflation factor (based on a 2018 start up year) is set at 1.00.
1.12. Indirect capital costs are assumed as site preparation (2%), engineering and design (10%), project contingency (15%), and upfront permitting cost (7.5%).
1.13. Fixed operating costs are set as: labor cost for manufacturing work, engineering, and management ($15 per hour), general and administrative (20% of $/yr), property taxes and insurance (2% of $/yr), and production maintenance and repairs (4% of $/yr).
1.14. Electricity costs are assumed to be 0.05 $/kWh, consistent with the average price of electricity to industrial customers.
1.15. For the GaAs microcell processing, we assume a chemical bath reuse of 5 and a material usage yield efficiency of 99%.
1.16. This analysis assumes a mature manufacturing process, thus expenses from R&D cost are not included as it is expected to be negligible.

Operating Parameters	**Value**	**Units**
Design Capacity	1,000,000	kW / year
Production Plant Size	1,000	sq. ft.
Module Efficiency	0.9	percent
Optical Density (at 600nm)	2.0	unitless
Module Size	1	m^2
Incident Irradiation	1,353 (AM0)	W/m^2

Table 9: Operating parameters assumed for large-scale LSC ultra-light modules.

Stage	Raw Material	Cost Rates		Materials Cost ($\$/\mathrm{m}^2$ of LSC)
CP1 substrate	CP1	1,000.00	$/kg	2.00
CP1 substrate	Diglyme	160.00	$/kg	0.11
Microcell processing	Full-size GaAs Wafers	4,184.00	$\$/\mathrm{m}^2$	Variable
Microcell processing	Hydrogen Peroxide	1.48	$/kg	Variable
Microcell processing	Hydrochloric Acid	6.20	$/kg	Variable
Microcell processing	Hydrofluoric Acid	1.08	$/kg	Variable
Microcell processing	Ammonia	9.50	$/kg	Variable
Microcell array printing	Al (paste)	52.00	$/kg	0.001
Microcell array printing	Cu soldering tabs	2.00	$/kg	0.001
PCWG Fabrication	Silane Gas	70.00	$/kg	0.0849
PCWG Fabrication	Hydrogen Gas	1.40	$/kg	0.0035
PCWG Fabrication	Methane	2.51	$/kg	0.0006
PCWG Fabrication	O_2 Gas	0.65	$/kg	0.0002
PCWG Fabrication	N_2 Gas	0.28	$/kg	0.0000
PCWG Fabrication	Master Stamp	1,000	$/unit	1
PCWG Fabrication	Topas Foil	2.60	$/lb	0.577
PCWG Fabrication	SF6	2.00	$/L	4.60
PCWG Fabrication	C4F8	3.00	$/L	0.13
PCWG Fabrication	LN_2	2.00	$/L	0.05
QD Integration	CuInS QDs (OEM)	3.86	$/mg	12.81
QD Integration	CP1	1,000	$/kg	1.848

Table 10: Materials cost for reference ultralight LSC module, used when calculating operating expenditures.

No.	Equipment	Electricity usage ($\mathrm{kWh/m}^2$)	Unit Price ($k)	
1	Sputtering Tool	7.80	2,000	[191]
2	Precision laser cutter	160	60	[191]
3	Cell Sorter	-	737	[192]
4	Cell Tester	2.93	156	[192]
5	Pick-and-Place Machine	-	212	[192]
6	Screen Printer	10.88	353	[192]
7	PECVD	3.35	1,496	[192]
8	Nanoimprint Lithography	83.68	400	[228]
9	DRIE	-	700	[104]
10	Spin Coater	6.34	6,060	[192]

Table 11: Equipment costs and associated equipment footprint used to calculate capital expenditures.

Note: equipment without an electricity usage listed is due to steps that involve multiple pieces of equipment. E.g., 83.68 $\mathrm{kWh/m}^2$ includes both the nanoimprint lithography and DRIE tools, so is listed only for the first so as not to double-count.

5.6. Conclusion

Space-based solar power could enable accessibility to constant solar power from anywhere on the globe. Luminescent solar concentrators present a promising option for space solar technology given their light-weight, flexible structure, radiation hard materials and potential for a high specific power. We design and fabricate the first ever LSC modules to be sent to outer space via Caltech’s Alba mission. The modules will be launched into low-earth orbit in November 2022 and results will be received springtime 2023. Next-generation space-based LSCs are further designed as an ultrathin, ultra-light, flexible module, which leverages a photonic crystal waveguide as both the waveguide and photoluminescence trapping filter. Such a design could achieve specific powers up to 11.55 kW/kg at an optimized cost as low as 0.24 $/W.

SECTION III: LUMINESCENT CONCENTRATORS IN COMBINATION WITH CONVENTIONAL SOLAR TECHNOLOGIES

CHAPTER 6: TANDEM INGAP/SI PHOTOVOLTAIC LUMINESCENT SOLAR CONCENTRATOR

This chapter reports the design, fabrication and outdoor characterization of a tandem luminescent solar concentrator/Si multi-junction photovoltaic module. The tandem LSC/Si device consists of an InGaP LSC functioning as a top cell and a passivated contact Si bottom cell. The LSC comprises of an InGaP microcell array coupled to a polymer waveguide, loaded with CdSe/CdS core-shell quantum dot luminophores. The light trapping efficiency of the LSC waveguide is enhanced by encapsulation with photoluminescence trapping mirrors consisting of dielectric multilayer thin films. We demonstrate the performance of the LSC/Si device through a series of outdoor tests under various irradiance conditions conducted at the National Renewable Energy Laboratory. I report the first outdoor testing data of an LSC/Si tandem module, displaying maintained performance across varied diffusivity conditions for the LSC component. Finally, modeled performance of the tandem module is presented using a ray optic simulation-based multiphysics model and forecast a pathway for high efficiency tandem LSC/Si module performance.

6.1. Introduction

Tandem LSC/Si modules address all critical requirements for tandem PV technology implementation: *i)* functionality in both direct and diffuse lighting conditions, *ii)* efficient solar spectrum utilization via a multi-junction module, and *iii)* reduced materials cost due to integration with silicon and the small area fraction for the III−V material (i.e., high GG). In this study, we analyze the first-ever fabricated LSC/Si tandem module, as shown schematically in Figure 45. The module consists of (from the top-down): *i)* a top dielectric aperiodic stack notch filter, *ii)* a polymeric LSC waveguide of poly(lauryl methacrylate) (PLMA) with uniformly dispersed CdSe/CdS core/shell quantum dots (QDs), *iii)* an InGaP III−V micro-cell array, *iv)* a bottom dielectric aperiodic stack notch filter, and *v)* a passivated contact Si subcell. Finally, we supply specular reflective acrylic-Al mirrors along each of the module edges to reduce photon losses from edge out-coupling.

While the performance of single-junction cells has been evaluated under diffuse irradiance conditions using many optical configurations (conventional texture-etched Si cells [229], dielectric nanosphere arrays [230], plasmon nanostructures [231]–[233], and light trapping wire arrays [234], [235]), device performance of tandem LSCs, has not been studied for varied irradiance conditions. Here we investigate designs for III−V/Si LSC devices that combine arrays of micro-processed InGaP cells embedded within an LSC and optically integrated with a flat plate Si cell for use as a four terminal (4T) tandem module. For an optically efficient LSC, the concentration factor can approach the geometrical gain (GG), defined to be the ratio between the total device illuminated surface area and the area of the III−V PV material. If high concentration factors (>30x) can be achieved, this tandem LSC/Si approach has the potential to increase module efficiencies beyond 30%, well beyond current single-junction performance limits, while dramatically reducing the cost per watt of the utilized III−V material [43], [51].

Figure 45 shows both photographic (Figure 45a,b) and rendered schematics (Figure 45c) of the LSC/Si tandem module. Figure 45d displays a conceptual schematic of the core/shell structure of the CdSe/CdS QDs, as well as a transmission electron microscope (TEM) image of the nanoparticles. To convert PL (Figure 45a) into electrical power, we fabricate a micro-cell array, composed of embedded III−V InGaP cells with active areas of 400μm x 400μm per cell, shown in the optical microscope image in Figure 45d. We set this array in tandem with a passivated contact silicon subcell optimized to harvest long-wavelength photons. Though the embedded InGaP micro-cell array has a small area fraction, it acts as a powerful optical sink, absorbing light in the micro-cells. The long wavelength portion of incident light spectrum not converted into PL is thereby transmitted to the Si cell. By optically coupling the LSC component to the InGaP micro-cell array and matching the PL of the QD luminophores to the InGaP energy bandgap, we concentrate sunlight irradiance in the ultraviolet/blue part of the spectrum onto high radiative efficiency InGaP micro-cells to enable higher module efficiency. Our fabricated module is a 4T structure, reducing the risk of J_{SC} mismatch and series resistance between the top LSC and bottom Si. Figure 45b shows the realized LSC-InGaP microcell array that is placed atop the silicon subcell. The PL of the QD-waveguide under UV-light is shown in Figure 45a.

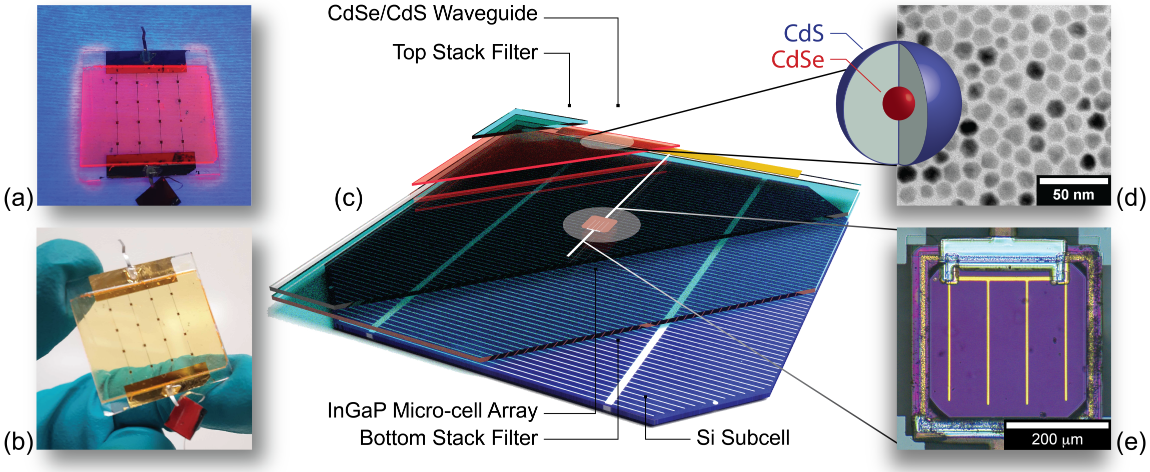

Figure 45. The tandem LSC/Si, four terminal module.
(a) The top LSC component consisting of a 4x4 InGaP micro-cell array encapsulated within a 30 micrometer (μm) thick CdSe/CdS core/shell QD waveguide under UV illumination, visibly displaying PL in the red. (b) The same top LSC component as (a), under ambient light held for scale. (c) A 3D rendering of the full tandem LSC/Si module with PL trapping stack filters coupled to the top and bottom surfaces of the LSC waveguide/InGaP micro-cell array component. (d) The core/shell structure of the CdSe/Cds QDs alongside a transmission electron microscope (TEM) image. (e) A confocal microscope image of the anchored InGaP micro-cell on the LSC glass substrate, with cell dimensions of approximately 400 μm x 400 μm.

Figure 46a,b show the measured, spectral characteristics for the LSC and Si components of the tandem module. The full AM1.5G spectrum impinges upon the top surface of the LSC device. CdSe/CdS QDs absorb photons in 400-500nm wavelength range and photoluminesce at a peak wavelength of 635nm, spectrally matching the InGaP electronic bandgap (Figure 46a). This PL is trapped within the waveguide by both TIR and top/bottom notch filters, which reflect photons centered around the QD PL (Figure 46a). Incident photons not absorbed by the QDs or reflected by the notch filters pass through the LSC to the Si subcell. Given the high external quantum efficiency (EQE) for the passivated contact Si cell at longer wavelengths (Figure 46b), this design actively splits the incident spectrum between high energy photons (LSC) and low energy photons (passivated contact Si). As shown in Figure 46b, the transmitted light incident on the Si subcell is a truncated AM1.5G spectrum due to photons that have been either absorbed and trapped by the top LSC component, or reflected by the notch filters. With proper spectral tuning of the notch filters, increased PL collection by the InGaP micro-cells outweighs filter reflection losses [43]. Figure 46c,d show the simulated and measured notch filter transmittance, respectively. In this design we use an aperiodic, dielectric layered structure consisting of Ta_2O_5 (high index) and SiO_2 (low index) in order to achieve this notch profile. We observe a close match between simulated and measured transmittance values, with slightly lower transmittance in the high photon energy pass band of the fabricated mirror owing to absorption from the thick, 2mm glass substrate of the dielectric stack.

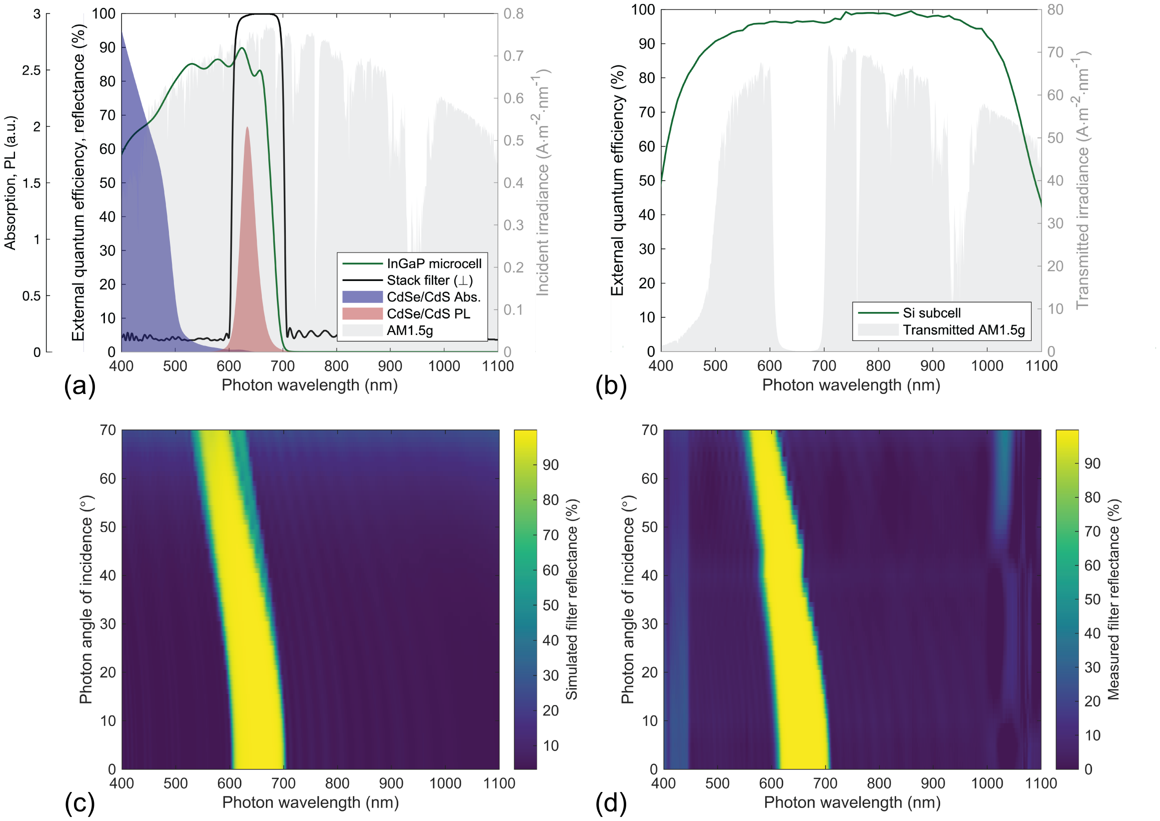

Figure 46. Spectral characteristics of the tandem LSC/Si module.
(a) The top LSC PV component, comparing the spectra of the absorption/PL of the CdSe/CdS QDs (far left y-axis), the external quantum efficiency (EQE) of the anchored InGaP micro-cell (left y-axis), the stack filter reflectance spectrum at normal incidence (left y-axis), and the incident AM1.5G spectrum (right y-axis). (b) The bottom Si component of the tandem LSC/Si module, comparing the spectra of the passivated contact Si cell EQE (left y-axis) against the transmitted irradiance through the LSC component (right y-axis). (c), (d) The simulated and measured dielectric, aperiodic stack filter with alternating layers of Ta_2O_5 and SiO_2, respectively. The realized stack filter (d) is deposited atop an approximately 2mm thick glass substrate.

We conducted indoor laboratory measurements, taken under one-sun solar simulation, to reveal the optical properties of each component in the module. Figure 47a,b illustrate the effects of individual LSC components on the EQE performance in an analogous layer-by-layer fashion. As the LSC components shape the incident light spectrum, fewer photons are collected by the Si subcell, as seen in Figure 47b. Light current-voltage (LIV) measurements reveal a J_{SC} = 29.3 mA/cm2 and a V_{OC} = 0.7 V for the bare Si subcell, and a J_{SC} = 12.9 µA/cm2 and a V_{OC} = 4.5V for the 4x3 InGaP micro-cell array under the LSC waveguide. With each layer added to the full device, the total output current from the Si is reduced and V_{OC} decreases slightly (Figure 47c). Additionally, the 4x3 InGaP array experiences a current drop off with the addition of the top filter (Figure 47b) as a result of the reduced EQE spectrum of the InGaP micro-cell. However, as discussed later, given proper tuning of the notch filter and LSC parameters (e.g., concentrated QD loading, GG), increased PL trapping will offset the drop-off in the InGaP micro-cell EQE spectrum with the addition of the top filter, thus resulting in an enhanced power output of the full device.

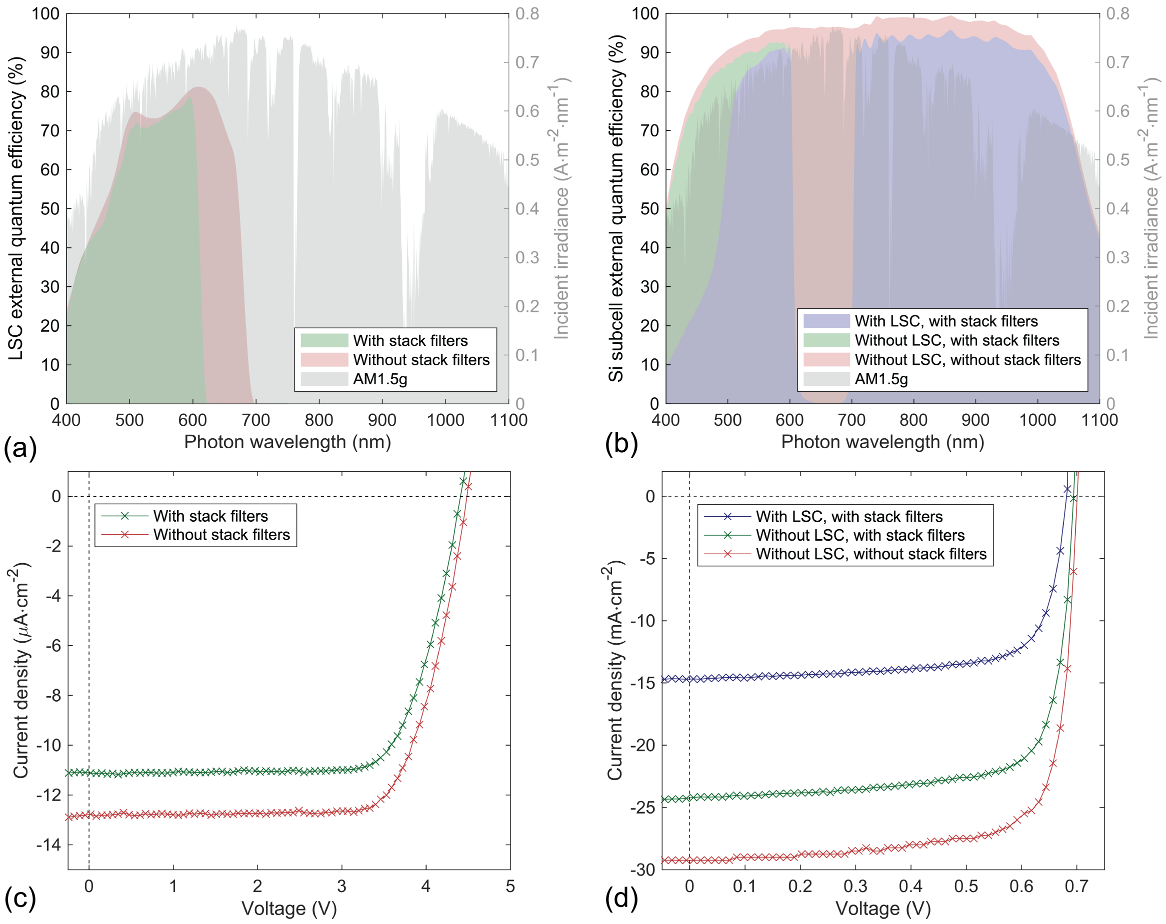

Figure 47. Measured electrical performance of the tandem LSC/Si device under artificial, AM1.5G light via a solar simulator.
(a) The EQE analysis for the top LSC component for the cases with and without PL-trapping stack filters. (b) The EQE analysis for the bottom, passivated contact Si component for the cases with the LSC and PL-trapping stack filters, with only the stack filters, and finally without the LSC or the filters. (c) Light IV measurements of a sparse InGaP micro-cell array top LSC component for the cases with and without PL-trapping stack filters, under AM1.5G illumination. (d) Light IV measurements of the Si passivated contact bottom cell for the same cases as in (b), under AM1.5G illumination.

We analyzed the power performance of a fabricated array of 12 InGaP micro-cells—four cells connected in series across three columns in parallel, spaced 4mm apart—optically coupled to a QD LSC with an overall GG of 250. Of note, the 4x3 microcell array tested corresponds with a sparser design than is optimal, as shown by the high GG, due to fabrication challenges of a fully-dense InGaP cell array; for a denser array with tighter InGaP cell spacing, we would expect a higher photocurrent density of the LSC top component as discussed in the final device modeling section. In order to ensure complete optical coupling, we deposit the LSC QD waveguide directly atop the InGaP micro-cell array. We show here periodic current-voltage (IV) measurements of the LSC/Si tandem module throughout an outdoor field test performed in the week of November 12th, 2018 at the National Renewable Energy Laboratory (NREL) in Golden, CO. In addition, we simulated loss mechanisms intrinsic to this design via a Monte Carlo ray-tracing algorithm. We spatially mapped the PL collection of a single InGaP micro-cell within the QD waveguide to determine photon travel distances within the LSC to further analyze efficiency loss mechanisms. Finally, we designed and optimized the tandem LSC/Si module addressing each identified loss mechanism and sources of inefficiency to forecast the performance limits for such tandem module designs.

6.2. Methods and Tandem LSC/Si Module Fabrication

Upright n-on-p InGaP solar cells were grown on GaAs substrates by atmospheric-pressure metal-organic vapor phase epitaxy (MOVPE) [227], [236]. The Zn-doped absorber layer was approximately 900nm thick with a 2 micron $Al_{.5}Ga_{.5}As$ lateral conduction layer (LCL) for transparency, which allowed bifacial operation of the device. An AlInP layer was used beneath the LCL as a sacrificial layer for lifting off micro-cells during transfer printing. For the fabrication of micro-cells, the geometry of the *n*-contact was first defined via photolithography. A contact layer with 10nm of Ni and 1μm of Au was then electrodeposited. The cell mesa was defined with a two-step wet etch, the first being a 1:100 bromine-hydrobromic (48% HBr, Sigma-Aldrich) acid etch, to non-selectively complete the main part of the etch; the second being a saturated HCl etch, to selectively remove the remaining InGaP and expose a smooth, undamaged LCL. The *p*-contact was deposited similarly, and the devices were isolated by another HCl etch, exposing the GaAs substrate. Silicon nitride was deposited over the device via plasma-enhanced chemical vapor deposition (PECVD) to reduce Fresnel losses and non-radiative recombination. Contact windows and lift-off edges were opened via CF_4 reactive ion etch (RIE). A secondary on-cell Au contact was deposited by sputtering. Photoresist was used to anchor the cells for lift off. A 1:4 HCl-H_2O etchant was used to remove the sacrificial layer. A 150 nm layer of spin-on-glass/epoxy (SOG-E) adhesive [237] was deposited on top of a soda-lime glass substrate. A polydimethylsiloxane (PDMS) stamp was then used to transfer the micro-cells to the glass substrate deterministically to form an array [83], [238]. The SOG-E layer was cured by sequential heating and UV exposure. The edges of the cells were insulated with SU-8 2025. A Cr/Cu/Al/Au interconnect was then sputtered to complete the array.

For the present design, we fabricated CdSe/CdS core/shell QDs closely following literature procedures [51]. Absorption spectra were measured using a Shimadzu UV-3600 double beam spectrometer. Measurements were conducted at dilute concentrations to minimize the influence of scattering. PL spectra were measured using a Horiba Jobin-Yvon FluoroLog steady-state spectrofluorometer, exciting above the bandgap at 430 nm. The detection PMT of the spectrofluorometer was calibrated for spectral sensitivity. For TEM analysis, dilute solutions of the nanocrystal stock solution were drop cast onto TEM grids (Electron Microscopy Sciences CF400-Cu). Multiple TEM images with thousands of quantum dots were sized using an automated analysis script to ensure consistency from the nanoparticle synthesis.

We dispersed these core/shell QD particles within the monomers lauryl methacrylate (LMA, Sigma-Aldrich) mixed with ethylene glycol dimethacrylate (EGDMA, Sigma-Aldrich) at a 10:1 ratio. Darocur 1173 (Sigma-Aldrich) photoinitiator was added at 0.05% volume and the mixture was polymerized under UV exposure at inert atmosphere. To obtain a 30μm waveguide thickness, we used a capillary force method, which employed soda lime spacers to induce uniformity across the 2.5cm x 2.5cm substrate. This LSC waveguide was then deposited directly atop the InGaP micro-cell array on soda-lime glass to allow for maximum photocurrent harvesting.

We designed and optimized the dielectric, aperiodic notch filter stack following a previously used optimization procedure [43]. We fabricated the stack filter onto a 2.5cm x 2.5cm x 2mm glass substrate with an anti-reflective coating opposite the dielectric stack (Evaporated Coatings Inc., Willow Grove, PA USA). We mechanically stacked the InGaP array/LSC component directly on the bottom dielectric stack filter and glass substrate. We similarly placed the top dielectric filter atop the PLMA-QD waveguide to complete our device design. Finally, we placed this bottom filter/InGaP micro-cell array/PLMA-QD waveguide/top filter structure atop a passivated contact Si cell with a window area of 1.6cm x 2.5 cm.

Our bottom Si subcell is a single side textured, rear junction cell with heavily doped n-type and p-type poly-Si/SiO_x passivation layers deposited at the front and the back of an n-type Cz wafer respectively. First, 170 microns thick, single side textured, 2.5—3 Ohm cm n-Cz wafers were cleaned using piranha, standard RCA 1 and RCA 2 process. Then, approximately 1.5nm thick low temperature thermal tunneling SiO_x was grown on an RCA cleaned single side textured n-Cz wafer. A 50 nm thick PECVD grown n-type and p-type doped hydrogenated amorphous silicon (a-Si:H) was then deposited on top of this tunneling oxide. The sample was placed inside a diffusion furnace in an N_2 environment at 850C for 30 minutes to simultaneously diffuse the dopants and crystallize amorphous Si to polycrystalline Si. 15 nm of alumina oxide is then added using atomic layer deposition and is activated at 400C in a forming gas environment to enhance the passivation. The resulting cell has a passivation that can reach above 730 mV in iV_{oc} and ~10 fA/cm^2 J_0 values. The metal contacts were formed by thermally evaporating titanium and silver through the openings of a shadow mask. We soldered metal ribbons to the pads at the end of the busbar and the back contact to provide electrical leads for the tandem configuration [239].

The passivated contact Si cell was measured using a solar simulator under 1 sun condition and then measured again under the CdSe/CdS waveguide and bottom filter stack to estimate the performance of the cell in the LSC/Si configuration. Under 1 sun, the cell achieves V_{oc} of 703.2 mV, J_{sc} 38.9 mA/cm^2, and an efficiency of 20.6%. When this cell is measured under the waveguide and the filter stack, the V_{oc} of the cell decreases to 694 mV, and J_{sc} to 27.3 mA/cm^2 due to the reduced incident illumination on the cell, resulting in an efficiency of 14.4% for Si subcell. We encapsulate this Si subcell with a mm-thick layer of Polydimethylsiloxane (PDMS). In order to approximate a large-area III−V micro-cell array via side loss reduction, we place this tandem LSC/Si device within a mirrored acrylic testbed [240]. We measure the reflectance of this rectangular trench with a Varian Cary 5G UV-Vis spectrophotometer.

6.3. Outdoor Testing Results From NREL

We determined the effects of irradiance and diffuse light illumination on tandem LSC/Si performance through outdoor field testing, with modules tilted at a fixed 40° relative to horizontal with continuous on-site irradiance measurements [241]. We found that power output as a function of the time-of-day (Figure 48a,b) achieves its maximum performance near 12:00 pm. As seen in Figure 48, this maximum power for both components coincides with maximum solar irradiance (Figure 48c) as well as an angle of incidence nearest to normal incidence of the module (Figure

48d) given the tilted axis of the field-test. By 4:00 pm and onwards, limited incident irradiance and large off-normal angle of incidence results in negligible output power of the module. We observe similar temporal trends for both the Si subcell and the LSC top cell. Shown in Figure 48a, the maximum power output decreases across the LSC over the course of the three testing days, a trend not seen in the Si subcell power output vs. time-of-day (Figure 48b). Such a power decrease implies a degradation mechanism of the LSC component itself, most likely attributed to photodegradation of the PLQY of the luminophores [241], [242].

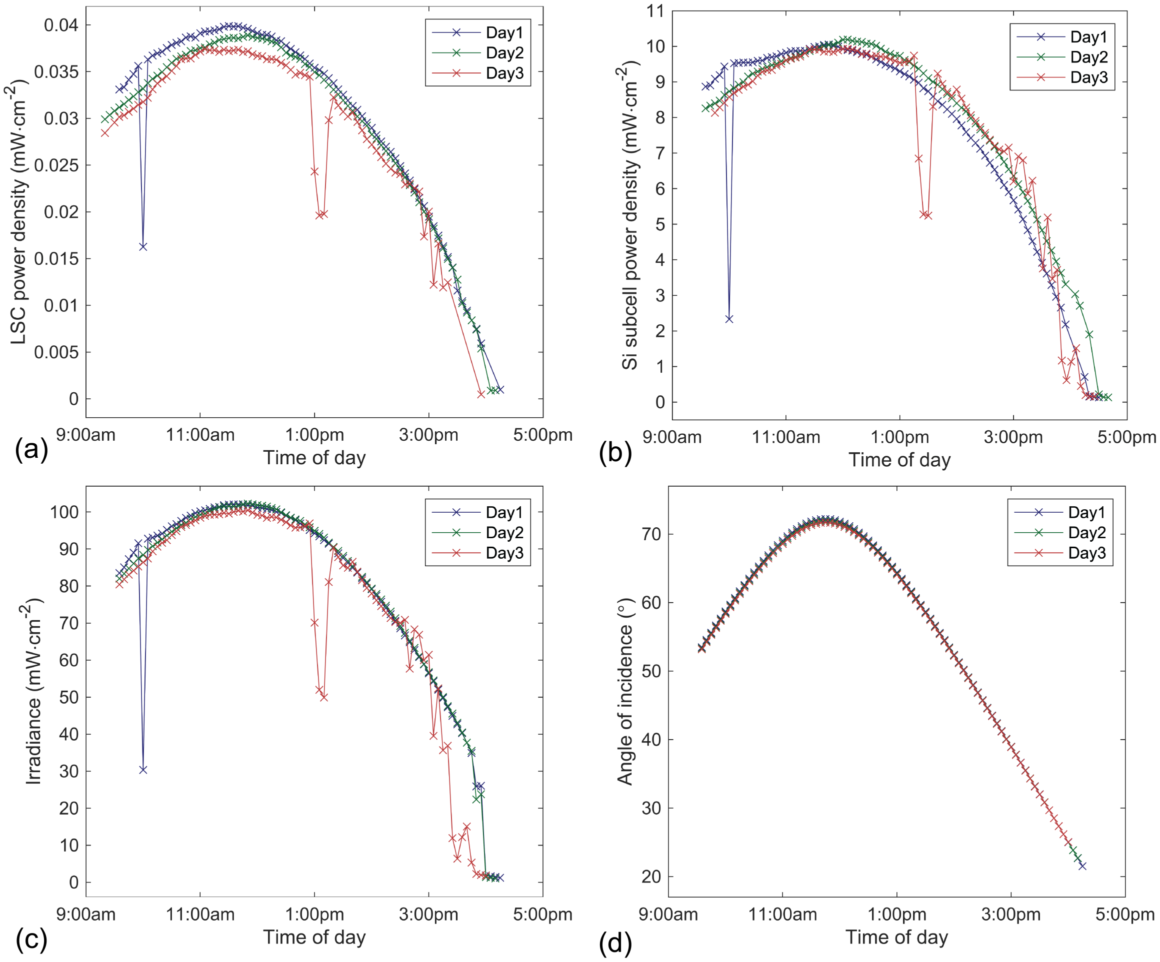

Figure 48. Outdoor testing results with respect to time of day.
Data was taken at the National Renewable Energy laboratory in Colorado, USA for November 13th, 14th, and 15th 2019. (a) The top LSC component and (b) the bottom Si cell component power output in mW per cm^2 over the course of three full days of testing. (c) The solar irradiance (mW per cm^2) and (d) angle of incidence (AoI) (degrees) relative to Earth's horizontal tangent line for each day of testing. Dips in the data correspond to brief periods of cloud and/or snow coverage at the testing facility.

One of the most promising features of such an active concentrator LSC design results from the sustained functionality in both direct and diffuse illumination conditions. Shown in Figure 49a, we demonstrated outdoor field testing data that is consistent with the PCE trends found in previous work for LSCs [45] as well as for simulated tandem LSC/Si devices operating under varied diffuse and direct irradiance conditions [43]. Seen in Figure 49b, the Si subcell power conversion efficiency begins to monotonically decrease once the amount of DNI light drops below 50mW/cm^2. In contrast, the top LSC component does not demonstrate a steady decreasing trend in PCE as a function of DNI. Of note, the slight spread in normalized efficiency for both the LSC and Si components is due to discrete trends associated with each day's data collection. These spreads may be a result of the day-to-day variations in testing conditions. Moreover, we hypothesize that the slight drop in normalized efficiency for the Si subcell towards maximum DNI * Irradiance of 100, which typically occurs near noon, may result from the change of the solar spectrum after noon. Fernandez, et. al., have shown that higher angles of incidence, as occur in the afternoon, produce a larger attenuation of the UV-visible region of the spectrum, resulting in a red-shifted spectrum [243]. A red-shifted solar spectrum is better matched to the silicon band edge, potentially leading to a slight increase in performance, as seen in Figure 49b.

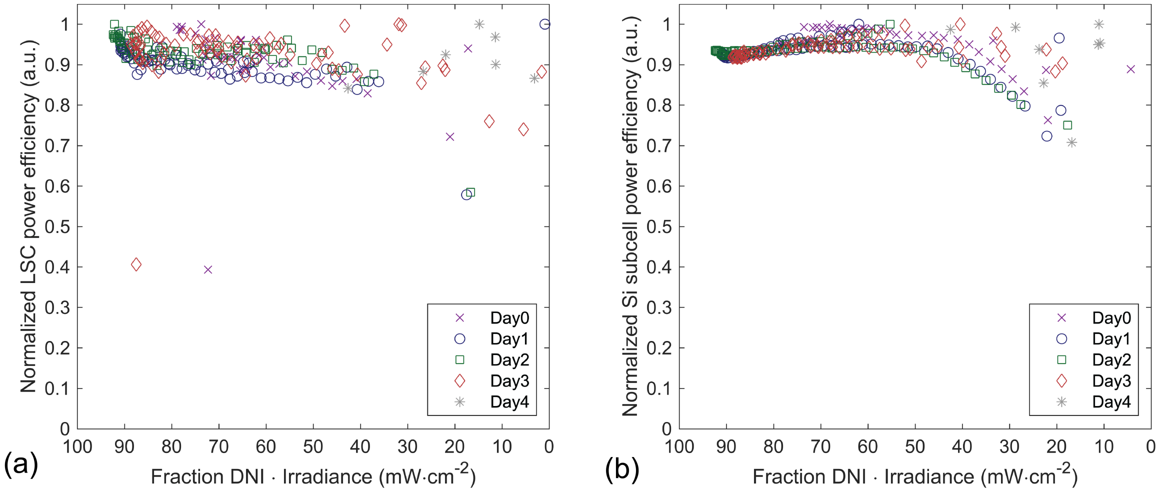

Figure 49. Outdoor testing results with respect to the fraction of DNI by total Irradiance. Data was taken at the National Renewable Energy laboratory in Colorado, USA for November 12th (partial day), 13th, 14th, 15th, and 16th 2019. Normalized efficiency with respect to the fraction of direct normal incidence (DNI) by total irradiance is shown for the (a) top LSC component and (b) bottom Si component. We normalize each individual day's power conversion efficiency to the highest efficiency for that given day. Days 3 and 4 of (a) correspond to the case with no top PL-trapping stack filter.

6.4. Tandem LSC/Si Device Performance Analysis

Our device underperforms previous simulated work of an LSC/Si tandem design, which suggests an optimized LSC/Si tandem module can reach power conversion efficiencies near 29% [43]. In this study, the Si subcell—when integrated in the LSC/Si tandem module—performed at a 10% PCE, and the LSC component contributed 0.04% PCE. To identify loss mechanisms and optimize our design performance, we simulated the LSC/Si tandem module design with a Monte Carlo ray-tracing algorithm and detailed balance model in order to observe how experimental data match with model predictions. Previous work shows this model to be in strong agreement with experimental observation [52]. We applied this computational tool to understand the causes of lowered output current by the top LSC component.

Figure 50 illustrates the primary loss mechanisms that limit the performance of such a tandem structure. We found the most significant areas of photon loss stem directly from: *i)* top filter reflection of incident irradiance, *ii)* non-radiative recombination of absorbed photons by the QD luminophores (i.e., non-unity PLQY), *iii)* scattered photons lost through the escape cone of the waveguide/filter component, and *iv)* parasitic Si subcell absorption (e.g., incomplete light coupling into the wafer by the front texture and antireflective coating (ARC), absorption of the trapped near infrared (NIR) light by the back reflector). We illustrate such loss mechanisms schematically and spectrally in Figure 50a,b, respectively.

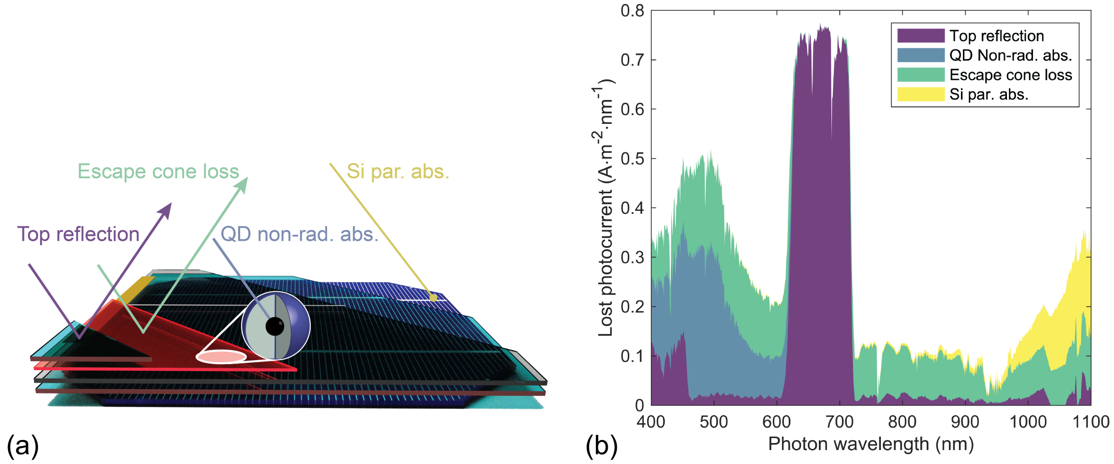

Figure 50. Computational results showing the primary loss mechanisms responsible for underperformance in the tandem LSC/Si system.
(a) A rendered schematic depicting the various loss mechanisms, including: top surface reflection of incident sunlight due, primarily, to the top notch filter (purple), escape cone loss from the LSC waveguide (green), QD non-radiative recombination absorption (blue), and Si parasitic absorption (yellow). (b) The spectral account for the full tandem LSC/Si loss mechanisms, given as the total lost photocurrent (amps per m^2 per nm).

In the short wavelength regime (wavelengths below the notch filter stop-band), the primary loss mechanism results from non-radiative QD absorption due to non-unity PLQY. From ray-tracing simulations and performance matching to outdoor data, we found QD PLQYs to decrease down to approximately 60% over the course of the testing period. As shown in Figure 48a, we found that the power output of the LSC degraded steadily over each day, implying potential generation of defects in QDs within the waveguide performance, which we attribute to decreasing QD PLQY. As the LSC PLQY degrades, the probability of photon loss due to QD absorption increases, thereby causing decreased power output.

For wavelengths within the stop-band of the filters, reflection due to this spectral feature is the main cause of photon loss. While the near-perfect reflectance from the notch filter around the 600-700nm spectral range increases PL trapping and photocurrent delivery to the InGaP micro-cells within the LSC waveguide, it also prevents photons within this frequency range to be transmitted through the top surface to reach either the InGaP array or Si subcell. With near-unity PLQY QDs, PL trapping within the LSC outweighs the reflected incident photon loss within this wavelength range. The finite top-filter reflectance below 500nm light correspondingly reduces the produced PL. Improved filters could increase spectral transmission down to at least 400nm and enhance QD photon absorption. Another cause of decreased LSC photocurrent results from PL photon loss through the escape cone of the PLMA waveguide due to top filter transmission. Peak filter reflectivity blue-shifts with angles of incidence as illustrated in figures Figure 46c,d. PL that scatters or emits into larger angles of the waveguide escape cone decreasingly reflects back into trapped modes. Finally, a fraction of the low energy photons (λ > 900nm) collected by the Si subcell is lost due to parasitic absorption.

As shown in the photocurrent loss mechanisms in Figure 50b, QD non-radiative absorption and waveguide escape cone re-emission account for a vast portion of loss mechanisms for the LSC component. Improved PL collection requires increased optical efficiency of the waveguide [65]. We spatially mapped the photoluminescence emission within the waveguide by scanning a 490nm wavelength, 10μm spot-size beam [244] across an analogous single InGaP micro-cell LSC. We illuminated the waveguide from the corner of the 0.16mm^2 micro-cell and extend into a spatial quadrant analyzing a 2.5cm x 2.5cm waveguide area—equivalent to a GG of 625—shown in Figure 51a. As seen, the measured photocurrent drops with the spatial separation between the illumination point and the micro-cell corner. An inflection point in the steep drop off located less than 0.2mm from the quadrant origin indicates a combination of PL and nearby scattered, short wavelength light collected in this small radius. Such an inflection reveals that the mean photon travel distances within the LSC waveguide are significantly limited by a convolution of escape-cone and non-radiative QD losses.

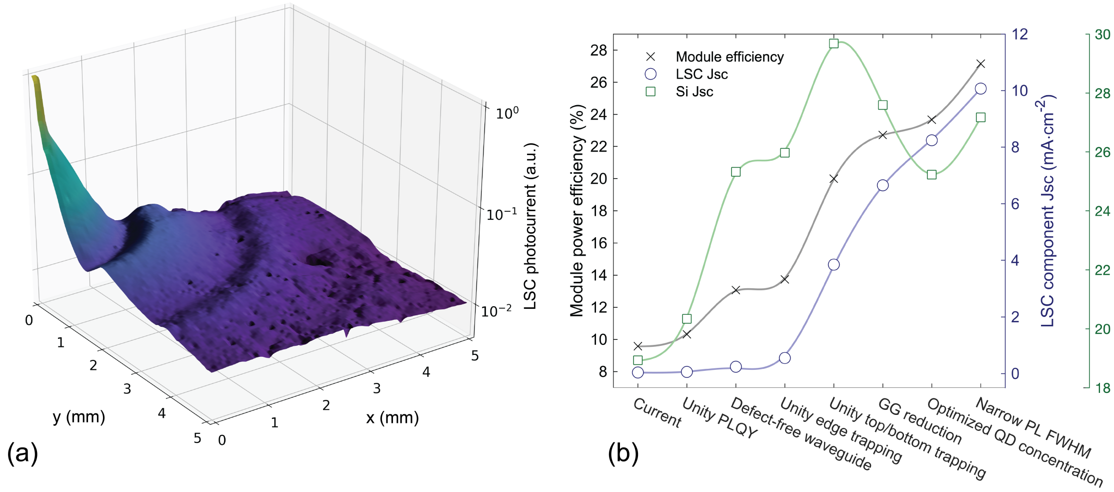

Figure 51. Waveguide photocurrent mapping and performance forecast for a tandem LSC/Si module.
(a) The photocurrent mapping of a single InGaP micro-cell embedded within a 30 μm waveguide doped with CdSe/CdS QDs plotted on a log scale. A 490nm laser source scans x- and y-distances up to 5 mm from the outside corner of the device active area (the origin corresponding to the cell center). (b) A performance forecast for the tandem LSC/Si module, illustrating approaches for increased module power efficiency (left y-axis, black x-markers) through optimization of the LSC component, alongside the predicted LSC photocurrent (right y-axis, blue circle-markers) and predicted Si subcell photocurrent (far right y-axis, green square-markers). Efficiencies are modeled for 100% DNI under standard AM1.5G conditions.

Via an understanding of the loss mechanisms in the LSC, we can design an improved tandem device. Figure 51b projects the modeled power conversion efficiency, as well as the associated photocurrents for each the LSC top component and Si subcell, possible for various approaches to component optimization for the tandem LSC device. One promising method for maintaining QD stability and enhancing PLQY performance involves the use of a siloxane film as a part of the waveguide matrix [245]. Further optimization could also include: *i)* a defect free waveguide, consisting of an increased quality factor of the QDs, defined as the ratio of absorption at the band edges of CdSe to CdS [54], and non-aggregated dispersion of luminophores within the polymer [246]; *ii)* minimized PL leakage from the device edges; *iii)* optimized top/bottom filters to reduce loss from low-wavelength incident photon reflection and scattered photon transmission through the waveguide escape cone; *iv)* a decreased geometric gain (from 250 to 10) of the LSC for higher PL micro-cell collection yields, without obscuring long-wavelength photons from reaching the Si component; *v)* a re-optimized concentration (i.e., optical density) of the QDs within the waveguide (from 0.33 to 2.4 at 450nm); and *vi)* a decreased QD PL full-width at half-maximum emission profile [247]. By optimizing for each of these components, the tandem device is expected to achieve an ultimate output photocurrent of 10.1mA/cm^2 and V_{OC} = 1.48V for the LSC component with 27.2mA/cm^2 and V_{OC} = 0.65V for the Si subcell. These optimizations are predicted to enable a total module power efficiency of 27.2% under 1-sun illumination, matching previous simulated work given the device spectral characteristics [43], [52]. Given this design, tandem LSC/Si devices show promise as a high PCE tandem device with sustained performance in highly diffuse settings.

6.5. Conclusion

We report an LSC/Si tandem module that demonstrates maintained performance under variable diffusivity conditions. Through outdoor testing at NREL (Golden, CO), we measure the effects of diffuse irradiance on performance of each the LSC top-component and Si subcell. In addition, we simulate a tandem LSC using a Monte Carlo ray-tracing model to quantify the various loss mechanisms present in the module design. We finally forecast that a tandem LSC has the potential to achieve up to 27.2% power conversion efficiency—a significant efficiency increase with respect to the baseline 20.6% efficient Si-only cell under 100% direct normal irradiance—while further maintaining performance across varied DNI conditions.

CHAPTER 7: HYBRID GEOMETRIC-LUMINESCENT PHOTOVOLTAIC CONCENTRATORS

Concentrating photovoltaics are attractive due to their ability to capture of a large area of incident sunlight on a small photovoltaic (PV) area, thereby keep the system costs low. Yet, implementation of concentrating photovoltaics is limited, due to associated challenges with reliability, the need for solar tracking, and high operating PV temperatures. We investigate how the addition of luminescent concentration could enable heightened performance when integrated with traditional geometric concentrators. We design and fabricate two separate hybrid geometric-luminescent concentrator systems—one that leverages a hemisphere as the geometric component and the other that uses a compound parabolic concentrator. We find performance is improved when moderate luminescence is added to the hemisphere system, both under direct illumination and at high angles of incidence. However, performance is diminished with the addition of luminescence for the compound parabolic system. This difference between the two hybrid systems is attributed to the placement of the photovoltaic device and the choice of geometric component. In the hemisphere system, an inverted photovoltaic cell isolates concetration as the sole contributer to photon collection and device performance, whereas an upright cell in the compound parabolic concentrator benefits from direct illumination as well. Moreover, the optimized geometry of the compound parabolic concentrator inhibits any additional improvements, and therefore the introduced luminophores act merely as scatterers that disadvantageously redirect photon paths. Given these two systems, we show that for certain geometries, such as the reflective hemisphere, the addition of moderate luminescence may help boost performance.

7.1. Introduction

Light concentration is one of the most fundamental and intuitive concepts of light-matter interaction. In fact, most people have experience with light concentration, whether or not to their knowledge, from a young age. When considering light interaction with a lens (e.g., a magnifying glass or a pair of glasses), we can envision how sunlight is redirected from sparse light to a single, concentrated beam. This seemingly commonplace imagery is an example of solar concentration. When photons—or, light particles—impinge upon certain structures (e.g., a Fresnel lens), the beam path is redirected toward a smaller output area, thus resulting in concentration. This concept enables light to be collected from a large area and redirected to a smaller area, which is advantageous for applications such as solar energy photovoltaics in order to reduce the amount of necessary photovoltaic material.

The magnifying glass example above depicts one type of concentration: geometric concentration. In a geometric concentrator, photons are redirected using geometry alone, without any resulting change in photon energy. As such, this concentration is also known as passive concentration [29]. Geometric concentrators can take a variety of forms, including Fresnel lenses, parabolic reflectors, array reflectors, V-trough reflectors, and multisectional planar concentrators [248]. For any such geometric concentrator, the maximum concentration, or the ratio of illumination at the exit vs. entrance apertures, can be calculated as shown below, where $A_{1(2)}$ is the entrance (exit) area, $\Phi_{1(2)}$ is the entrance (exit) flux, $\theta_{1(2)}$ is the incoming (outgoing) beam angle, and n is the refractive index of the medium.

$$C = \frac{\Phi_2/A_2}{\Phi_1/A_1} \leq \frac{n^2\, sin^2\theta_2}{sin^2\theta_1} \tag{1}$$

The majority of the aforementioned technologies, however, underperform the above concentration limit by up to a factor of four. In order to approach this limit, the following requirements are needed for a geometric concentrator: *i)* non-imaging, *ii)* an exit aperture angle of 90º, and *iii)* conservation of flux [29]. One such technology that meets these criteria, and thus approaches the concentration limit, is the compound parabolic concentrator (CPC), as will be discussed in Section 7.4.

The second school of concentration is luminescent concentration, which employs a waveguide with embedded luminophores and a PV collector that is in contact with the waveguide surface, either along the edge or coplanar. Figure 5, in Chapter 1, illustrates the differences between both types of concentrator systems. In a luminescent concentrator, absorbed light is down-shifted to a lower energy, thus resulting in active concentration[29]. As a result, thermalization occurs at the luminophore waveguide, away from the PV cell. Furthermore, the planar design of a luminescent concentrator enables both direct and diffuse concentration, thereby averting any need for solar tracking. In a luminescent concentrator, concentration is dependent on the Stokes shift of the luminophores [48], or the extent at which the absorbed photon is downconverted, as shown in equation (2). Here, $e_{1(2)}$ refers to the energy of the absorbed (emitted) photon, k is the Boltzmann constant, and T is temperature.

$$C \leq \frac{e_2^2}{e_1^2} \exp\left(\frac{e_1 - e_2}{kT}\right) \tag{2}$$

Ideation for solar concentration dates back to 200 BC when Greek myths state that Archimedes used bronze shields to concentrate solar rays onto invading Roman ships [249]. However, the first documented use of concentrated solar occurred in 1866 when Auguste Mouchet used parabolic troughs to heat water. Over a century later, in 1968, the first operational concentrated solar plant was built[249]. At this point, only geometric concentration was considered. By 1973, the concept for luminescent concentration for photovolatics was introduced [33]. Yet, as of 2016, the global incidence of installed (geometric) concentrated photovoltaics was 360MW, a mere 0.2% of total PV installations[250], and installations of luminescent concentration are negligible.

Despite centuries of development and implementation, geometric concentration has failed to achieve reliable solar power output[251]. Given existing flaws in geometric concentration, the vast majority of installed solar concentrators generates thermal (concentrated solar power, CSP, 4,800 MW) instead of photovoltaic (concentrated photovoltaics, CPV, 360MW) power [252]. In order to optimize photovoltaic energy generation from CPV, the current outstanding challenges associated with geometric concentration must be addressed. Given the inverse relationship of concentration with angle of incidence (θ_1), as shown in equation (1), a small angle of incidence is required to achieve a high concentration ratio. As such, geometric concentrators require direct illumination and therefore tracking mechanisms [33], [34], which are often costly and bulky, to track the sun's trajectory throughout the day. Additionally, incident photon energies are conserved and essentially added together in geometric concentration, resulting in increased operating at the PV cell [253], which causes underperformance as discussed in Chapter 2. While luminescent concentration has been able to address these two challenges, luminescent concentrators require near-perfect materials in order to convert and trap photons [54]. As such, the record efficiency for luminescent concentrators is currently 7.1% [67], leaving much room for improvement for a PV concentrator system.

Here we explore how hybridizing geometric and luminescent photovoltaic concentration could mitigate some of these challenges, including *i)* improved thermal management at the PV collector, *ii)* reduced need for solar tracking, and *iii)* improvements in overall PV power output.

To hybridize these two schools of concentration, we propose incorporating luminescent materials into a geometric structure. In doing so, the luminophore species could enable isotropic light absorption, as is seen for LSCs, thereby reducing the need for tracking. Moreover, thermalization can be redirected to the luminophore waveguide, away from the PV cell, as discussed in Chapter 2, to reduce PV efficiency losses due to high temperatures. Finally, by leveraging both forms of concentration, and reducing these two challenges, heightened power output could be achieved. Previous works that investigated use of both geometric and luminescent concentrators have proposed stacking the two technologies or placing LSCs in parallel to leverage geometrical concentration [254], [255]; however, no work, to this date, has proposed hybridizing the two concepts into one standalone technology.

In this work, we investigate two types of hybrid geometric-luminescent concentrators—one that leverages a hemispherical geometric design and the other that utilizes a compound parabolic concentrator (CPC). For each system, we design and fabricate the hybridized device. We experimentally measure performance via power output for each system across varied optical density solutions and varied angles of incidence. We begin by designing the hemispherical-luminescent concentrator. After assessing performance of such a device, we next design and fabricate the CPC-luminescent concentrator. We compare the hybrid device with its bare geometric (hemisphere or CPC) counterpart (e.g., with no luminescent medium). We aim to understand how power output is affected when luminescent solutions are introduced, under each direct illumination and high angles of incidence, thereby understanding the effects on both efficiency and tracking requirements.

7.2. Hemispherical-Luminescent Solar Concentrator

We first explore a hybrid geometric-luminescent design that leverages a hemispherical shell as the geometric portion. For this hybridized system, we propose using a reflective, hollow hemispherical shell that is then filled with a luminescent solution. In doing so, we integrate both the luminescent and geometric components so that they act as a single concentrator mechanism, as opposed to acting in parallel. Our design proposes using a reflecting hemisphere that is filled with a toluene solution with embedded luminophore quantum dots, and placing an inverted PV cell at the top, as shown in Figure 52a. Incident photons are absorbed by the quantum dot luminophore and re-emitted within the toluene solution as photoluminescence (PL). The PL is then trapped and redirected by the reflecting hemisphere geometric component until it comes in contact with the top inverted PV cell, as pictured in Figure 52a.

For this study, we use $CuInS_2/ZnS$ quantum dots as the luminophore, GaAs as the PV cell, and coat 200nm of Ag along the outside of a glass hemisphere, via e-beam evaporation, as the reflecting surface. The spectral response of each of these components is found in Figure 52b; of note, the quantum dot PL matches the band-edge of the GaAs EQE and the Ag-reflecting shell boasts a reflection >90% in the PL regime. Figure 52c,d shows rendered versions of such a design, from a top-down view and a double-cross sectional view of the top left quadrant, respectively. As shown, the PV cell sits inverted in the center of the hemisphere, in contact with the luminescent solution.

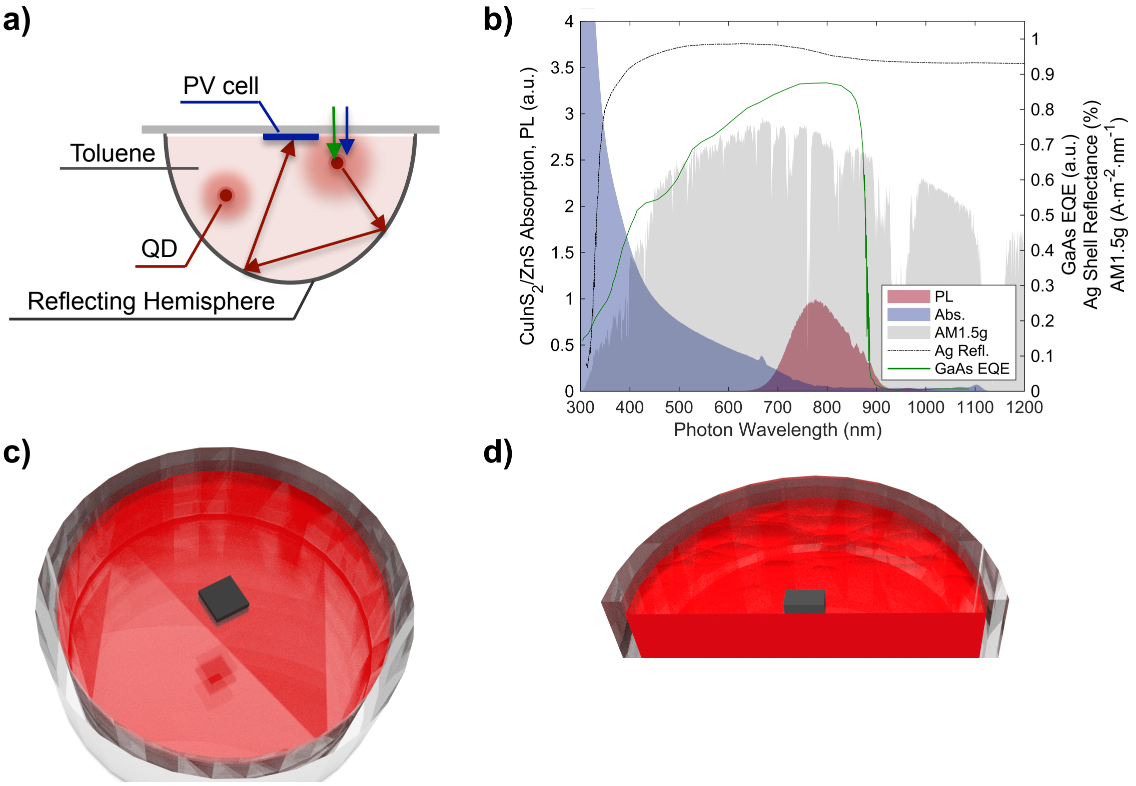

Figure 52: Experimental setup for hybrid hemispherical-luminescent concentrator system.
a) Schematic of fabricated hybrid hemisphere-luminescent concentrator—including a reflective hemisphere, filled with a QD-toluene solution, with an inverted PV cell atop the hemisphere that is in contact with the luminescent solution—and respective b) spectral responses for each component. Rendered images show the inverted PV cell atop the luminescent solution in the hemisphere from each a c) top-down and d) double cross-sectional view.

To assess the performance of the hybrid hemispherical-luminescent concentrator system, we first investigate the effects of luminescence and optical density (OD) on PV performance. To do so, we measure current-voltage (IV) curves under an ABET Technologies solar simulator (AM 1.5D) across three optical densities—OD = 0, OD = 0.7, OD = 1.43—as shown in Figure 53a. The OD = 0 case represents the base-case—a toluene solution with no embedded quantum dots—i.e., a purely geometric concentrator with no luminescence. As shown in Figure 53a, PV performance is improved for the lower OD solution (OD = 0.7, blue dashed line), but is worsened for the high OD solution (OD = 1.43, dark blue dotted line) in comparison to the base case (OD = 0, cyan solid line).

We next study the effects of angle of incidence on hybrid hemisphere-luminescent concentrator performance. To do so, we shine a blue (450nm) laser—blue is chosen given the absorption spectra of the $CuInS_2/ZnS$ QDs—on the hemisphere surface at varying angles of incidence. We see that luminescent solutions (OD>0) do not result in heightened performance, in comparison with the base case (OD = 0, black dotted line), until high angles of incidence (e.g., 60°). At this angle, we see slight performance improvements with optical density—i.e., higher OD solutions result in slightly higher short-circuit current—however, the improvements are negligible, as shown in Figure 53b. This suggests that adding luminescence to a hemispherical concentrator may improve performance at oblique angles, but improvements only occur at angles of incidence above 50°, as shown by the crossover point in Figure 53b.

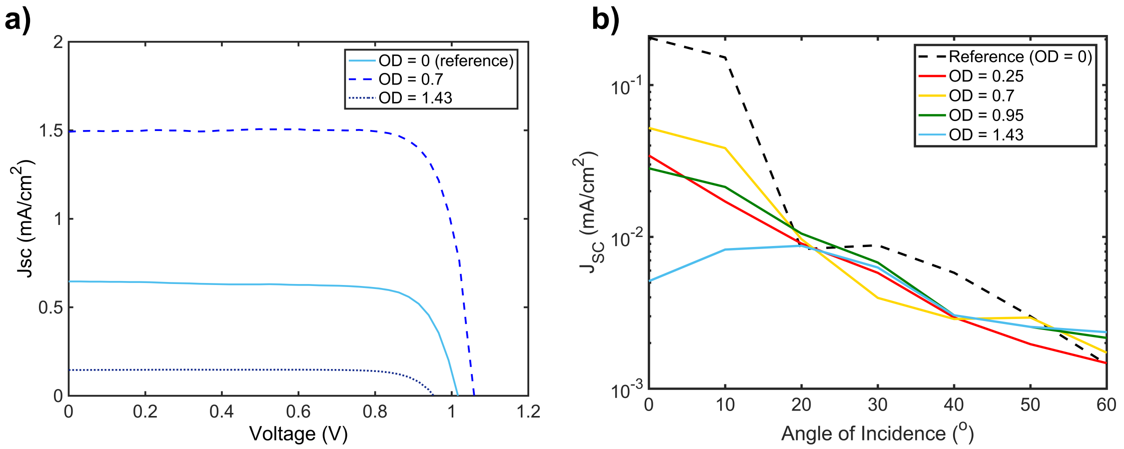

Figure 53: Performance measurements of hemispherical hybrid concentrator under AM1.5D.
Effects of varied optical density solutions on a) current-voltage measurements under direct illumination and b) short-circuit current under varied angles of incidence.

To understand why high OD solutions worsen performance in the hybrid hemisphere-luminescent concentrator under direct illumination, as seen in Figure 53a, we take spectrally-resolved photocurrent measurements across varied OD solutions (Figure 54). We use an NKT supercontinuum laser, in conjunction with a monochromator, to achieve spectral resolution. Since the sample involves a liquid solution, the beam path must be redirected to the bottom surface of the optical table using a 45° mirror. A simplified trace of the beam path through the mirror is shown in Figure 54a, with the associated pictorial image in Figure 54b. The results of the collected photocurrent vs. wavelength for each OD solution are shown in Figure 54c, with the base case (OD = 0) plotted as a black dotted line. As shown, a low OD solution (e.g., OD = 0.3, red line) enables a performance boost across all wavelengths, in comparison with the base case. However, for higher OD solutions, performance is decreased, particularly in the <700nm range. The shaded gray area in Figure 54c displays the quantum dot absorption; as shown, performance drops occur where the quantum dots are absorbing. Moreover, with higher OD solutions, we see a greater drop in photocurrent, particularly where the QDs absorb. This implies that at high ODs, parasitic absorption outweighs any performance boost from the luminescent solution. Parasitic absorption occurs due to non-unity PL quantum yield (QY); for unity PLQY systems, we would expect heightened performance across all OD solutions.

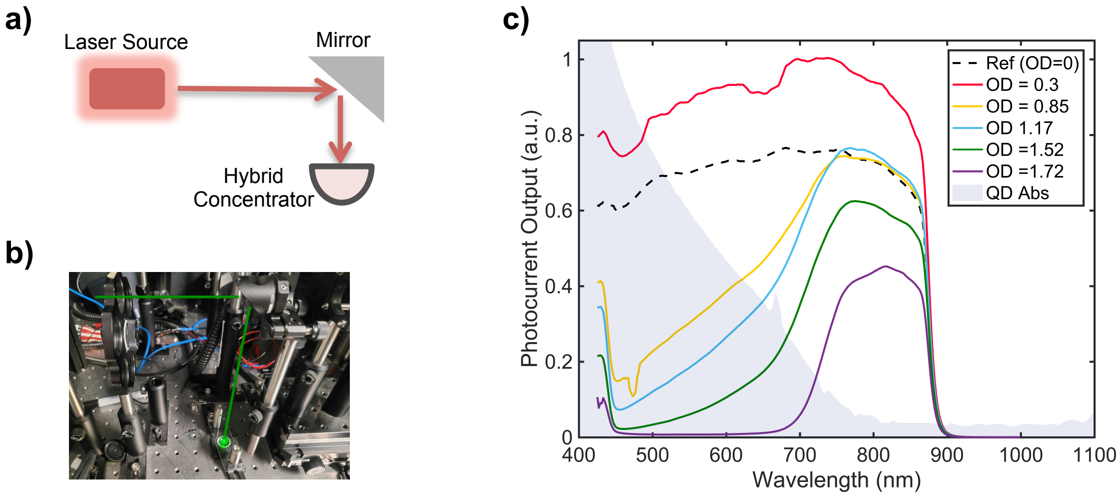

Figure 54: Spectrally-resolved photocurrent response for hemispherical hybrid concentrator. Optical set-up for the spectrally-resolved measurements shown via a a) simplified laser trace and b) pictorial image including an added green line to trace the beam path towards the bottom sample. Results from these measurements are shown in c) via spectrally-resolved photocurrent output across varied optical density solutions.

7.3. CPC-Luminescent Solar Concentrator

We next investigate a hybrid geometric-luminescent design that instead leverages a hollow CPC as the geometric component, keeping the luminescent component constant—$CuInS_2/ZnS$

quantum dots in a toluene solution. Again, we use a reflective, hollow geometric shell that is then filled with the luminescent solution. We use a 45° 2.5mm output diameter molded compound parabolic concentrator from Edmund Optics as the target CPC. To fabricate the CPC shell, we place the glass 45° 2.5mm CPC into an uncured polydimethylsiloxane (PDMS) solution and thermally cure the polymer for 2 hours at 80°C. Once cured, we remove the glass CPC and puncture a hole at the 2.5mm output diameter, where the PV cell would be placed, thus resulting in a hollow CPC mold made from PDMS. To create a reflective surface, we then deposit 400nm of Ag inside the CPC mold via e-beam evaporation.

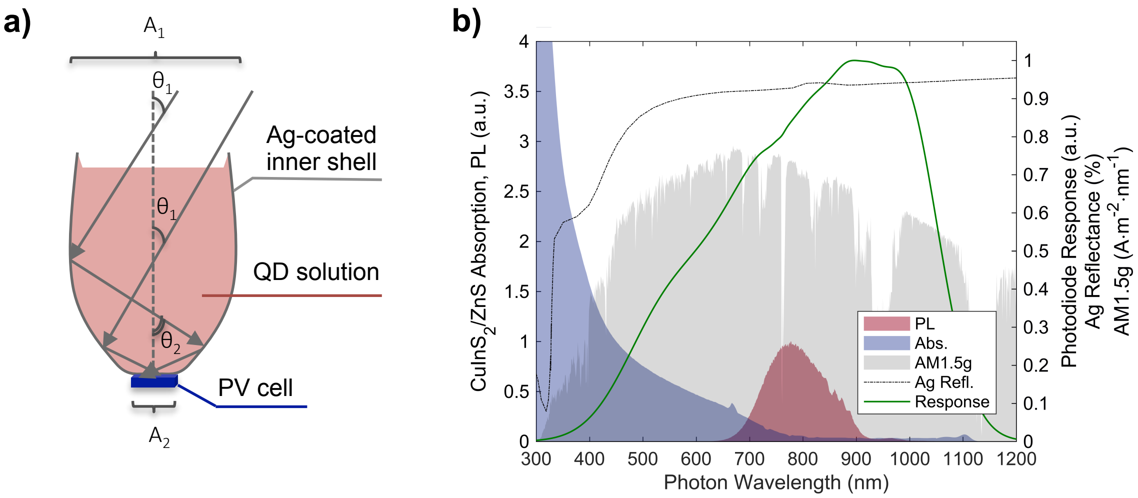

Figure 55: Experimental setup for hybrid CPC-luminescent concentrator system.
a) Schematic of fabricated hybrid CPC-luminescent concentrator—including a hollow CPC shell with a reflective Ag inner coating, a QD-toluene solution, and a bottom inverted PV cell that is in contact with the luminescent solution—and respective b) spectral responses for each component.

The mold is then placed atop a PV cell or photodiode; for this study we use a silicon photodiode (Luna Optoelectronics PDB-C152SM) as the photo-collector. The photodiode is mounted on a glass slide with soldered leads coming off each the positive and negative terminals for ease of contacting during measurements. Since the CPC mold has a hole at the bottom, we seal the mold on top of the mounted diode using uncured PDMS as a glue to prevent leaks, and then finish with another thermal cure. The CPC mold is then filled with a QD-toluene solution of varying OD, as shown in Figure 55a. The corresponding spectral response for each of these components is found in Figure 55b.

To test performance, we again measure IV response under an ABET Technologies solar simulator direct illumination (AM 1.5D). As shown in Figure 56, CPC performance is enhanced when the toluene solution is injected into the CPC shell. However, once quantum dots are introduced (i.e., OD > 0), performance steadily decreases with optical density. This behavior suggests that the CPC performance improvement results from the increased refractive index ($n_{toluene} = 1.5$ vs. $n_{air} = 1$) as opposed to the introduction of luminescence. Given the concentration factor relationship in equation (1), as derived from Snell's law, we see that concentration factor is directly dependent on refractive index. When comparing performance of the empty CPC (black dotted line) with the CPC + OD = 0 (i.e., pure toluene, red solid line) we see a recovery of the refractive index term, where the empty CPC performance is amplified by approximately $n_{toluene}^2$.

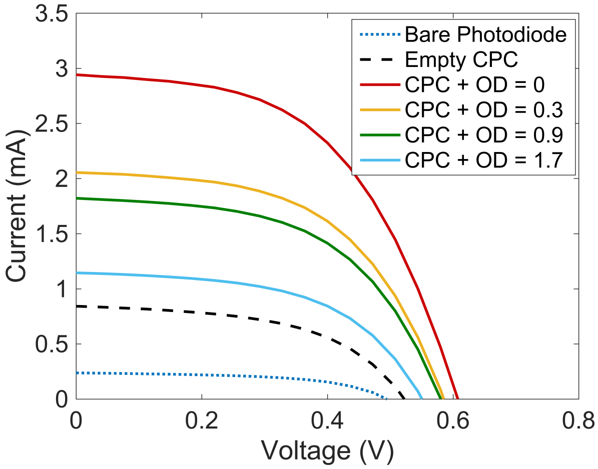

Figure 56: Hybrid CPC-Luminescent Concentrator Performance
Current-Voltage (IV) measurements of a fabricated hybrid CPC-Luminescent concentrator across varied optical density luminescent solutions.

Since the same quantum dot solution is used for this system, we again use a 450nm blue laser to assess performance under varied angle of incidence. As with the results under direct illumination (Figure 56), we find that luminescence worsens performance across all angles of incidence. The results of these measurements and the IV curves in Figure 56 indicate that the introduction of luminophore quantum dots in the toluene solution worsens overall performance. This demonstrates that the quantum dots act as scatterers within the system, thereby scattering photons, which would otherwise be redirected to the cell, out of the concentrating system. This phenomenon suggests that the CPC, which is known as the gold standard of geometric concentrators, as discussed in Section

7.1, is already optimized for concentrating performance and the introduction of additional components only diminishes its performance.

7.4. Discussion of Hybrid Performance for Varied Geometric Concentrator Systems

As shown in Section 7.2, hybrid hemispherical-luminescent concentrators experience a slight performance boost, in comparison to the bare hemispherical concentrator, for modest OD solutions. However, the hybrid CPC-luminescent concentrator displays reduced performance as soon as luminescence is introduced. The difference between these two responses lies in both *i)* the placement of the PV cell in the overall system design and *ii)* the selection of the geometric component.

To begin, the design for each system involves a different placement of the PV device. In the hemispherical system, the PV cell is placed inverted, at the top of the hemisphere, whereas for the CPC system, the device is upright at the bottom. By inverting the cell in the hemisphere system, the cell does not benefit from any direct illumination, therefore only redirected photons, from either the geometric or luminescent component, will reach the device. As such, when photons are emitted upward via photoluminescence, they have a greater chance of interacting with the inverted cell since it is placed at the top. Further, for PL that is emitted in the remaining direction (e.g., downward or to the side), the geometric component redirects such luminesced photons towards the solar cell given its placement. Thus, by placing the device in such a fashion, the hemispherical system isolates the concentrating components and demonstrates that use of moderate luminescence can boost total concentration.

For the CPC system, the device is instead placed upright at the bottom, meaning that the device benefits from direct illumination [256] in addition to both concentrating mechanisms. When luminescence is introduced, incident photons are absorbed by the luminophores, as a function of OD and absorption spectra. Luminophore absorption reduces the amount of light that could otherwise directly illuminate the cell; a portion of this absorbed light is emitted upward, due to isotropic luminescence, into the escape cone, thus preventing this light from hitting the PV device. For higher OD solutions, this phenomenon increases due to more absorbed light. As such, by placing the PV cell on the device bottom and relying on both concentration and direct illumination, the introduction of additional concentration via luminescence is unable to outweigh the detriment of reduced direct illumination.

In addition to the placement of the PV cell, the geometry of the concentrator affects performance when luminescence is introduced. Specifically, the CPC is an optimized geometric concentrator, as discussed in Section 7.1, which essentially funnels incident photons to the bottom PV device. As a result, the quantum dot luminophores act as scatterers, thereby reducing the funneling effect and worsening overall performance [257], [258]. In contrast, the hemisphere design reflects photons towards the spherical center of curvature [14], where the PV device is located; thus, the introduction of isotropic luminophores can synergistically redirect photons and enhance performance. By comparing these two geometries, we see that performance of a hybrid geometric-luminescent concentrator is dependent on the selected geometric component.

7.5. Conclusion

We fabricate two hybrid geometric-luminescent concentrators, each leveraging either a reflective hemisphere or a CPC as the geometric component. The designed systems consist of a hollow, reflective geometric component—either the hemisphere or CPC—which is then filled with a luminescent quantum dot-toluene solution. On its own, geometric concentration suffers from high PV operating temperatures and a need for solar tracking, whereas luminescent concentration avoids both of these challenges, but has yet to achieve high power efficiencies. By integrating these concentrating mechanisms, we aim to understand if a hybridized system can synergistically improve overall PV performance. We find that performance for the hybrid hemispherical-luminescent concentrator benefits from moderate OD solutions under direct illumination, and that luminescence improves performance for angles of incidence greater than 50°. However, for the hybrid CPC-luminescent concentrator, PV performance decreases when luminescence is introduced. The difference in the effects of luminescence for the two systems results from the placement of the PV device in each system, as well as the geometric component itself. In the hemisphere system, the inverted PV cell benefits from isotropic luminescence for moderate OD; whereas in the CPC system, luminophores act as scatterers and reduce direct illumination of the upright PV cell, thereby worsening performance. Future investigations could study the optimal geometric design for a hybrid system, as well as the potential effects of an ideal (e.g., unity PLQY) luminescent solution.

CHAPTER 8: CONCLUSION & OUTLOOK

8.1. Summary

In this thesis, we demonstrate how luminescent solar concentrators (LSCs) present a promising emerging photovoltaic technology. We begin by providing the necessary background and motivation for LSCs and discussing the photovoltaic (PV) considerations needed for a high performance luminescent concentrator system. By exploring parametrization of each LSC component—microcell form factor, luminophore species, and light trapping—on PV performance, we determine that photons are not collected homogenously in an LSC waveguide. We find the ideal configuration, in terms of PV efficiency, to be microcells placed coplanar with the waveguide, luminophores with photoluminescence peaks that match the PV bandedge, and highly reflective PL trapping. We next design and fabricate the first ever silicon heterojunction microcell for use case in such an LSC. In doing so, we achieve the highest Si microcell V_{OC} to date (588mV for a 400μm x 400μm device) and outline a roadmap for highetend performance given edge passivation.

Throughout this thesis, we further illustrate the versatility of LSCs and their candidacy across three use cases: building integrated PV, space-based solar, and utility PV. The tunability associated with LSCs—transparency, color, efficiency—make them advantageous for BIPV applications, which boast both power and aesthetic requirements. Specifically, we calculate that an optimized LSC window could achieve power efficiencies up to 7% under direct illumination. We next investigate the potential for LSCs as space-based PV candidates, given their flexibility and lightweight design. An ultra-thin LSC design could enable specific powers that are over 100x that of the currently employed commercial space PV, at a cost (0.24 $/W) that is competitive with conventional c-Si devices.

We finally explore possibilities for LSC integration with conventional PV technology, including Si wafers and geometric concentrators, for proposed utility applications. The first ever outdoor testing of a tandem-on-Si LSC demonstrates the ability for LSCs to maintain performance across diffuse lighting. Moreover, hybridization of multiple concentrator technologies suggests that the addition of luminescence may help boost performance for certain geometric concentrator designs. Throughout this thesis we have identified potential areas for improvement in LSC design and end use. In the next sections, we investigate four future directions for LSC research: *i)* improved photoluminescent trapping via optimized luminophores and anisotropic emission; *ii)* electrochromic-LSC integration for next-generation windows; *iii)* next steps for space-based LSCs; and *iv)* directing PL out of the waveguide towards an external PV source.

8.2. Amplified Photoluminescence: Optimized Luminophores and Anisotropic Emission

Throughout this thesis, we demonstrate the influence of luminophore parameters—photoluminescence (PL) quantum yield (QY), full-width at half-max (FWHM), Stokes shift, etc.—on maximizing photoluminescence output and overall LSC system performance. As shown in Hanifi et al., near perfect luminophores have been achieved for CdSe/CdS quantum dots—PLQY = 99.6% ± 0.2%, FWHM = 28—32nm, Stokes ratio ≈ 100, Stokes shift ≈ 0.53eV [76]—however other luminophore systems have yet to achieve such optimizations. As discussed in Chapter 2, the luminophore PL peak must match the PV bandedge in order to optimize performance. This implies that the optimized CdSe/CdS dots, which luminesce around 635nm, only match certain PV collectors and applications, such as the InGaP cells for the tandem-on-Si module discussed in Chapter 6. In order to expand LSC performance for different PV systems (e.g., Si or GaAs), additional luminophores with PL spectra that match these PV systems, such as the CuInS or InAs quantum dots discussed in this thesis, must also be optimized. Currently, CuInS dots have very large FWHM (115nm) and low Stokes ratios [156], [259], [260], while InAs quantum dots have not been able to achieve high PLQY (up to ~60%), have large FWHM (75nm) and also lag in stokes ratio[53]. By optimizing these other luminophore species, LSCs could potentially achieve high performance across all three application areas—utility, BIPV, and space-based.

In addition to optimized luminophores, which result in reduced parasitic loss and PV thermalization, anisotropic emission will enable enhanced PL trapping within the LSC waveguide. As discussed in Bauser et al., by placing quantum dots in a photonic crystal waveguide (PCWG), we can incite anisotropic emission in the desired direction. As shown in Figure 57b and c, respectively, isotropic emission results in PL leaking in all directions, whereas anisotropic emission, resulting from a PCWG, enables trapped PL within the z-plane. Moreover, the Purcell enhancement associated with PCWGs results in heightened PLQY for the respective quantum dots (Figure 57a). This suggests that the unoptimized quantum dots discussed above could display performance improvements, in terms of PLQY, even given their current metrics.

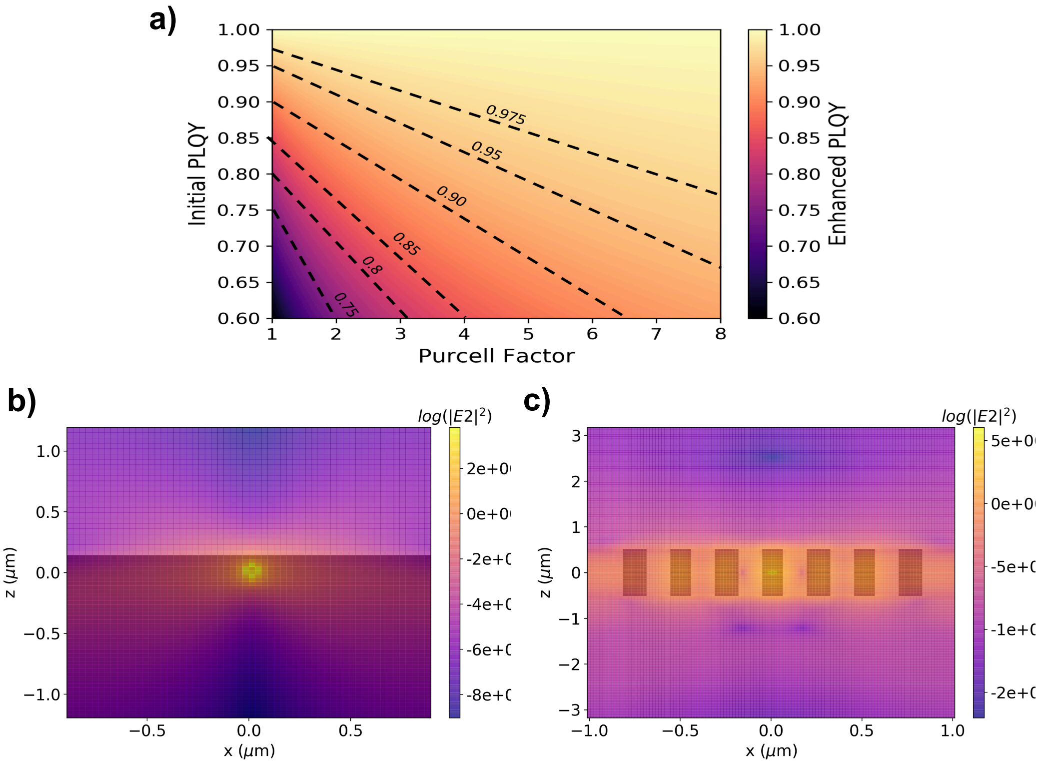

Figure 57: Anisotropic emission effects on PLQY and PL trapping.
a) PLQY enhancements as a function of Purcell factor resulting from anisotropic emission. Light trapping mappings are shown for b) isotropic emission of a quantum dot and c) emission trapped into z-plane when quantum dots are placed in a photonic crystal waveguide, as shown in Bauser et al. [185]

8.3. Next-Generation BIPV: Electrochromic-LSC Integration

Another direction for future LSC research is in the power-generating window space, as discussed in Chapter 4. For a building integrated photovoltaic window to be successful, it must add additional value for the end user. One potential innovation for next-generation power-generating windows is a hybrid concept combining a dynamically transparent (e.g., electrochromic) insulated glass unit (IGU) with an LSC power-generating window. As shown in Figure 58a, an electrochromic window transmits visible and infrared radiation (light and heat) when configured in its off (clear) state. However, when switched to the on (dark) state, such windows reflect solar heat at the first glass surface (S1), thereby optimizing the daylighting and heating within a commercial building [261]–[268]. Given the ability to switch between tinted states, this technology is also known as an active window.

To date, most deployed active window technologies rely upon switching mechanisms driven by externally supplied power from the building's electric infrastructure [269]. The high labor-related installation cost for replacing traditional IGUs with externally-powered dynamic windows creates a limited market size, in which dynamic windows would only be practical in new building projects [93], [270]. However, retrofitting projects far outnumber those of new builds [271]. Figure 58a shows a 3D rendering of a dynamic, electrochromic double pane IGU coupled with transparent LSC BIPV technology in order to illustrate a self-powered tinting window [93], [263], [268], [270]. This standalone self-powered window unit would not incur any labor cost related to integration into the building electrical infrastructure. Figure 58b estimates the impact that self-powered dynamic window technology could have for U.S. high-rise CO_2 emissions if widely adopted. From this, we can expect a comparable decrease in CO_2 emissions resulting from widespread adoption of self-powered active windows as from on-site electricity generation by power-generating LSC windows (Figure 30b), owing to decreased HVAC use in buildings featuring self-powered dynamic window technology [272]. The above suggests BIPV window technology have untapped potential to transform energy use in high-rise commercial buildings.

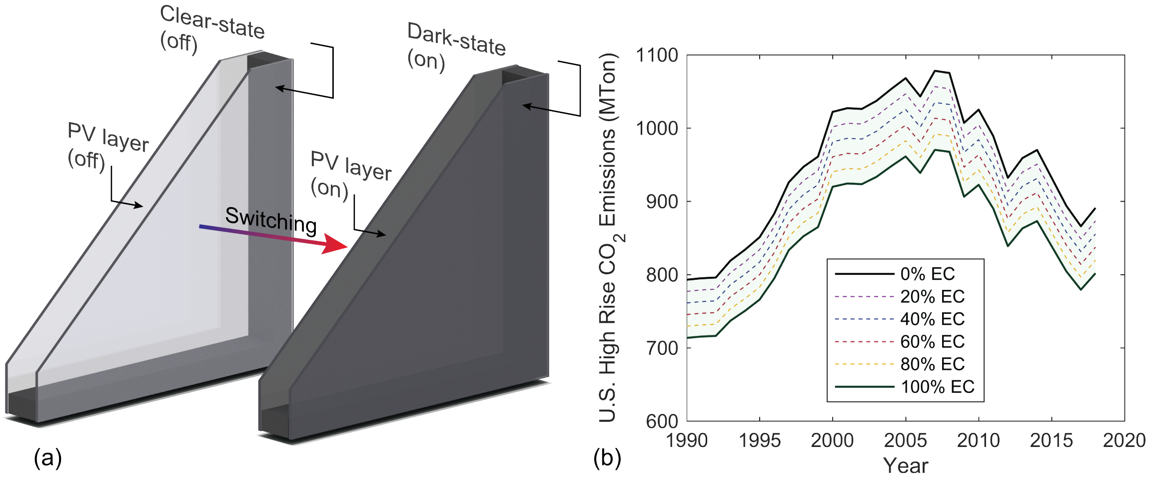

Figure 58. Electrochromic-LSC next-generation window design and impact.
(a) 3D rendering of a dynamic, double pane insulated glass unit (IGU) coupled with transparent BIPV window technology, conceptually illustrating the effect of self-powered switching from the off, clear state to the on, dark state. (b) An estimate for the amount of CO_2 emissions in megatons (MTon) resulting from U.S. high-rise buildings with respect to varying the total amount of BIPV-powered, dynamic IGU integration. Here we assume energy production of a BIPV module sufficient to operate the switching energy demands of the dynamic component, geographically set to a temperate, sunny climate comparable to Los Angeles, CA[26], [141]–[144].

8.4. A New Odyssey: LSCs in Outer Space

Next, we investigate the outlook of LSCs in space. In order for LSCs to be suitable for space-based solar power applications, we aim to reach specific powers greater than 10 kg/kW. We discuss in Chapter 5 why LSCs are potentially promising candidates for space-based solar, however this success hinges on the realization of such specific powers. High specific power is the result of two criteria: *i)* high efficiency and *ii)* low module weight. To achieve both, we require module thickness to be as thin, and therefore lightweight, as possible. To this point, we have demonstrated the successful fabrication of each ultrathin component—1.2μm PCWG and < 2μm polymer substrate—needed for the targeted design. However, integration of such components to realize a complete ultrathin module may present additional performance challenges that must first be addressed in order to achieve the necessary high efficiency component. As modules get thinner and waveguides approach subwavelength thicnknesses, behavior shifts from the ray tracing to the wave optical regime. As such, performance modeling must be able to account for any issues that may arise with subwavelength thick waveguides. Moreover, for an ultrathin waveguide, we are limited in the loading potential, and therefore optical density, of luminophores. High efficiencies for such a design require optical densities of at least 0.5 (measured at 450nm); a high enough density of luminophores must be integrated within the waveguide, without resulting in clumping, in order to achieve sufficient light absorption. While challenges still exist for ultrathin LSC integration, once addressed, LSCs could present a leading space-solar technology and unlock unmatched solar energy generation potential.

8.5. Moving Out: Directing PL to Escape the Waveguide

Finally, we propose a new goal for PL in LSCs: directing PL out of the waveguide as opposed to trapping the PL within the waveguide. While this design may seem contrary to traditional LSC designs, it could enable heightened performance and concentration at an external collector. To direct the PL, the luminescent waveguide could leverage anisotropic emission to push PL into the escape cone and towards the external photocollector, as shown in Figure 59, as opposed to directing PL towards an integrated PV device within the waveguide. Advantages of this design include potential scaling and ease of fabrication, as the interconnected microcell grid embedded within the waveguide would no longer be needed.

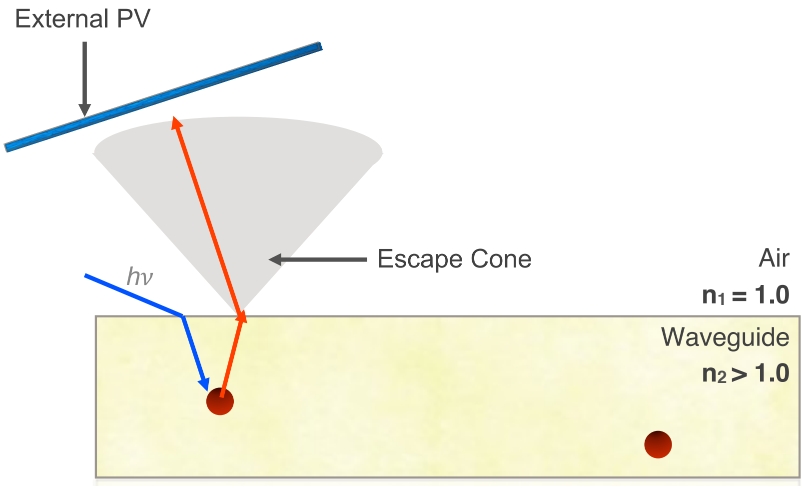

Figure 59: External LSC diagram.
Diagram demonstrating how luminophore PL (red line) could be directed into the escape cone of a luminescent waveguide, as determined by the waveguide index of refraction, and directed instead towards an external PV device (blue rectangle) for improved performance.

BIBLIOGRAPHY

[1] IPCC, *Global Warming of 1.5°C*. 2022.

[2] IEP, "Ecological Threat Register 2020," *Inst. Econ. Peace*, pp. 1–95, 2020.

[3] IPCC, "Climate Change 2014: Synthesis Report," 2014.

[4] NOAA, "Climate Change Impacts," 2021. [Online]. Available: https://www.noaa.gov/education/resource-collections/climate/climate-change-impacts.

[5] EPA, "How Climate Change May Impact Ozone Pollution and Public Health through the 21st Century," 2022. [Online]. Available: https://www.epa.gov/sciencematters/how-climate-change-may-impact-ozone-pollution-and-public-health-through-21st-century#:~:text=Higher levels of GHG emissions,other respiratory and cardiovascular conditions.

[6] S. Gorjian and H. Ebadi, *Photovoltaic Solar Energy Conversion*. Academic Press, 2020.

[7] C. Ferrie and K. Petrou, *Climate Change for Babies*. Sourcebooks eXplore, 2020.

[8] G. Velders, "Effect of greenhouse gas emissions on stratospheric ozone depletion," *PBL Netherlands Environmental Assessment Agency*. [Online]. Available: https://www.pbl.nl/en/publications/Effect_of_greenhouse_gas_emissions_on_stratospheric_ozone_depletion#:~:text=The depletion of the ozone,ozone layer through atmospheric interaction.

[9] EPA, "Global Greenhouse Gas Emissions Data," *United States Environmental Protection Agency*, 2022. [Online]. Available: https://www.epa.gov/ghgemissions/global-greenhouse-gas-emissions-data.

[10] H. Ritchie, "Sector by sector: where do global greenhouse gas emissions come from?," *Our World in Data*, 2020. [Online]. Available: https://ourworldindata.org/ghg-emissions-by-sector.

[11] C. Brahic, "World on track for worst-case warming scenario," *NewScientist*, 2014. [Online]. Available: https://www.newscientist.com/article/dn26243-world-on-track-for-worst-case-warming-scenario/.

[12] P. Phongsavan, "Energy on a Sphere," *NOAA*, 2015. .

[13] E. Pierce, "Top 6 Things You Didn't Know About Solar Energy," *Department of Energy*, 2016. [Online]. Available: https://www.energy.gov/articles/top-6-things-you-didnt-know-about-solar-energy.

[14] C. Kittel, *Introduction to solid state physics*. 1953.

[15] N. D. Mermin and N. Ashcroft, *Solid State Physics*. Saunders College Publishing, 1976.

[16] "How a Solar Cell Works," *ACS*, 2014. [Online]. Available: https://www.acs.org/content/acs/en/education/resources/highschool/chemmatters/past-issues/archive-2013-2014/how-a-solar-cell-works.html.

[17] "Solar Photovoltaic Cell Basics," *Office of Energy Efficiency & Renewable Energy*. [Online]. Available: https://www.energy.gov/eere/solar/solar-photovoltaic-cell-basics.

[18] S. Bowden and C. Honsberg, "PVEducation," 2022.

[19] BP, "BP Statistical Review of World Energy," 2019.

[20] G. Kavlak, J. McNerney, and J. E. Trancik, "Evaluating the causes of cost reduction in photovoltaic modules," *Energy Policy*, vol. 123, no. October, pp. 700–710, 2018.

[21] D. S. Philips and W. Warmuth, "Photovoltaics Report," 2019.

[22] NREL, "Best Research Cell Efficiencies," 2018.

[23] D. M. Powell, R. Fu, K. Horowitz, P. A. Basore, M. Woodhouse, and T. Buonassisi, "The capital intensity of photovoltaics manufacturing: Barrier to scale and opportunity for innovation," *Energy Environ. Sci.*, vol. 8, no. 12, pp. 3395–3408, 2015.

[24] H. Helmers *et al.*, "68.9% Efficient GaAs-Based Photonic Power Conversion Enabled by Photon Recycling and Optical Resonance," *Phys. Status Solidi - Rapid Res. Lett.*, vol. 15, no. 7, pp. 1–7, 2021.

[25] "GaAs Wafer | Gallium Arsenide vs Silicon," *Wafer World Incorporated*, 2018. .

[26] R. Fu *et al.*, "U.S. Solar Photovoltaic System Cost Benchmark: Q1 2018," *Natl. Renew. Energy Lab.*, vol. NREL/TP-6A, 2018.

[27] E. C. Boes, B. D. Shafer, and D. G. Schueler, "Economic motivation for photovoltaic concentrator technology," *Sol. Cells*, vol. 6, no. 1, pp. 3–15, 1982.

[28] A. Krothapalli and B. Greska, "Solar concentrators," *Handb. Clim. Chang. Mitig.*, vol. 3, no. June 2014, pp. 1263–1294, 2012.

[29] G. Smestad, H. Ries, R. Winston, and E. Yablonovitch, "The thermodynamic limits of light concentrators," *Sol. Energy Mater.*, vol. 21, no. 2–3, pp. 99–111, 1990.

[30] "Concentrating Solar Power: Clean Power on Demand 24/7," *The World Bank*, 2020. .

[31] C. A. Gueymard, "Fixed or tracking solar collectors? Helping the decision process with the Solar Resource Enhancement Factor," in *Proceedings of SPIE*, 2008, vol. 7046, no. September 2008, pp. 70460D1-11.

[32] "Concentrating Solar-Thermal Power," *Office of Energy Efficiency & Renewable Energy*. .

[33] M. G. Debije and P. P. C. Verbunt, "Thirty years of luminescent solar concentrator research: Solar energy for the built environment," *Adv. Energy Mater.*, vol. 2, no. 1, pp. 12–35, 2012.

[34] M. Phelan *et al.*, "Outdoor performance of a tandem InGaP/Si photovoltaic luminescent solar concentrator," *Sol. Energy Mater. Sol. Cells*, vol. 223, no. October 2020, p. 110945, 2021.

[35] B. Herteleer, J. Cappelle, and J. Driesen, "Quantifying low-light behaviour of photovoltaic modules by identifying their irradiance- dependent efficiency from data sheets," *27th Eur. Photovolt. Sol. Energy Conf.*, pp. 3714–3719, 2012.

[36] M. Donovan, B. Bourne, and J. Roche, "Efficiency vs. irradiance characterization of PV modules requires angle-of-incidence and spectral corrections," *Conf. Rec. IEEE Photovolt. Spec. Conf.*, pp. 2301–2305, 2010.

[37] J. L. Kafka and M. A. Miller, "A climatology of solar irradiance and its controls across the United States : Implications for solar panel orientation," vol. 135, pp. 897–907, 2019.

[38] W. Shockley and H. J. Queisser, "Detailed balance limit of efficiency of p-n junction solar cells," *J. Appl. Phys.*, vol. 32, no. 3, pp. 510–519, 1961.

[39] M. A. Green *et al.*, "Solar cell efficiency tables (version 50)," *Prog. Photovoltaics Res. Appl.*, vol. 25, no. 7, pp. 668–676, 2017.

[40] M. A. Green *et al.*, "Solar cell efficiency tables (Version 53)," *Prog. Photovoltaics Res. Appl.*, vol. 27, no. 1, 2019.

[41] J. S. Ward *et al.*, "Techno-economic analysis of three different substrate removal and reuse strategies for III-V solar cells," *Prog. Photovoltaics Res. Appl.*, vol. 24, pp. 1284–1292, 2016.

[42] P. S. C. Schulze *et al.*, "25.1% High-Efficiency Monolithic Perovskite Silicon Tandem Solar Cell with a High Bandgap Perovskite Absorber," *Sol. RRL*, vol. 4, no. 7, pp. 1–10, 2020.

[43] D. R. Needell *et al.*, "Design Criteria for Micro-optical Tandem Luminescent Solar Concentrators," *IEEE J. Photovoltaics*, vol. 8, no. 6, pp. 1560–1567, 2018.

[44] M. Carrascosa and S. Unamuno, "Monte Carlo simulation of the performance of PMMA luminescent solar collectors," *Appl. Opt.*, vol. 22, no. 20, pp. 3236–3241, 1983.

[45] M. G. Debije and V. A. Rajkumar, "Direct versus indirect illumination of a prototype luminescent solar concentrator," *Sol. Energy*, vol. 122, pp. 334–340, 2015.

[46] A. J. Chatten, K. W. J. Barnham, B. F. Buxton, N. J. Ekins-Daukes, and M. A. Malik, "A new approach to modelling quantum dot concentrators," *Sol. Energy Mater. Sol. Cells*, vol. 75, no. 3–4, pp. 363–371, 2003.

[47] V. Wittwer, W. Stahl, and A. Goetzberger, "Fluorescent planar concentrators," *Sol. Energy Mater.*, vol. 11, no. 3, pp. 187–197, 1984.

[48] E. Yablonovitch, "Thermodynamics of the Fluorescent Planar Concentrator," *J. Opt. Soc. Am.*, vol. 70, no. 11, pp. 1362–1363, 1980.

[49] D. K. G. de Boer, "Optimizing wavelength-selective filters for luminescent solar concentrators," *Sol. Energy*, vol. 7725, pp. 77250Q--77250Q--9, 2010.

[50] R. Connell, C. Pinnell, and V. E. Ferry, "Designing spectrally-selective mirrors for use in luminescent solar concentrators," *J. Opt. (United Kingdom)*, vol. 20, no. 2, 2018.

[51] N. D. Bronstein *et al.*, "Quantum Dot Luminescent Concentrator Cavity Exhibiting 30-fold Concentration," *ACS Photonics*, p. 150821134054007, 2015.

[52] D. R. Needell, C. R. Bukowsky, S. Darbe, H. Bauser, O. Ilic, and H. A. Atwater, "Spectrally Matched Quantum Dot Photoluminescence in GaAs-Si Tandem Luminescent Solar Concentrators," *IEEE J. Photovoltaics*, vol. 9, no. 2, pp. 397–401, 2019.

[53] M. J. Enright *et al.*, "Role of Atomic Structure on Exciton Dynamics and Photoluminescence in NIR Emissive InAs/InP/ZnSe Quantum Dots," *J. Phys. Chem. C*, vol. 126, no. 17, pp. 7576–7587, 2022.

[54] V. I. Klimov, T. A. Baker, J. Lim, K. A. Velizhanin, and H. McDaniel, "Quality Factor of Luminescent Solar Concentrators and Practical Concentration Limits Attainable with Semiconductor Quantum Dots," *ACS Photonics*, vol. 3, no. 6, pp. 1138–1148, 2016.

[55] F. Meinardi, F. Bruni, and S. Brovelli, "Luminescent solar concentrators for building-integrated photovoltaics," *Nat. Rev. Mater.*, vol. 2, pp. 1–9, 2017.

[56] F. Meinardi *et al.*, "Highly Efficient Luminescent Solar Concentrators based on Ultra-Earth-Abundant Indirect Band Gap Silicon Quantum Dots," *Nat. Photonics*, vol. 11, no. 3, pp. 177–185, 2017.

[57] H. Bauser *et al.*, "Amorphous Silicon Carbide High Contrast Gratings As Highly Efficient Spectrally Selective Visible Reflectors," *Opt. Express*, vol. 30, no. 15, pp. 26787–26793, 2022.

[58] D. R. Needell *et al.*, "Micro-optical Tandem Luminescent Solar Concentrator," in *Photovoltaic Specialist Conference (PVSC), 2017 IEEE 44th*, 2017.

[59] D. R. Needell *et al.*, "Ultralight Luminescent Solar Concentrators for Space Solar Power Systems," *Conf. Rec. IEEE Photovolt. Spec. Conf.*, pp. 2798–2801, 2019.

[60] D. R. Needell, M. E. Phelan, J. T. Hartlove, and H. A. Atwater, "Solar power windows : Connecting scientific advances to market signals," *Energy*, vol. 219, p. 119567, 2021.

[61] J. S. Batchelder, "The Luminescent Solar Concentrator." 1982.

[62] J. S. Batchelder, a H. Zewail, and T. Cole, "Luminescent solar concentrators . 1 : Theory of operation and techniques for performance evaluation," *Appl. Opt.*, vol. 18, no. 18, pp. 3090–3110, 1979.

[63] J. S. Batchelder, a H. Zewail, and T. Cole, "Luminescent solar concentrators. 2: Experimental and theoretical analysis of their possible efficiencies.," *Appl. Opt.*, vol. 20, no. 21, pp. 3733–3754, 1981.

[64] A. M. Hermann, "Luminescent Solar Concentrators -- A Review," *Sol. Energy*, vol. 29, no. 4, pp. 323–329, 1982.

[65] W. G. J. H. M. Van Sark, Z. Krumer, C. D. M. Donegá, and R. E. I. Schropp, "Luminescent Solar Concentrators : the route to 10 % efficiency," *IEEE J. Photovoltaics*, pp. 2276–2279, 2014.

[66] C. Tummeltshammer, A. Taylor, A. J. Kenyon, and I. Papakonstantinou, "Losses in luminescent solar concentrators unveiled," *Sol. Energy Mater. Sol. Cells*, vol. 144, 2016.

[67] L. H. Slooff *et al.*, "A Luminescent Solar Concentrator with 7.1% power conversion efficiency," *Phys. Status Solidi - Rapid Res. Lett.*, vol. 2, no. 6, pp. 257–259, 2008.

[68] G. Knier, "How do Photovoltaics Work?," *NASA Sci.*

[69] P. K. Nayak, S. Mahesh, H. J. Snaith, and D. Cahen, "Photovoltaic solar cell technologies: analysing the state of the art," *Nat. Rev. Mater.*, vol. 4, no. 4, pp. 269–285, 2019.

[70] A. B. Sproul, M. A. Green, and J. Zhao, "Improved value for the silicon intrinsic carrier concentration at 300 K," *Appl. Phys. Lett.*, vol. 57, no. 3, pp. 255–257, 1990.

[71] A. O. M. Maka and T. S. O'Donovan, "Effect of thermal load on performance parameters of solar concentrating photovoltaic: High-efficiency solar cells," *Energy Built Environ.*, vol. 3, no. 2, pp. 201–209, 2022.

[72] T. J. Silverman, M. G. Deceglie, B. Marion, S. Cowley, B. Kayes, and S. R. Kurtz, "Outdoor performance of a thin-film gallium-arsenide photovoltaic module," *IEEE 39th Photovolt. Spec. Conf.*, pp. 103–108, 2013.

[73] P. Santhanam, D. J. Gray, and R. J. Ram, "Thermoelectrically pumped light-emitting diodes operating above unity efficiency," *Phys. Rev. Lett.*, vol. 108, no. 9, pp. 1–5, 2012.

[74] V. A. Rajkumar, C. Weijers, and M. G. Debije, "Distribution of absorbed heat in luminescent solar concentrator lightguides and effect on temperatures of mounted photovoltaic cells," *Renew. Energy*, vol. 80, pp. 308–315, 2015.

[75] S. Haviv *et al.*, "Luminescent Solar Power - PV/Thermal Hybrid Electricity Generation for Cost-Effective Dispatchable Solar Energy," *ACS Appl. Mater. Interfaces*, vol. 12, no. 32, pp. 36040–36045, 2020.

[76] D. A. Hanifi *et al.*, "Redefining near-unity luminescence in quantum dots with photothermal threshold quantum yield," *Science (80-.).*, vol. 1202, no. March, pp. 1199–1202, 2019.

[77] N. D. Bronstein *et al.*, "Quantum Dot Luminescent Concentrator Cavity Exhibiting 30-fold Concentration - SI," *ACS Photonics*, vol. 2, no. 11, pp. 1576–1583, 2015.

[78] M. A. Green, *Thermal Behavior of Photovoltaic Devices*. 2017.

[79] M. A. Green, *Solar cells: Operating principles, technology, and system applications*. 1982.

[80] E. E. Gdoutos *et al.*, “A lightweight tile structure integrating photovoltaic conversion and RF power transfer for space solar power applications,” *AIAA Spacecr. Struct. Conf. 2018*, no. 210019, pp. 1–12, 2018.

[81] Y. Chen *et al.*, “‘ Giant ’ Multishell CdSe Nanocrystal Quantum Dots with Suppressed Blinking ‘ Giant ’ Multishell CdSe Nanocrystal Quantum Dots with Suppressed Blinking,” *J. Am. Chem. Soc.*, vol. 130, no. 15, pp. 5026–5027, 2008.

[82] K. Wu, H. Li, and V. I. Klimov, “Tandem luminescent solar concentrators based on engineered quantum dots,” *Nat. Photonics*, vol. 12, no. February, pp. 1–6, 2018.

[83] A. Carlson, A. M. Bowen, Y. Huang, R. G. Nuzzo, and J. A. Rogers, “Transfer printing techniques for materials assembly and micro/nanodevice fabrication,” *Adv. Mater.*, vol. 24, no. 39, pp. 5284–5318, 2012.

[84] J. Yoon *et al.*, “Flexible concentrator photovoltaics based on microscale silicon solar cells embedded in luminescent waveguides,” *Nat. Commun.*, vol. 2, no. 1, 2011.

[85] J. Yoon *et al.*, “Ultrathin silicon solar microcells for semitransparent, mechanically flexible and microconcentrator module designs,” *Nat. Mater.*, vol. 7, no. 11, pp. 907–915, 2008.

[86] M. A. Meitl *et al.*, “Transfer printing by kinetic control of adhesion to an elastomeric stamp,” *Nat. Mater.*, vol. 5, no. 1, pp. 33–38, Jan. 2006.

[87] T.-H. Kim *et al.*, “Kinetically controlled, adhesiveless transfer printing using microstructured stamps,” *Appl. Phys. Lett.*, vol. 94, no. 11, p. 113502, Mar. 2009.

[88] B. Furman *et al.*, “A high concentration photovoltaic module utilizing micro-transfer printing and surface mount technology,” in *2010 35th IEEE Photovoltaic Specialists Conference*, 2010, pp. 000475–000480.

[89] X. Feng, M. A. Meitl, A. M. Bowen, Y. Huang, R. G. Nuzzo, and J. A. Rogers, “Competing Fracture in Kinetically Controlled Transfer Printing,” *Langmuir*, vol. 23, no. 25, pp. 12555–12560, Dec. 2007.

[90] J. Bomm *et al.*, “Fabrication and spectroscopic studies on highly luminescent CdSe/CdS nanorod polymer composites,” *Beilstein J. Nanotechnol.*, vol. 1, no. 1, pp. 94–100, 2010.

[91] M. S. Chowdhury *et al.*, “An overview of solar photovoltaic panels’ end-of-life material recycling,” *Energy Strateg. Rev.*, vol. 27, 2020.

[92] N. M. HAEGEL *et al.*, “Terawatt-scale photovoltaics: Trajectories and challenges,” *Science*, 2017. .

[93] M. M. Potter *et al.*, “Autonomous Light Management in Flexible Photoelectrochromic Films Integrating High Performance Silicon Solar Microcells,” *ACS Appl. Energy Mater.*, vol. 3, no. 2, pp. 1540–1551, 2020.

[94] Y. Yao, E. Brueckner, L. Li, and R. Nuzzo, “Fabrication and assembly of ultrathin high-efficiency silicon solar microcells integrating electrical passivation and anti-reflection coatings,” *Energy Environ. Sci.*, vol. 6, no. 10, pp. 3071–3079, 2013.

[95] M. A. Yoder, Y. Yao, J. He, and R. G. Nuzzo, “Optimization of Photon and Electron Collection Efficiencies in Silicon Solar Microcells for Use in Concentration-Based Photovoltaic Systems,” *Adv. Mater. Technol.*, vol. 1700169, no. 2, pp. 1–9, 2017.

[96] N. D. Bronstein *et al.*, “Luminescent solar concentration with semiconductor nanorods and transfer-printed micro-silicon solar cells,” *ACS Nano*, vol. 8, no. 1, pp. 44–53, 2014.

[97] Y. Song, D. Mukasa, H. Zhang, and W. Gao, “Self-Powered Wearable Biosensors,” *Accounts Mater. Res.*, vol. 2, no. 3, pp. 184–197, 2021.

[98] S. Gupta, W. T. Navaraj, L. Lorenzelli, and R. Dahiya, “Ultra-thin chips for high-performance flexible electronics,” *npj Flex. Electron.*, vol. 2, no. 1, 2018.

[99] C. J. Traverse, R. Pandey, M. C. Barr, and R. R. Lunt, “Emergence of highly transparent photovoltaics for distributed applications,” *Nat. Energy*, vol. 2, no. November, pp. 1–12, 2017.

[100] Y. Chen *et al.*, “Energy-Autonomous Wireless Communication for Millimeter-Scale Internet-of-Things Sensor Nodes,” *IEEE J. Sel. Areas Commun.*, vol. 34, no. 12, pp. 3962–3977, 2016.

[101] H. C. Lee and K. H. Ke, “Monitoring of Large-Area IoT Sensors Using a LoRa Wireless Mesh Network System: Design and Evaluation,” *IEEE Trans. Instrum. Meas.*, vol. 67, no. 9, pp. 2177–2187, 2018.

[102] J. L. Gonzalez, A. Rubio, and F. Moll, “Human Powered Piezoelectric Batteries to Supply Power to Wearable Electronic,” *Int. J. Soc. Mater. Eng. Resour.*, vol. 10, no. 1, pp. 34–40, 2002.

[103] D. H. Kim and J. A. Rogers, “Stretchable electronics: Materials strategies and devices,” *Adv. Mater.*, vol. 20, no. 24, pp. 4887–4892, 2008.

[104] R. A. Lawes, “Manufacturing costs for microsystems/MEMS using high aspect ratio microfabrication techniques,” *Microsyst. Technol.*, vol. 13, no. 1, pp. 85–95, 2007.

[105] J. W. Judy, “Microelectromechanical systems (MEMS): Fabrication, design and applications,” *Smart Mater. Struct.*, vol. 10, no. 6, pp. 1115–1134, 2001.

[106] C. Battaglia, A. Cuevas, and S. De Wolf, “High-efficiency crystalline silicon solar cells: Status and perspectives,” *Energy Environ. Sci.*, vol. 9, no. 5, pp. 1552–1576, 2016.

[107] A. Goodrich *et al.*, “A wafer-based monocrystalline silicon photovoltaics road map: Utilizing known technology improvement opportunities for further reductions in manufacturing costs,” *Sol. Energy Mater. Sol. Cells*, vol. 114, pp. 110–135, 2013.

[108] A. Augusto, K. Tyler, S. Y. Herasimenka, and S. G. Bowden, “Flexible Modules Using <70 μm Thick Silicon Solar Cells,” *Energy Procedia*, vol. 92, pp. 493–499, 2016.

[109] K. Masuko *et al.*, “Achievement of More Than 25% Conversion Efficiency With Crystalline Silicon Heterojunction Solar Cell,” *IEEE J. Photovoltaics*, vol. 4, no. 6, pp. 1433–1435, 2014.

[110] Y. Tsunomura *et al.*, “Twenty-two percent efficiency HIT solar cell,” *Sol. Energy Mater. Sol. Cells*, vol. 93, no. 6–7, pp. 670–673, 2009.

[111] A. Augusto, P. Balaji, J. Karas, and S. G. Bowden, “Impact of substrate thickness on the surface passivation in high performance n-type solar cells,” *2018 IEEE 7th World Conf. Photovolt. Energy Conversion, WCPEC 2018 - A Jt. Conf. 45th IEEE PVSC, 28th PVSEC 34th EU PVSEC*, pp. 2792–2794, 2018.

[112] M. Edwards, S. Bowden, U. Das, and M. Burrows, “Effect of texturing and surface preparation on lifetime and cell performance in heterojunction silicon solar cells,” *Sol. Energy Mater. Sol. Cells*, vol. 92, no. 11, pp. 1373–1377, 2008.

[113] A. Augusto, J. Karas, P. Balaji, S. G. Bowden, and R. R. King, “Exploring the practical efficiency limit of silicon solar cells using thin solar-grade substrates,” *J. Mater. Chem. A*, vol. 8, no. 32, pp. 16599–16608, 2020.

[114] A. Augusto, S. Y. Herasimenka, R. R. King, S. G. Bowden, and C. Honsberg, “Analysis of the recombination mechanisms of a silicon solar cell with low bandgap-voltage offset,” *J. Appl. Phys.*, vol. 121, no. 20, 2017.

[115] P. Balaji, W. J. Dauksher, S. G. Bowden, and A. Augusto, “Improving surface passivation on very thin substrates for high efficiency silicon heterojunction solar cells,” *Sol. Energy Mater. Sol. Cells*, vol. 216, no. July, pp. 4–11, 2020.

[116] A. Killam and S. Bowden, “Characterization of Modules and Arrays with Suns Voc,” pp. 2719–2722, 2018.

[117] D. Nilsson, S. Jensen, and A. Menon, “Fabrication of silicon molds for polymer optics,” *J. Micromechanics Microengineering*, vol. 13, no. 4, pp. 1–6, 2003.

[118] Y.-R. Wu, Y.-C.; Jhan, “3D TCAD Simulation for CMOS Nanoeletronic Devices,” Singapore: Springer Singapore, 2018, pp. 1–17.

[119] H. Fujiwara, T. Kaneko, and M. Kondo, “Application of hydrogenated amorphous silicon oxide layers to c-Si heterojunction solar cells,” *Appl. Phys. Lett.*, vol. 91, no. 13, pp. 1–4, 2007.

[120] G. Dingemans and W. M. M. Kessels, “ Status and prospects of Al 2 O 3 -based surface passivation schemes for silicon solar cells ,” *J. Vac. Sci. Technol. A Vacuum, Surfaces, Film.*, vol. 30, no. 4, p. 040802, 2012.

[121] L. C. Andreani, A. Bozzola, P. Kowalczewski, M. Liscidini, and L. Redorici, “Silicon solar cells: Toward the efficiency limits,” *Adv. Phys. X*, vol. 4, no. 1, 2019.

[122] T. Tiedje, E. Yablonovitch, G. D. Cody, and B. G. Brooks, “Limiting Efficiency of Silicon Solar Cells,” *IEEE Trans. Electron Devices*, vol. 31, no. 5, pp. 711–716, 1984.

[123] M. A. Green, “Self-consistent optical parameters of intrinsic silicon at 300 K including temperature coefficients,” *Sol. Energy Mater. Sol. Cells*, vol. 92, no. 11, pp. 1305–1310, 2008.

[124] M. A. Green and M. J. Keevers, “Optical properties of intrinsic silicon at 300 K,” *Prog. Photovoltaics Res. Appl.*, vol. 3, no. 3, pp. 189–192, 1995.

[125] W. D. Eades and R. M. Swanson, “Calculation of surface generation and recombination velocities at the Si-SiO2 interface,” *J. Appl. Phys.*, vol. 58, no. 11, pp. 4267–4276, 1985.

[126] J. G. Fossum, “Physical Operation of Back-Surface-Field Silicon Solar Cells,” *IEEE Trans. Electron Devices*, vol. ED-24, no. 4, pp. 322–325, 1977.

[127] P. Balaji, S. Bowden, and A. Augusto, “Studying edge losses in silicon heterojunction solar cells,” *Conf. Rec. IEEE Photovolt. Spec. Conf.*, vol. 2020-June, pp. 2203–2206, 2020.

[128] P. P. Altermatt *et al.*, “Spatially resolved analysis and minimization of resistive losses in high-efficiency Si solar cells,” *Prog. Photovoltaics Res. Appl.*, vol. 4, no. 6, pp. 399–414, 1996.

[129] R. A. Sinton *et al.*, “Large-area 21% efficient Si solar cells,” *Conf. Rec. IEEE Photovolt. Spec. Conf.*, pp. 157–161, 1993.

[130] A. Fell, J. Schön, M. Müller, N. Wöhrle, M. C. Schubert, and S. W. Glunz, “Modeling Edge Recombination in Silicon Solar Cells,” *IEEE J. Photovoltaics*, vol. 8, no. 2, pp. 428–434, 2018.

[131] K. M. Gad *et al.*, “Ultrathin titanium dioxide nanolayers by atomic layer deposition for surface passivation of crystalline silicon,” *IEEE J. Photovoltaics*, vol. 6, no. 3, pp. 649–653, 2016.

[132] Z. C. Holman *et al.*, “Current Losses at the Front of Silicon Heterojunction Solar Cells Zachary,” *IEEE J. Photovoltaics*, vol. 2, no. 1, pp. 7–15, 2012.

[133] N. Derhacobian, P. Fine, J. T. Walton, Y. K. Wong, C. S. Rossington, and P. N. Luke, "Determination of Surface Recombination Velocity and Bulk Lifetime in Detector Grade Silicon and Germanium Crystals," *IEEE Trans. Nucl. Sci.*, vol. 41, no. 4, pp. 1026–1030, 1994.

[134] R. Gogolin *et al.*, "Analysis of series resistance losses in a-Si:H/c-Si heterojunction solar cells," *IEEE J. Photovoltaics*, vol. 4, no. 5, pp. 1169–1176, 2014.

[135] R. Fu, D. Feldman, and R. Margolis, "U.S. Solar Photovoltaic System Cost Benchmark: Q1 2018," 2018.

[136] CTBUH, "The Skyscraper Center," *Council on Tall Buildings and Urban Habitat*, 2016. .

[137] "Charts – Data & Statistics," *IEA*, 2020. .

[138] IEA, "Tracking Buildings 2019," *IEA*, 2019. .

[139] J. Michaels, "A Look at the U.S. Commercial Building Stock: Results from EIA's 2012 Commercial Buildings Energy Consumption Survey (CBECS)," 2015.

[140] T. James, A. Goodrich, M. Woodhouse, R. Margolis, and S. Ong, "Building-Integrated Photovoltaics (BIPV) in the residential section: An analysis of installed rooftop prices," 2011.

[141] U. Energy Information Administration, "U.S. Energy-Related Carbon Dioxide Emissions, 2018," 2019.

[142] "Los Angeles Department of Water and Power Residential Rates," *LADWP*. .

[143] "Solar Energy & Solar Power in Los Angeles, CA," *Solar Energy Local*. .

[144] T. Abergel, B. Dean, and J. Dulac, "Towards a zero-emission, efficient, and resilient buildings and construction sector," 2017.

[145] T. E. Kuhn, C. Erban, M. Heinrich, J. Eisenlohr, F. Ensslen, and D. H. Neuhaus, "Review of Technological Design Options for Building Integrated Photovoltaics (BIPV)," *Energy Build.*, p. 110381, Sep. 2020.

[146] A. Prieto, U. Knaack, T. Auer, and T. Klein, "Solar coolfacades: Framework for the integration of solar cooling technologies in the building envelope," *Energy*, vol. 137, pp. 353–368, Oct. 2017.

[147] Q. Xue, R. Xia, C. J. Brabec, and H. L. Yip, "Recent advances in semi-transparent polymer and perovskite solar cells for power generating window applications," *Energy Environ. Sci.*, vol. 11, no. 7, pp. 1688–1709, 2018.

[148] A. K. Shukla, K. Sudhakar, and P. Baredar, "A comprehensive review on design of building integrated photovoltaic system," *Energy and Buildings*, vol. 128. Elsevier Ltd, pp. 99–110, Sep-2016.

[149] B. P. Jelle and C. Breivik, "State-of-the-art building integrated photovoltaics," *Energy Procedia*, vol. 20, no. 1876, pp. 68–77, 2012.

[150] M. Kryszak and L. W. Wang, "The value of aesthetics in the BIPV roof products segment: a multiperspective study under European market conditions," *Energy Sources, Part A Recover. Util. Environ. Eff.*, pp. 1–22, Aug. 2020.

[151] S. Attia, S. Bilir, T. Safy, C. Struck, R. Loonen, and F. Goia, "Current trends and future challenges in the performance assessment of adaptive façade systems," *Energy Build.*, vol. 179, pp. 165–182, Nov. 2018.

[152] M. Meir, "State-of-the-art and SWOT analysis of building integrated solar envelope systems," Nov. 2019.

[153] P. Macé *et al.*, "Development of BIPV Business Cases - Guide for stakeholders," 2020.

[154] K. S. Chen, J. F. Salinas, H. L. Yip, L. Huo, J. Hou, and A. K. Y. Jen, "Semi-transparent polymer solar cells with 6% PCE, 25% average visible transmittance

and a color rendering index close to 100 for power generating window applications," *Energy Environ. Sci.*, vol. 5, no. 11, pp. 9551–9557, 2012.

[155] J. W. Lim, D. J. Lee, and S. J. Yun, "Semi-Transparent Amorphous Silicon Solar Cells Using a Thin p-Si Layer and a Buffer Layer," *ECS Solid State Lett.*, vol. 2, no. 6, pp. Q47–Q49, Apr. 2013.

[156] M. R. Bergren, N. S. Makarov, K. Ramasamy, A. Jackson, R. Guglielmetti, and H. McDaniel, "High-Performance CuInS2 Quantum Dot Laminated Glass Luminescent Solar Concentrators for Windows," *ACS Energy Lett.*, vol. 3, no. 3, pp. 520–525, 2018.

[157] W. H. Weber and J. Lambe, "Luminescent greenhouse collector for solar radiation," *Appl. Opt.*, vol. 15, no. 10, pp. 3–4, 1976.

[158] a. Goetzberger and W. Greubel, "Applied Physics Solar Energy Conversion with Fluorescent Collectors," *Appl. Phys.*, vol. 14, pp. 123–139, 1977.

[159] F. Meinardi *et al.*, "Large-area luminescent solar concentrators based on /`Stokes-shift-engineered/' nanocrystals in a mass-polymerized PMMA matrix," *Nat Phot.*, vol. 8, no. 5, pp. 392–399, 2014.

[160] W. G. J. H. M. van Sark *et al.*, "Luminescent Solar Concentrators--a review of recent results.," *Opt. Express*, vol. 16, no. 26, pp. 21773–21792, 2008.

[161] V. I. Klimov, T. A. Baker, J. Lim, K. A. Velizhanin, and H. McDaniel, "Quality Factor of Luminescent Solar Concentrators and Practical Concentration Limits Attainable with Semiconductor Quantum Dots," *ACS Photonics*, vol. 3, no. 6, 2016.

[162] H. J. Song, B. G. Jeong, J. Lim, D. C. Lee, W. K. Bae, and V. I. Klimov, "Performance Limits of Luminescent Solar Concentrators Tested with Seed/Quantum-Well Quantum Dots in a Selective-Reflector-Based Optical Cavity," *Nano Lett.*, vol. 18, no. 1, pp. 395–404, 2018.

[163] M. Rafiee, S. Chandra, H. Ahmed, and S. J. McCormack, "An overview of various configurations of Luminescent Solar Concentrators for photovoltaic applications," *Opt. Mater. (Amst).*, vol. 91, no. March, pp. 212–227, 2019.

[164] B. Vishwanathan *et al.*, "A comparison of performance of flat and bent photovoltaic luminescent solar concentrators," *Sol. Energy*, vol. 112, 2015.

[165] R. Xie, K. Chen, X. Chen, and X. Peng, "InAs/InP/ZnSe core/shell/shell quantum dots as near-infrared emitters: Bright, narrow-band, non-cadmium containing, and biocompatible," *Nano Res.*, vol. 1, no. 6, pp. 457–464, 2008.

[166] V. Grigel, D. Dupont, K. De Nolf, Z. Hens, and M. D. Tessier, "InAs Colloidal Quantum Dots Synthesis via Aminopnictogen Precursor Chemistry," *J. Am. Chem. Soc.*, vol. 138, no. 41, pp. 13485–13488, 2016.

[167] H. Wijaya, D. Darwan, K. R. G. Lim, T. Wang, K. H. Khoo, and Z. K. Tan, "Large-Stokes-Shifted Infrared-Emitting InAs-In(Zn)P-ZnSe-ZnS Giant-Shell Quantum Dots by One-Pot Continuous-Injection Synthesis," *Chem. Mater.*, vol. 31, no. 6, pp. 2019–2026, 2019.

[168] J. Gutmann, H. Zappe, and J. C. Goldschmidt, "Predicting the performance of photonic luminescent solar concentrators," *IEEE J. Photovoltaics*, pp. 1864–1868, 2013.

[169] J. C. Goldschmidt *et al.*, "Increasing the efficiency of fluorescent concentrator systems," *Sol. Energy Mater. Sol. Cells*, vol. 93, no. 2, pp. 176–182, 2009.

[170] C. G. Grangqvist, *Materials science for solar energy conversion systems*, Vol. 1. Elsevier, 2013.

[171] D. J. Naczynski *et al.*, "Rare-earth-doped biological composites as in vivo shortwave infrared reporters," *Nat. Commun.*, vol. 4, no. 1, pp. 1–10, Jul. 2013.

[172] R. Wang, X. Li, L. Zhou, and F. Zhang, “Epitaxial Seeded Growth of Rare-Earth Nanocrystals with Efficient 800 nm Near-Infrared to 1525 nm Short-Wavelength Infrared Downconversion Photoluminescence for In Vivo Bioimaging,” *Angew. Chemie Int. Ed.*, vol. 53, no. 45, pp. 12086–12090, Nov. 2014.

[173] Y. Zhang *et al.*, “Ag 2S quantum dot: A bright and biocompatible fluorescent nanoprobe in the second near-infrared window,” *ACS Nano*, vol. 6, no. 5, pp. 3695–3702, May 2012.

[174] S. Hatami *et al.*, “Absolute photoluminescence quantum yields of IR26 and IR-emissive Cd1-xHgxTe and PbS quantum dots-method- and material-inherent challenges,” *Nanoscale*, vol. 7, no. 1, pp. 133–143, Jan. 2015.

[175] O. E. Semonin, J. C. Johnson, J. M. Luther, A. G. Midgett, A. J. Nozik, and M. C. Beard, “Absolute photoluminescence quantum yields of IR-26 Dye, PbS, and PbSe quantum dots,” *J. Phys. Chem. Lett.*, vol. 1, no. 16, pp. 2445–2450, Aug. 2010.

[176] K. Rurack and M. Spieles, “Fluorescence quantum yields of a series of red and near-infrared dyes emitting at 600-1000 nm,” *Anal. Chem.*, vol. 83, no. 4, pp. 1232–1242, Feb. 2011.

[177] V. Srivastava, V. Kamysbayev, L. Hong, E. Dunietz, R. F. Klie, and D. V. Talapin, “Colloidal Chemistry in Molten Salts: Synthesis of Luminescent In1- xGaxP and In1- xGaxAs Quantum Dots,” *J. Am. Chem. Soc.*, vol. 140, no. 38, pp. 12144–12151, Sep. 2018.

[178] L. K. Sagar *et al.*, “Single-Precursor Intermediate Shelling Enables Bright, Narrow Line Width InAs/InZnP-Based QD Emitters,” *Chem. Mater.*, vol. 32, no. 7, pp. 2919–2925, Apr. 2020.

[179] P. Reiss, M. Protière, and L. Li, “Core/Shell Semiconductor Nanocrystals,” *Small*, vol. 5, no. 2, pp. 154–168, Jan. 2009.

[180] D. Franke *et al.*, “Continuous injection synthesis of indium arsenide quantum dots emissive in the short-wavelength infrared,” *Nat. Commun.*, vol. 7, no. 1, pp. 1–9, Nov. 2016.

[181] A. Aharoni, T. Mokari, I. Popov, and U. Banin, “Synthesis of InAs/CdSe/ZnSe core/shell1/shell2 structures with bright and stable near-infrared fluorescence,” *J. Am. Chem. Soc.*, vol. 128, no. 1, pp. 257–264, Jan. 2006.

[182] O. T. Bruns *et al.*, “Next-generation in vivo optical imaging with short-wave infrared quantum dots,” *Nat. Biomed. Eng.*, vol. 1, no. 4, p. 56, Apr. 2017.

[183] M. J. Enright *et al.*, “Seeded Growth of Nanoscale Semiconductor Tetrapods: Generality and the Role of Cation Exchange,” *Chem. Mater.*, vol. 32, no. 11, pp. 4774–4784, Jun. 2020.

[184] J. L. Stein *et al.*, “Cation Exchange Induced Transformation of InP Magic-Sized Clusters,” *Chem. Mater.*, vol. 29, no. 18, pp. 7984–7992, Sep. 2017.

[185] H. C. Bauser *et al.*, “Photonic Crystal Waveguides for >90% Light Trapping Efficiency in Luminescent Solar Concentrators,” *ACS Photonics*, vol. 7, no. 8, pp. 2122–2131, 2020.

[186] Y. Li *et al.*, “Stoichiometry-Controlled InP-Based Quantum Dots: Synthesis, Photoluminescence, and Electroluminescence,” *J. Am. Chem. Soc.*, vol. 141, no. 16, pp. 6448–6452, Apr. 2019.

[187] F. Pietra *et al.*, “Ga for Zn Cation Exchange Allows for Highly Luminescent and Photostable InZnP-Based Quantum Dots,” *Chem. Mater.*, vol. 29, no. 12, pp. 5192–5199, Jun. 2017.

[188] S. Kim *et al.*, “Highly luminescent InP/GaP/ZnS nanocrystals and their application to white light-emitting diodes,” *J. Am. Chem. Soc.*, vol. 134, no. 8, pp. 3804–3809, Feb. 2012.

[189] Y. W. Cao and U. Banin, “Growth and properties of semiconductor core/shell nanocrystals with InAs cores,” *J. Am. Chem. Soc.*, vol. 122, no. 40, pp. 9692–9702, Oct. 2000.

[190] H. Wijaya *et al.*, “Efficient Near-Infrared Light-Emitting Diodes based on In(Zn)As–In(Zn)P–GaP–ZnS Quantum Dots,” *Adv. Funct. Mater.*, vol. 30, no. 4, p. 1906483, Jan. 2020.

[191] Z. Song *et al.*, “A technoeconomic analysis of perovskite solar module manufacturing with low-cost materials and techniques,” *Energy Environ. Sci.*, vol. 10, no. 6, pp. 1297–1305, 2017.

[192] A. Louwen, W. Van Sark, R. Schropp, and A. Faaij, “A cost roadmap for silicon heterojunction solar cells,” *Sol. Energy Mater. Sol. Cells*, vol. 147, pp. 295–314, 2016.

[193] K. Burrows and V. Fthenakis, “Glass needs for a growing photovoltaics industry,” *Sol. Energy Mater. Sol. Cells*, vol. 132, pp. 455–459, 2015.

[194] K. A. W. Horowitz, M. Woodhouse, H. Lee, and G. P. Smestad, “A bottom-up cost analysis of a high concentration PV module,” in *AIP Conference Proceedings*, 2015, vol. 1679.

[195] K. A. Horowitz, T. W. Remo, B. Smith, and A. J. Ptak, “A Techno-Economic Analysis and Cost Reduction Roadmap for III-V Solar Cells,” Golden, CO (United States), Nov. 2018.

[196] W. G. J. H. M. van Sark, E. A. Alsema, H. M. Junginger, H. H. C. de Moor, and G. J. Schaeffer, “Accuracy of Progress Ratios Determined From Experience Curves: The Case of Crystalline Silicon Photovoltaic Module Technology Development,” *Prog. Photovoltaics Res. Appl.*, vol. 16, pp. 441–453, 2008.

[197] G. F. Nemet, “Beyond the learning curve: factors influencing cost reductions in photovoltaics,” *Energy Policy*, vol. 34, no. 17, pp. 3218–3232, 2006.

[198] Z. J. Yu, J. V. Carpenter, and Z. C. Holman, “Techno-economic viability of silicon-based tandem photovoltaic modules in the United States,” *Nat. Energy*, vol. 3, no. 9, pp. 747–753, 2018.

[199] D. Wood, “Space-Based Solar Power,” *Department of Energy*, 2014. [Online]. Available: https://www.energy.gov/articles/space-based-solar-power.

[200] “Reference Air Mass 1.5 Spectra,” *NREL2*, 2022.

[201] “Space Solar Power Project,” *Caltech*, 2022. [Online]. Available: https://www.spacesolar.caltech.edu/timeline.

[202] P. E. Glaser, “Power from the sun: Its future,” *Science (80-.).*, vol. 162, no. 3856, pp. 857–861, 1968.

[203] “Satellite Power System (SPS) Concept Development and Evaluation Program Plan,” *Dep. Energy, NASA*, 1978.

[204] P. E. Glaser, O. E. Maynard, J. Mackovciak, and E. L. Ralph, “Feasibility Study of a Satellite Solar Power Station.,” *NASA Contract. Reports*, no. February, 1974.

[205] J. H. Gibbons, “Solar Power Satellites August 1981,” *US Congr.*, no. August, 1981.

[206] D. Ernst, “Beam it down, scotty: The regulatory framework for space-based solar power,” *Rev. Eur. Comp. Int. Environ. Law*, vol. 22, no. 3, pp. 354–365, 2013.

[207] J. C. Mankins and N. Kaya, “The First International Assessment of Space Solar Power: Opportunities, Issues and Potential Pathways Forward,” *Natl. Sp. Soc. Int. Acad. Astronaut.*, pp. 1–14, 2011.

[208] E. Rosenbaum and D. Russo, “China plans a solar power play in space that NASA abandoned decades ago,” 2022. [Online]. Available: https://www.cnbc.com/2019/03/15/china-plans-a-solar-power-play-in-space-that-nasa-abandoned-long-ago.html.

[209] “UK government commissions space solar power stations research,” *UK Space Agency*, 2020. [Online]. Available: https://www.gov.uk/government/news/uk-government-commissions-space-solar-power-stations-research.

[210] A. Jones, “China aims for space-based solar power test in LEO in 2028, GEO in 2030,” *SpaceNews*, 2022. [Online]. Available: https://spacenews.com/china-aims-for-space-based-solar-power-test-in-leo-in-2028-geo-in-2030/.

[211] M. Brown, “ARIANE 6 VS. SPACEX: HOW THE ROCKETS STACK UP,” *Inverse*, 2022. [Online]. Available: https://www.inverse.com/innovation/ariane-6-vs-spacex.

[212] “Capabilities & Services,” *SpaceX*, 2022. [Online]. Available: https://www.spacex.com/media/Capabilities&Services.pdf.

[213] A. Mann, “SpaceX now dominates rocket flight, bringing big benefits—and risks—to NASA,” *Science*, 2020. .

[214] M. Holladay, “Testing a Thirty-Year-Old Photovoltaic Module,” *Green Building Advisor*, 2010. [Online]. Available: https://www.greenbuildingadvisor.com/article/testing-a-thirty-year-old-photovoltaic-module.

[215] H. Matsumoto, “Space Solar Power Satellite/Station and the Politics,” *Int. Symp. Electromagn. Compat.*, pp. 37–39, 2009.

[216] T. Murphy, “Space-Based Solar Power,” *UCSD*, 2012. [Online]. Available: https://dothemath.ucsd.edu/2012/03/space-based-solar-power/.

[217] K. Doyle, “Elon Musk on SpaceX, Tesla, and Why Space Solar Power Must Die,” *Popular Mechanics*, 2012. [Online]. Available: https://www.popularmechanics.com/technology/a8101/elon-musk-on-spacex-tesla-and-why-space-solar-power-must-die-13386162/.

[218] P. Espinet-Gonzalez *et al.*, “Radiation Tolerant Nanowire Array Solar Cells,” *ACS Nano*, vol. 13, no. 11, pp. 12860–12869, 2019.

[219] R. M. France *et al.*, “Development of Lattice-Mismatched GaInAsP for Radiation Hardness,” *IEEE J. Photovoltaics*, vol. 10, no. 1, pp. 103–108, 2020.

[220] P. Espinet-Gonzalez *et al.*, “Nanowire Solar Cells: A New Radiation Hard PV Technology for Space Applications,” *IEEE J. Photovoltaics*, vol. 10, no. 2, pp. 502–507, 2020.

[221] S. I. Maximenko, M. P. Lumb, J. Moore, L. C. Hirst, M. K. Yakes, and P. P. Jenkins, “Thin GaAs Solar Cells for High Irradiation Levels,” *Conf. Rec. IEEE Photovolt. Spec. Conf.*, pp. 2814–2817, 2019.

[222] “Clear Colorless Polyimides,” *NexSolve*. [Online]. Available: https://nexolve.com/advanced-materials/clear-colorless-polyimides/.

[223] “SOA-2021,” *NASA*, 2021. .

[224] K. Reed and H. J. Willenberg, “Early commercial demonstration of space solar power using ultra-lightweight arrays,” *Acta Astronaut.*, vol. 65, no. 9–10, pp. 1250–1260, 2009.

[225] A. van Geelen, P. R. Hageman, G. J. Bauhuis, P. C. van Rijsingen, P. Schmidt, and L. J. Giling, “Epitaxial lift-off GaAs solar cell from a reusable GaAs substrate,” *Mater. Sci. Eng. B*, vol. 45, no. 1–3, pp. 162–171, 1997.

[226] T. If and W. Rose, “Paths to light trapping in thin film GaAs solar cells,” *Opt. Express*, vol. 26, no. 6, pp. a341–a351, 2018.

[227] S. Essig *et al.*, “Raising the one-sun conversion efficiency of III-V/Si solar cells to 32.8% for two junctions and 35.9% for three junctions,” *Nat. Energy*, vol. 2, no. 9, 2017.

[228] D. J. Resnick and J. Iwasa, “Nanoimprint lithography and a perspective on cost of ownership,” vol. 10810, no. May, p. 14, 2018.

[229] J. Kim, D. Inns, K. Fogel, and D. K. Sadana, “Surface texturing of single-crystalline silicon solar cells using low density SiO 2 films as an anisotropic etch mask,” *Sol. Energy Mater. Sol. Cells*, vol. 94, pp. 2091–2093, 2010.

[230] J. Grandidier *et al.*, “Solar cell efficiency enhancement via light trapping in printable resonant dielectric nanosphere arrays,” *Phys. Status Solidi Appl. Mater. Sci.*, vol. 210, no. 2, pp. 255–260, 2013.

[231] R. H. Fan *et al.*, “Broadband antireflection and light-trapping enhancement of plasmonic solar cells,” *Phys. Rev. B - Condens. Matter Mater. Phys.*, vol. 87, no. 19, pp. 1–7, 2013.

[232] J. N. Munday and H. A. Atwater, “Large integrated absorption enhancement in plasmonic solar cells by combining metallic gratings and antireflection coatings,” *Nano Lett.*, vol. 11, no. 6, pp. 2195–2201, 2011.

[233] V. E. Ferry, L. A. Sweatlock, D. Pacifici, and H. A. Atwater, “Plasmonic Nanostructure Design for Efficient Light Coupling into Solar Cells Vivian,” *Nano Lett.*, vol. 8, no. 12, pp. 4391–4397, 2008.

[234] S. W. Boettcher *et al.*, “Energy-conversion properties of vapor-liquid-solid-grown silicon wire-array photocathodes.,” *Science (80-.).*, vol. 327, no. 5962, pp. 185–7, 2010.

[235] M. D. Kelzenberg *et al.*, “Enhanced absorption and carrier collection in Si wire arrays for photovoltaic applications,” *Nat. Mater.*, vol. 9, no. 3, pp. 239–244, 2010.

[236] J. F. Geisz, M. A. Steiner, I. García, S. R. Kurtz, and D. J. Friedman, “Enhanced external radiative efficiency for 20.8% efficient single-junction GaInP solar cells,” *Appl. Phys. Lett.*, vol. 103, no. 4, 2013.

[237] C. Dagdeviren *et al.*, “Thin Film Receiver Materials for Deterministic Assembly by Transfer Printing,” *Chem. Mater.*, vol. 26, no. 11, pp. 3502–3507, 2014.

[238] R. Nuzzo, I. L. Us, E. Menard, and N. C. Us, “Optical Systems Fabricated By Printing-Based Assembly,” *US Pat.*, vol. 2, no. 12, 2015.

[239] D. L. Young *et al.*, “Low-cost plasma immersion ion implantation doping for Interdigitated back passivated contact (IBPC) solar cells,” *Sol. Energy Mater. Sol. Cells*, vol. 158, pp. 68–76, 2016.

[240] T. S. Parel, C. Pistolas, L. Danos, and T. Markvart, “Modelling and experimental analysis of the angular distribution of the emitted light from the edge of luminescent solar concentrators,” *Opt. Mater. (Amst).*, vol. 42, 2015.

[241] R. An *et al.*, “Photostability and Photodegradation Processes in Colloidal CsPbI3 Perovskite Quantum Dots,” *ACS Appl. Mater. Interfaces*, vol. 10, no. 45, pp. 39222–39227, 2018.

[242] T. Aubert *et al.*, “Bright and stable CdSe/CdS@SiO2nanoparticles suitable for long-term cell labeling,” *ACS Appl. Mater. Interfaces*, vol. 6, no. 14, pp. 11714–11723, 2014.

[243] E. F. Fernández, F. Almonacid, P. M. Rodrigo, and P. J. Pérez-Higueras, “CPV systems,” in *McEvoy’s Handbook of Photovoltaics: Fundamentals and Applications*, Elsevier Inc., 2018, pp. 931–985.

[244] D. Fleischman, K. T. Fountaine, C. R. Bukowsky, G. Tagliabue, L. A. Sweatlock, and H. A. Atwater, "High Spectral Resolution Plasmonic Color Filters with Subwavelength Dimensions," *ACS Photonics*, vol. 6, pp. 332–338, 2019.

[245] H. Y. Kim, D. E. Yoon, J. Jang, G. M. Choi, D. C. Lee, and B. S. Bae, "Quantum dot/siloxane composite film exceptionally stable against heat and moisture," *Dig. Tech. Pap. - SID Int. Symp.*, vol. 48, no. 1, pp. 452–454, 2017.

[246] Y. J. Choi, D. Hwang, H. Chung, D. Y. Kim, and D. Kim, "Controlling the spatial distribution of quantum dots in nanofiber for light-harvesting devices," *Npg Asia Mater.*, vol. 7, p. e202, Jul. 2015.

[247] O. Chen *et al.*, "Compact high-quality CdSe-CdS core-shell nanocrystals with narrow emission linewidths and suppressed blinking.," *Nat. Mater.*, vol. 12, no. 5, pp. 445–451, 2013.

[248] M. Fedkin and J. A. Dutton, "Utility Solar Power and Concentration," *Penn State University*, 2022. [Online]. Available: https://www.e-education.psu.edu/eme812/node/7.

[249] "History of Concentrated Solar Power (CSP)," *Aalborg CSP*, 2010. .

[250] S. P. Philipps, A. W. Bett, K. Horowitz, and S. Kurtz, "Current Status of Concentrator Photovoltaic (CPV) Technology," *Fraunhofer ISE NREL*, pp. 1–25, 2015.

[251] National Renewable Energy Laboratory, "PV FAQs: What's new in concentrating PV?," 2005.

[252] J. Gosens, A. Gilmanova, and J. Lilliestam, "Windows of opportunity for catching up in formative clean-tech sectors and the rise of China in concentrated solar power," *Cent. Clim. Energy Policy, Crawford Sch. Public Policy, Aust. Natl. Univ.*, 2021.

[253] M. Wiesenfarth, I. Anton, and A. W. Bett, "Challenges in the design of concentrator photovoltaic (CPV) modules to achieve highest efficiencies," *Appl. Phys. Rev.*, vol. 5, no. 4, 2018.

[254] A. J. Chatten *et al.*, "Luminescent and geometric concentrators for building integrated photovoltaics," *Conf. Rec. IEEE Photovolt. Spec. Conf.*, pp. 000852–000857, 2011.

[255] J. J. H. Videira, E. Bilotti, and A. J. Chatten, "Cylindrical array luminescent solar concentrators: performance boosts by geometric effects," *Opt. Express*, vol. 24, no. 14, p. A1188, 2016.

[256] J. Wong, D. Stadtherr, and A. Taleb-Bendiab, "CPC-type reflector designs for LED DRL and front turn signal lighting," *SAE Tech. Pap.*, vol. 115, pp. 225–232, 2006.

[257] N. Sarmah, B. S. Richards, and T. K. Mallick, "Design, development and indoor performance analysis of a low concentrating dielectric photovoltaic module," *Sol. Energy*, vol. 103, pp. 390–401, 2014.

[258] R. Xu, Y. Ma, M. Yan, C. Zhang, S. Xu, and R. Wang, "Effects of deformation of cylindrical compound parabolic concentrator (CPC) on concentration characteristics," *Sol. Energy*, vol. 176, no. September, pp. 73–86, 2018.

[259] A. R. M. Velarde *et al.*, "Optimizing the Aesthetics of High-Performance CuInS2/ZnS Quantum Dot Luminescent Solar Concentrator Windows," *ACS Appl. Energy Mater.*, vol. 3, no. 9, pp. 8159–8163, 2020.

[260] "Copper Indium Disulfide/Zinc Sulfide Quantum Dots Safety Data Sheet," *UbiQD*.

[261] A. Shehabi *et al.*, "U.S. energy savings potential from dynamic daylighting control glazings," *Energy Build.*, vol. 66, pp. 415–423, Nov. 2013.

[262] N. DeForest *et al.*, "United States energy and CO2 savings potential from deployment of near-infrared electrochromic window glazings," *Build. Environ.*, vol. 89, pp. 107–117, Jul. 2015.

[263] S. K. Deb, S. H. Lee, C. Edwin Tracy, J. Roland Pitts, B. A. Gregg, and H. M. Branz, "Stand-alone photovoltaic-powered electrochromic smart window," *Electrochim. Acta*, 2001.

[264] J. R. Platt, "Electroehromism, a possible change of color producible in dyes by an electric field," *J. Chem. Phys.*, vol. 34, no. 3, pp. 862–863, Mar. 1961.

[265] A. P. Schuster, D. Nguyen, and O. Caporaletti, "Solid state electrochromic infrared switchable windows," *Sol. Energy Mater.*, vol. 13, no. 2, pp. 153–160, Feb. 1986.

[266] M. Cui, J. Guo, H. Xie, Z. Wu, and S. Qiu, "All-solid-state complementary electrochromic windows based on the oxymethylene-linked polyoxyethylene complexed with LiClO4," *J. Appl. Polym. Sci.*, vol. 65, no. 9, pp. 1739–1744, Aug. 1997.

[267] Y. Wang, E. L. Runnerstrom, and D. J. Milliron, "Switchable Materials for Smart Windows," *Annu. Rev. Chem. Biomol. Eng.*, vol. 7, no. 1, pp. 283–304, 2016.

[268] N. C. Davy *et al.*, "Pairing of near-ultraviolet solar cells with electrochromic windows for smart management of the solar spectrum," *Nat. Energy*, vol. 2, no. 8, 2017.

[269] R. Baetens, B. P. Jelle, and A. Gustavsen, "Properties, requirements and possibilities of smart windows for dynamic daylight and solar energy control in buildings: A state-of-the-art review," *Solar Energy Materials and Solar Cells*, vol. 94, no. 2. North-Holland, pp. 87–105, Feb-2010.

[270] C. Bechinger *et al.*, "Low-voltage electrochromic device for photovoltaic-powered smart windows," *J. Appl. Phys.*, vol. 80, no. 2, pp. 1226–1232, 1996.

[271] "The Skyscraper Center," *Council on Tall Buildings and Urban Habitat*, 2020. .

[272] R. Pacheco, J. Ordóñez, and G. Martínez, "Energy efficient design of building: A review," *Renew. Sustain. Energy Rev.*, vol. 16, no. 6, pp. 3559–3573, 2012.

APPENDIX A: SI HETEROJUNCTION MICROCELLS FABRICATION METHODS

Silicon Heterojunction (SHJ) μ-cell Device Fabrication

SHJ solar microcells were fabricated from non-metallized macro-scale 6 in × 6 in SHJ devices from Arizona State University (ASU). The 6 in × 6 in SHJ devices [(100) orientation] were fractured along the <110> planes into smaller devices sized ca. 1.5 in × 1.5 in for subsequent processing.

DRIE and Laser Cutting: SiNx Deposition

The samples were initially coated with 360 nm of SiNx via plasma-enhanced chemical vapor deposition (PECVD) (Oxford Instruments, Plasmalab System 100) on the front and back as a protective and adhesion layer. The deposition was done at a pressure of 1800 mTorr, an RF power of 90 W with a pulse time of 12 s, an LF power of 90 W with a pulse time of 8 s, a temperature of 200°C, a 5% SiH_4 in Ar flow rate of 500 sccm, a NH_3 flow rate of 30 sccm, and an N_2 flow rate of 1300 sccm. A deposition time of 4 minutes resulted in a SiNx layer thickness of 360 nm, as measured by ellipsometry (J. A. Woolam Company, M-2000 with CompleteEASE control and analysis software).

Laser Cutting

After deposition of the protective SiNx coating, samples were sent to Micron Laser Technology (Hillsboro, Oregon) for cutting in the microcell array pattern at a cutting velocity of 1.3 mm/s, according to proprietary cutting parameters.

DRIE: SiNx and ITO Etching

The microcell array was patterned onto the SiNx with alignment to the <110> planes using standard photolithography (AZ 9260, AZ Electronic Materials, 10 μm Thick):

- Dehydration bake on hotplate at 110°C for 5 minutes
- HMDS vapor treatment at room temperature for 5 minutes
- Spin-coat AZ 9260 at 2400 rpm for 60 seconds
- Softbake at 110°C for 2 minutes and 45 seconds
- Expose to 1500 mJ/cm^2 at 405 nm (Suss MicroTec, MA6 and MA6/BA6)
- Develop in AZ 400K 1:4 (1 part developer, 4 parts water) for 4 minutes
- O_2 plasma treatment for 3 minutes (ca. 250 mTorr, 150 W, 6 sccm O_2) (PIE Scientific, Tergeo Plus)

The microcell array pattern was etched into the SiNx by submersion in buffered oxide etchant (BOE) 6:1 solution (Sigma-Aldrich or Transene) for ca. 90 s. Then, the μ-cell array pattern was etched into the ITO by submersion in a fresh 9 M HCl (J. T. Baker, Hydrochloric Acid, 36.5–38%) solution for 5–6 minutes.

ITO Etching and DRIE of Si

Subsequently, the photoresist was removed from the back side of the wafer only using acetone, and the Si was etched all the way through using deep reactive ion etching (DRIE) (Oxford Instruments, Plasmalab System 100). For the "fast" rate DRIE etching, the sample was adhered directly to a 6-inch–diameter sapphire carrier wafer using Fomblin oil prior to etching. The etch cycle was 17 s long with an SF_6 flow rate of 160 sccm, a valve position set to 31.5° (80 mTorr—90 mTorr), a coil power of 2500 W, and a platen power of 100 W. The deposition cycle was 11 s long and used a C_4F_8 flow rate of 90 sccm, a pressure of 30 mTorr, a coil power of 2150 W, and a platen power of 10 W. The etch temperature was -5°C, and 18–30 cycles etched through 80 μm of Si (etch rate roughly 3.2 μm/cycle). For the "slow" rate DRIE etching, the sample was adhered directly to a 6-inch-diameter silicon carrier wafer using Fomblin oil prior to etching. The etch cycle was 10 s with an SF_6 flow rate of 150 sccm, a pressure of 30 mTorr, a coil power of 1500 W, and a platen power of 40 W. The deposition cycle was 7 s long and used a C_4F_8 flow rate of 110 sccm, a pressure of 30 mTorr, a coil power of 1500 W, and a platen power of 10 W. The etch temperature was -5°C, and ca. 340 cycles etched through 80 μm of Si (etch rate roughly 0.25 μm/cycle). After completion of the DRIE etch, the carrier wafer + sample was rinsed in acetone and IPA to release the sample from the carrier wafer. Residual photoresist and Fomblin oil were removed from the sample by O_2 plasma cleaning (Plasma-Therm, SLR 720) on both sides of the sample for 15–20 minutes at room temperature and 20 mTorr, with an O_2 flow rate of 20 sccm, and a power of 80 W.

Damage Removal and Cleaning

After both DRIE and micro-laser cutting, sidewall damage was removed by first dipping in BOE 6:1 for 6 s to remove the native oxide from the devices sidewalls, followed by etching in 3 M KOH/2 M IPA (Macron Fine Chemicals, Potassium Hydroxide, Pellets) (Sigma Aldrich, 2-Propanol) solution in DI water at 60°C or 45 wt.% KOH (Sigma Aldrich) at 60°C. The samples were then cleaned using standard RCA cleaning procedures as shown below:

- *RCA-1 Clean:* Etch in RCA-1 solution ($H_2O:NH_3:H_2O_2 = 5:1:1$) at 70°C–80°C for 10 min
- *RCA-2 Clean:* Etch in RCA-2 solution ($H_2O:HCl:H_2O_2 = 5:1:1$) at 70°C–80°C for 10 min

Native oxide on the sidewalls was removed by a dip in BOE 6:1 for 6 s in before and after each cleaning step. After cleaning, the SiNx protective layer was removed from the front/back of samples by submersion in BOE 6:1 for 50 s–90 s. The "slow" rate DRIE samples were cleaned in RCA-1 only, and lacked a SiNx protective/adhesion layer due to poor selectivity inherent to DRIE etching recipe.

Passivation

Prior to passivation, the sample was submerged in BOE 6:1 for 6 s to remove the native oxide from the device sidewalls. The sample was then immediately transferred to the atomic layer deposition (ALD) or PECVD chamber (Ultratech, Simply ALD, Fiji G2) (Oxford Instruments, Plasmalab System 100) for deposition of passivation coatings. Deposition parameters for each film type were as follows:

- *PECVD a-Si, recipe 1:* temperature of 200°C, pressure of 800 mTorr, power of 10 W (30.3 mW/cm^2), 5% SiH_4 in Ar of 250 sccm, deposition time of 4 minutes.
- *PECVD a-Si, recipe 2:* temperature of 200°C, pressure of 400 mTorr, power of 10 W (30.3 mW/cm2), 5% SiH4 in Ar of 250 sccm, deposition time of 8 minutes.
- *PECVD SiNx:* temperature of 200°C, pressure of 1800 mTorr, an RF power of 90 W with a pulse time of 12 s, an LF power of 90 W with a pulse time of 8 s, a 5% SiH_4 in Ar flow rate of 500 sccm, a NH_3 flow rate of 30 sccm, and an N_2 flow rate of 1300 sccm.
- *ALD TiO_2:* temperature of 80°C, TTiP precursor with H_2O pulses, 104 total cycles for 1.5 nm total deposition (90 cycles for 1.3 nm, 69 cycles for 1 nm, and 49 cycles for 0.7 nm).

To remove PECVD films selectively from the top of the devices after passivation, a thick Si carrier wafer was first treated according to the following using standard photolithography (AZ 9260, AZ Electronic Materials, 10 μm Thick):

- Dehydration bake on hotplate at 110°C for 5 minutes
- HMDS vapor treatment at room temperature for 5 minutes
- Spin-coat AZ 9260 at 2400 rpm for 60 s

The samples with the devices suspended in the microcell array were then gently placed on top of the thick photoresist-coated carrier wafer, and the device-carrier assembly was softbaked at 110°C for an additional 2 minutes and 45 seconds. Then, the device-carrier assembly was re-patterned with photoresist (AZ 9260, AZ Electronic Materials, 10 μm Thick) (recipe as previously described) with alignment to previous patterning for the purpose of covering the device edges. The films on the top of the devices were then removed by inductively coupled plasma-reactive ion etching (ICP-RIE) (Oxford Instruments, Plasmalab System 100) using the following etching parameters: T = 20°C, C_4F_8 = 45 sccm, O_2 = 2 sccm, P = 7 mTorr, ICP generator power (AKA coil power) = 2100 W, RF power (AKA platen power) = 200 W.

Printing

To test the devices, the anchor bars were broken to release each device from the array using either a syringe needle or an appropriately-sized PDMS stamp. The devices were then placed atop a Cr/Au (10 nm/300 nm) interconnection deposited by e-beam (Kurt J. Lesker Company, Labline) on a transparent, double-sided, ITO-compatible tape from 3M (25 μm thick, 3M OCA 8146-1) on a standard glass substrate.

Solar μ-cell Characterization and Testing

RHEED

Reflection high-energy electron diffraction (RHEED) images were acquired with a STAIB Instruments RHEED 30 at 20 kV voltage and 1.5 A filament current. With the electron beam at a low incidence angle, the diffraction pattern depends on the crystal structure of the surface layers. When the beam is incident on an amorphous surface, no coherent diffraction occurs, and the electrons reach the detector in an incoherent cloud, as seen in Figure 26. [Single crystal surfaces appear as vertically oriented streaks, corresponding to the Ewald sphere that defines the coherent diffraction condition intersecting with the surface layer reciprocal lattice rods. Such defined streaks are clearly absent on the samples, confirming an amorphous structure.]

Suns-Voc

Suns-Voc (Sinton Instruments) measurements were taken on both bulk (unpatterned) SHJ wafers and SHJ microcells to measure the PV cell IV curve without the effects of series resistance. These measurements enabled comparison of microcell performance to that of the bulk unprocessed wafer.

Light JV

Current-Voltage measurements were taken under a calibrated AM1.5G (1000 W/m^2) solar simulator (ABET 2000, 1000W) using a voltage sweep of -0.5 V to 0.8 V, compliance = 1 mA.

Photocurrent Mapping

Light Beam Induced Current (LBIC) images were taken by raster scanning a 633 nm laser across the region of interest. The process was done using a confocal microscope (Zeiss Axio LSM 710) at 5× magnification.

Imaging

Confocal images were taken using a Zeiss Axio LSM 710 at magnifications ranging from 5×–20×. Scanning electron microscope (SEM) images were obtained using either of the following manufacturers/models: FEI (now ThermoFisher), Quanta 200F or FEI (now ThermoFisher), Nova 200 NanoLab.

Lifetime

To test the surface recombination velocity (SRV) of each passivation coating, we deposited each passivation material on the front and back of high-lifetime <110> wafers (Siltronix, (110) ± 0.5°). We then measured the lifetime of the passivated surface using a Lifetime Tool (Freiberg Instruments, MDPspot). SRV was then calculated using the following formula, where W = 450 µm:

$$\frac{1}{\tau_{eff}} = \frac{1}{\tau_{bulk}} + \frac{2 * SRV}{W}$$

Tables

ID	Thickness (µm)	Annealing	pVoc (V)	pFF
H10603-10	80	Before	0.743	0.830
		After	0.746	0.833
H10603-11	80	Before	0.740	0.822
		After	0.737	0.818
H10603-12	80	Before	0.744	0.829
		After	0.745	0.832

Table 12: pseudo-Voc and pseudo-FF of bulk wafer from ASU from Suns-Voc measurements from **Figure 62**.

Dicing	Etching	Description	# Wafers	# Devices	Jsc [mA/cm^2]	Voc [mV]	FF	Eff. [%]
DRIE	As-cut	Average	3	33	20.8 ± 1.1	533 ± 13	65.3 ± 2.8	7.2 ± 0.7
DRIE	13 min KOH	Average	11	114	22.5 ± 1.4	540 ± 13	62.7 ± 3.9	7.6 ± 0.7
DRIE	13 min KOH	Best	1	8	26.3 ± 3.8	560 ± 17	61.1 ± 4.1	8.9 ± 1.1
DRIE	13 min KOH	Best. Device 2	1	1	31.1	588	58.4	10.7
Laser	As-cut	Average	1	15	21.0 ± 0.5	385 ± 28	46.3 ± 3.8	3.7 ± 0.5
Laser	13 min KOH	Average	2	26	22.4 ± 0.7	531 ± 8	64.8 ± 2.2	7.7 ± 0.3
Laser	16 min KOH	Average	1	15	21.4 ± 0.6	541 ± 1	67.2 ± 1.4	7.8 ± 0.3
Laser	13 min KOH	Best, Device 1	1	1	20.3	546	65.1	7.5
Model	**-**		**-**	**-**	**29.5**	**609**	**79.0**	**14.2**

Table 13: 3 M KOH/2 M IPA sample performances of DRIE and laser cut-diced devices, from **Figure 24**e.

Processing		Before Anneal		After Anneal	
Coating	**Deposition**	**Lifetime [μs]**	**SRV [cm/s]**	**Lifetime [μs]**	**SRV [cm/s]**
TiO_2, 0.7 nm	ALD	204	110	144	156
TiO_2, 1 nm	ALD	403	56	354	64
TiO_2, 1.3 nm	ALD	257	88	270	83
TiO_2, 1.5 nm	ALD	363	62	342	66
a-Si 1	PECVD	249	90	167	135
a-Si 2	PECVD	104	216	768	29
Native Oxide	-	31.8	708	-	-

Table 14: Passivation characteristics of ALD and PECVD films before and after annealing on (110) substrates, 450 μm thickness.

Passivation	Etching	DRIE	# Devices	Jsc [mA/cm^2]	Voc [mV]	FF	Eff. [%]
Native Oxide	As-cut	Slow	3	25.0 ± 0.7	543 ± 6	63.6 ± 0.6	8.6 ± 0.3
a-Si/SiNx	As-cut	Slow	11	26.0 ± 0.9	561 ± 11	61.9 ± 4.1	9.0 ± 0.6
Native Oxide	6 min KOH	Slow	6	23.3 ± 2.0	530 ± 20	62.2 ± 1.2	7.7 ± 0.7
TiO_2 (1.5 nm)	6 min KOH	Slow	5	25.4 ± 1.6	554 ± 24	55.8 ± 1.5	7.8 ± 1.0

Table 15: Variance in 400x400 μm device performance depicted in **Figure 26**.

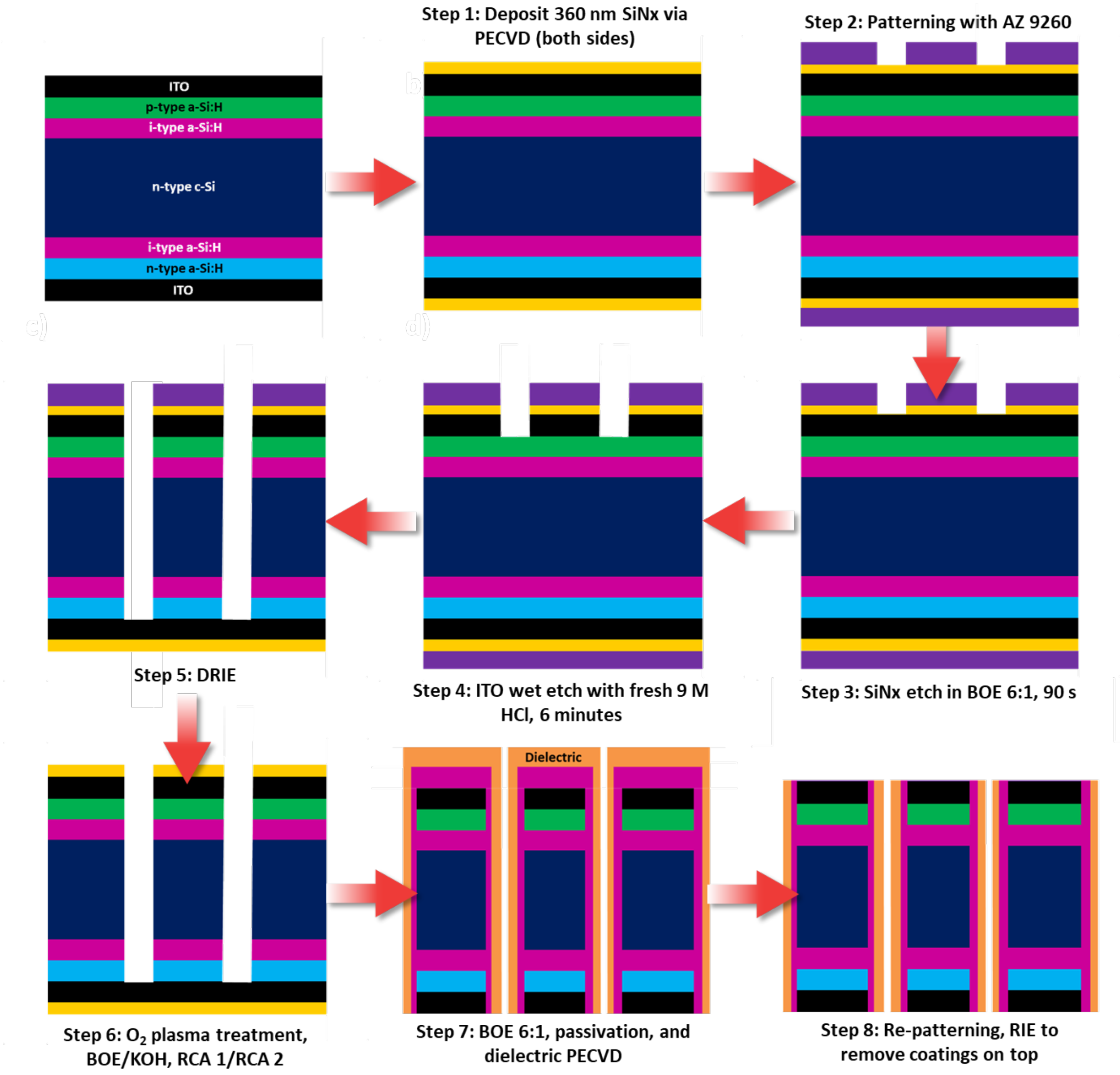

Figure 60: Processing flow for dicing, damage removal, and passivation of DRIE-fabricated SHJ microcells.

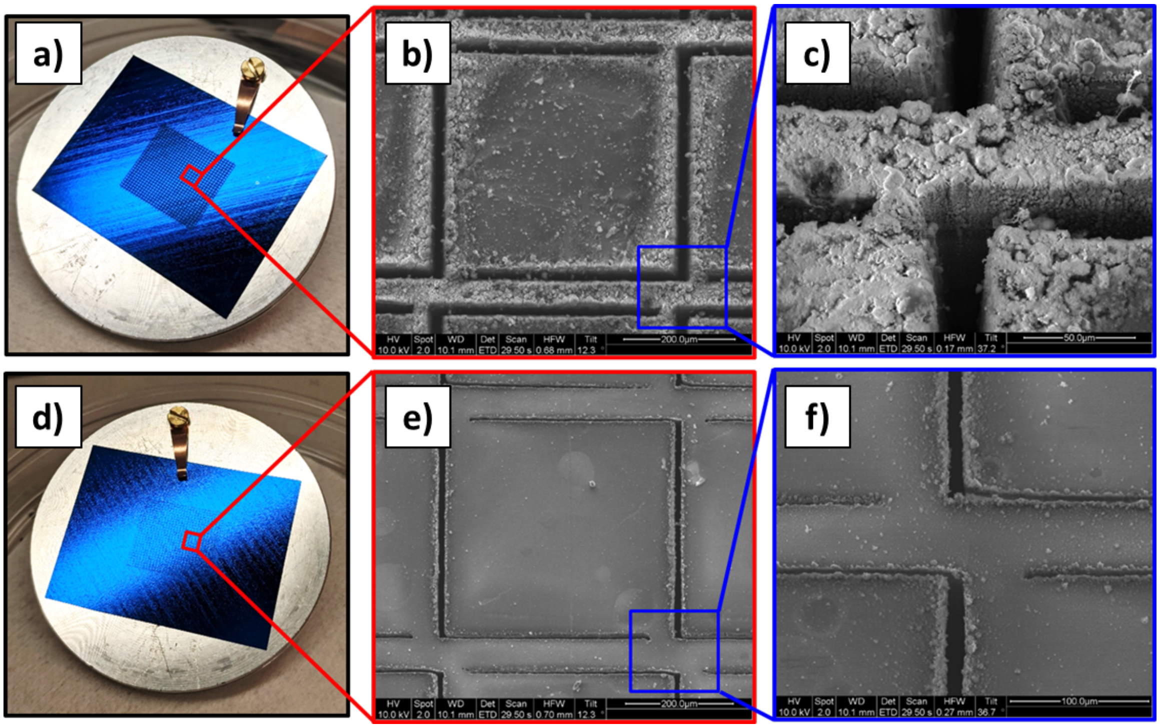

Figure 61: Residual sidewall powder on laser-cut SHJ microcells.
Laser cut samples, residual powder a) camera image of sample front after laser cutting; b) SEM image of microcell in array, sample front; c) SEM image of microcell anchor bars in array, sample front; d) camera image of sample back after laser cutting; e) SEM image of microcell in array, sample back; f) SEM image of microcell anchor bars in array, sample back.

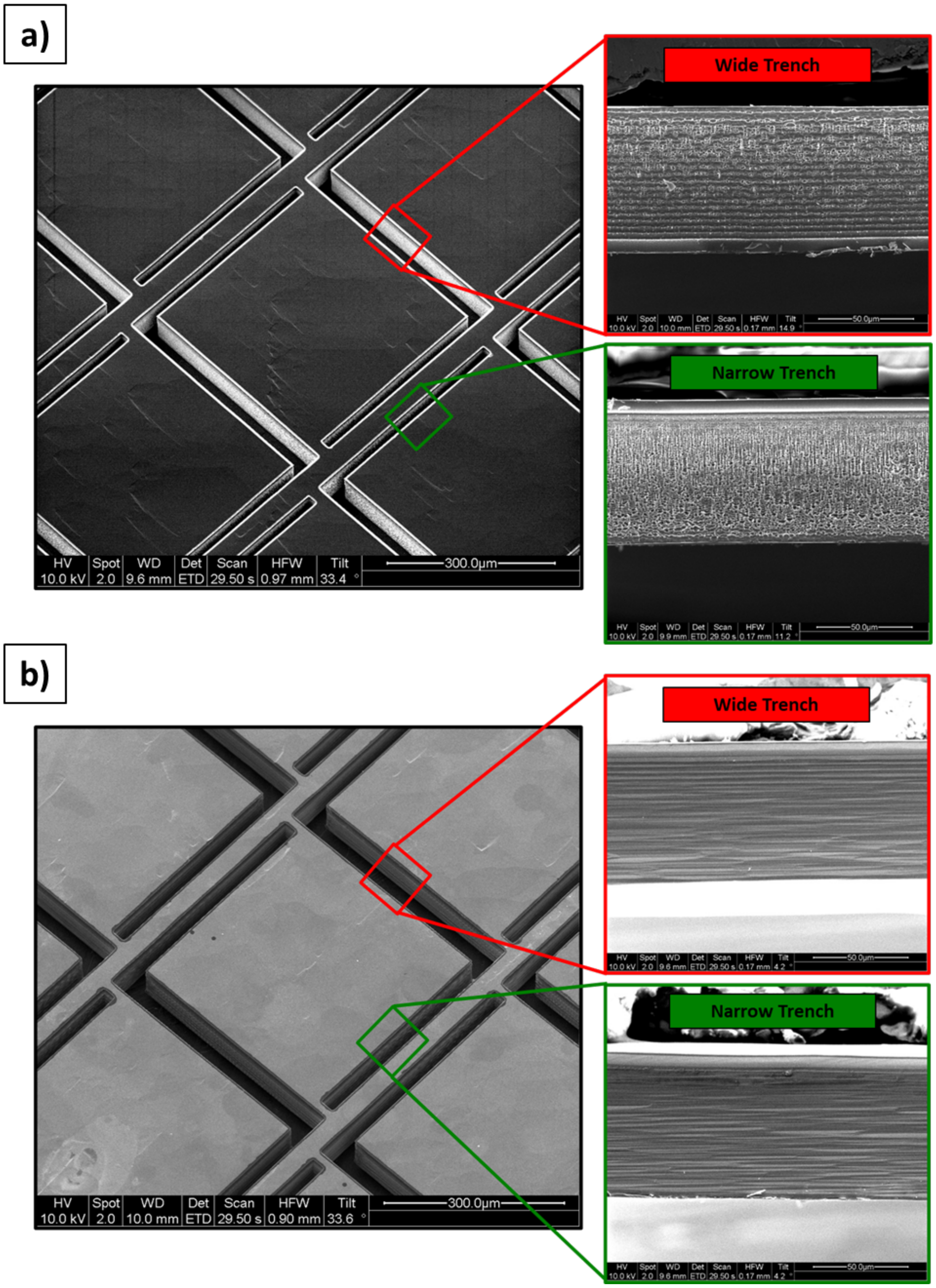

Figure 62: SEM images of DRIE-processed microcell sidewalls.
Microcell array SEM images for DRIE processing, indicating sidewall morphology with trench width, a) as-cut and b) after etching in 3 M KOH/2 M IPA for 13 minutes at 60°C.

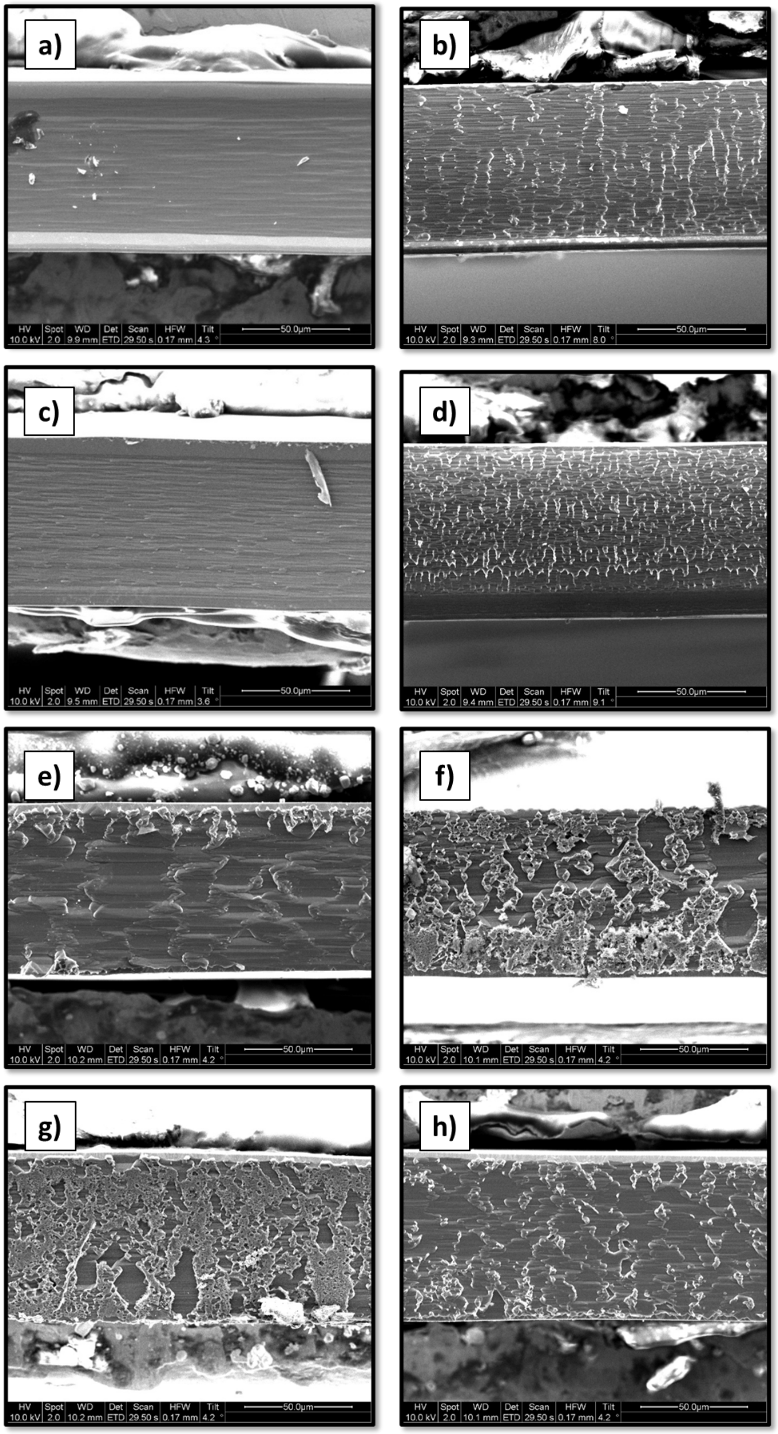

Figure 63: Sidewall geometry after damage removal for both DRIE- and laser-cut processed microcells. Varying microcell sidewall geometry after damage removal in 3 M KOH/2 M IPA for 13 minutes at 60°C, a) DRIE device; b) DRIE device; c) DRIE device; d) DRIE device; e) laser cut device; f) laser cut device; g) laser cut device; h) laser cut device.

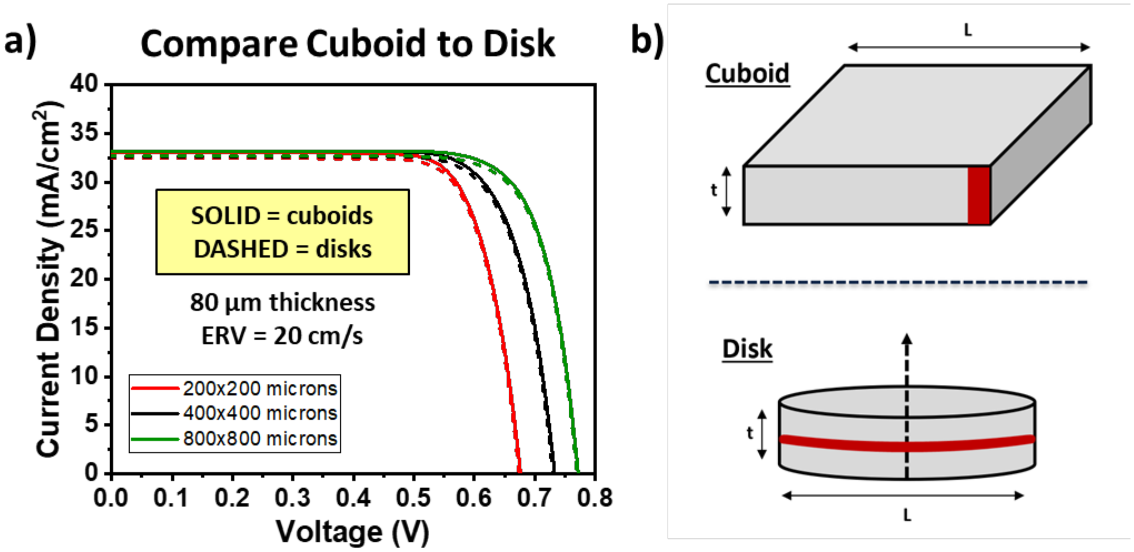

Figure 64: Simulated results for a disk vs. cuboid microcell geometry.
Sentaurus simulation results, a) simulated JV characteristic curves of both cuboid and disk microcell geometries; b) visual comparison of disk and cuboid geometries, wherein red indicates position of non-passivated anchor bar (L = width, t = thickness).

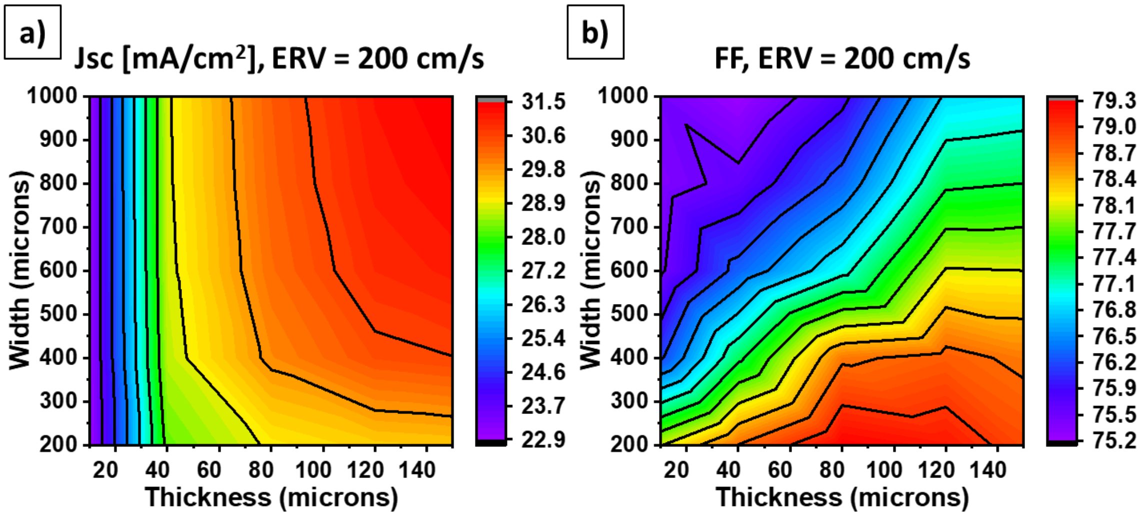

Figure 65: Simulated Jsc and FF microcell results for varied dimensions.
Sentaurus simulation results, a) microcell Jsc with varying width and thickness; b) microcell FF with varying width and thickness.

APPENDIX B: NSF I-CORPS WHITE PAPER: A PATH TOWARDS COMMERCIALIZATION FOR POWER-GENERATING WINDOWS

I. Introduction

The National Science Foundation (NSF) Innovation Corps (I-Corps) program is a 7-week intensive program, aimed at bridging the information gap between basic scientific research and technological commercialization. The program enables scientists and engineers to investigate a target industry, identify the top customer needs in this area, and evaluate product-market fit between the original scientific research and market findings. Each team accepted to this program accomplishes these tasks by conducting over 100 in-person interviews with professionals in the chosen industry and searching for commonly cited market needs across interviews. In addition, each team prepares weekly market-finding presentations before a teaching staff of established entrepreneurs. As part of the fall 2019 cohort, we chronicle the market findings learned throughout this process. We begin by introducing the team, identifying the target market as a possible commercialization pathway given our scientific research, and outline the discovery process over the 7-weeks.

As structured by the NSF, each I-Corps team consists of three distinct roles: *i)* the entrepreneurial lead(s) (EL), *ii)* the technical lead (TL), and *iii)* the industry mentor (IM). Here, David Needell and Megan Phelan, current PhD candidates at the California Institute of Technology (Caltech), serve as the ELs. In addition to conducting every interview together, ELs process the information learned and relay this interpreted data to the entire I-Corps cohort—consisting of approximately 20 teams. Harry Atwater, a professor of Applied Physics and Materials Science at Caltech, serves as the TL, providing the fundamental scientific knowledge for the intended technology. Jason Hartlove, CEO and President of Nanosys Inc., serves as the IM, coaching the team to navigate the selected industry's ecosystem, connecting the team with and strategizing for market interviews, and developing a finer sense of interview data analysis.

As described in section IV of this report, our team specializes in the research and development of solar energy technology. Through I-Corps, we investigate a singular application of a branch of our research: a power-generating, double-pane window using solar energy. Despite our team's technical expertise and demonstrated lab-scale prototypes, there exist no publicly available customer discovery and market research analyses in this application area to determine the desirability of such a product in the commercial glass and window market. However, in order to reduce potential biases in our own discovery process, we omit the intended power-generating window technology from the interview process. Instead, we focus on the commercial building industry as a whole — from window and glass manufacturing to building development to end-users — in order to understand current needs in this market. Section II describes the specific market segment and the commercial window and glass ecosystem.

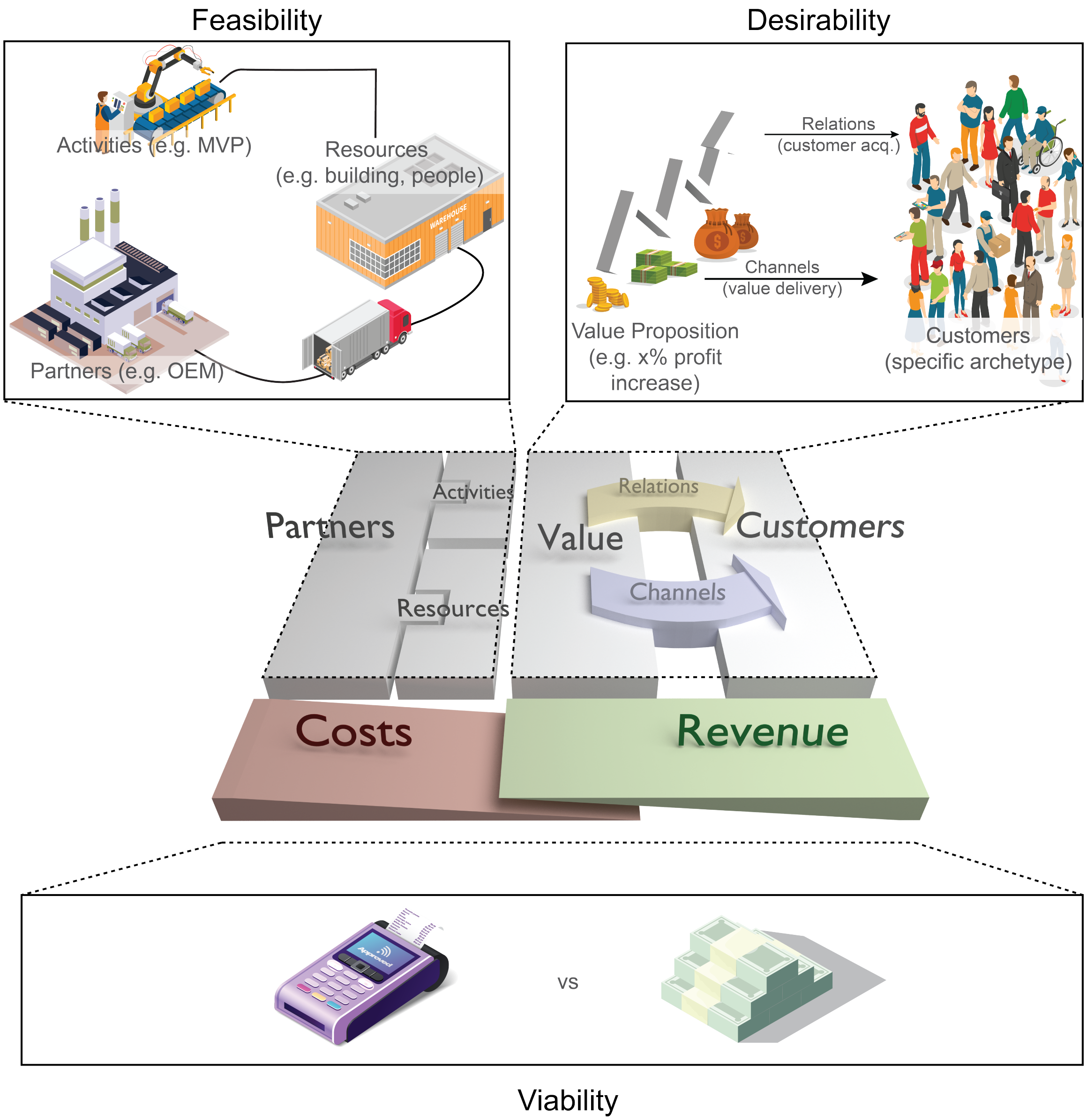

Figure 66: Business Model Canvas.
An illustration of the business model canvas (BMC) broken into three major segments: feasibility, desirability, and viability. Feasibility requires understanding how the product(s) in question can be built or developed for sale. Desirability, focused on here in this white paper, includes researching the needs and primary pain points of the potential customer and understanding what value can be given to them with the intended product. Finally, viability weighs the full costs of the product and distribution against the revenue stream from the customers.

To organize our findings and categorize how such a power-generating window product might enter into the existing commercial building market, we apply the Business Model Canvas (BMC), shown in Figure 66. Throughout this 7-week study, we continuously investigate whether there exists a product-market fit for our intended technology, or whether the technology needs to be updated to fit the market's needs. As shown in Figure 66, here we define product-market fit as an identification of a customer segment with a specific need, where our technology can meet this need and deliver value to that customer. Discovery of both the customer segment and their specific need must be identified through the interview process, with no biasing of the interviewee by discussion of our team's technology. As such, Figure 66 shows what a potential business model could look like, as well as how each component of the BMC relates to one-another and how this I-Corps customer discovery process enables identification of product-market fit.

Here we focus on the identification of specific customer segments within this commercial building ecosystem, the needs or major pain-points they experience in this role, and the top value propositions that could alleviate such pain-points. As shown in Figure 67(a), we investigate these topics through nearly 150 customer interviews across 4 countries, 14 US states, and 41 cities. Given the size and complexity of the commercial building market, as detailed in section II, we arrange our interviews to cover each step of the window value chain. Figure 67(b) illustrates the breakdown of our discovery interviews during this 7-week timeframe (October 20th through December 5th 2019): 37% of our total interviews come from manufacturers in this glass and window ecosystem; 15% from suppliers; 28% from the real estate developers, architects, engineers, and contractors; 12% from regulators; and 8% from building occupants and end-users.

In this report, we begin by carefully defining the intended market segment and providing a high-level overview into the value chain of a commercial, double-pane window. We next discuss our interview findings as they pertain to the customer segments and value propositions within this market. We then include a brief description of our team's core technology, including a review of how such a power-generating window could operate in layman's terms. Finally, we offer a conclusion of our findings and a glimpse into how power-producing windows could obtain product-market fit in certain commercial window sub-markets.

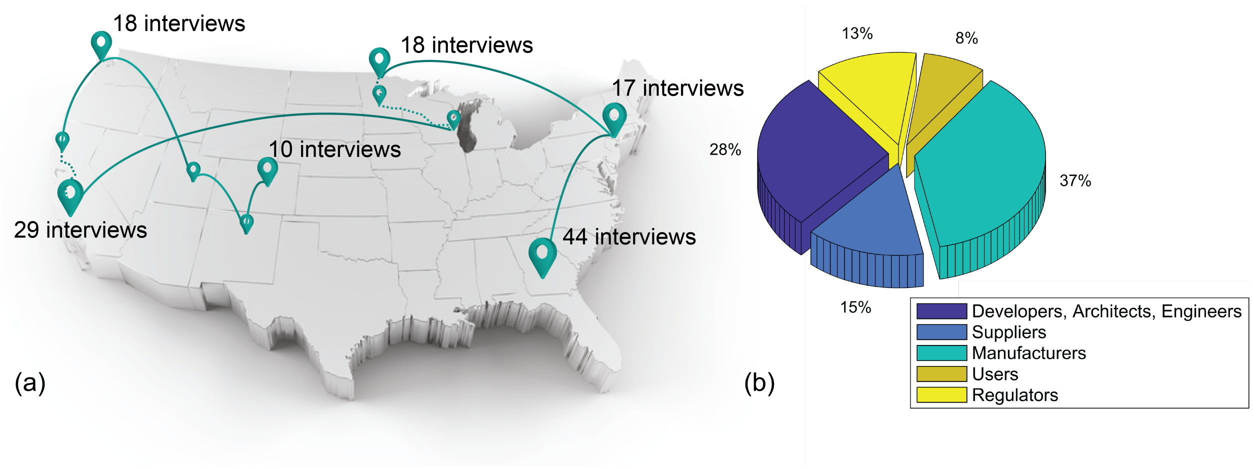

Figure 67: Map and breakdown of interviews during I-Corps program.
(a) a geographical depiction of the I-Corps interview trip across the United States (international interviews not shown here). (b) a breakdown of a total of 142 interviews with respect to the role of the interviewee within the commercial window market.

II. Commercial Building and Window Ecosystem

Before analysis of our market discovery results in terms of customer segments and key value propositions, we first develop a high-level understanding for the types of roles and window value chain within the commercial building market. More precisely, as a subsegment, we specify our ecosystem to be large-scale (>100,000 ft^2), urban high-rise building developments. Given the variability in building size, design, intended use, and development structure, this subsegmentation enables our team to both acutely pinpoint customer segments within this market and identify specific pain points and current needs of such individuals.

The value chain of a commercial building, double-pane window describes how the product goes from manufacturing, through distribution, to installation, and eventually to its end use in a large-scale high-rise. To enable a finer understanding of how customer segments of the commercial window value chain relate to one-another, we categorize roles in this ecosystem as *i)* influencer, *ii)* key decision maker, *iii)* economic buyer, and *iv)* saboteur. Influencers within the ecosystem play no direct role in either the purchase of or decision to install a given window product, but rather serve as a role that can sway such purchases or decisions. The singular key decision maker within our given subsegmented market determines whether or not to adopt a particular window technology, while the economic buyer is the customer segment that purchases the window product. Notably, the economic buyer and key decision maker may not be the same customer, as is the case for our subsegmentation. Finally, the saboteur role can either directly or indirectly stagnate and/or limit the adoption of the window product into the market.

Given these four primary roles, Figure 68 illustrates the commercial window value chain as it applies to our concept technology. As shown, we broadly arrange roles into five distinct areas: manufacturer, supplier, developer, owner, and user. Here we trace the flow of the window/glass product with dark blue arrows through the ecosystem. For the manufacturing of a window, the process starts with a glass manufacturer (e.g., Guardian Glass, Saint-Gobain, AGC, etc.) that fabricates and applies low-emissivity (low-E) coatings to large glass panes.

While power-generating windows would require wires within the window itself to deliver power to the entire building, there currently exists technology that requires wires in the glass for the building to deliver power to the window. Electrochromic (EC) windows allow building occupants to dim the brightness of their window. Such EC applications could represent a possible technology-to-market pathway for power-generating windows to follow-in or, as discussed in section III, might be a tremendous opportunity for partnership. As such, we build our window value chain by considering how EC windows fit in. For these EC window applications, EC coaters (e.g., Sage Glass, View, etc.) apply chemical films to the glass panes, following the low-E coatings from the glass manufacturer, in order to equip the glass with this dimmable feature.

Next, window manufacturers construct insulated glass units (IGUs) by adhering the electrochromic panes to standard low-E coated glass, separated by a spacer layer and filled with argon gas (e.g., Guardian Glass, Marvin Windows, etc.). Upon fabrication of the IGU by the window manufacturer, window distributors (e.g., Viracon) deliver full sets of IGUs to the construction project's on-site contact, the glazier (e.g., Benson). The IGUs often require a level of project customization of the window sizes, number of units, and low-E coatings for both aesthetic and thermal efficiency requirements. Often, the glazier works directly with the general contractor of the commercial building development team in order to coordinate the installation logistics and timelines.

For this given market subsegmentation, the real estate development company (e.g., KDC) determines which types of windows are used for a given project. However, while most developers ultimately execute the final bill of materials, they often collaborate amongst a large team with specialized skills and roles. Roles such as architects, engineers, general contractors, sub-contractors, and municipality code directors/regulators provide examples of teams that work directly with the real estate developer. Note, while Figure 68 presents a detailed value chain of the commercial building ecosystem for windows, it is not a comprehensive diagram of each involved role (e.g., sub-contractors).

Here we observe that not only do influencers, indicated in Figure 68 via blue text, contribute to the developers' choice of materials, but so do saboteurs, as shown in red text. From our discovery, one potential saboteur role stems from the municipality regulators, often requiring building aesthetics to fit within the confines of the local code. A second, higher level, saboteur relationship can occur between the real estate developer and the real estate investment trust (REIT) that finances the project. For example, if a given window technology has not demonstrated sufficient reliability and durability, REITs can prevent the adoption for such products in order to minimize risk of a project.

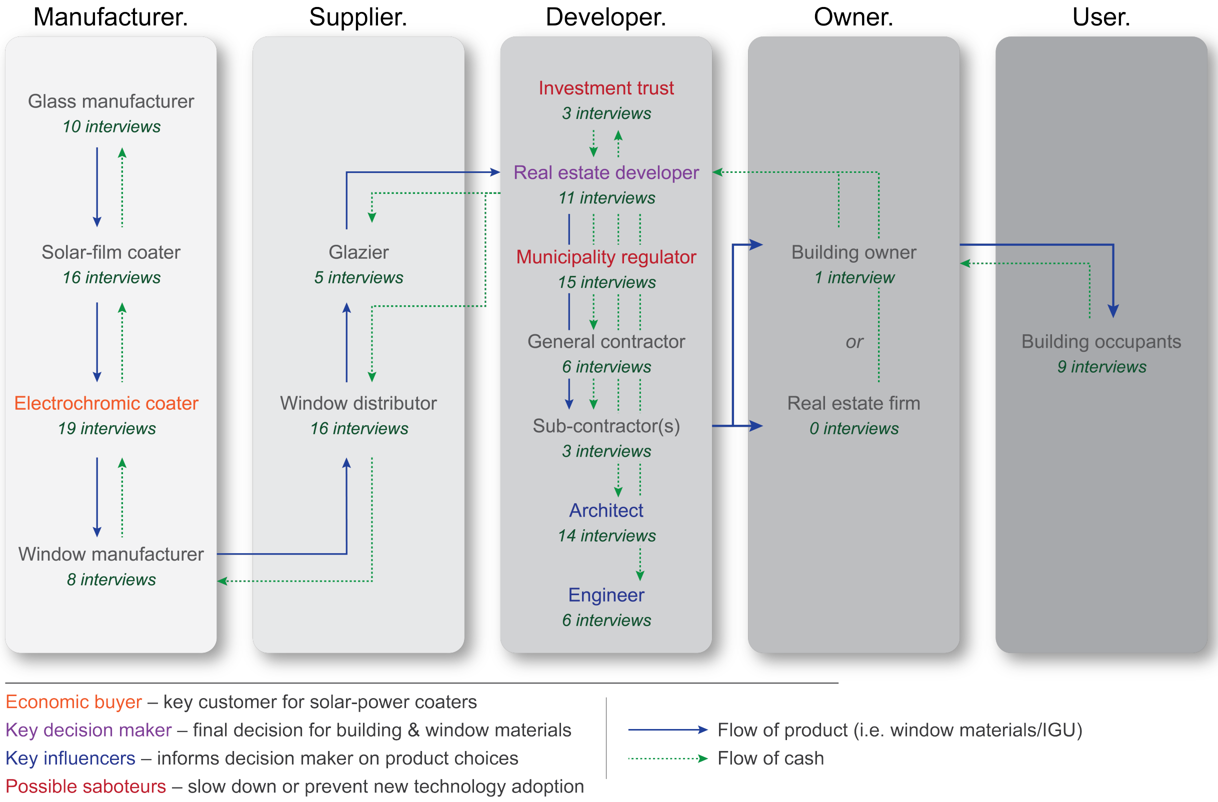

Figure 68: Commercial window value chain.
A conceptual diagram of the commercial window and glass ecosystem, tracing both the flow of product (i.e., window materials, IGU, etc.) and flow of cash through the five primary divisions and specific roles within each division. Here we also identify roles within the ecosystem: economic buyer, key decision maker, influencers, and possibly saboteurs to the adoption of new window technology. Below each specific role we give the number of interviews conducted with an employee at a firm/company that corresponds to that role.

By explicitly organizing the roles and relationships of the large-scale, commercial building window value chain, we achieve two important insights. First, the key decision maker and the economic buyer occupy two distinct roles in this value chain. For a window with power-generating capability, the intended power-generating component must either be applied before the EC coating or positioned to replace the EC coating step altogether, thereby restricting where this technology can feasibly fit into the existing value chain. As a result, the economic buyer becomes either the EC coating company or the window manufacturer. In contrast, we identify the key decision maker in this market as the commercial building developer. Second, the value proposition of the real estate developer does not always align with the value proposition of the building occupant. Real estate developers build in one of two modes: built-to-suit or speculative (spec). Built-to-suit development requires funding by the building owner before construction has begun, whereas spec projects predict that there will exist customers/occupants to whom the building can be leased after construction has ended. In either case, developers rarely own the building and, subsequently, do not value added technology to decrease the electricity or operating costs of the building.

By understanding the relationships and roles within this market, we can distinguish who becomes a customer segment, why they would need an advanced window product, and how the presence of a new technology could affect down-stream segments. To be successful, our value propositions need to apply to each of the customer roles within the ecosystem: the economic buyer, key decision maker, primary influencer(s), and end-users. With this in mind, a crucial step in evaluating product-market fit lies in interviewing a sufficient number of each customer archetype to uncover these value propositions.

III. Value Propositions and Customer Segments

Given our focus on product-market fit, here we map out the applicable customer segments for the commercial building market, and their respective value propositions. Intuitively, the most obvious value proposition for a power-generating window appears to be the lowered environmental impact. One hypothesis is that windows which could provide a lowered carbon footprint for the building envelope, due to reduced utilities, could result in a higher Leadership in Energy and Environmental Design (LEED) certification rating, which might benefit the architects, engineers, and commercial real estate developers designing a new commercial building. However, conversations with architects, engineers and developers reveal that LEED certification is not a priority to increase building occupancy. Even in regions where LEED certification is more popular in the U.S. (e.g., Northeast, West Coast), building developers do not need such certification for higher building occupancy. As key influencers, architects also do not need LEED certification in their buildings, but rather need new tools and materials to focus on building and building envelope aesthetics. Hence, for a window to provide value to an architectural firm, it must offer a novel design for a high profile building.

Although aesthetics address a necessary value proposition for the architect, different pain points exist for the commercial building developer. While a power-producing window could lead to reduced utility bills, rarely does this provide value for a developer. Few commercial building developers pay electricity bills, and so do not need energy savings for new buildings. From interviews with presidents, vice-presidents, and managers at commercial real estate development firms, we observe that achieving an increased return on investment (ROI) for a given project is their primary need. Further, we observe that developers rely heavily on increasing the occupancy rates within a building to achieve a higher ROI. Even though such developers do not need LEED certification to increase occupancy rates, many development firms do however need "soft" values (e.g., daylighting, unobstructed views, comfortable environment) to distinguish their new building and attract tenants. From our discovery, a window that could lead to increased occupancy rates would result in an increased ROI, and thus be needed by commercial real-estate developers.

Currently in the market, there exist a few types of double-pane windows that address this need for soft values. One category of such windows includes "smart glass," glass that is able to dynamically adjust the tint of the glass when voltage, light, or heat is applied. EC windows, described in the previous section, constitute one of the most common examples of smart glass in windows. Given the tunable tinting of an EC window, heating from incident sunlight can be controlled and optimized for the user experience. Moreover, such EC windows eliminate the need for building blinds, allowing for unobstructed views and continued daylighting to the building occupants. EC companies (e.g. Sage Glass, View) capitalize on both the comfortability increase for the building occupants, as well as businesses looking to yield higher productivity from each employee through the mental health benefits that accompanies an increase in natural daylighting.

Despite an emerging EC market aimed at providing commercial developers with these soft values, most smart window technology requires a small amount of input electricity. Given this, the retrofit market for US windows, which is potentially 75% larger than that of new builds, can be economically prohibitive to access for most EC companies. As a result, the majority of EC window installations today focus on new buildings. However, according to interviews with commercial window installers, most clients who choose higher end, energy efficient windows only decide to do so for their 2nd (or more) round of renovations within a building. Such installers suspect that this is due to the fact that most people do not identify the need for energy efficiency and a more comfortable environment until after they have had first hand experience with less thermally efficient windows. As such, there is potential opportunity in enabling ease of installation for EC windows by eliminating the need for electrical wiring into the building.

Through these customer discovery interviews, we observe that the original, power-generating window technology envisioned by our team does not meet the observed pain points. However, given the design flexibility in the product, coupling the originally proposed solar window technology with an EC IGU could provide a solution and enable product-market fit. As a technological pivot, we thus transition into analyzing how a self-powered EC window (using our solar energy technology) could meet the large-scale, commercial building market's needs.

Given this pivot, we develop a new set of value propositions, according to customer interviews, for a self-powered EC commercial window. Architects and engineers at commercial building firms, as previously discussed, rely on aesthetics for high-profile building designs. As such, the first value proposition (VP #1) addresses the requirement to increase project acquisition by designing high profile buildings with novel aesthetics. Self-powered EC windows accomplish VP #1 by offering an optimized user experience via tunable window tints. Discussions with commercial real estate developers reveal that the most important factor when developing a new property is a heightened ROI, which is typically achieved though increased occupancy rates. Hence, the second value proposition (VP #2) addresses the need to increase the annual ROI to >4% through increased occupancy rates. VP #2 is achieved given the additional soft values that EC windows provide, thereby leading to increased occupancy rates and heightened ROI for the commercial developer. Finally, through interviews with both EC glass coaters and commercial window installers, it is evident that the current cost of installation for an EC window is a major pain point. The third value proposition (VP #3) of such a window addresses the need to increase profit margins by 10 - 20% through decreased cost of window installation. VP #3 is achieved by enabling self-powered EC windows, which no longer require an electrician for installation.

During each interview that we conduct, we track whether our hypothesized value propositions are a *i)* must have, *ii)* nice to have (but not necessary), or *iii)* not needed for the interviewed person. Figure 69 displays the breakdown of responses for each of the value propositions tested in this market subsegmentation. As shown in Figure 69, increasing the number of LEED points (VP#4) is not needed, and thus has been invalidated as a hypothesis and not included in our final value propositions list for a self-powered electrochromic window.

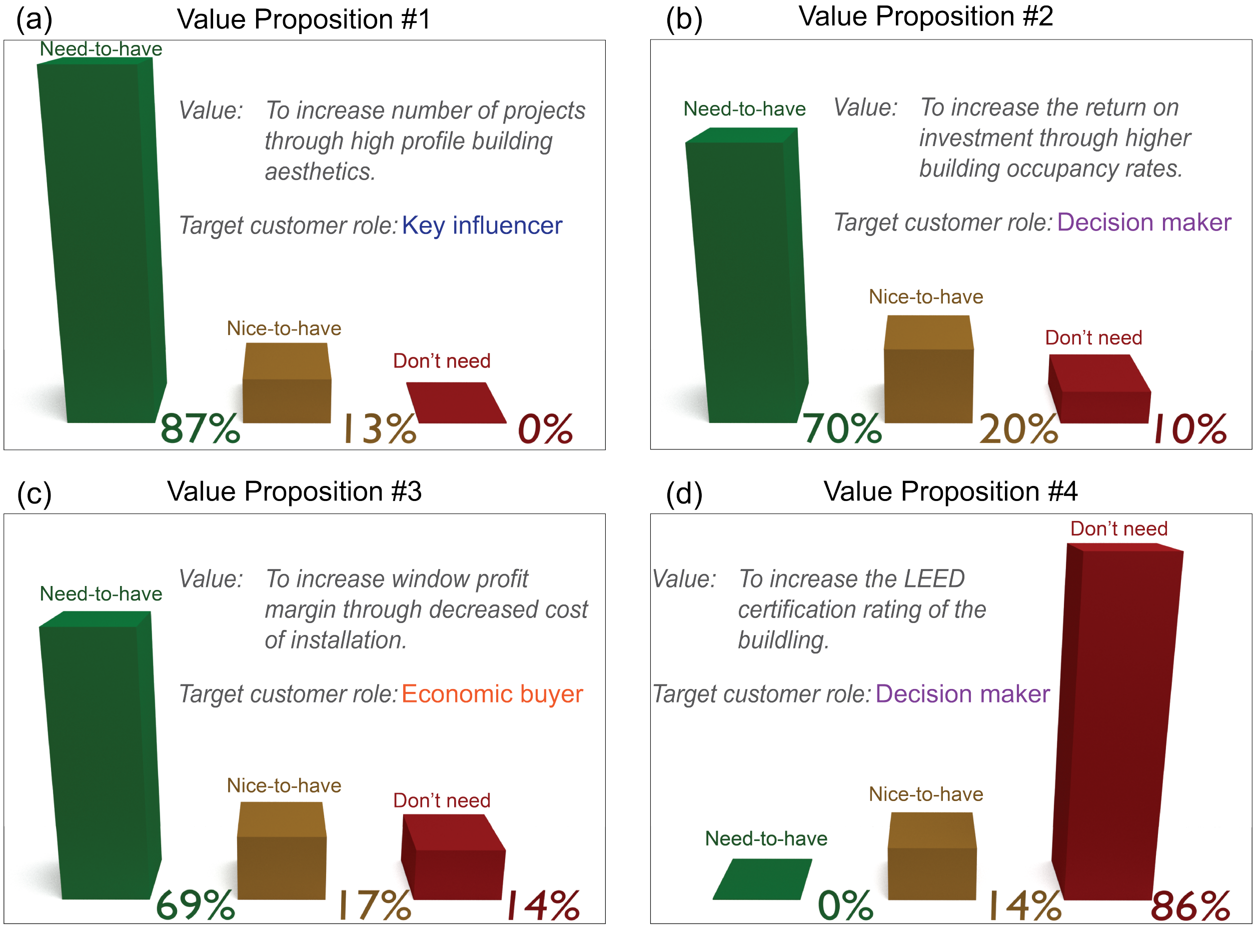

Figure 69: Potential value propositions for a power-generating window
An analysis of how four key value propositions, relevance tested through interviews, map to customer segments in the commercial window market. Green, yellow, and red bars correspond to customer interview's identifying the specific value proposition (1, 2, 3, 4) as a "need-to-have," "nice-to-have," or "don't need." For each value shown in (a), (b), (c), and (d), we identify the customer role targeted for that value.

When determining customer segments, it is important to understand who will benefit from each of the above value propositions. As shown in the Business Model Canvas (Figure 66), value propositions must map to a specific customer segment (i.e., a single value should not be proposed for all customers). The role of each customer segment in the value chain—*i)* economic buyer, *ii)* key influencer, and *iii)* decision maker—must further be understood, as discussed in section II. In other words, who would buy the window film, who would influence adoption of these new windows, and who would ultimately decide to install the window in a new building. Within each box in Figure 69, which identify the specific value chain position that would benefit from the respective value proposition.

IV. Intended Technology for Commercialization

To build the intended power-generating component for such windows, we propose an alternative solar energy technology. Solar photovoltaic (PV) energy is the process of transforming sunlight into usable electricity. Currently, nearly 90% of the global market share of installed energy generation technology consists of non-renewable sources of energy (e.g., coal, natural gas, petroleum). However, renewable technology has quickly gained traction over the past two decades, more than doubling its market share since the beginning of the 21st century. Solar PV, specifically, has grown by more than 300 times in this timeframe. The dramatic decrease in cost of PV technology has represented one of the main drivers in this market growth.

Despite over seven decades of research into novel materials and methods to transform sunlight to electricity, crystalline silicon (c-Si) remains the dominant element used in PV. In fact, c-Si solar panels make up close to 93% of the total deployed PV market. Over the past 40 years, the cost of c-Si material and processing has decreased by more than 99%; this reduction in cost coupled with the ubiquity of c-Si technology in the PV market has enabled the 300-fold increase in solar energy generation capacity. As a result of this decrease in materials cost, the most expensive part of a solar panel today is not actually the panel itself. Rather, aspects of solar PV—like the system hardware (racking/mounting the panels) and the land permits—now occupy over 60% of the total cost of solar energy.

Given the shift in solar energy from materials costs to systems/installation costs, new application areas for solar PV are actively being investigated. One such application is known as building-integrated PV (BIPV), which attempts to unify two, traditionally, distinct concepts: building materials (walls, windows, roof shingles, etc.) and solar PV panels. By joining these two areas, additional installation costs (system hardware, land permits) for the solar PV are minimized, as these costs are seamlessly integrated into the installation cost of the building material. While promising from an economic perspective, in order to disseminate BIPV as a commercial product into the building market, each customer segments' key value propositions must be met, as evidenced in this study.

An active area of scientific research, on both the academic and industrial levels, involves blending solar PV with double-paned windows (i.e. IGUs). Most commercial building windows transmit less than half of the incident light through their windows, typically reflecting the other 50% of light. By blending solar PV with window glass, the concept involves transforming the otherwise reflected light into electricity. This on-site, clean energy could provide a significant amount of generated power directly to the building. Several companies and research/development teams are actively working in this area of BIPV window technology (e.g. Ubiquitous, UbiQD, Next Energy Technologies, Onyx Solar).

While there is a singular challenge to provide a glass pane with the dual functionality of both transparency and electricity generation, there are several PV materials and methods to approach this task. One such method involves redirecting a portion of the incident sunlight to hidden cells throughout the window. This technology, known as a luminescent solar concentrator (LSC), accomplishes this light-redirection through nanoscale particles (naked to the human eye), which are specialized to appear colorless within the glass pane. These nano-particles, termed luminophores, can absorb a fixed portion of incident light and redirect that light at wavelengths beyond the visible spectrum. By printing micro-scale solar PV devices or "cells"—each smaller than a single grain of sand—uniformly across the glass pane, the redirected light can reach these nearly invisible solar cells and generate electricity. **Figure 70** conceptualizes this LSC device as it applies to a commercial window IGU.

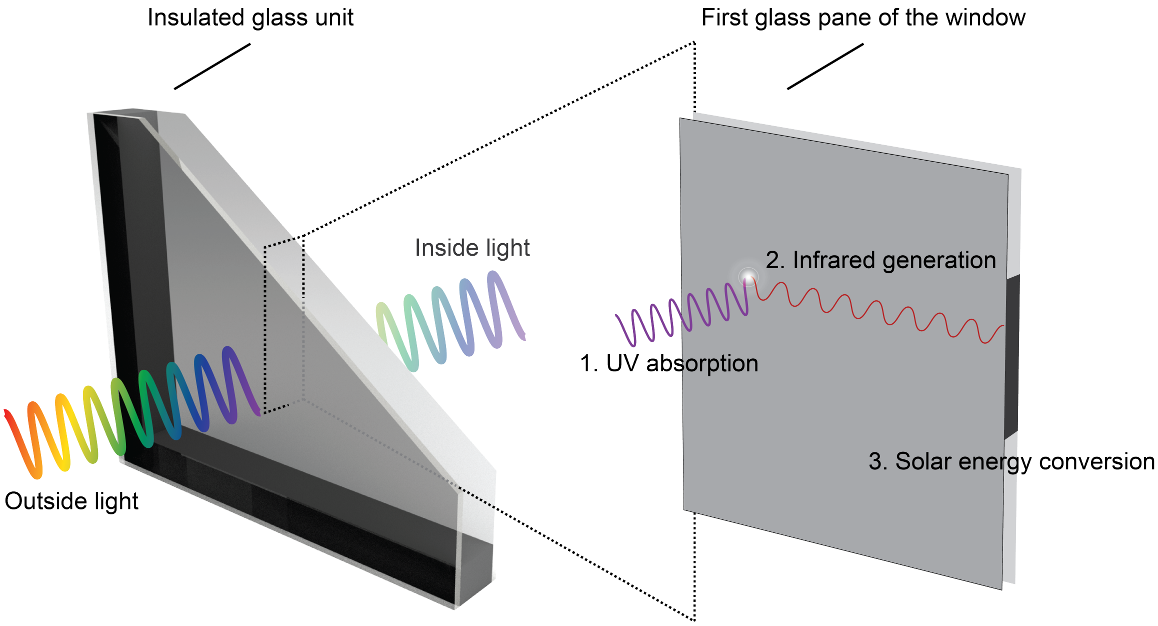

Figure 70: Illustration of a power-generating IGU design.
The concept of an insulated glass unit window that can generate electricity. Outside light, which a portion consists of ultraviolet (UV) light, is incident upon the first surface of the window (S1). Within this first glass plane, nanoscale particles absorb UV light and from this generate infrared (IR) light within the pane. The IR light can then be collected by solar cells. The remainder of the incident light passes through for building daylighting.

Despite the potential of BIPV to decrease the cost of solar energy, we find that the key value proposition for the commercial building window market is to reach higher building occupancy rates for the developer (and in turn a higher ROI). As discussed in section III, this increase in occupancy rate can be achieved through "soft" values, not necessarily through on-site energy generation. The data shown here implies that a technological paradigm shift is needed, away from valuing the electrical power generated from the window and toward boosting the comfort and aesthetics of a commercial building. One promising method, as discussed in section III, involves enabling a self-powered electrochromic (EC) window. Such a window could act as a drop-in replacement for traditional IGUs, thereby spurring higher market penetration of tintable windows. Moreover, this could open a new market for ECs: an economically viable method for ECs as window retrofits in existing/older buildings. Despite the potential product-market fit for this technology, there exists significant risk in the window market as a whole given the historically inertial technology adoption in this space. Further, EC technology itself presents as a potential risk due to varied desirability and product assessment by end-users.

V. Conclusion

Through 150 customer discovery interviews, we identify and detail the value chain of a commercial, double-pane window, and further pinpoint the value propositions and customer segments associated with a power-generating commercial window. We find that the key influencers in this ecosystem (architects) are most concerned with aesthetics, and thus a next-generation commercial window technology must bring novel aesthetics to a building. We additionally identify that the key value proposition for the decision maker in this ecosystem (commercial real estate developer) is an increased return-on-investment due to heightened occupancy rates, which are commonly achieved through soft values. Although power-generating windows do not address this need, electrochromic windows, which enable dimmable window tinting, provide these soft values through additional thermal comfort, daylighting, and unobstructed views. However, EC windows require independent power generation in order to reach new markets (e.g., retrofit). By coupling power-generating window technology with an EC window, a self-powered EC window could increase the market impact of existing EC windows. However, significant risk exists in this commercial window value chain given that the mismatch of incentives within this ecosystem. Namely, the key decision maker (developer) and the economic buyer (EC coater) occupy two distinct roles, and the value proposition of the real estate developer does not often align with that of the end user (building occupant). While there is exciting opportunity for a self-powered EC window technology, additional customer discovery is necessary to assess both the desirability and feasibility of such a technology.

VI. Acknowledgements

We would like to thank the National Science Foundation and the California Institute of Technology for the opportunity to participate in this immersive program, as well as the Venture Well teaching staff for their continued instruction throughout the 7-week program. Thank you to Harry Atwater, our Technical Lead, and Jason Hartlove, our Industry Mentor, for constant mentoring, support and guidance while conducting interviews and building out our analyses. Finally, thank you to each of the individuals with whom we spoke and interviewed during this process. We thank you for taking the time to speak with us and helping us understand each part of the commercial building window ecosystem.